FINAL REPORT

NASA GRANT NSG-2075

Covering the Period

September 1, 1975

To

August 31, 1978

(NASA-CR-157784) [LUNAR MAGNETIC PERMEABILITY, MAGNETIC FIELDS, AND ELECTRICAL CONDUCTIVITY TEMPERATURE] Final Report, 1 Sep. 1975 - 31 Aug. 1978 (Santa Clara Univ.) 131 p HC A07/MF A01 G3/91 N79-10985 Unclas 35816

Submitted by

Curtis W. Parkin

Principal Investigator

Department of Physics

University of Santa Clara

Santa Clara, California

TABLE OF CONTENTS

		Page
I.	INTRODUCTION	1
II.	SCIENTIFIC RESULTS	2
	A. Electrical Conductivity Temperature, and Structure of the Lunar Crust and Deep Interior	2
	B. Lunar Magnetic Permeability and Iron Abundance; Limits on Size of a Highly Conducting Lunar Core	6
	C. Lunar Remanent Magnetic Fields: Present-Day Properties; Interaction with the Solar wind; Thermoelectric Origin Model .	8
III.	PUBLICATIONS AND PRESENTED PAPERS	12
	APPENDIX - Publications Listed in Section III	14

I. INTRODUCTION

In the time period 1969-1972 a total of five magnetometers were deployed on the lunar surface during four Apollo missions. Data from these instruments, along with simultaneous measurements from other experiments on the moon and in lunar orbit, have been used to study properties of the lunar interior and the lunar environment. The principal scientific results resulting from analyses of the magnetic field data are discussed in Section II. The results are presented in the following main categories: (1) Lunar electrical conductivity, temperature, and structure; (2) Lunar magnetic permeability, iron abundance, and core size limits; (3) the Local remanent magnetic fields, their interaction with the solar wind, and a thermoelectric generation model for their origin. In Section III relevant publications and presented papers are listed. Copies of publications resulting from the research funded by this grant are included in the appendix.

II. SCIENTIFIC RESULTS

Magnetometers placed on the lunar surface and in orbit about the moon have returned a wealth of information about the moon which was not anticipated prior to the Apollo manned lunar missions. Analyses of lunar magnetic data have been used to study the following properties of the moon: Electrical conductivity, temperature, and structure of the lunar crust and deep interior; Lunar magnetic permeability and iron abundance, and inferred limits on size of a highly conducting lunar core; and Lunar surface remanent magnetic fields: present-day properties, interaction with the solar wind, and origin by thermoelectric generation.

A. Electrical Conductivity, Temperature, and Structure of the Lunar Crust and Deep Interior

Electrical conductivity of the lunar interior can be studied by analysis of two types of global induction fields: the poloidal field due to eddy currents driven by time-varying external magnetic fields, and the toroidal field due to unipolar currents driven through the moon by the motional solar wind $\underline{V}x\underline{B}$ electric field. Poloidal field induction has been used by many researchers to investigate lunar electrical conductivity, and to date poloidal induction analysis has yielded the most accurate conductivity information at depths greater than 200 km. At shallower depths where the poloidal technique is limited by instrumental frequency response and number of measurement sites, a toroidal induction analysis technique is used to determine the upper limit of conductivity of the lunar crust. Since the conductivity is related to temperature, a global temperature profile can be calculated for an assumed compositional model of the lunar interior. Furthermore, structural properties of the lunar interior can be inferred from characteristics of conductivity and temperature profiles and correlations with results from other

geophysical instruments on the moon.

1. Conductivity at depths greater than 200 km. When the moon is in the solar wind, lunar eddy current fields form an induced lunar magnetosphere which is distorted in a complex manner due to flow of solar wind plasma past the moon. The eddy current field is compressed on the day side of the moon and is swept downstream and confined to the "cavity" on the lunar night side. Because of the complexity, early analysis included a theory for transient response of a sphere in a vacuum to model lunar response as measured on the lunar night side. An analysis was also applied to time series magnetometer data taken on the lunar day side using a theory for transient response of a sphere immersed in a completely confining plasma.

The most thorough and accurate analysis, using time-dependent poloidal response of a sphere in a vacuum, has been applied to data measured in the geomagnetic tail where plasma confinement effects are minimized. Two basic techniques have been applied to analysis of poloidal induction data measured with the moon in the geomagnetic tail. The first method used simultaneous measurements by the Apollo 12 lunar surface magnetometer (which measures total response field at the lunar surface) and an Explorer 35 orbiting magnetometer (which measures the external driving field). The second uses simultaneous measurements of the total response field by two surface magnetometers (Apollo 15 and 16 LSM's) and one close-orbiting magnetometer (Apollo 16 subsatellite). The first technique has been applied to the single largest transient measured with the moon in the geomagnetic tail; both techniques are applicable to aggregate "transient events" made up of a linear superposition of smaller events.

Results of the different poloidal induction analysis techniques have been consistent, and an evolution of improved computer analysis capabilities and use of more data as it has become available, have yielded the following

characteristics of the conductivity profile: The lunar conductivity rises rapidly with depth in the crust to $\sim 10^{-3}$ mhos/meter at a 200 to 300 km depth, which corresponds to the upper-mantle boundary reported in seismic results. From 300 to 900 km depth the conductivity rises more gradually to 3×10^{-2} mhos/m.

2. Conductivity of lunar crust, at depths less than 200 km. Studies of crustal conductivity have been completed using toroidal induction analysis. In the toroidal mode a unipolar current $\underline{J}_T$ is driven by an electric field $\underline{E} = \underline{V} \times \underline{B}_E$ which is produced as the solar magnetic field $\underline{B}_E$, frozen in the solar plasma, sweeps by the moon. $\underline{V}$ is the velocity of the moon relative to the solar plasma. Corresponding to the induced current $\underline{J}_T$ is the toroidal field $\underline{B}_T$ which has a magnitude inversely proportional to the total resistance to current flow through the moon; the magnitude of $\underline{J}_T$ (or likewise, $\underline{B}_T$) is limited by the region of lowest conductivity in the current path, that is, the lunar crust.

An upper limit on the electrical conductivity of the lunar crust has been determined from upper limits on toroidal induction in the moon by the solar wind $\underline{V} \times \underline{B}$ electric field. The toroidal induction theory is used for the spherically symmetric case of the induction field totally confined to the lunar interior or near-surface regions by a highly conducting plasma. Components of toroidal field are calculated by subtracting components of the external field $\underline{B}_E$ measured by the Explorer 35-Ames magnetometer, from the total field $\underline{B}_A$ measured by the Apollo 12 lunar surface magnetometer. By comparing the appropriate components of toroidal magnetic field and electric field, the upper limit of the proportionality factor relating these variables is determined.

The quality $B_{Ty} = B_{Ay} - B_{Ey}$ is compared to the electric field

component, E_z, which is the largest of the three components for average solar wind conditions. These data are linearly correlated, with a least-squares slope $A = (-6.2 \pm 4.3) \times 10^{-2}$ sec/m, where the limits include only random statistical measurement errors. Estimates of systematic instrumental errors are based upon comparisons between Apollo 12 LSM, Explorer 35-Ames, and Explorer 35-Goddard magnetometers. From this comparison we estimate the systematic error inherent in the analysis. When systematic errors due to uncertainties in instrumental gain factors are included, the upper limit slop becomes $A \simeq 2 \times 10^{-7}$ sec/m. This factor is related to the average crustal conductivity upper limit of $\sigma_{crust} \sim 10^{-8}$ mhos/m for an assumed crustal thickness of 80 km. We note that the average crust conductivity is not a strong function of crust thickness for thicknesses $\sim$ 80 km (e.g., a 100 km crust would correspond to a 1.2×10^{-8} upper limit, and a 60 km crust would correspond to about 7×10^{-7} mhos/m.) A very thin outer shell of even lower conductivity (indicated by radar and sample measurements for depths up to $\sim$ 1 km) are consistent with this upper limit. The surface conductivity upper limit, derived from toroidal induction analysis, places an important constraint on the previous lunar conductivity profile obtained from poloidal induction analysis: it lowers the previous crust conductivity limit nearly four orders of magnitude. Electrical conductivity profile results of the lunar interior are summarized in Figure 1.

3. Lunar temperature and structure. The lunar temperature profile has been inferred from the electrical conductivity profile along with the experimentally known dependence of the conductivity on the temperature for materials used to model the composition of the lunar interior. For the thermal profile corresponding to the conductivity profile in Figure 1, assuming a lunar com-

position of olivine, the temperature rises rapidly with depth to 1100°K at 200 km. depth, then less rapidly to 1800°K at 1000 km. depth.

Structure of the lunar interior (see Figure 1) can also be inferred from electrical conductivity results. The conductivity is low for the first 200 km.; no conductivity transition is seen at the 60 km. seismic discontinuity reported by Nakamura et al. (1974, 1976) and Dainty et al. (1975), but conductivity resolution is limited at that depth. Between 200 to 300 km. depths the conductivity rises rapidly, to a value of $\sim 10^{-3}$ mhos/m. That region corresponds to the location of the seismic discontinuity between the upper and middle mantle boundary reported by Nakamura et al. (1974, 1976).

From 300 to 900 km. depth the conductivity increases steadily from 10^{-3} mhos/m to about 3×10^{-2} mhos/m. This is the region of greatest accuracy for magnetomerer results, as indicated by the error limits in Figure 1. The shape of the profile indicates that a temperature rise is responsible for this steady increase. As will be shown in the next section, a highly conducting core of maximum radius 535 km is found to be consistent with, but not required by results of permeability and conductivity analyses.

B. Lunar Magnetic Permeability and Iron Abundance; Limits on Size of a Highly Conducting Lunar Core

1. Lunar permeability. Magnetic permeability and iron abundance of the moon have been calculated by analysis of magnetization fields induced in the permeable material of the moon. When the moon is immersed in an external field it is magnetized; the induced magnetization is a function of the distribution of permeable material in the interior. Deployment of Apollo magnetometers on the lunar surface has allowed simultaneous measurements of the external inducing field by Explorer 35 and the total response field at the lunar surface by an Apollo magnetometer. The total response field measured

at the surface by an Apollo magnetometer is the sum of the external and induced fields.

From a data plot of the radial component of the surface field versus the radial component of the external field, the global lunar permeability has been determined to be $\mu = 1.012 \pm 0.006$. The corresponding global induced dipole moment is $\sim 2 \times 10^{18}$ gauss-cm^3 for typical inducing fields of 10^{-4} gauss in the lunar environment. The measured permeability indicates that the moon responds as a paramagnetic or weakly ferromagnetic sphere and that the moon is not composed entirely of paramagnetic material, but that ferromagnetic material such as free iron exists in sufficient amounts to dominate the bulk lunar susceptibility.

2. Iron abundance. After permeability μ has been determined, the magnetic susceptibility k is found from $\mu = 1 + 4\pi k$; thereafter iron abundance can be calculated for the lunar interior using compositional and thermal models of the moon. In the outer region of the moon where temperature T is below the iron Curie point T_c, the magnetic susceptibility k is $k = k_a + k_p$, where k_a is "apparent" ferromagnetic susceptibility and k_p is paramagnetic susceptibility. In the deeper interior where $T > T_c$, $k = k_p$. Furthermore, $k_a = p\, k_f/(1 + N\, k_f)$, where N is the demagnetization factor, k_f is intrinsic ferromagnetic susceptibility of iron, and p is volume fraction of iron. Using magnetic data to determine susceptibilities, p is calculated for suitable compositional and thermal models of the lunar interior, which also incorporate and require lunar density and moment of inertia constraints.

Under the assumption that the permeable material in the moon is predominately free iron and iron-bearing minerals, the lunar free iron abundance has been determined to be 2.5 ± 2.0 wt %. Total iron abundance has been

calcualted to be 9.0 ± 4.7 wt. %. Other lunar models with a small iron core and with a shallow iron-rich layer have also been examined in light of the measured global permeability.

3. Core size limits. The lunar magnetic permeability determined from magnetometer measurements has also been used to place limits on a possible highly conducting core in the moon. For this analysis the moon is represented by a three-layer magnetic model: an outer shell of temperature (T) below the Curie point (T_c), whose permeability μ is dominated by ferromagnetic free iron; an intermediate shell of $T > T_c$ where permeability $\sim \mu_o$, that of free space; and a highly conducting core ($\sigma > 10^{+2}$ mhos/m) modeled by $\mu = 0$. This core effectively excludes external magnetic fields over time lengths of days and therefore acts as a strongly diamagnetic region ($\mu \to 0$).

A theoretical analysis has been carried out to relate the induced magnetic dipole moment to the core size. The induced dipole moment has been determined from simultaneous Apollo 12 and Ames Explorer 35 measurements to be $2.1 \pm 1.0 \times 10^{18}$ gauss-cm^3 and from simultaneous Apollo 15 and 16 measurements to be $1.4 \pm 0.9 \times 10^{18}$ gauss-cm^3. The theoretical results indicate that the core size is a function of the depth of the Curie isotherm and lunar composition, and that a highly conducting core of maximum radius 535 km is possible for the extreme case of a magnesium-silicate dominated orthopyroxene moon with a Curie isotherm depth of 250 km. Conductivity results verify this upper limit for a core of conductivity > 10 mhos/m. The minimum radius for a highly conducting core is zero, however; i.e., there is no positive indication at this time that any core of conductivity > 10 mhos/m need exist in the moon.

C. Lunar Remanent Magnetic Fields

1. Present-day properties of the remanent fields. The permanent mag-

netic fields of the moon have been investigated using surface magnetometer measurements at four Apollo sites. A lunar remanent magnetic field was first measured in situ by the Apollo 12 lunar surface magnetometer which was deployed on the eastern edge of Oceanus Procellarum. The permanent field magnitude was measured to be 38 $\pm$ 3 gammas, and the source of this field was determined to be local in extent. Subsequent to this measurement of an intrinsic lunar magnetic field, surface magnetometers have measured fields at the Apollo 14, 15, and 16 sites. Fields of 103 $\pm$ 5 and 43 $\pm$ 6 gammas, at two sites located about a kilometer apart, were measured by the Apollo 14 lunar portable magnetometer at Fra Mauro. A steady field of 3.4 $\pm$ 2.9 gammas was measured near Hadley Rille by the Apollo 15 lunar surface magnetometer. At the Apollo 16 landing site both a portable and stationary magnetometer were deployed; magnetic fields ranging between 112 and 327 gammas were measured at five different locations over a total distance of 7.1 kilometers at the Descartes landing site. These are the largest lunar fields yet measured.

2. Remanent field-solar wind interaction. Interaction of the solar wind with the remanent magnetic field has been measured at the Apollo 12 and 16 landing sites. The solar plasma is directly measured at the Apollo 12 and 15 sites and simultaneous magnetic field and plasma data show a compression of the steady field as a function of the solar wind pressure at the Apollo 12 and 16 sites. The nature of the correlation between magnetic field and plasma bulk flow pressures is shown in Figure 2, which shows data from the Apollo 12 and 16 LSM sites. The plasma bulk flow pressure and the change in the magnetic pressure from uncompressed values are related throughout the measurement range, and the magnitudes of magnetic pressure changes are in proportion to the unperturbed steady field magnitudes at each site.

2. Thermoelectric origin for crustal remanent magnetism. Measurements

of remanent magnetization in returned lunar samples indicate that magnetic fields of $\sim 10^3$ to $\sim 10^5$ gammas existed at the surface of the moon at the time of crustal solidification and cooling. A thermoelectric mechanism has been derived to model these magnetic fields as having resulted from currents flowing through cooling lava basins early in lunar history. When the crust was still only a few kilometers thick, infalling material could have penetrated it, exposing the magma beneath and forming many lava-filled basins. The resulting model (see Figure 3) has two lava basins with different surface temperatures, connected beneath the surface by magma. The model has the basic elements of a thermoelectric circuit: two dissimilar conductors joined at two junctions which are at different temperatures. The thermal emf in the circuit depends on the electronic properties of the lunar crust and the plasma; in particular, on the difference in their Seebeck coefficients. For a relative Seebeck coefficient of 10^3 $\mu V/^oK$, thermoelectrically generated magnetic fields ranging from $\sim 10^3$ gammas to $\sim 10^4$ gammas are calculated as functions of basin sizes and separations. These fields are large enough to have produced the remanence in most of the returned lunar samples. Fields as high as $\sim 10^5$ gammas (indicated for some returned lunar samples) are attainable from our model if we use upper-limit values of the Seebeck coefficient and include effects of solar-wind compression of lunar surface fields. The thermoelectric mechanism is compatible with the high degree of inhomogeneity found in measured remanent fields and with the absence of a measureable net global magnetic moment.

FIGURE CAPTIONS

Figure 1 Electrical conductivity and inferred structure of the lunar crust and interior. Results from toroidal calculations place and upper limit surface conductivity $\sim 10^{-8}$ mho/m for an assumed 80 km. lunar crust thickness. This lowers the upper limit determined in poloidal induction analysis (Dyal et al., 1976) by nearly four orders of magnitude.

Figure 2 Magnetic energy density versus plasma energy density at two Apollo sites which have different remanent magnetic fields. The magnetic energy density is computed from the difference between the compressed and uncompressed remanent fields at the Apollo sites. Plasma energy density data are calculated from Apollo solar wind spectrometer (SWS) measurements. N is the proton number density, m is the proton mass, and v is the plasma bulk speed. Apollo 12 magnetometer data are plotted versus Apollo 12 solar wind spectrometer data, while Apollo 16 magnetometer data are plotted versus Apollo 15 SWS data. SWS data are courtesy of C. W. Snyder and D. R. Clay of the Jet Propulsion Laboratory. Uncompressed remanent field magnitudes are 38 gammas at Apollo 12 and 235 gammas at Apollo 16 LSM sites.

Figure 3 Magnetic field generation by thermoelectrically driven currents. A thermoelectric voltage resulting from the thermal gradient at the surface of the cooling lava basin drives currents through the highly conducting lunar interior and solar wind. The resulting magnetic field is maximum in the crustal region lying between the two lava basins.

III. PUBLICATIONS AND PRESENTED PAPERS

A. PUBLICATIONS:

1. Dyal, P., C. W. Parkin, and W. D. Daily, "Lunar Electrical Conductivity and Magnetic Permeability," Proc. Sixth Lunar Sci. Conf., Geochim, Cosmochim. Acta, Suppl. 6, vol. 3, pp. 2909-2926, 1975.

2. Dyal, P., C. W. Parkin, and W. D. Daily, "Structure of the Lunar Interior from Magnetic Field Measurments," Proc. Seventh Lunar Sci. Conf., Geochim. Cosmochim, Acta, Suppl. 7, vol 3, pp. 3077-3095, 1976.

3. Daily, W. D., W. A. Barker, M. Clark, P. Dyal, and C. W. Parkin, "Ionosphere and Atmosphere of the Moon in the Geomagnetic Tail," J. Geophys. Res. 82, pp. 5441-5451, 1977.

4. Dyal, P., C. W. Parkin, and W. D. Daily, "Lunar Electrical Conductivity, Permeability and Temperature from Apollo Magnetometer Experiments," in the Soviet-American Conference on Cosmochemistry of the Moon and Planets; NASA SP-370 (Edited by J. H. Pomeroy and N. J. Hubbard), pp. 447-491, 1977.

5. Dyal, P., C. W. Parkin, and W. D. Daily, "Global Lunar Crust: Electrical Conductivity and Thermoelectric Origin of Remanent Magnetism," Proc. Lunar Sci. Conf. 8th, pp. 767-783, 1977.

6. Vanyan, L. L., T. A. Vnutchokova, E. B. Fainberg, E. A. Eroschenko, P. Dyal, C. W. Parkin, and W. D. Daily, "Electromagnetic Sounding of the Moon using Apollo 16 and Lunokhod 2 Surface Magnetometer Observations (Preliminary Results)," The Moon, 259-262, 1978.

B. PRESENTED PAPERS:

1. Dyal, P., C. W. Parkin, and W. D. Daily, "Global Lunar Properties from Surface Magnetometer Measurements," Lunar Science VI (6th Lunar Science Conference abstracts), pp. 226, Houston, March 1975.

2. Parkin, C. W., W. D. Daily, and P. Dyal, "Relative Magnetic Permeability and Iron Abundance of the Moon," American Geophysical Union Annual Spring Meeting, abstract no. P 16A, Washington, D. C., June 1975.

3. Daily, W. D., W. A. Barker, P. Dyal, and C. W. Parkin, "A Model Lunar Ionosphere for the Moon in the Geomagnetic Tail," American Geophysical Union Annual Spring Meeting, Abstract no. SM 70A, Washington, D. C., June 1975.

4. Barker, W. A., W. D. Daily, M. S. Clark, and P. Dyal, "The 'Lunar Wind': A Hydrodynamic Model of the Lunar Ionosphere," EOS (Trnas. Amer. Geophys. Union), 56, 1013, Dec. 1975.

5. Dyal, P., C. W. Parkin, and W. D. Daily, "Structure of the Lunar Interior from Magnetic Field Measurments," Lunar Science VII (7th Lunar Science Conference abstracts), pp. 224-226, March 1976.

6. Daily, W. D., P. Dyal, and C. W. Parkin, "Lunar Electrical Conductivity Profile from Magnetometer Network," EOS (Trans. Amer. Geophys. Union), 57, 271, April 1976.

7. Parkin, C. W., P. Dyal, and W. D. Daily, "Lunar Structure from Magnetic Induction Measurments," 3rd Workshop on Electromagnetic Induction in the Earth, Sopron, Hungary, July 1976.

8. Parkin, C. W., P. Dyal, and W. D. Daily, "Electrical Conductivity of the Lunar Crust," EOS (Trans. Amer. Geophys. Union), 57, 946, Dec. 1976.

9. Daily, W. D., P. Dyal, W. A. Barker, C. W. Parkin, and D. S. Michniuk, "Thermoelectric Origin of Lunar Remanent Magnetization," EOS (Trans. Amer. Geophys. Union), 57, 946, Dec. 1976.

10. Dyal, P., C. W. Parkin, and W. D. Daily, "Global Lunar Crust: Electrical Conductivity and Thermoelectric Origin of Remanent Magnetism," Lunar Science VIII (8th Lunar Science Conference abstracts), pp. 269-271, March 1977.

11. Parkin, C. W., P. Dyal, and W. D. Daily, "Electrical Conductivity of the Lunar Crust and Interior," Third General Scientific Assembly of the International Association of Geomagnetism and Aeronomy, Seattle, August 1977.

12. Dyal, P., W. D. Daily, W. A. Barker, and C. W. Parkin, "A Thermoelectric Model for the Origin of Lunar Magnetism," Third General Scientific Assembly of the International Association of Geomagnetism and Aeronomy, Seattle, August 1977.

13. Daily, W. D., W. A. Barker, P. Dyal, and C. W. Parkin, "Ionosphere and Atmosphere of the Moon in the Geomagnetic Tail," Third General Scientific Assembly of the International Association of Geomagnetism and Aeronomy, Seattle, August 1977.

APPENDIX - Publications Listed in Section III.

Proc. Lunar Sci Conf. 6th (1975), p 2909–2926
Printed in the United States of America

Lunar electrical conductivity and magnetic permeability

PALMER DYAL

NASA Ames Research Center, Moffett Field, California 94035

CURTIS W. PARKIN

Department of Physics, University of Santa Clara, Santa Clara, California 95053

WILLIAM D. DAILY

Department of Physics and Astronomy, Brigham Young University, Provo, Utah 84602

Abstract—Improved analytical techniques are applied to a larger Apollo magnetometer data set to yield values of electrical conductivity, temperature, magnetic permeability, and iron abundance. Average bulk electrical conductivity of the moon is calculated to be 7×10^{-4} mho/m. Allowable solutions for electrical conductivity indicate a rapid increase with depth to $\sim10^{-3}$ mho/m within 250 km. The upper limit on the calculated size of a hypothetical highly conducting core ($\geq7\times10^{-3}$ mho/m) is $0.57R/R_{moon}$. The temperature profile, obtained from the electrical conductivity profile using the laboratory data of Duba *et al.* (1974) for olivine, indicates high lunar temperatures at relatively shallow depths. These results imply that the Curie isotherm is at a depth of less than 200 km. Magnetic permeability of the moon relative to its environment is calculated to be 1.008 ± 0.005. Adjustment of this result to account for a diamagnetic lunar ionosphere yields a lunar permeability, relative to free space, of $1.012^{+0.011}_{-0.008}$. Lunar iron abundances corresponding to this permeability value are $2.5^{+2.3}_{-1.7}$ wt.% free iron, and 5.0–13.5 wt.% total iron for a moon composed of a combination of free iron, olivine, and orthopyroxene.

INTRODUCTION

DATA FROM the network of magnetometers placed on the moon by Apollo astronauts have allowed investigation of internal lunar properties. The purpose of this paper is to report our latest results of lunar electrical conductivity, temperature, magnetic permeability, and iron abundance.

Previous electrical conductivity analyses using a time-dependent transient response technique have been applied to nightside lunar data with the moon in the solar wind (e.g., Dyal and Parkin, 1971a; Dyal *et al.*, 1972), dayside data in the solar wind (Dyal *et al.*, 1973), and to geomagnetic tail data (Dyal *et al.*, 1974). Results to be presented here are calculated using data from deep in the geomagnetic tail lobes. A new transient-superposition technique is used which improves the signal-to-noise ratio in the analysis. In addition, amplitude and phase information are used for all three vector components of magnetic field data.

In our earlier work on magnetic permeability and iron abundance of the moon (Dyal and Parkin, 1971b; Parkin *et al.*, 1973, 1974), the analytical technique involved use of simultaneous data from the lunar orbiting Explorer 35 magnetometer and the Apollo 12 or 15 surface magnetometer. With the present

technique, simultaneous data from the Apollo 15 and 16 surface magnetometers are used, requiring no orbital magnetic field data. This method has the advantages of using only the higher-resolution surface magnetometers, and is insensitive to instrument offsets. The lunar ionosphere in the geomagnetic tail is modeled, and results are compared with those of Apollo subsatellite measurements (Russell *et al.*, 1974a,b). Values of lunar magnetic permeability and iron abundance are calculated taking into account effects of the diamagnetic ionosphere.

LUNAR ELECTRICAL CONDUCTIVITY AND TEMPERATURE

Lunar electrical conductivity is calculated using measurements of global eddy current fields induced by changes in the magnetic field external to the moon. The time dependence of the induced field response is a function of the electrical conductivity distribution in the lunar interior. Simultaneous measurements of the transient driving field and the lunar response field, by Explorer 35 and Apollo surface magnetometers, allow calculations of the conductivity. Detailed descriptions of the Apollo and Explorer 35 instruments are reported in Dyal *et al.* (1970) and Sonett *et al.* (1967).

Analytical technique

Data have been selected from measurements obtained in the lobes of the geomagnetic tail, during times when there is no indication of plasma effects (Anderson, 1965). The individual data sets are also subject to the following data selection criteria: (1) the magnitude of the field external to the moon (measured by the Explorer 35 magnetometer) is required to be at all times greater than 8 gammas; (2) the external field is directed approximately along the sun-earth line; (3) main qualitative features of each event are required to appear in both surface and orbital data in all three vector coordinate axes to minimize use of data with large field gradients between the two magnetometers; and (4) no plasma data are measured above the solar-wind spectrometer instrument threshold. Criteria (1) and (2) are used to insure that no neutral sheet crossings are used in the analysis. Therefore, we have chosen data for times when the lunar response can be modeled by that of a conducting sphere in a vacuum. Details of the vacuum theory are reported in Dyal *et al.* (1972, 1974).

Since the field equations governing the electromagnetic response of a sphere in a vacuum are linear, the sum of any two solutions is itself a solution. We take advantage of this principle by superimposing many driving functions (measured by the Explorer 35 orbiting magnetometer) to form an aggregate data event, and comparing this with the aggregate formed by superposition of the corresponding response functions (measured by an Apollo surface magnetometer). These aggregates have much higher signal-to-noise characteristics than do the individual events since errors such as those due to magnetometer digitization and to geotail gradients will be gaussian and tend to average out in the event-addition process. The response to the driving field aggregate is calculated for an assumed electrical

conductivity profile $\sigma(r)$, compared to the measured time series response (Apollo magnetometer data aggregate) and then reiterated by adjusting $\sigma(r)$ until the error between the calculated response and measured response is minimized.

Electrical conductivity results

The eighteen data events used in our analysis have been linearly superimposed using a 20-inch IMLAC programmable display system in a real-time interactive mode with the Ames IBM 360/67 computer. For an assumed conductivity profile the IMLAC display is used to compare the calculated response with the measured Apollo aggregate. The conductivity profile is then iteratively adjusted until the calculated response function matches the measured Apollo response. Transient aggregates for the radial and two tangential axes are shown in Figs. 1, 2, and 3. The "computer response field" in each of these figures is calculated from the conductivity profile displayed in Fig. 4. The figure insert shows a family of profiles which also fit the data and give bounds on lunar conductivity. One of the profiles shown in the insert is the homogeneous-moon profile, which gives a value of 7×10^{-4} for the average bulk conductivity of the moon.

In our analysis we assume that the electrical conductivity increases monotonically with depth from 10^{-9} mho/m at the surface (Dyal and Parkin, 1971b) and that

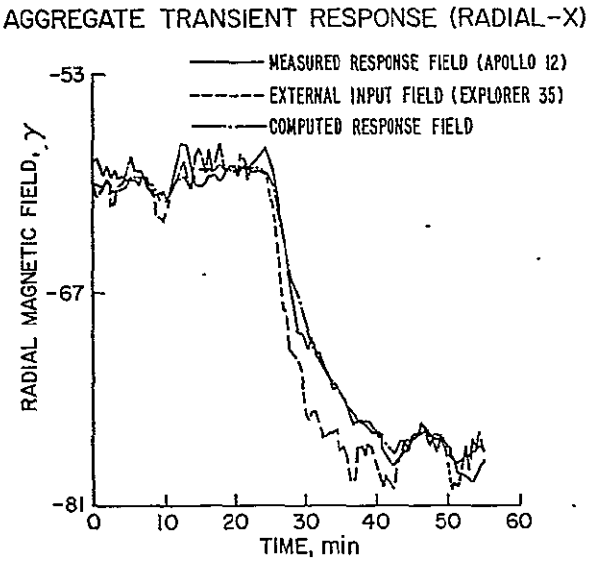

Fig. 1. Aggregate transient response (radial-x). The aggregate is the sum of radial (ALSEP x-axis) magnetic field components for eighteen events in the geomagnetic tail lobes, selected to minimize plasma effects. The external field is a sum of events measured by lunar orbiting Explorer 35 magnetometer; measured response field is the surface magnetic field aggregate of the same events measured by the Apollo 12 magnetometer. Computed response field is a theoretical response calculated for a sphere of electrical conductivity $\sigma(r)$ shown in Fig. 4.

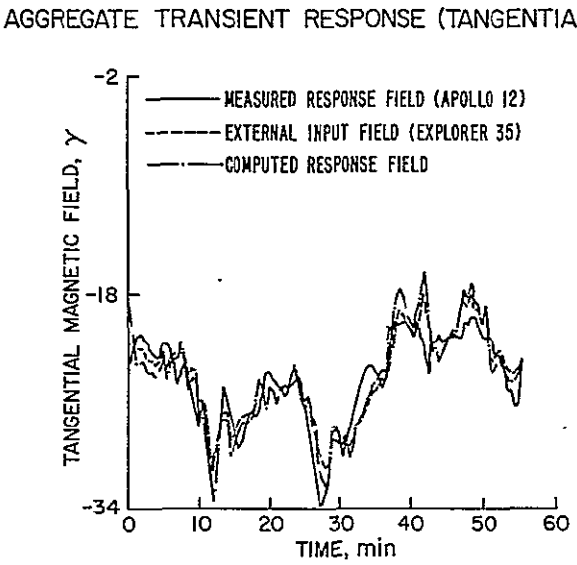

Fig 2. Aggregate transient response (tangential-y). Aggregates are the external, computed, and measured response fields for the tangential (eastward) ALSEP Y-axis corresponding to the radial X-axis data illustrated in Fig. 1.

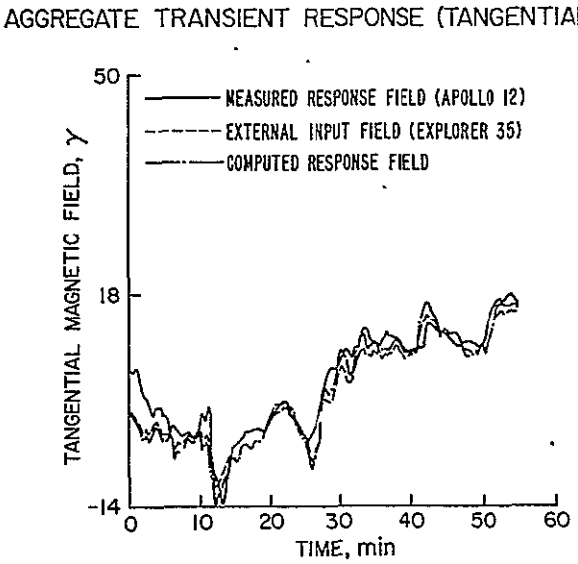

Fig. 3. Aggregate transient response (tangential-z). Aggregates are the external, computed, and measured response fields for the tangential (northward) ALSEP Z-axis corresponding to the radial X-axis data illustrated in Fig. 1.

ORIGINAL PAGE IS
OF POOR QUALITY

ORIGINAL PAGE IS
OF POOR QUALITY

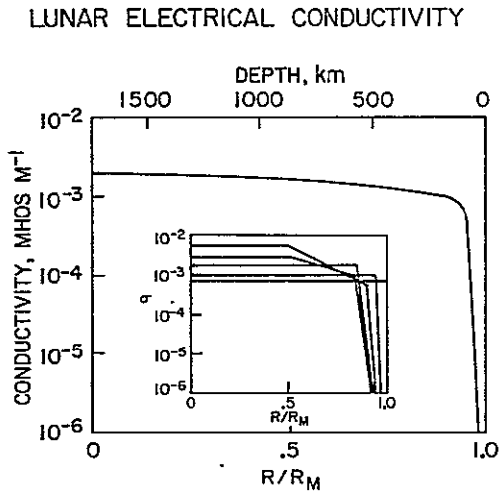

Fig. 4. Lunar electrical conductivity profile which gives "best-fit" response to the aggregate event shown in Figs. 1, 2, and 3. Insert shows other conductivity profiles which give approximate bounds on the range of allowed solutions.

it is a continuous function from the surface to the center of the moon. (The conductivity is shown for all radii in Figs. 4 and 5 since the analysis requires that the conductivity be defined throughout the entire lunar sphere.) The uncertainty in the electrical conductivity is reflected in the spread of allowable profiles shown in Fig. 4 insert. These profiles are the simplest forms that we consider appropriate for our data set: the conductivity below $0.3R_m$, however, can vary by orders of magnitude without being discriminated by our technique. These uncertainties cannot be delineated by error bars associated with individual depths because errors in the analysis are reflected by the entire conductivity function. The uncertainty in the profile arises from several factors: (1) the nonuniqueness of

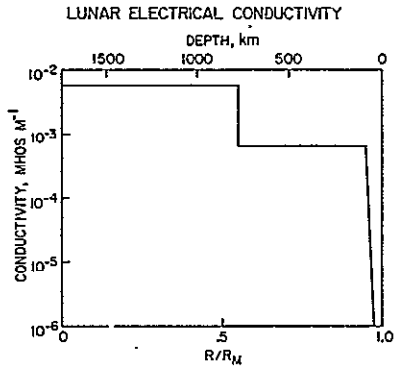

Fig. 5. Electrical conductivity profile illustrating the maximum size of a hypothetical highly conducting core of conductivity 7×10^{-3} mho/m: $R_{core} \leq 0.57R_m$

profile determination as discussed by Backus and Gilbert (1970), Phillips (1972), and Hobbs (1973); (2) the penetration depth allowed by the length of the data set used and its frequency content; (3) the frequency response limitations of the Explorer 35 and Apollo magnetometers; (4) nonhomogeneities in the external field over the dimensions of the moon; and (5) instrumental errors in the measured fields. The conductivity profiles shown in Fig. 4 are consistent with previous transient-analysis results (Dyal and Parkin, 1971a; Dyal *et al.*, 1974).

An important result of this analysis is that the lunar conductivity rises rapidly to 10^{-3} mho/m within 250-km depth and remains relatively constant to 800-km depth. We have also investigated the possibility that a partially molten core exists in the moon at a depth of approximately 800 km, as indicated by seismic results (Nakamura *et al.*, 1974). We have examined the limits that electrical conductivity analysis places upon a partially molten core, using an order-of-magnitude increase in conductivity to represent a phase change (Khitarov *et al.*, 1970; Presnall *et al.*, 1972), then determining where such a highly conducting core could exist consistent with magnetic field data. The upper limit on the size of such a core is determined to be 0.57 lunar radius, close to the value $0.55R_{moon}$ determined from seismic measurements (Nakamura *et al.*, 1974). Analysis of longer transient-event aggregates will further define the size limit on a highly conducting core in the moon.

Inferred lunar temperature

For minerals which are probable constituents of the lunar interior, the electrical conductivity can be expressed as a function of temperature, and therefore a thermal profile of the lunar interior can be inferred from the conductivity profile in Fig. 3 for an assumed material composition. Many investigators have published laboratory results relating conductivity to temperature for materials which are geochemical candidates for the lunar interior (e.g., England *et al.*, 1968; Duba *et al.*, 1972; Schwerer *et al.*, 1972; Duba and Ringwood, 1973; Olhoeft *et al.*, 1973).

Recently Duba *et al.* (1974) have measured conductivity of olivine as a function of temperature under controlled oxygen fugacity and have found the measurements to be essentially pressure independent up to 8 kbar. These measurements for olivine have been used to convert our conductivity profile of Fig. 4 to a temperature profile (Fig. 6). The Fig. 6 insert shows a family of temperature profiles which reflect the error limits of our conductivity calculations. We see from Fig. 6 that the iron Curie isotherm (~780°C) should be reached within a depth of 200 km, allowing permanently magnetized material to exist only at shallow depths in the moon. The results imply a high temperature gradient to 250-km depth (averaging 6°K/km), and rather uniform temperature from 250 to 800-km depth. Similar conclusions have been reached by Kuckes (1974) using harmonic analysis of magnetometer data with the interpretation that convection is an important process in the present day moon. Also Hanks and Anderson (1972) have theoretically calculated a thin thermal boundary layer and high temperature interior for the moon, consistent with our results.

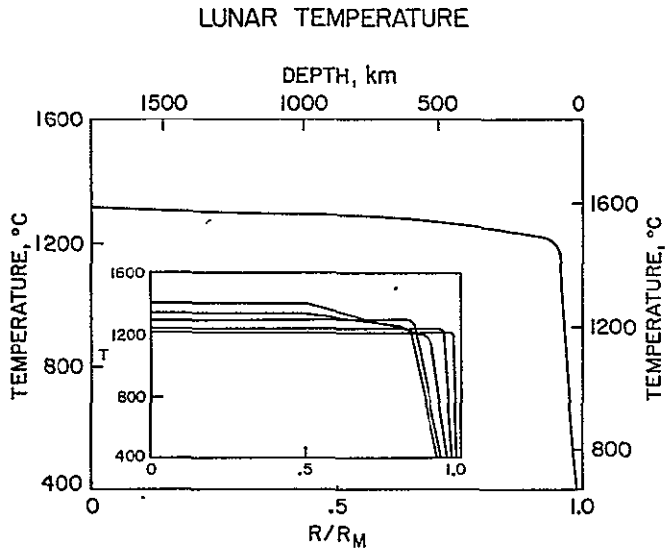

Fig. 6. Temperature profiles of the lunar interior, determined from the conductivity profiles in Fig. 4. A lunar interior composition of olivine is assumed; laboratory data for olivine from Duba *et al.* (1974) are used in the calculation.

Lunar Magnetic Permeability and Iron Abundance

Relative magnetic permeability of the moon can be calculated using data measured during times when the global magnetization field is the dominant induced lunar field. This type of induction dominates when the moon is in magnetically quiet regions of the geomagnetic tail, where the ambient external field is essentially constant and therefore eddy current induction is minimal.

Analytical technique

In previous reports (Parkin *et al.*, 1973, 1974) we calculated permeability μ using simultaneous measurements of the external field **H** by the lunar orbiting Explorer 35 magnetometer and the total surface field **B** using the Apollo 12 or 15 lunar surface magnetometer (LSM). In the present analytical method, simultaneous magnetic field data from Apollo 15 and 16 LSM's are used, requiring no orbital magnetometer data. This method has the advantages of (1) higher resolution of the LSM's and (2) results are not sensitive to instrument offsets, since calculations involve field differences, and offsets are canceled out of the analytical equations. Also, data are selected from deep in geomagnetic tail lobes where plasma effects are minimized, and 10-min averages of steady data are used so that eddy current induction effects are negligible.

Our present method involves using sets of field measurements **B** made at *two* times, each simultaneously at *two* Apollo sites (by the Apollo 15 and 16 LSM's). A description of the theoretical development is given in Appendix A. In this method

a system of twelve equations is used plus a transformation matrix relating fields measured at the two surface sites, yielding a total of 13 equations with 10 unknowns. These equations are solved for the lunar bulk relative magnetic permeability μ_b, expressed as follows:

$$\mu_b = \frac{\Delta B_{2x} - a_{11}\Delta B_{1x}}{a_{12}\Delta B_{1y} + a_{13}\Delta B_{1z}} \tag{1}$$

$$= \frac{a_{21}\Delta B_{1x}}{\Delta B_{2y} - a_{22}\Delta B_{1y} - a_{23}\Delta B_{1z}} \tag{2}$$

$$= \frac{a_{31}\Delta B_{1x}}{\Delta B_{2z} - a_{32}\Delta B_{1y} - a_{33}\Delta B_{1z}} \tag{3}$$

where subscripts 1 and 2 denote Apollo sites, e.g. site 1 can be designated Apollo 15 and site 2, Apollo 16; subscripts x, y, z, denote vector components in the ALSEP coordinate system with origin at either site, where $\hat{x}$ is directed radially outward from the lunar surface, and $\hat{y}$ and $\hat{z}$ are tangent to the surface, directed eastward and northward, respectively; a_{ij} is an element in the transformation matrix from site 1 to site 2. Each field-difference term $\Delta B_{ij} = B_{ij}(t_m) - B_{ij}(t_n)$ denotes a difference in a field component measured at the same site at two different times when field values are different. We use the generalized notation $\mu_b = \Delta_1/\Delta_2$, where Δ_1 and Δ_2 are defined as numerator and denominator, respectively, of either Eq. (1), (2), or (3).

Relative magnetic permeability results

To solve for bulk relative permeability of the moon we perform a regression analysis on the generalized field-difference parameters Δ_1 and Δ_2, shown in Fig. 7. This curve has been constructed using over 2000 simultaneous Apollo 15 and Apollo 16 magnetometer data sets, measured during five orbits of the moon through the geomagnetic tail. These data have been carefully selected to eliminate data measured in the plasma sheet or contaminated by other induction modes such as eddy current induction (see Parkin *et al.*, 1974).

Effects of plasma diamagnetism and confinement are minimized by eliminating data points for which the magnitude of the external magnetizing field $H < 7 \times 10^{-5}$ Oe. Since poloidal eddy current induction is dependent upon time rate of change of **H**, inclusion of poloidal fields is minimized by averaging over 10-min intervals during which Apollo 15 and 16 data peak-to-peak variations are small. Then pairs of data points are selected from different times, using criteria to insure that the denominators in Eqs. (1) to (3) are non-zero. Finally, a regression analysis is performed on the set of ordered pairs (Δ_1, Δ_2) plotted in Fig. 7. The least-squares best estimate of the slope, calculated using the method of York (1966), is $\mu_b = 1.008 \pm 0.005$.

Lunar magnetic permeability results adjusted for ionospheric effects

We have calculated a value for relative magnetic permeability of the moon. To determine the absolute lunar permeability and iron abundance in the moon, we

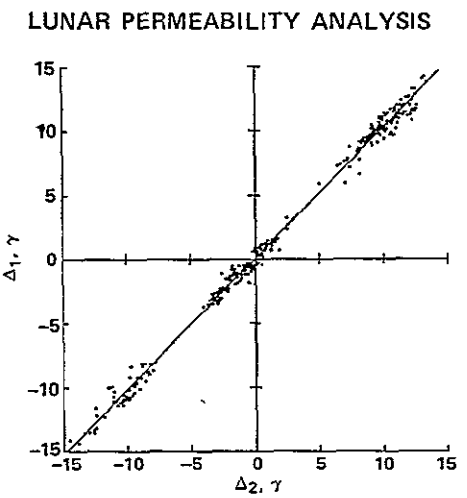

Fig. 7. Lunar permeability analysis, using all three vector axes of simultaneous Apollo 15 and 16 surface magnetometer data for five lunations in the geomagnetic tail lobes. The least-squares slope gives a value for the bulk lunar relative permeability: 1.008 ± 0.005. The parameters Δ_1 and Δ_2 are defined in the text.

consider the magnetic permeability of the environment exterior to the moon, in particular, the lunar ionosphere in the geomagnetic tail.

The lunar atmosphere (see Johnson, 1971; Hodges *et al.*, 1974) is the source of the ionosphere. The lunar atmosphere is an exosphere whose sources are neutralized solar-wind ions and neutral atoms outgassed from the moon. The species of solar-wind origin are ^{36}Ar, ^{20}Ne, ^{4}He, H_2, and H. Hydrogen and helium escape thermally with lifetimes ranging from 10^3 to 10^5 sec while ^{36}Ar and ^{20}Ne have much longer lifetimes which are controlled by photoionization.

Previous work on the lunar ionosphere has been confined to time periods when the moon is in the solar wind (Manka, 1972; Vondrak and Freeman, 1974). During the four-day period when the moon is in the geomagnetic tail, the solar wind is no longer a primary source of neutral atmosphere. He, H_2, and H thermally escape within several hours and do not contribute significantly to the lunar ionosphere. ^{20}Ne, ^{36}Ar, and ^{40}Ar are the main atmospheric constituents due to their long residence times. The ionization of the atmosphere in the solar wind is dominated by charge exchange (Weil and Barasch, 1963), whereas in the geomagnetic tail the principal process is photoionization by ultraviolet radiation from the sun. In addition, acceleration by the motional electric field has been considered to be the principal loss mechanism for ionospheric particles when the moon is in the solar wind. In the geomagnetic tail, plasma conditions are different; thermal escape, electric field acceleration, and ballistic collision with the surface are possible loss mechanisms.

The photoionization of the sunlit lunar atmosphere is determined by the solar spectrum and the photoproduction cross sections of each species. In this photoionization process the photon energy is used to ionize the neutral atoms and

ORIGINAL PAGE IS
OF POOR QUALITY

the excess energy is converted to photoelectron kinetic energy. By considering the peak photon flux and cross sections, we estimate the photoelectron energy to be about 20 eV for both Ne and Ar. We assume that the ions remain at the effective temperature of the neutral atmosphere which is in thermal equilibrium with the surface at 300°K. The thermal speeds of the high energy electrons are in excess of the escape velocity (2.4×10^5 cm/sec). However, the electrons are also electrically attracted to the ions which are gravitationally bound to the moon at the low temperature of 300°K. To consider these competing effects we consider the equations governing the behavior of both the ions and electrons of each ionized species:

$$\frac{1}{n^+}\frac{dn^+}{dz} = \frac{-g(r)m^+}{kT^+} + \frac{eE}{kT^+} \tag{4}$$

$$\frac{1}{n_e}\frac{dn_e}{dz} = \frac{-g(r)m_e}{kT_e} - \frac{eE}{kT_e} \tag{5}$$

where n^+, m^+, T^+, and n_e, m_e, T_e are the density, mass, and temperature of the ions and electrons, respectively; z is altitude above the lunar surface; $g(r)$ is the lunar gravitational acceleration; e is charge on the electron; and k is Boltzmann's constant. The electric field E is the Rosseland field, which is responsible for maintaining local charge neutrality. Since $g(r)$ takes into account the finite mass of the lunar atmosphere, solution of Eqs. (4) and (5) for the density is valid far from the moon as well as near the lunar surface. A scale height can be calculated from this distribution which depends, for the model described above, on the ion mass and the electron temperature and is about 1100 km for both neon and argon. Using an expression given by Johnson (1971) for the mean residence time τ, we can now estimate the loss rate of the ionosphere by thermal escape. We also calculate the production rate for the ionospheric constituents. Using this information we then calculate the time derivative of the ion density:

$$\frac{dn}{dt} = p - n/\tau \tag{6}$$

where p is the production rate and n/τ is the loss rate. At equilibrium $n = p\tau$.

Results indicate a characteristic ion density of approximately 10 cm^{-3} between the surface and 100-km altitude. The energy density of this ionospheric plasma is dominated by the energetic electrons, and the geomagnetic tail field is about 10 gammas. The ionospheric plasma diamagnetic permeability μ_i is derived from $\mathbf{B} = \mu\mathbf{H} = \mathbf{H} + 4\pi\mathbf{M}$, where $\mathbf{M} = -nkT\mathbf{B}/B^2$:

$$\mu_i = (1 + \beta/2)^{-1} \tag{7}$$

where $\beta = 8\pi nkT/B^2$. Using ion density $n = 10$ ions/cm^3, plasma temperature $T \cong T_e = 1.5 \times 10^5$°K and $B = 10$ gammas, we calculate the ionospheric relative magnetic permeability to be $\mu_i = 0.8$. This theoretical diamagnetic permeability for the ionosphere compares favorably with the experimental value obtained by simultaneously considering our lunar relative permeability result and the experimental lunar induced dipole moment determined by Russell *et al.* (1974a). A

two-layer (ionosphere-moon) model is used to calculate permeability of the moon and the ionosphere relative to free space (see Parkin *et al.*, 1974). The ionosphere diamagnetic permeability is calculated to be $\mu_i = 0.76^{+0.11}_{-0.10}$ and the paramagnetic permeability of the moon, adjusted for ionospheric effects, is $\mu = 1.012^{+0.011}_{-0.008}$. This result is in general agreement with previous measurements using Explorer 35 and Apollo 12 magnetometer data reported by Parkin *et al.* (1974).

Iron abundance

Using the value of global lunar magnetic permeability, we can determine free iron and total iron abundances. The free and total iron values are also constrained by lunar density and moment of inertia, and are functions of thermal and compositional models of the lunar interior.

The lunar bulk permeability $\mu = 1.012^{+0.011}_{-0.008}$ is too high to be accounted for by any paramagnetic mineral which is a likely constituent of the lunar interior, implying that some material inside the moon must be in the ferromagnetic state. Assuming the ferromagnetic material is free iron of noninteracting multidomain grains, the lunar free iron abundance can be determined using a thermal model of the lunar interior. The thermal profile is approximated by a two-layer model with the boundary located at the iron Curie point isotherm. Figures 8 and 9 show free iron abundance (q) and total iron abundance (Q) related to ($\mu - 1$) and thermal profile. Q is shown for two compositional models; we assume the moon is composed of a homogeneous mineral (olivine or orthopyroxene) of uniform density 3.34 g/cm^3, with free iron grains disbursed uniformly throughout the sphere. All assumptions and the theoretical formulation leading to Figs. 8 and 9 are outlined in Appendix B. Using the temperature profiles shown in Fig. 6, we find that the iron Curie isotherm radius R_c should be in the range $\lambda \geq 0.88$, where $\lambda = R_c/R_m$. In our calculations we use $\lambda = 0.88$.

Without adjusting our measured bulk permeability for ionospheric effects we determine free iron abundance to be 1.6 ± 1.0 wt.%. This corresponds to a total iron abundance of 6.7 ± 0.6 wt.% for the free iron/olivine model and 13.2 ± 0.4 wt.% for the free iron/orthopyroxene model. Using $\mu = 1.012^{+0.011}_{-0.008}$, which does account for the lunar ionosphere, we determine free iron abundance to be $2.5^{+2.3}_{-1.7}$ wt.%. The free iron abundance corresponds to total iron abundance of 6.0 ± 1.0 wt.% for the free iron/olivine lunar model, or 12.5 ± 1.0 wt.% for the free iron/orthopyroxene model. If we assume the lunar composition to be one or a combination of these minerals, the total iron abundance will be between 5.0 and 13.5 wt.%.

Summary and Conclusions

Lunar electrical conductivity and temperature

(1) Conductivity results presented in this paper have been determined using a new transient-superposition technique which increases the data signal-to-noise

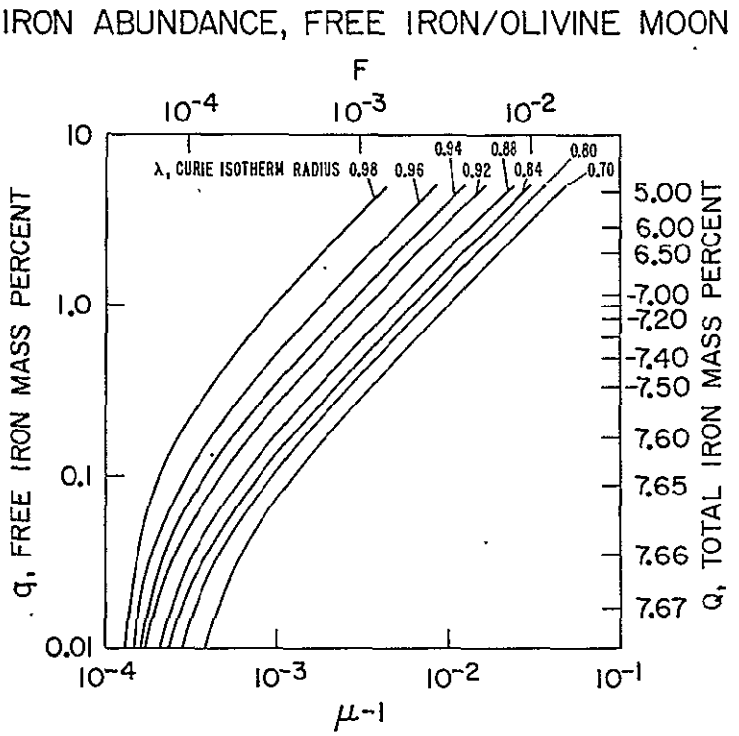

Fig. 8. Free and total iron abundances in the moon as a function of the bulk magnetic permeability μ and temperature profile of the moon, for a free iron/olivine compositional model.

ratio and uses both radial and tangential response data in the geomagnetic tail lobes.

(2) The average bulk electrical conductivity of the moon is calculated to be 7×10^{-4} mho/m.

(3) The calculated radially varying conductivity profile (see Fig. 4) rises rapidly with depth to $\sim 10^{-3}$ mho/m within the first 250 km, then remains relatively constant to 800-km depth.

(4) The limiting maximum size of a highly conducting core ($\geq 7 \times 10^{-3}$ mho/m) is calculated to be $\leq 0.57 R/R_{\text{moon}}$; that is, our present resolution allows us to probe to depths where moonquake foci have been located by seismic studies.

(5) A conversion of electrical conductivity to temperature using the data of Duba *et al.* (1974) for olivine yields a thermal profile which is relatively hot, implying that the Curie point is within 200 km of the lunar surface.

Lunar magnetic permeability and iron abundance

(1) Magnetic permeability results have been obtained using simultaneous data from the Apollo 15 and 16 surface magnetometers and requiring no orbital

ORIGINAL PAGE IS
OF POOR QUALITY

ORIGINAL PAGE IS
OF POOR QUALITY

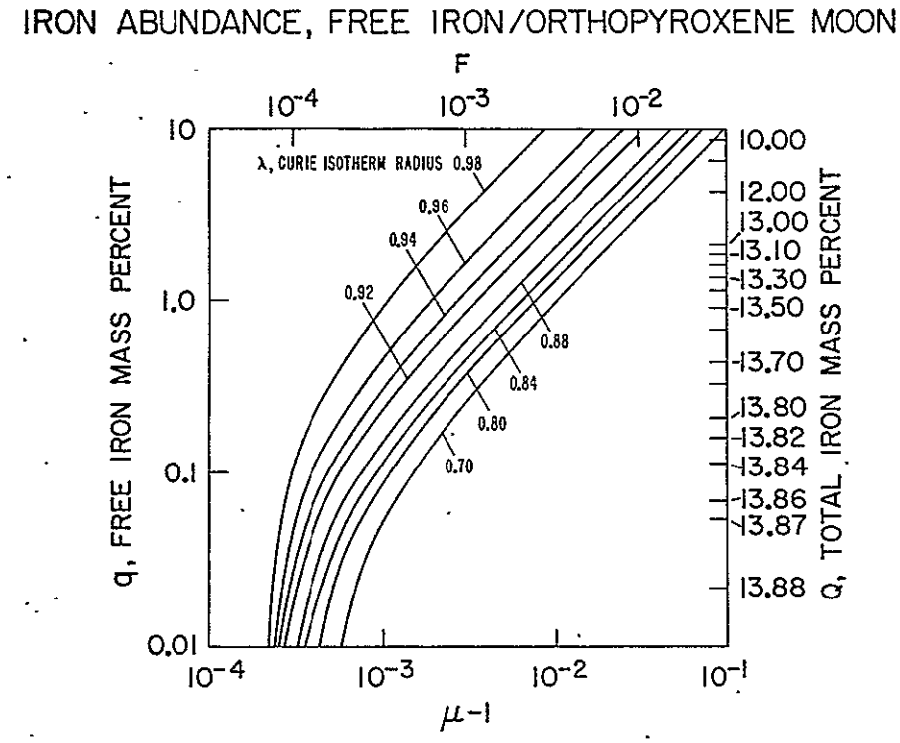

Fig. 9. Free and total iron abundances in the moon for a free iron/orthopyroxene lunar model.

magnetic field data. Both radial and tangential magnetic data are used in the analysis.

(2) The bulk magnetic permeability of the moon relative to its environment is calculated directly from magnetometer data to be $\mu_b = 1.008 \pm 0.005$.

(3) The lunar ionosphere in the geomagnetic tail is modeled, and theoretical calculations yield an ionospheric permeability of 0.8, a value consistent with surface and orbital magnetometer measurements.

(4) The magnetic permeability of the moon, adjusted for effects of its diamagnetic environment, is calculated to be $\mu = 1.012^{+0.011}_{-0.008}$.

(5) Free iron abundance is determined from our permeability and temperature calculations to be $2.5^{+2.3}_{-1.7}$ wt.%.

(6) Total iron abundance is found for two compositional models of the moon: free iron/olivine model, 6.0 ± 1.0 wt.%; free iron/orthopyroxene model, 12.5 ± 1.0 wt.%. Assuming the moon is composed of one or a combination of these minerals, the overall iron abundance will be between 5.0 and 13.5 wt.%.

Acknowledgments—The authors are especially grateful to James Arvin and Karen Neier of Computer Sciences Corporation for their diligence in rapidly developing the IMLAC programs necessary for the present analysis. We wish to thank Dr. William Barker of the University of Santa Clara and Dr.

Thomas Mucha of CSC for their theoretical work on properties of the lunar ionosphere. And once again we thank Marion Legg and her coworkers at Adia Interim Services for their excellent data reduction services. We are pleased to acknowledge research support for C. W. P. under NASA grant number NGR-05-017-027 and for W. D. D. under NASA grant number NGR-45-001-040.

REFERENCES

Akimoto S., Horai K., and Boku T. (1958) Magnetic susceptibility of orthopyroxenes. *J. Geomag. Geoelect.* **10**, 7–11.

Anderson K. A. (1965) Energetic electron fluxes in the tail of the geomagnetic field. *J. Geophys. Res.* **70**, 4741–4763.

Backus G. and Gilbert F. (1970) Uniqueness in the inversion of inaccurate gross earth data. *Phil. Trans. Roy. Soc.* A266, 123.

Bozorth R. M. (1951) *Ferromagnetism.* D. Van Nostrand.

Dana E. S. (1966) *Textbook of Mineralogy.* 4th edition by W. E. Ford, John Wiley & Sons.

Deer W. A., Howie R. A., and Zussman J. (1962) *Rock-forming Minerals.* John Wiley Co.

Duba A. and Ringwood A. E. (1973) Electrical conductivity, internal temperatures and thermal evolution of the moon. *The Moon* **7**, 356.

Duba A., Heard H. C., and Schock R. N. (1972) The lunar temperature profile. *Earth Planet. Sci. Lett.* **15**, 301.

Duba A., Heard H. C., and Schock R. N. (1974) Electrical conductivity of olivine at high pressure and under controlled oxygen fugacity. *J Geophys. Res.* **79**, 1667.

Dyal P. and Parkin C. W. (1971a) Electrical conductivity and temperature of the lunar interior from magnetic transient-response measurements. *J. Geophys. Res.* **76**, 5947.

Dyal P. and Parkin C. W. (1971b) The Apollo 12 magnetometer experiment: Internal lunar properties from transient and steady magnetic field measurements. *Proc. Lunar Sci. Conf. 2nd*, p. 2391–2413.

Dyal P., Parkin C. W., and Sonett C. P. (1970) Lunar surface magnetometer. *IEEE Trans. on Geoscience Electronics GE-8(4)*, 203–215.

Dyal P., Parkin C. W., and Cassen P. (1972) Surface magnetometer experiments: Internal lunar properties and lunar surface interactions with the solar plasma. *Proc. Lunar Sci. Conf. 3rd*, p. 2287–2307.

Dyal P., Parkin C. W., and Daily W. D. (1973) Surface magnetometer experiments: Internal lunar properties. *Proc. Lunar Sci. Conf. 4th*, p. 2229–2945.

Dyal P., Parkin C. W., and Daily W. D. (1974) Temperature and electrical conductivity of the lunar interior from magnetic transient measurements in the geomagnetic tail. *Proc. Lunar Sci. Conf. 5th*, p. 3059–3071.

England A. W., Simmons G., and Strangway D. (1968) Electrical conductivity of the moon. *J. Geophys. Res.* **73**, 3219.

Hanks T. C. and Anderson D. L. (1972) Origin, evolution and present thermal state of the moon. *Phys. Earth Planet. Interiors* **5**, 409–425.

Hobbs B. A. (1973) The inversion problem of the moon's electrical conductivity. *Earth Planet. Sci. Lett.* **17**, 380–384.

Hodges R. R., Hoffman J. H., and Johnson F. S. (1974) The lunar atmosphere. *Icarus* **21**, 415–426.

Johnson F. S. (1971) Lunar atmosphere. *Rev. Geophys. Space Phys.* **9**, 813–823.

Khitarov N. I., Slutskiy A. B., and Pugin V. A. (1970) Electrical conductivity of basalts at high T–P and phase transitions under upper mantle conditions. *Phys. Earth Planet. Interiors* **3**, 334–342

Kuckes A. F. (1974) Lunar magnetometry and mantle convection. *Nature* **252**, 670–672.

Manka R. H. (1972) The lunar atmosphere and ionosphere. Ph.D. Dissertation, Department of Space Science, Rice University, Houston, Texas.

Nagata T. (1961) *Rock Magnetism.* Maruzen Co. Ltd.

Nagata T., Yukutake T., and Uyeda S. (1957) On magnetic susceptibility of olivines. *J. Geomag. Geoelect.* **9**, 51–56.

Nakamura Y., Latham G., Lammlein D., Ewing M., Duennebier F., and Dorman J. (1974) Deep lunar interior from recent seismic data. *Geophys. Res. Lett.* 1, 137–140.

Olhoeft G. R., Frisillo A. L., Strangway D. W., and Sharpe H. (1973) Electrical properties of lunar solid samples (abstract). In *Lunar Science IV*, p. 575–577. The Lunar Science Institute, Houston.

Parkin C. W., Dyal P., and Daily W. D. (1973) Iron abundance in the moon from magnetometer measurements. *Proc. Lunar Sci. Conf. 4th*, p. 2947–2961.

Parkin C. W., Daily W. D., and Dyal P. (1974) Iron abundance and magnetic permeability of the moon. *Proc. Lunar Sci. Conf. 5th*, p. 2761–2778.

Phillips R. J. (1972) The lunar conductivity profile and the nonuniqueness of electromagnetic data inversion. *Icarus* 17, 88–103

Presnall D. C., Simmons C. L., and Porath H. (1972) Changes in electrical conductivity of a synthetic basalt during melting. *J. Geophys. Res.* 77, 5665–5672.

Ringwood A. E. and Essene E. (1970) Petrogenesis of lunar basalts and the internal constitution and origin of the moon. *Science* 167, 607–610.

Russell C. T., Coleman P. J. Jr., Lichtenstein B. R., and Schubert G. (1974a) The permanent and induced magnetic dipole moment of the moon. *Proc. Lunar Sci. Conf. 5th*, p. 2747–2760.

Russell C. T., Coleman P. J. Jr., and Schubert G. (1974b) Lunar magnetic field: Permanent and induced dipole moments. *Science* 186, 825–826.

Schwerer F. C., Huffman G. P., Fisher R. M., and Nagata T. (1972) D. C. electrical conductivity of lunar surface rocks. *The Moon* 4, 187.

Sonett C. P., Colburn D. S., Currie R. G., and Mihalov J. D. (1967) The geomagnetic tail; topology, reconnection and interaction with the moon. In *Physics of the Magnetosphere* (editors R. L. Carovillano, J. F. McClay, and H. R. Radoski), p. 380. D. Reidel.

Tebble R. S. and Craik D. J. (1969) *Magnetic Materials*. Wiley-Interscience, p. 107.

Vondrak R. R. and Freeman J. W. (1974) The lunar ionosphere. Conf. on Interactions of the Solar Wind with the Ancient and Modern Moon. (abs.), Williams Bay, Wisconsin, 1–3.

Weil H. and Barasch M. L. (1963) A theoretical lunar ionosphere. *Icarus* 1, 346–356.

York D. (1966) Least-squares fitting of a straight line. *Canadian J. Phys.* 44, 1079–1086.

Appendix A

It has been shown by Parkin *et al.* (1973) that the field on the surface of a spherically symmetric two-layer magnetically permeable sphere can be expressed as:

$$\mathbf{B} = H_x(1+2F)\hat{x} + H_y(1-F)\hat{y} + H_z(1-F)\hat{z} \tag{1}$$

where

$$F = \frac{(2\eta+1)(\mu_1-1) - \lambda^3(\eta-1)(2\mu_1+1)}{(2\eta+1)(\mu_1+2) - 2\lambda^3(\eta-1)(\mu_1-1)} \tag{2}$$

Here H is the field external to the sphere at large distances; $\eta = \mu_1/\mu_2$; μ_1 and μ_2 are relative magnetic permeability of the shell and core respectively (permeability of free space $\mu_0 = 1$); $\lambda = R_2/R_1$ where R_2 is the radius of the boundary between the two permeable regions and R_1 is the radius of the sphere. As applied to the lunar sphere Eq. (1) is expressed in the ALSEP coordinate system which has its origin on the lunar surface. The x axis is directed radially outward from the surface; the y and z axes are tangential to the surface, directed eastward and northward, respectively.

In order to measure the dipole induced in the moon by the external field H we subtract two values of B in Eq. (1) for which H is different: $\Delta\mathbf{B} = \mathbf{B} - \mathbf{B}'$. Forming this difference at two different points on the moon for the two values of the external field we have in component form:

$$\begin{aligned} \Delta B_{ix} &= (1+2F)\Delta H_x \\ \Delta B_{iy} &= (1-F)\Delta H_y \\ \Delta B_{iz} &= (1-F)\Delta H_z \end{aligned} \tag{3}$$

where $i = 1, 2$ for the two different magnetometer sites. The two fields $\mathbf{H}_i$ can be related by the transformation

$$\begin{aligned} \mathbf{H}_2 &= |\mathrm{A}|\mathbf{H}_1 \\ \mathbf{H}_1 &= |\mathrm{A}|^{-1}\mathbf{H}_2 \end{aligned} \tag{4}$$

where $|\mathrm{A}|$ is the transformation matrix relating the ALSEP coordinate systems at the two sites. Equations (3) and (4) can be solved simultaneously eliminating $\mathbf{H}_i$ to give

$$\begin{aligned} \Delta B_{2x} &= (1+2F)\left[a_{11}\frac{\Delta B_{1x}}{(1+2F)} + a_{12}\frac{\Delta B_{1y}}{(1-F)} + a_{13}\frac{\Delta B_{1z}}{(1-F)}\right] \\ \Delta B_{2y} &= (1-F)\left[a_{21}\frac{\Delta B_{1x}}{(1+2F)} + a_{22}\frac{\Delta B_{1y}}{(1-F)} + a_{23}\frac{\Delta B_{1z}}{(1-F)}\right] \\ \Delta B_{2z} &= (1-F)\left[a_{31}\frac{\Delta B_{1x}}{(1+2F)} + a_{32}\frac{\Delta B_{1y}}{(1-F)} + a_{33}\frac{\Delta B_{1z}}{(1-F)}\right] \end{aligned} \tag{5}$$

where a_{ij} are the elements of $|\mathrm{A}|$. From Eqs. (5) we have three expressions involving the induced magnetic moment HR_1^3F which are:

$$\begin{aligned} \mu_b &= \frac{\Delta B_{2x} - a_{11}\Delta B_{1x}}{a_{12}\Delta B_{1y} + a_{13}\Delta B_{1z}} \\ \mu_b &= \frac{a_{21}\Delta B_{1x}}{\Delta B_{2y} - a_{22}\Delta B_{1y} - a_{23}\Delta B_{1z}} \\ \mu_b &= \frac{a_{31}\Delta B_{1x}}{\Delta B_{2z} - a_{32}\Delta B_{1y} - a_{33}\Delta B_{1z}} \end{aligned} \tag{6}$$

with

$$\mu_b = \frac{1+2F}{1-F} \tag{7}$$

since Eqs. (5) could have been expressed with ΔB_1 as the dependent variable, Eqs. (6) can also be written interchanging 1 and 2 subscripts on the ΔB quantities and using the matrix elements of $|\mathrm{A}|^{-1}$ instead of those from $|\mathrm{A}|$.

APPENDIX B

Limits imposed on μ of Eqs. (6) in Appendix A by the LSM data can be used to calculate the lunar iron abundance for suitable lunar compositional and thermal models. Two of the models are described, including magnetic and other geophysical constraints. In both cases the lunar interior is modeled by a sphere of homogeneous composition. Free iron of multidomain noninteracting grains is assumed to be uniformly distributed throughout a paramagnetic mineral. The paramagnetic component in one case is olivine $[y\mathrm{Fe_2SiO_4} \cdot (1-y)\mathrm{Mg_2SiO_4}]$ and in the other case is orthopyroxene $[y\mathrm{FeSiO_3} \cdot (1-y)\mathrm{MgSiO_3}]$. The free iron is ferromagnetic in the regions where the temperature T is less than the iron Curie temperature T_c, and it is paramagnetic where $T > T_c$. Therefore, each model is a two layer permeable sphere where μ_1 and μ_2 are the relative magnetic permeability of the spherically symmetric shell and core respectively; R_2 is the core-shell boundary. [Equation (2) of Appendix A relates these variables to the measured magnetic moment HR_1^3F.] We consider the magnetic contributions from both free and combined iron in both the shell and core of the model with $\mu_{1,2} = 1 + 4\pi K_{1,2}$ where

$$\begin{aligned} K_1 &= K_P(y, T_1) + K_F(q) \\ K_2 &= K_P(y, T_2) + K_F'(q) \end{aligned} \tag{1}$$

and K_P is the paramagnetic susceptibility of the olivine or orthopyroxene, y is the mole fraction of ferrosilicate in the mineral, T_1 is the uniform temperature of the shell, T_2 is the uniform temperature of

ORIGINAL PAGE IS
OF POOR QUALITY

the core, K_F is the apparent ferromagnetic susceptibility of free iron in emu/cm^3, K'_F is the apparent paramagnetic susceptibility of free iron (above the Curie temperature), and q is the mass fraction of free iron in the moon.

The measured susceptibility of the free iron K_F is an apparent value which differs from the intrinsic susceptibility of iron K because of self-demagnetization of the iron grains and the fraction of iron in the moon. The apparent and intrinsic susceptibility of the free iron are related (see Nagata, 1961) by

$$K_F = \frac{q\rho}{\rho_F} \frac{K}{1+NK} \tag{2}$$

where ρ is the lunar density (assumed uniform throughout the moon), and ρ_F is the density of iron. An analogous expression relates K'_F, the apparent paramagnetic susceptibility, and K', the intrinsic paramagnetic susceptibility of free iron ($T > T_c$).

Nagata *et al.* (1957) found the susceptibility of olivine to be $2.4y \times 10^{-2}$ emu/mole at room temperature. Using this expression, the Curie law temperature dependence, and the following empirical equation for olivine density (Dana, 1966)

$$\rho_P(y) = 0.94y + 3.26\,\text{g/cm}^3, \tag{3}$$

we obtain for olivine

$$K_P = 0.14 \frac{y}{T} \frac{46y + 158}{63y + 141} \text{emu/cm}^3. \tag{4}$$

Similarly Akimoto *et al.* (1958) give the susceptibility for pyroxenes: $1.1y \times 10^{-2}$ emu/mole. From Deer *et al.* (1962) we obtain the following empirical expression for pyroxene density:

$$\rho_P(y) = 0.71y + 3.15\,\text{g/cm}^3. \tag{5}$$

Again, combining the expressions from Akimoto *et al.* and Deer *et al.* with the Curie law temperature dependence, we obtain for pyroxene

$$K_P = 0.095 \frac{y}{T} \frac{24y + 108}{32y + 100} \text{emu/cm}^3. \tag{6}$$

The lunar moment of inertia is approximately that of a sphere of uniform density (Ringwood and Essene, 1970). Choosing a uniform density for our lunar model we can write

$$\frac{1}{\rho} = \frac{q}{\rho_F} + \frac{1-q}{\rho_P(y)} \tag{7}$$

The free iron abundance q can be determined as a function of μ for the orthopyroxene/free iron model by simultaneously solving Eqs. (2) and (7) of Appendix A and Eqs. (1), (2), (5), (6), and (7) above. The olivine/free iron model solution is determined by solving Eqs. (2) and (7) of Appendix A and Eqs. (1), (2), (3), (4), and (7) above. Results for iron abundances as a function of lunar magnetic permeability are given in Figs. 8 and 9. Q, the fractional lunar mass due to both chemically uncombined and combined iron, is constrained by q and the lunar density. For the orthopyroxene/free iron model

$$Q = q + \frac{56y}{32y + 100}(1 - q) \tag{8}$$

and for the olivine/free iron model

$$Q = q + \frac{112y}{64y + 140}(1 - q). \tag{9}$$

In Eqs. (8) and (9) y can be eliminated by substitution of Eqs. (3), (5), and (7); therefore, the total iron and free iron abundances are directly related. Figures 8 and 9 show the results of these calculations relating q, Q and $\mu - 1$.

Constants used in the calculations for both models are:

uniform density of moon	$\rho = 3.34$ g/cm^3
density of free iron	$\rho_F = 7.85$ g/cm^3
demagnetization factor of iron grains	$N = 3.5$ (Nagata, 1961)
initial intrinsic ferromagnetic susceptibility of iron	$K = 12$ emu/cm^3 (Bozorth, 1951)
intrinsic paramagnetic susceptibility of iron	$K' = 2.2 \times 10^{-4}$ emu/cm^3 (Tebble and Craik, 1969)
thermal models	$T_1 = 900$°K, $T_2 = 1700$°K, $\lambda = 0.98, 0.96, 0.94, 0.92$
	$T_1 = 800$°K, $T_2 = 1600$°K, $\lambda = 0.88, 0.84$
	$T_1 = 700$°K, $T_2 = 1400$°K, $\lambda = 0.80$
	$T_1 = 600$°K, $T_2 = 1000$°K, $\lambda = 0.70$

ORIGINAL PAGE IS
OF POOR QUALITY

Proc Lunar Sci. Conf 7th (1976), p. 3077–3095.
Printed in the United States of America

Structure of the lunar interior from magnetic field measurements

PALMER DYAL

NASA-Ames Research Center, Moffett Field, California 94035

CURTIS W. PARKIN

Department of Physics, University of Santa Clara, Santa Clara, California 95053

WILLIAM D. DAILY

Eyring Research Institute, Provo, Utah 86401

Abstract—The electrical conductivity and magnetic permeability of the lunar interior have been determined from measurements by a total of six lunar surface and orbiting magnetometers. From these results, characteristics of lunar internal structure are inferred. During examination of six years of data one exceptionally large, well-behaved transient was found to be recorded when the moon was in a geomagnetic tail lobe. This single event has allowed substantial improvement in resolution and sounding depth for conductivity analysis. Also, a new technique has been applied to conductivity analysis in which simultaneous geomagnetic tail lobe data are used from a network of three instruments: the Apollo 15 and 16 lunar surface magnetometers and the Apollo 16 subsatellite magnetometer, which provides coverage around the entire global circumference. The lunar conductivity rises rapidly from $<10^{-9}$ mhos/m at the surface to $\sim 10^{-3}$ mhos/m at a depth of 200 to 300 km. This region corresponds to the upper-middle mantle boundary reported in seismic results (Nakamura *et al.*, 1974, 1976). From 300 to 900 km depth the conductivity rises more gradually to 3×10^{-2} mhos/m. In addition, the lunar magnetic permeability determined from magnetometer measurements has been used to place limits on a possible highly conducting core in the moon. Results show that the core size is a function of the depth of the Curie isotherm and lunar composition. The maximum allowable core size is 535 km for an orthopyroxene moon. Conductivity results verify this upper limit for a core of conductivity >10 mhos/m. However, both magnetic permeability and electrical conductivity analyses are consistent with the absence of a highly conducting lunar core.

INTRODUCTION

THE INTERNAL ELECTRICAL CONDUCTIVITY and magnetic permeability of the moon have been determined from measurements obtained by a network of Apollo magnetometers. In this paper we report results using an exceptionally large, unique solar transient event, which has been analyzed to give our deepest and most accurate lunar electromagnetic sounding information to date. We also report a new analytical technique using a network of three lunar magnetometers (Apollo 15 and 16 surface magnetometers and Apollo 16 subsatellite magnetometer) to calculate the electrical conductivity of the moon. This technique superimposes many time series measurements to improve the signal-to-noise ratio and utilizes both the amplitude and phase information of all three vector components of magnetic field data. The results are more accurate extensions of earlier analyses

which have been obtained from nightside lunar data with the moon in the solar wind (e.g., Dyal and Parkin, 1971a; Dyal *et al.*, 1972; Sill, 1972) dayside data in the solar wind (Sonett *et al.*, 1971; Kuckes, 1971; Sill, 1972; Hobbs, 1973; Dyal *et al.*, 1973; Leavy and Madden, 1974) and geomagnetic tail data (Dyal *et al.*, 1974, 1975; Kuckes, 1974). The magnetic permeability of the moon has been determined from both simultaneous lunar orbiting Explorer 35 and the Apollo 12 or 15 surface magnetometer data (Dyal and Parkin, 1971b; Parkin *et al.*, 1973, 1974) and by Apollo subsatellite magnetometer data (Russell *et al.*, 1974). In this paper we investigate size constraints on a hypothetical highly conducting lunar core (Goldstein *et al.*, 1976) using permeability results. Finally, we use conductivity and permeability results and other geophysical information to infer structure of the lunar interior.

LUNAR ELECTRICAL CONDUCTIVITY PROFILE

Changes in the magnetic field external to the moon induce electrical eddy currents inside the lunar sphere. The amplitude and time dependence of the magnetic fields resulting from these global eddy currents are a function of the electrical conductivity distribution in the lunar interior. Magnetic field measurements of the transient driving field and the lunar response field are obtained by Explorer 35; Apollo 12, 15, and 16 ALSEP; and Apollo 15 and 16 subsatellite magnetometers. Detailed descriptions are reported for the Apollo ALSEP instruments by Dyal *et al.* (1970); for Explorer 35 by Sonett *et al.* (1967) and Ness (1970); and for the Apollo subsatellite instruments by Coleman *et al.* (1971a, 1971b).

ANALYTICAL TECHNIQUES

Two analytical techniques have been used in this paper to calculate the lunar electrical conductivity profile. In the first technique magnetic transients are recorded simultaneously by Explorer 35 magnetometers, which measure the driving field external to the moon, and by the Apollo 12 ALSEP magnetometer, which measures the lunar response. The second technique involves transients measured on the moon by Apollo 15 and 16 surface magnetometers and in the near lunar orbit by the Apollo 16 subsatellite magnetometer. Both techniques utilize data selected in the lobes of the geomagnetic tail, during times when there is no indication of plasma effects measured by the magnetometers or by the solar wind spectrometers (Snyder *et al.*, 1970). We note that spherically symmetric vacuum theory has not been proven to be rigorously applicable to lunar induction in the geomagnetic tail lobes (Schubert *et al*, 1975). At present the theory does not exist to account for effects (if any) of low levels of lobe plasma. Lichtenstein and Schubert (1976) are investigating the theory for this case, but their results have not yet been published. Until such a theory is developed we feel analysis using vacuum theory with time-series data provides the most accurate means of lunar conductivity analysis. In our analyses we assume the moon is spherically symmetric and has relative permeability equal to unity, and that the scale length of the transient is large compared to the diameter of the moon. Since the field equations governing the electromagnetic response of a sphere in a vacuum are linear, the sum of many solutions is itself a solution, allowing us to superimpose many driving and response time series in order to enhance signal-to-noise characteristics of the data set used in the analysis.

The theory for the first technique, which has been used previously on earlier data sets, is reported in Dyal *et al.* (1972, 1974). The second technique that has just been developed during the last year uses only data obtained on or near the surface of the lunar globe. Simultaneous data measured in high-latitude regions of the geomagnetic tail are obtained by a network of three instruments: The Apollo 15 and the Apollo 16 lunar surface magnetometers and the Apollo 16 subsatellite magnetometer, the latter of which provides coverage around the entire global circumference (see Fig. 1). Measurement of the induced fields at different locations around the lunar sphere and with the inducing field in different directions permit us to examine global rather than local lunar responses. Assuming no displacement currents and that conduction currents are confined to the lunar interior, the total magnetic field can be separated into parts of external and internal origin (Chapman and Bartels, 1940). The numerical analysis program basically uses total magnetic field (B) measurements from two surface magnetometers and one near-surface magnetometer to calculate and separate the time-dependent external geomagnetic field H from the internal poloidal eddy current field P, induced in the moon by changes in H. Total fields measured at sites 1, 2, and 3 are denoted, respectively

$$\begin{aligned} {}^1\mathbf{B} &= {}^1\mathbf{H} + {}^1\mathbf{P} \\ {}^2\mathbf{B} &= {}^2\mathbf{H} + {}^2\mathbf{P} \\ {}^3\mathbf{B} &= {}^3\mathbf{H} + {}^3\mathbf{P} \end{aligned} \tag{1}$$

(All superscripts refer to site locations.) The measured field $^1\mathbf{B}$ can be transformed to site 2 and 3 coordinate systems by the transformation matrices ^2A and ^3A, respectively. The solution for the components of the poloidal field in site 1 ALSEP coordinates is

$$\begin{aligned} {}^1P_x &= -\frac{2}{3}\frac{{}^2M_y}{{}^2a_{21}} = -\frac{2}{3}\frac{{}^3M_y}{{}^3a_{21}} = -\frac{2}{3}\frac{{}^2M_z}{{}^2a_{31}} = -\frac{2}{3}\frac{{}^3M_z}{{}^3a_{31}} \\ {}^1P_y &= \frac{1}{3}\left(\frac{{}^2a_{13}{}^3M_x - {}^3a_{13}{}^2M_x}{{}^2a_{12}{}^3a_{13} - {}^3a_{12}{}^2a_{13}}\right) \\ {}^1P_z &= -\frac{1}{3}\frac{{}^2M_x}{{}^2a_{13}} + \frac{{}^2a_{12}{}^1P_y}{{}^2a_{13}} = -\frac{1}{3}\frac{{}^3M_x}{{}^3a_{13}} + \frac{{}^3a_{12}{}^1P_y}{{}^3a_{13}} \end{aligned} \tag{2}$$

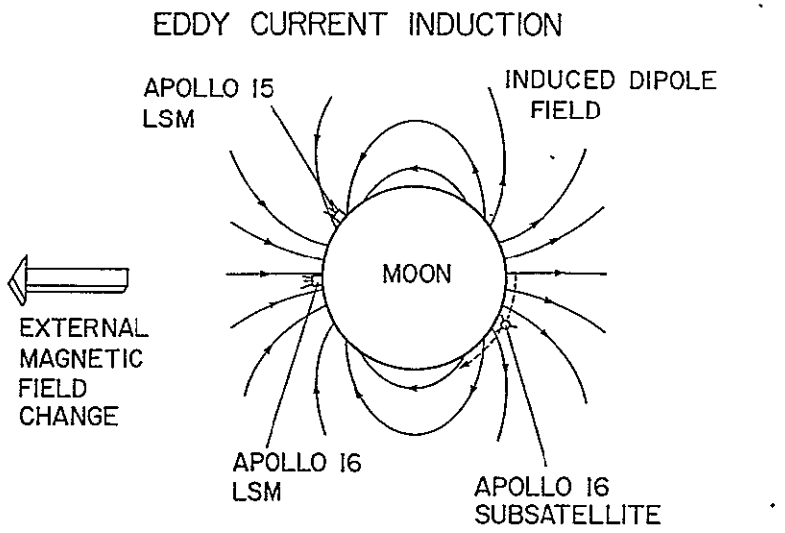

Fig. 1. Induction of poloidal eddy current magnetic fields in the moon by an external changing magnetic field. The Apollo 15 and 16 lunar surface magnetometers measure the sum of the external and induced fields at the surface. The orbiting Apollo 16 subsatellite magnetometer measures these fields from an orbit of 100 km average altitude.

where ${}^{n}\mathbf{M} = {}^{n}\mathbf{B} - {}^{n}\mathbf{A}^{1}\mathbf{B}$, n = site 1, 2, or 3. The ALSEP coordinate system has its origin at a surface site, with $\hat{x}$ directed radially outward from the moon and $\hat{y}$ and $\hat{z}$ tangent to the surface, directed eastward and northward, respectively.

Once P has been determined for a geomagnetic tail event (or for a superposition of several events), H can be obtained from $\mathbf{H} = \mathbf{B} - \mathbf{P}$. Then H is used as the external driving field in the same computer program developed in the first technique (Dyal *et al.*, 1973) which models the moon with an arbitrary radial conductivity profile $\sigma(r)$, allowing a theoretical calculation of B as a function of $\sigma(r)$. The calculated B is compared with the measured B adjusting $\sigma(r)$ iteratively until the calculated and measured values coincide. In this way a family of conductivity profiles can be determined which delineate the allowable range of conductivity versus depth. This conductivity distribution reflects errors in the data set and the nonuniqueness of the profile determination. A mathematical description of this new technique is given in Appendix A.

Large solar event

On 20 April 1970 an exceptionally large magnetic transient event was recorded at the lunar surface. The moon was located at high latitude in the north lobe of the geomagnetic tail. Magnetic field and plasma detector measurements indicated the following conditions during the entire $5\frac{1}{2}$ hour event: (1) the magnitude of the field external to the moon (measured by the Explorer 35 magnetometer) was at all times between 12 and 25 gammas; (2) the external field was directed approximately along the sun-earth line; (3) main qualitative features of the event appeared in both surface and orbital data in all three vector coordinate axes, implying no large field gradients between the two magnetometers; and (4) no plasma data were measured above the Apollo 12 solar wind spectrometer threshold during the entire solar event that was analyzed. The solar event was recorded by radio and optical solar observatories located on earth, by the interplanetary Pioneer and Vela satellites, by the earth orbiting OGO satellite, and by magnetometers on the earth and moon. The magnetic observatories on earth indicated a geomagnetic storm sudden commencement (peak K_p of 8+) eleven minutes prior to its detection at the moon. Figure 2 depicts the solar origin and propagation of this event past the earth and moon. The earth orbiting Vela satellite measured a solar wind velocity up to 400 km/sec during the passage of this large event, which accounts for the 11 minute lag between the commencement of the event at the earth and moon. The Alfvén speed in the geomagnetic tail is approximately 1000 km/sec; therefore this event is most probably the result of perturbations on the geomagnetic tail boundary by the transport of the solar disturbance through the magnetosheath. This large event was unique in that the orbital position of the moon was in the region of the geomagnetic tail where the vacuum response analytical technique could be used. This event was discovered in the Apollo data some years ago, however, it was not analyzed due to data gaps in the Ames Explorer 35 magnetometer data. The complete record of this event was obtained last year from the NSSDC which had just received the magnetometer data from the Goddard magnetometer instrument on board Explorer 35. This is the largest selenomagnetic storm event recorded under nearly ideal conditions that has been observed in over six years of lunar surface magnetic field measurements.

ORIGINAL PAGE IS
OF POOR QUALITY

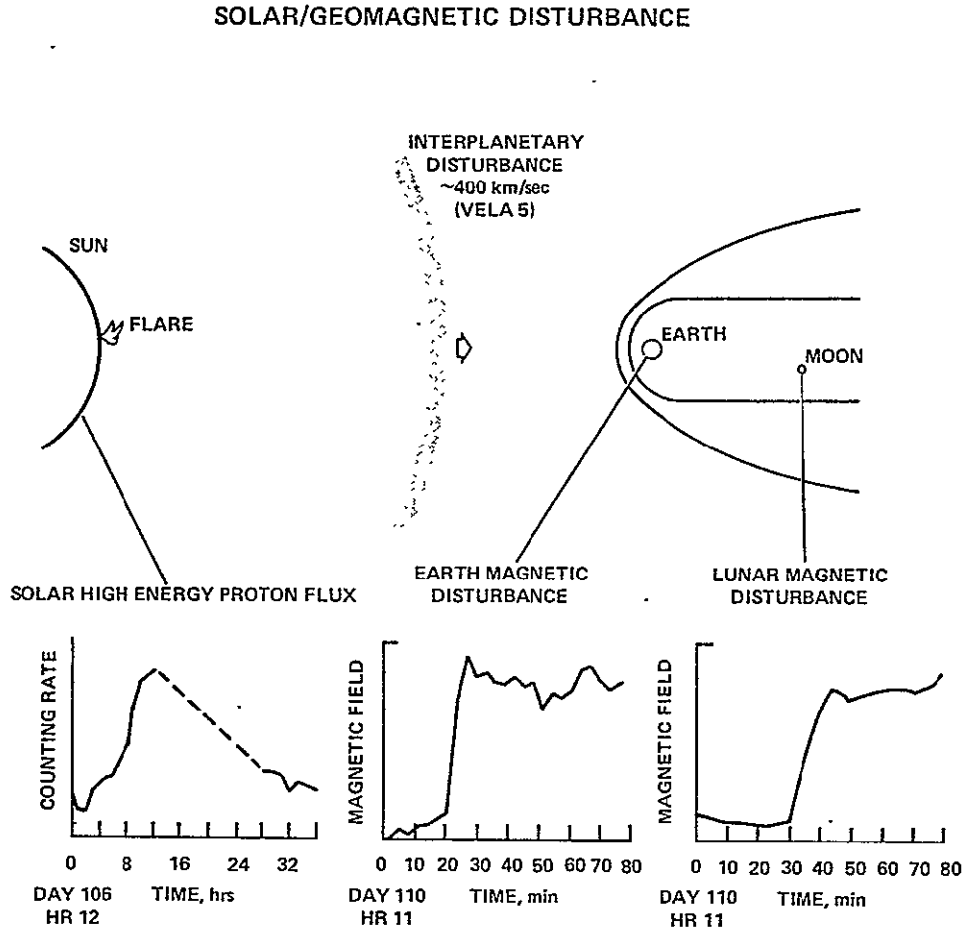

Fig. 2. Solar magnetic event. A solar disturbance propagated through the interplanetary medium and initiated a geomagnetic storm in April 1970, with a peak planetary magnetic activity index K_p of 8+. The proton flux from 5–21 MeV represents the solar event seen on day 106. The geomagnetic and selenomagnetic disturbances were initiated on day 110 about 11 min apart.

Data analysis and electrical conductivity results

Analysis of the large selenomagnetic storm event has involved displaying the data on a 20-inch programmable display system in a real-time interactive mode with the Ames IBM 360/67 computer. The input Explorer 35 data is convolved with an assumed conductivity profile and displayed on the screen to compare the calculated response with the measured Apollo 12 data. The difference between the measured and calculated responses is also displayed. The theoretical lunar response has been calculated for each of over 200 conductivity (σ) profiles. A total of seven basic shapes of profiles has been used, relating monotonically

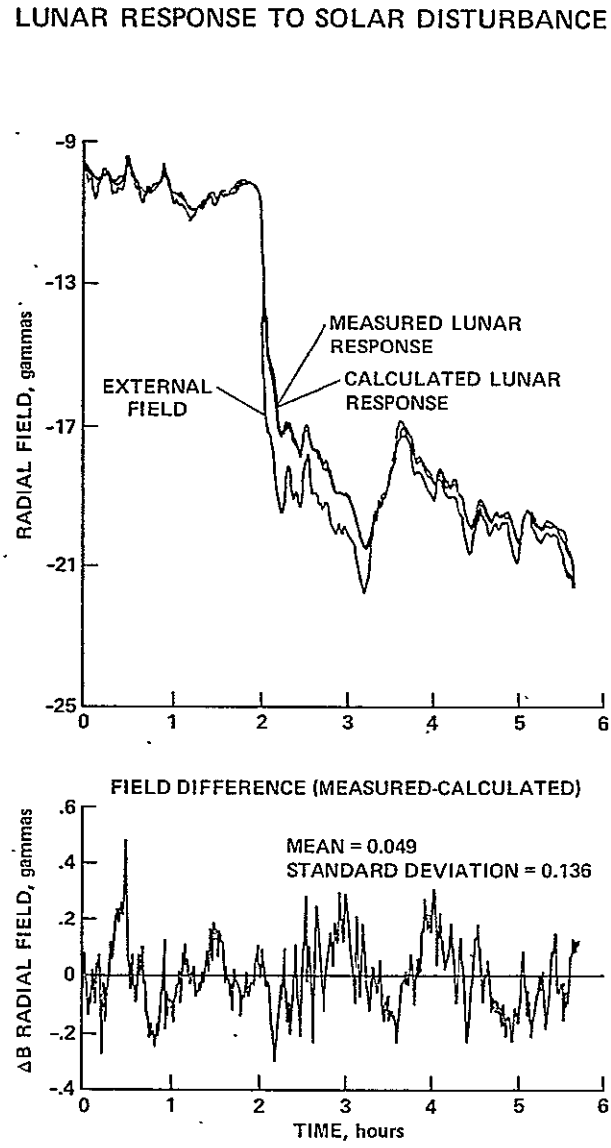

Fig. 3. Lunar radial response to solar event. Response to the solar disturbance of Fig. 2, measured in the geomagnetic tail by the orbiting Explorer 35 magnetometer (external field) and on moon by Apollo 12 surface magnetometer (measured response) is shown in the upper part of the figure. The lunar radial (ALSEP-x) components are plotted The calculated lunar response is based on the conductivity profile of Fig. 5. Measured and calculated response fields are compared by plotting their difference ΔB in the lower part of the figure. For the $5\frac{1}{2}$ hour data set the mean and standard deviation of the field difference are 0.049 and 0.136 gamma respectively.

ORIGINAL PAGE IS
OF POOR QUALITY

increasing log σ to depth using families of first, second, third, or fourth order polynomials. For each type of curve the constants of the polynomial are iteratively adjusted until the calculated response function matches the measured Apollo response within criteria selected for the mean, standard deviation, and peak-to-peak values of the difference curve. The data and analytical results are shown in Fig. 3 for the field component radial to the lunar sphere at the Apollo 12 site, and Fig. 4 for the tangential field component. An "acceptable fit" of the

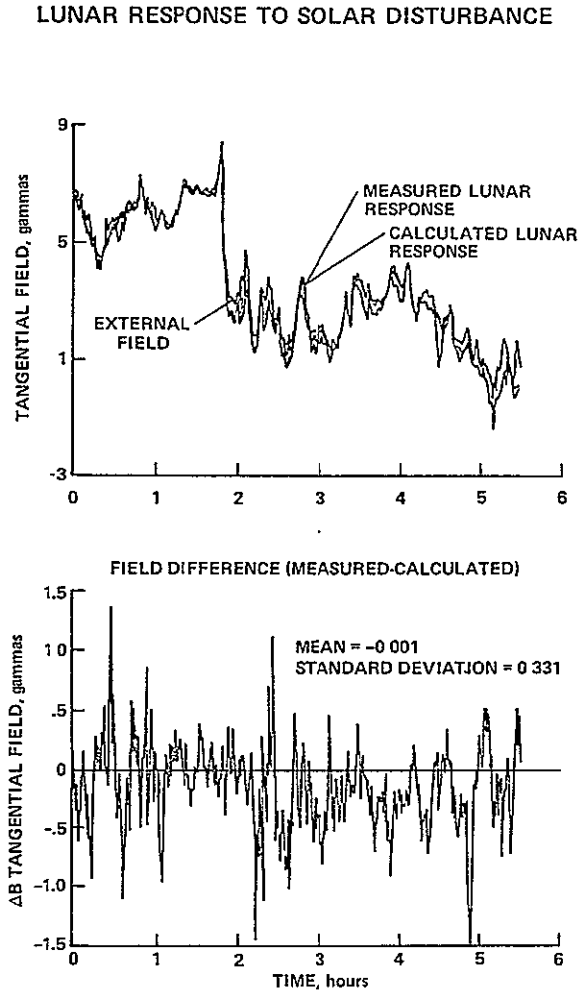

Fig. 4. Lunar tangential response to solar event. Response to the solar disturbance of Fig. 2, plotted using the format of Fig 3. The lunar tangential ALSEP components are plotted. Calculated lunar response is based on the conductivity profile of Fig. 5. Measured and calculated response fields are compared by plotting their difference ΔB in the lower part of the figure. Mean and standard deviation of the field difference are −0.001 and 0.331 gamma respectively.

calculated response to the measured response requires the difference plot in the lower half of Fig. 3 to satisfy the following criteria: mean ≤ 0.050 gamma, standard deviation ≤ 0.145 gamma, and peak-to-peak ≤ 0.850 gamma. These criteria were chosen after an empirical examination of the complex error propagation in profile determination due to instrumental errors, data reduction and analysis errors, and assumptions and approximations in lunar modeling. The criteria allow generation of a family of profiles which fit the data. The family of conductivity profiles which meet these criteria lie within the shaded region of Fig. 5.

To determine the "best-fit" conductivity profile (the solid curve in Fig. 5), we have selected a profile with minimum mean, standard deviation, and peak values, plus one additional criterion: that the conductivity be less than 10^{-9} mhos/m at the lunar surface. This requirement is based on the following experimental evidence: (1) lack of a measurable toroidal field due to unipolar currents when the moon is in the solar wind, implying near-surface conductivity is less than 10^{-9} mhos/m (Dyal and Parkin, 1971b); (2) low surface conductivity (10^{-13}–10^{-16} mhos/m) inferred from radar scattering from the lunar surface (Strangway, 1969); and (3) laboratory measurements of lunar basalt conductivity $\sim 10^{-10}$ mhos/m at 250°K (Schwerer *et al.*, 1973). We also assume that the electrical conductivity increases monotonically with depth and that it is a continuous function from the surface to the center of the moon. The best-fit profile rises rapidly from $<10^{-9}$ mhos/m at the surface to $\sim 10^{3}$ mhos/m at a depth of 200 to 300 km. Thereafter the conductivity rises more gradually to $\sim 3 \times 10^{-2}$ mhos/m at 900 km depth.

Uncertainties in the lunar conductivity profile determination arise from several causes: (1) the nonuniqueness of profile determination as discussed by Backus

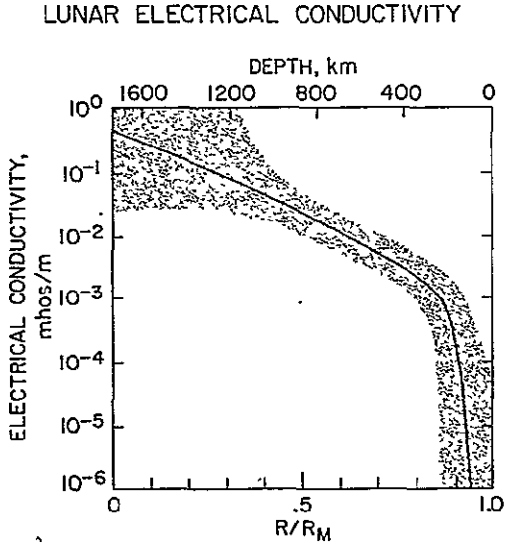

Fig. 5. Electrical conductivity profile of the moon The solid line is a preferred profile which fits the data. The set of profiles which fit the data within the error criteria discussed in the text are bounded by the shaded region.

ORIGINAL PAGE IS OF POOR QUALITY

ORIGINAL PAGE IS
OF POOR QUALITY

and Gilbert (1970), Parker (1970), Phillips (1972), and Hobbs (1973); (2) the penetration depth allowed by the length and amplitude of the data time series; (3) the frequency response limitations of the Explorer 35 and Apollo magnetometers (4) inhomogeneities in the external field over the dimensions of the moon; and (5) instrumental errors in the measured field. Our analysis has concentrated on conductivity profiles monotonically increasing with depth since conductivity is a function of temperature for a given material, and temperature is expected to increase monotonically with depth (e.g., Fricker *et al.*, 1967; Hanks and Anderson; 1972; Toksöz *et al.*, 1972). However, we have tried several other types of profiles. Published non-monotonically-increasing profiles (Sonett *et al.*, 1971; Sill, 1972; Leavy and Madden, 1972) do not provide good fits in our analysis and are rejected as possibilities. Only a profile with a very thin (<50 km at 200 km depth for at least an order of magnitude conductivity increase) could possibly be consistent with the data; the search for such fine structure is felt to be unwarranted at this stage of our analysis.

The three-instrument network consisting of the Apollo 15 and 16 ALSEP and the Apollo 16 subsatellite instruments has been used to generate a data set with the data selection criteria previously discussed for the two instrument-technique. An aggregate event has been constructed by superimposing eleven geomagnetic tail lobe transient events (see Table 1) to produce a step function. The result is shown in Fig. 6 for the radial vector field component at the Apollo 16 site. The external field is calculated (see Appendix A) from simultaneous measurements of surface fields at the stationary ALSEP 15 and 16 sites and at the close-orbiting Apollo 16 subsatellite magnetometer. Conductivity profiles are iteratively selected, allowing calculation of the computed response field until a best fit is obtained with the measured Apollo 16 ALSEP response field. The lunar conductivity profile determined with this three-instrument technique measures the global response in many different configurations due to the orbital motion of the subsatellite; therefore this technique is not as sensitive to errors due to gradients

Table 1. Three-magnetometer network events.

	Start time				Stop time			Year 1972
Event	Day	Hr	Min	Sec	Day	Hr	Min	Sec
1	118	10	30	18	118	12	05	00
2	119	04	16	06	119	05	51	00
3	119	06	14	30	119	07	29	00
4	119	08	20	07	119	09	47	00
5	120	09	49	13	120	11	25	00
6	120	11	47	07	120	13	20	00
7	120	17	41	08	120	19	15	00
8	120	19	41	21	120	21	12	00
9	119	14	10	09	119	15	40	00
10	120	02	00	00	120	03	34	00
11	120	13	46	31	120	15	18	00

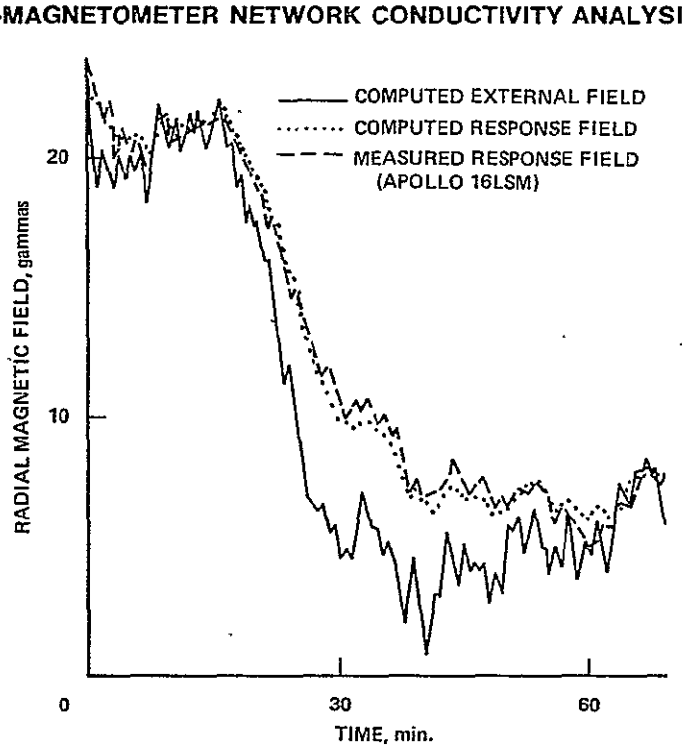

Fig. 6. Conductivity analysis using simultaneous data from a network of three magnetometers. These curves are constructed by superposition of eleven transient events (radial ALSEP-x axis) measured in the high-latitude geomagnetic tail. The external field is calculated from fields measured simultaneously by the Apollo 15 and 16 surface magnetometers and the Apollo 16 subsatellite magnetometer. The computed response field is calculated using the lunar conductivity profile in Fig. 5.

in the external driving field and the assumption of spherical symmetry as is the two-instrument technique. The family of conductivity profiles determined by this technique is consistent with the results shown in Fig. 5. As an internal check the best profile determined from the two instrument technique on the large solar event has been used to calculate the response field using the three-instrument technique; the result is shown in Fig. 6. The agreement between results of the two-magnetometer and three-magnetometer methods (involving a total of five different instruments) gives evidence that the inductive response of the moon is a whole-body spherically symmetric response, not dominated by local anomalies (e.g., the Mare Imbrium anomaly reported by Schubert *et al.*, 1974) or azimuthal asymmetries in the lunar conductivity profile.

Limits on a Highly Conducting Lunar Core from Permeability Studies

Our investigations of magnetic permeability and iron abundance of the moon have involved the use of two different analytical techniques and a total of four different instruments. In the first technique a total of eight lunations of quiet geomagnetic tail data are used from one Apollo surface magnetometer and the lunar orbiting Explorer 35 Ames magnetometer (Parkin *et al.*, 1974). In the second technique we have used 5 lunations of simultaneous data from two Apollo surface magnetometers (Dyal *et al.*, 1975). The latter technique, which employs a method of subtracting measured fields at the two sites, has the advantages of (a) using all three vector components in the analysis rather than just the radial component, (b) subtracting out all constant fields measured at either site, making its analysis independent of offset errors and remanent field determination at either site, and (c) making use of high resolution Apollo surface magnetometer data only. The two independent analytical techniques have yielded global relative permeability values of 1.012 ± 0.006 and 1.008 ± 0.005, respectively. It should be noted that both of these values have been calculated under the assumption that lunar ionospheric effects in the geotail are negligible. Reports that originally emphasized ionospheric effects (Russell *et al.*, 1974a,b) have since been discredited (Goldstein and Russell, 1975).

It has been shown (Goldstein and Russell, 1975; Goldstein *et al.*, 1976) that the moon could have a small highly conducting core with a Cowling time constant of the order of at least a few days which would exclude the external geomagnetic tail field and thus act as a "diamagnetic" region of effective zero permeability. Therefore the lunar magnetic permeability results from magnetometer measurements can be used to place limits on a possible highly conducting core in the moon. The treatment of Goldstein *et al.* (1976) did not consider core size as an explicit function of lunar composition, as we do in this section. In our analysis the moon is represented by a three-layer magnetic model: an outer shell of temperature (T) below the Curie point (T_c), whose permeability μ is dominated by ferromagnetic free iron; an intermediate shell of $T > T_c$ where permeability $\approx \mu_0$, that of free space; and a highly conducting core ($\sigma \gg 10^{-2}$ mhos/m) modeled by $\mu = 0$.

The general solution for magnetization induction in a three-layer permeable moon is given in Appendix B. For the case of a spherically symmetric permeable moon in a vacuum, immersed in a constant external (geomagnetic high-latitude lobe) field (H) the total magnetic field (B) measured at a surface site, in ALSEP coordinates, is

$$\mathbf{B} = \mu_0[(1+2G)H_x\hat{x} + (1-G)H_y\hat{y} + (1-G)H_z\hat{z}] \tag{3}$$

where the expression G for a three-layer permeable moon is defined in Appendix B (Eq. (B4)). We define in Eq. (B4) the relative magnetic permeability in the different regions of the moon as follows: external to the moon $\mu_0 = 1$; in the outer layer of the moon of temperature $T < T_c$, $\mu_1 = \mu$; in the intermediate shell where

$T > T_c$, $\mu_2 = 1$. We consider the case of a hypothetical highly conducting core and let $\mu_3 = 0$. For these conditions the expression for G in Eq. (B4) becomes

$$G = \frac{-2a^3c^3(\mu-1)^2 + a^3b^3(2\mu+1)(\mu+2) + 2b^6(2\mu+1)(\mu-1) - 2b^3c^3(2\mu+1)(\mu-1)}{-2a^3c^3(\mu+2)(\mu-1) + 2a^3b^3(\mu-1)(\mu+2) + 4b^6(\mu-1)^2 - 2b^3c^3(\mu+2)(2\mu+1)} \quad (4)$$

where a is the radius of the core, b is the outer radius of the intermediate shell, and c is the radius of the moon.

The magnetic permeability of the outer shell is expressed $\mu = 1 + 4\pi K$; the magnetic susceptibility $K = K_F + K_P$, where K_F is the apparent ferromagnetic susceptibility of free iron (in emu/cm^3) and K_P is paramagnetic susceptibility of the rock matrix in the outer shell. We have assumed that the composition of the outer shell is homogeneous, with free iron multidomain, noninteracting grains uniformly distributed throughout a paramagnetic mineral (either olivine or orthopyroxene). All geochemical and geophysical constraints and expressions for K_F and K_P used in our calculations are reported in Dyal *et al.* (1975).

In order to consider *upper* limits on such a hypothetical highly conducting lunar core, we impose the extreme (rather unrealistic) condition that the olivine or orthopyroxene matrix has no iron silicate (thus is composed entirely of magnesium silicate). In this extreme case the allowable free iron content is maximized and therefore size of the core is maximized. Using Eq. (4) above and equations in Appendix B of Dyal *et al.* (1975) we calculate the parameter G as a function of a, the core radius, for the case of zero iron silicate content, with an assumed Curie isotherm depth of 250 km. Results are shown in Fig. 7. Also shown in Fig. 7 are G values obtained from our experimental results (Parkin *et al.*, 1974; Dyal *et al.*, 1975). The upper limit core radius consistent with our measurements is 535 km for an orthopyroxene moon and 385 km for an olivine moon. It is noted that for both lunar compositional models the *minimum* core radius is *zero*, that is, all our measurements to date do not require the existence of a highly conducting core. Also shown are limits on G determined from results using Apollo subsatellite magnetometer data (Russell *et al.*, 1974); these latter results, which are in conflict with our results, indicate the definite existence of a highly conducting core (Goldstein *et al.*, 1976). This discrepancy is unresolved at present and warrants further study, including direct comparison of data from Apollo lunar surface magnetometers and orbiting subsatellite magnetometers.

Implications for Lunar Internal Structure

Structure of the lunar interior (see Fig. 8) can be inferred from electrical conductivity and magnetic permeability results:

(1) Absence of a measurable toroidal magnetic field places an electrical conductivity upper limit of 10^{-9} mhos/m (Dyal and Parkin, 1971b) at the lunar surface, which probably applies for at least the first few tens of kilometers depth in the moon. The first 150 km depth has low conductivity ($<10^{-3}$ mhos/m). No

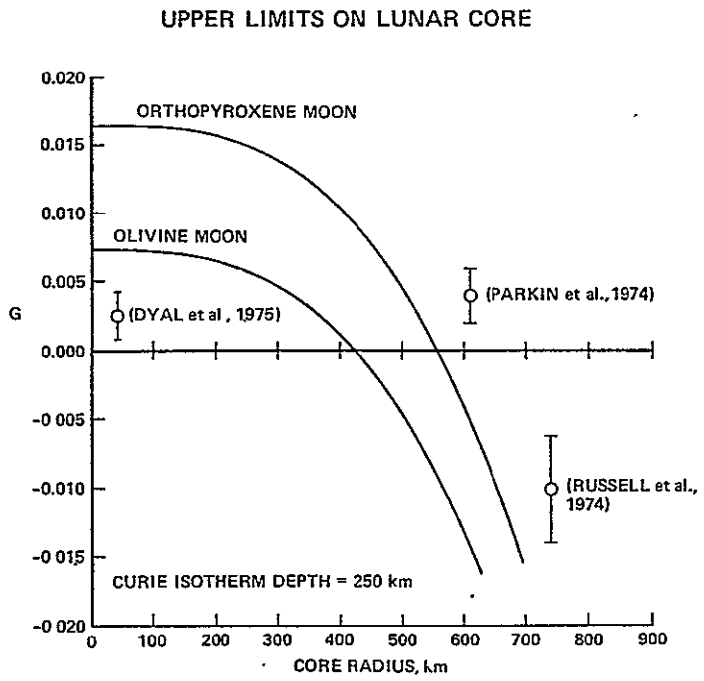

Fig. 7. Size upper limits on a highly conducting lunar core. Upper limits are determined from measurement of the lunar magnetic permeability, $\mu = (1+2G)/(1-G)$. The lunar model assumes a Curie isotherm depth of 250 km for an olivine or orthopyroxene lunar composition. Limits placed on G by Parkin *et al.* (1974) are from Apollo 12 surface orbiting magnetometer data. Dyal *et al.* (1975) used data from the Apollo 15 and 16 surface magnetometers. Results of Russell *et al.* (1974) are from Apollo subsatellite magnetometer data.

conductivity transition is seen at the 60 km seismic discontinuity (Nakamura *et al.*, 1974, 1976; Dainty *et al.*, 1975), but our resolution is limited at these depths.

(2) Between 200–300 km depths the conductivity increases rapidly, to a value of $\sim 10^{-3}$ mhos/m. This region corresponds to the location of the seismic discontinuity between the upper and middle mantle boundary reported by Nakamura *et al.* (1974, 1976).

(3) From 300–900 km depth the conductivity increases steadily from 10^{-3} mhos/m to about 3×10^{-2} mhos/m. This is the region of greatest accuracy for magnetometer results, as indicated by the error limits in Fig. 5. The shape of the profile indicates that a temperature rise is responsible for this steady increase.

(4) From permeability results a highly conducting core of maximum radius 535 km is found to be possible for the extreme case of a magnesium-silicate dominated orthopyroxene moon with Curie isotherm depth of 250 km. Conductivity results (Fig. 5) verify this upper limit for a core of conductivity >10 mhos/m. However, the minimum radius of this hypothetical core is zero, i.e., there is no positive indication at this time that any core of conductivity >10 mhos/m need exist in the moon.

ORIGINAL PAGE IS
OF POOR QUALITY

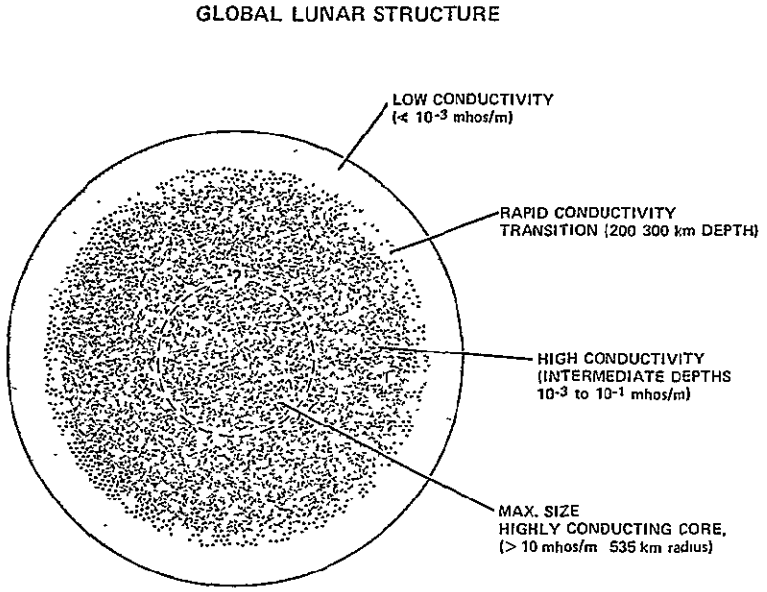

Fig. 8. Summary of lunar interior structure inferred from Apollo magnetometer data. Limitations placed on the size of a possible highly conducting core are discussed in the text.

Acknowledgments—The authors are grateful to James Arvin and Karen Neier of Computer Sciences Corporation for their rapid development and implementation of the IMLAC programs, and to Dr. Thomas Mucha of CSC for his work on the theoretical development of the three-magnetometer conductivity analysis technique. We wish to thank Marion Legg and her coworkers Chris Mitchell, Cynthia Harlow, Jan Hom, Anna Hood, and Donna Hafeman of Diversified Computer Applications for their assistance during various phases of data reduction and analysis. We are pleased to acknowledge research support for C.W.P. under NASA grants NGR-05-017-027 and NSG-2075, and for W.D.D. under NASA grant NGR-45-001-040.

REFERENCES

Backus G. and Gilbert F. (1970) Uniqueness in the inversion of inaccurate gross earth data. *Phil. Trans. Roy. Soc.* A226, 123.

Chapman S. and Bartels J. (1940) *Geomagnetism.* Clarendon Press, Oxford. 1049 pp.

Coleman P. J., Jr., Schubert G., Russell C. T., and Sharp L. R. (1972) The particles and fields subsatellite magnetometer experiment. In *Apollo 15 Prelim. Sci. Rep.*, NASA publication SP-289, p. 22-1 to 22-9.

Coleman P. J., Jr., Lichtenstein B. R., Russell C. T., Schubert G., and Sharp L. R. (1976) The particles and fields subsatellite magnetometer experiment. In *Apollo 16 Prelim. Sci. Rep.*, NASA publication SP-315, p. 23-1 to 23-13.

Dainty A. M., Goins N. R., and Toksöz M. N. (1975) Natural lunar seismic events and the structure of the moon. *Proc. Lunar Sci. Conf. 6th*, p. 2887–2897.

Dyal P. and Parkin C. W. (1971a) Electrical conductivity and temperature of the lunar interior from magnetic transient-response measurements. *J. Geophys. Res.* 76, 5947.

Dyal P. and Parkin C. W. (1971b) The Apollo 12 magnetometer experiment: Internal lunar properties from transient and steady magnetic field measurements. *Proc. Lunar Sci. Conf. 2nd*, p. 2391–2413.

Dyal P., Parkin C. W., and Sonett C. P. (1970) Lunar surface magnetometer. *IEEE Trans. on Geoscience Electronics* GE-8(4), 203–215.

Dyal P., Parkin C. W., and Cassen P. (1972) Surface magnetometer experiments: Internal lunar properties and lunar surface interactions with the solar plasma. *Proc. Lunar Sci. Conf. 3rd*, p. 2287–2307.

Dyal P., Parkin C. W., and Daily W. D. (1973) Surface magnetometer experiments: Internal lunar properties. *Proc. Lunar Sci. Conf. 4th*, p. 2229–2945.

Dyal P., Parkin C. W., and Daily W. D. (1974) Temperature and electrical conductivity of the lunar interior from magnetic transient measurements in the geomagnetic tail. *Proc. Lunar Sci. Conf. 5th*, p. 3059–3071.

Dyal P., Parkin C. W., and Daily W. D. (1975) Lunar electrical conductivity and magnetic permeability. *Proc. Lunar Sci. Conf. 6th*, p. 2909–2926.

Fricker P. E., Reynolds R. T., and Summers A. L. (1967) On the thermal history of the moon. *J. Geophys. Res.* 72, 2649.

Goldstein B. E. and Russell C. T. (1975) On the apparent diamagnetism of the lunar environment in the geomagnetic tail lobes. *Proc. Lunar Sci. Conf. 6th*, p. 2999–3012.

Goldstein B. E., Phillips R J., Tsay F. D., and Russell C. T. (1976) The lunar core and magnetic permeability measurements. *Geophys. Res. Lett.* In press.

Hanks T. C. and Anderson D. L. (1972) Origin, evolution, and present thermal state of the moon. *Phys. Earth Planet. Interiors* 5, 409–425.

Hobbs B. A. (1973) The inversion problem of the moon's electrical conductivity. *Earth Planet. Sci. Lett.* 17, 380–384.

Jackson J. D. (1962) *Classical Electrodynamics*, p. 162–164. John Wiley and Sons.

Kuckes A. F. (1971) Lunar electrical conductivity. *Nature* 232, 249–251.

Kuckes A. F. (1974) Lunar magnetometry and mantle convection. *Nature* 252, 670–672.

Leavy D. and Madden T. (1974) Lunar electrical conductivity. *Nature* 250, 553–555.

Lichtenstein B. R. and Schubert G. (1976) Hydromagnetic theory for the scattering of Alfvén waves by the moon in the magnetic tail lobes (abstract). In *Lunar Science VII*, p. 488. The Lunar Science Institute, Houston.

Nakamura Y., Latham G., Lammlein D., Ewing M., Duennebier F., and Dorman J. (1974) Deep lunar interior from recent seismic data. *Geophys. Res. Lett.* 1, 137–140.

Nakamura Y., Latham G. V., and Dorman H. J. (1976) Seismic structure of the moon (abstract). In *Lunar Science VII*, p. 602–603. The Lunar Science Institute, Houston.

Ness N. F. (1970) Magnetometers for space research. *Space Sci. Rev.* 11, 459–544.

Parker R. L. (1970) The inverse problem of electrical conductivity in the mantle. *Geophys. J. Roy. Astron. Soc.* 22, 121–138.

Parkin C. W., Dyal P., and Daily W. D. (1973) Iron abundance in the moon from magnetometer measurements. *Proc. Lunar Sci. Conf. 4th*, p. 2947–2961.

Parkin C. W., Daily W. D., and Dyal P. (1974) Iron abundance and magnetic permeability of the moon. *Proc. Lunar Sci. Conf. 5th*, p. 2761–2778.

Phillips R. J. (1972) The Lunar conductivity profile and the nonuniqueness of electromagnetic data inversion. *Icarus* 17, 88–103.

Russell C. T., Coleman P. J., Jr., Lichtenstein B. R., and Schubert G. (1974a) Lunar magnetic field: Permanent and induced dipole moments. *Science* 186, 825–826.

Russell C. T., Coleman P. J., Jr., Lichtenstein B. R., and Schubert G. (1974b) The permanent and induced magnetic dipole moment of the moon. *Proc. Lunar Sci. Conf. 5th*, p. 2747–2760.

Schubert G., Smith B. F., Sonett C. P., Colburn D. S., and Schwartz K. (1974) Polarized magnetic field fluctuations at the Apollo 15 site: Possible regional influence on lunar induction. *Science* 183, 1194.

Schubert G., Sonett C. P., Smith B. F., Schwartz K., and Colburn D. S. (1975) Using the moon to probe the geomagnetic tail lobe plasma. *Geophys. Res. Lett.* 2, 277–280.

Schwerer F. C., Huffman G. P., Fisher R. M., and Nagata T. (1973) Electrical conductivity of lunar surface rocks at elevated temperatures. *Proc. Lunar Sci. Conf. 4th*, p. 3151–3166.

Sill W. R. (1972) Lunar conductivity models from the Apollo 12 magnetometer experiment. *The Moon* 4, 3–17.

Snyder C. W., Clay D. R., and Neugebauer M. (1970) The solar-wind spectrometer experiment. In *Apollo 12 Prelim. Sci. Rep.* NASA publication SP-235, p. 75–82.

Sonett C. P., Colburn D. S., Currie R. G., and Mihalov J. D. (1967) The geomagnetic tail; topology, reconnection and interaction with the moon. In *Physics of the Magnetosphere* (R. L. Carovillano, J. F. McClay, and H. R. Radoski, eds.), p. 380. D. Reidel.

Sonett C. P., Schubert G., Smith B. F., Schwartz K., and Colburn D. S. (1971) Lunar electrical conductivity from Apollo 12 magnetometer measurements: Compositional and thermal inferences. *Proc. Lunar Sci. Conf. 2nd*, p. 2415–2431.

Strangway D. W. (1969) Moon: Electrical properties of the uppermost layers. *Science* 165, 1012–1013.

Toksöz M. N., Solomon S. C., and Minear J. W. (1972) Thermal evolution of the moon. *The Moon* 4, 331–355.

APPENDIX A

Three-magnetometer conductivity analysis technique

This technique, applied to conductivity analysis, uses simultaneous data measured in high-latitude regions of the geomagnetic tail by a network of three instruments: the Apollo 15 lunar surface magnetometer (LSM), the Apollo 16 LSM, and the Apollo 16 subsatellite magnetometer, the latter of which provides coverage around the entire global circumference. The numerical analysis program basically uses total-magnetic-field (B) measurements from two surface magnetometers and one near-surface magnetometer to separate the time-dependent external geomagnetic field (H) from the poloidal eddy current field (P) induced in the moon by changes in H. Total fields (excluding remanent fields) measured at sites 1, 2, and 3 are denoted, respectively,

$$\begin{aligned} {}^1\mathbf{B} &= {}^1\mathbf{H} + {}^1\mathbf{P} \\ {}^2\mathbf{B} &= {}^2\mathbf{H} = {}^2\mathbf{P} \\ {}^3\mathbf{B} &= {}^3\mathbf{H} + {}^3\mathbf{P} \end{aligned} \tag{A1}$$

(Here and throughout this section, the superscripts denote site location.) We define site 1 as the "reference site." The external field at sites $n = 2$ or 3 can be expressed in terms of the external field at site 1:

$$ {}^n\mathbf{H} = {}^nA\,{}^1\mathbf{H} \tag{A2}$$

where ${}^nA$ is the transformation matrix from site 1 to site $n = 2$ or 3.

Likewise we can express the poloidal field P at site $n = 2$ or 3 in terms of the poloidal field at site 1. The poloidal field is induced by time-dependent changes in the external field. In a numerical solution, the changing field $\mathbf{H}(t)$ can be approximated to a high degree of accuracy by a summation of small step-changes: $\mathbf{H}(t) \simeq \Sigma_m\, \Delta H_m(t)$. The poloidal field at site n can then be expressed, in ALSEP coordinates (also see Dyal and Parkin, 1971a) as

$$ {}^n\mathbf{P} = Q \sum_m [-2\,{}^n\Delta H_{xm}\hat{x} + {}^n\Delta H_{ym}\hat{y} + {}^n\Delta H_{zm}\hat{z}]F(t - t_m) \tag{A3}$$

where Q is a constant.

Referring to Eq. (A2) we can write a step change in H at site n in terms of H at site 1:

$$ {}^n\Delta H = {}^nA\,{}^1\Delta H. \tag{A4}$$

We write out the transformation matrix

$$ n_A = \begin{bmatrix} {}^na_{11} & {}^na_{12} & {}^na_{13} \\ {}^na_{21} & {}^na_{22} & {}^na_{23} \\ {}^na_{31} & {}^na_{32} & {}^na_{33} \end{bmatrix} \tag{A5}$$

Then using Eqs. (A4) and (A5), Eq. (A3) can be expanded to

$$
\begin{aligned}
{}^{n}\mathbf{P} = Q\sum_{m}\{-2({}^{n}a_{11}{}^{1}\Delta H_{xm} + {}^{n}a_{12}{}^{1}\Delta H_{ym} + {}^{n}a_{13}{}^{1}\Delta H_{zm})\hat{x} + ({}^{n}a_{21}{}^{1}\Delta H_{xm} + {}^{n}a_{22}{}^{1}\Delta H_{ym} \\
+ {}^{n}a_{23}{}^{1}\Delta H_{zm})\hat{y} + ({}^{n}a_{31}{}^{1}\Delta H_{xm} + {}^{n}a_{32}{}^{1}\Delta H_{ym} + {}^{n}a_{33}{}^{1}\Delta H_{zm})\hat{z}][F(t-t_m)]
\end{aligned} \tag{A6}
$$

But also

$$
\begin{aligned}
{}^{1}P_x &= -2Q\sum_{m}{}^{1}\Delta H_{xm}F(t-t_m) \\
{}^{1}P_y &= Q\sum_{m}{}^{1}\Delta H_{ym}F(t-t_m) \\
{}^{1}P_z &= Q\sum_{m}{}^{1}\Delta H_{zm}F(t-t_m)
\end{aligned} \tag{A7}
$$

So (A6) becomes

$$
\begin{aligned}
{}^{n}\mathbf{P} = [{}^{n}a_{11}{}^{1}P_x - 2{}^{n}a_{12}{}^{1}P_y - 2{}^{n}a_{13}{}^{1}P_z]\hat{x} + [-\tfrac{1}{2}{}^{n}a_{21}{}^{1}P_x + {}^{n}a_{22}{}^{1}P_y + {}^{n}a_{23}{}^{1}P_z]\hat{y} \\
+ [-\tfrac{1}{2}{}^{n}a_{31}{}^{1}P_x + {}^{n}a_{32}{}^{1}P_y + {}^{n}a_{33}{}^{1}P_z]\hat{z}
\end{aligned} \tag{A8}
$$

or in matrix form

$$
{}^{n}\mathbf{P} = {}^{n}C\,{}^{1}\mathbf{P} \tag{A9}
$$

where

$$
{}^{n}C = \begin{bmatrix} {}^{n}a_{11} & -2{}^{n}a_{12} & -2{}^{n}a_{13} \\ -\frac{1}{2}{}^{n}a_{21} & {}^{n}a_{22} & {}^{n}a_{23} \\ -\frac{1}{2}{}^{n}a_{31} & {}^{n}a_{32} & {}^{n}a_{33} \end{bmatrix} \tag{A10}
$$

Using Eqs. (A2) and (A9), we can now express the magnetic fields at either site 2 or 3 in terms of fields at the "reference" site 1:

$$
{}^{n}\mathbf{B} = {}^{n}\mathbf{H} + {}^{n}\mathbf{P} = {}^{n}A\,{}^{1}\mathbf{H} + {}^{n}C\,{}^{1}\mathbf{P} \tag{A11}
$$

Combining ${}^{1}\mathbf{B} = {}^{1}\mathbf{H} + {}^{1}\mathbf{P}$ with Eqs. (A11) and eliminating ${}^{1}\mathbf{H}$, we obtain

$$
{}^{n}\mathbf{B} = {}^{n}A\,{}^{1}\mathbf{B} + ({}^{n}C - {}^{n}A)\,{}^{1}\mathbf{P} \tag{A12}
$$

which can be rewritten as

$$
{}^{n}\mathbf{M} = {}^{n}D\,{}^{1}\mathbf{P}. \tag{A13}
$$

Here we define ${}^{n}\mathbf{M} \equiv {}^{n}\mathbf{B} - {}^{n}A\,{}^{1}\mathbf{B}$ (note ${}^{n}\mathbf{M}$ can be found from fields B measured simultaneously at sites 1, 2, and 3), and for either site 2 or 3, ${}^{n}D = {}^{n}C - {}^{n}A$ is

$$
{}^{n}D = \begin{bmatrix} 0 & -3{}^{n}a_{12} & -3{}^{n}a_{13} \\ -\frac{3}{2}{}^{n}a_{21} & 0 & 0 \\ -\frac{3}{2}{}^{n}a_{31} & 0 & 0 \end{bmatrix} \tag{A14}
$$

We note that since ${}^{n}D$ is a singular matrix, ${}^{1}\mathbf{P}$ cannot be found using data from only two magnetometer sites. However, using three sites, Eq. (A13) can be written in terms of x, y, and z components, obtaining four equations in three unknowns. The solutions for components of ${}^{1}\mathbf{P}$ are then expressed, parameterizing on ${}^{1}P_y$,

$$
\begin{aligned}
{}^{1}P_x &= -\frac{2}{3}\frac{{}^{2}M_y}{{}^{2}a_{21}} = -\frac{2}{3}\frac{{}^{3}M_y}{{}^{3}a_{21}} = -\frac{2}{3}\frac{{}^{2}M_z}{{}^{2}a_{31}} = -\frac{2}{3}\frac{{}^{3}M_z}{{}^{3}a_{31}} \\
{}^{1}P_y &= \frac{1}{3}\left(\frac{{}^{2}a_{13}{}^{3}M_x - {}^{3}a_{13}{}^{2}M_x}{{}^{2}a_{12}{}^{3}a_{13} - {}^{3}a_{12}{}^{2}a_{13}}\right) \\
{}^{1}P_z &= -\frac{1}{3}\frac{{}^{2}M_x}{{}^{2}a_{13}} + \frac{{}^{2}a_{12}{}^{1}P_y}{{}^{2}a_{13}} = -\frac{1}{3}\frac{{}^{3}M_x}{{}^{3}a_{13}} + \frac{{}^{3}a_{12}{}^{1}P_y}{{}^{3}a_{13}}
\end{aligned} \tag{A15}
$$

ORIGINAL PAGE IS
OF POOR QUALITY

ORIGINAL PAGE IS
OF POOR QUALITY

Once **P** has been determined for a geomagnetic tail event (or for an aggregate of several events), **H** can be obtained from $\mathbf{H} = \mathbf{B} - \mathbf{P}$. Then **H** is used as the external driving field in a program which can model the moon with an arbitrary radial conductivity profile $\sigma(r)$, allowing a theoretical calculation of **B** as a function of $\sigma(r)$. The calculated **B** is compared with measured **B**, adjusting $\sigma(r)$ iteratively (see Dyal *et al.*, 1974, 1975) until calculated and measured values coincide. Thus a family of conductivity profiles can be determined and a profile, with error limits, of conductivity versus depth can be determined.

APPENDIX B

Permeability analysis for a three-layer model of the moon

Consider a radially inhomogeneous three-layer permeable sphere in an initially uniform magnetic field $\mathbf{H}_0$. In the absence of currents $\mathbf{H} = -\nabla\Phi$ and since $\mathbf{B} = \mu\mathbf{H}$, at any point $\nabla \cdot \mathbf{H} = 0$. Therefore Φ satisfies Laplace's equation consistent with the continuity of normal components of **B** and tangential components of **H** at the spherical boundaries. In the various regions the potentials are

$$\Phi = \begin{cases} -H_0 r\cos\theta + \sum_{i=0}^{\infty} \frac{\alpha_i}{r^{i+1}} P_i(\cos\theta) & r > c \\ \sum_{i=0}^{\infty} \left(\beta_i r^i + \gamma_i \frac{1}{r^{i+1}}\right) P_i(\cos\theta) & b < r < c \\ \sum_{i=0}^{\infty} \left(\delta_i r^i + \epsilon_i \frac{1}{r^{i+1}}\right) P_i(\cos\theta) & a < r < b \\ \sum_{i=0}^{\infty} (\xi_i r^i P_i(\cos\theta)) & r < a \end{cases} \tag{B1}$$

Here a, b, and c are radius of the inner core, outer radius of the intermediate shell, and radius of the whole sphere, respectively. Using the notation convention of Jackson (1962), we match the boundary conditions as follows.

$$\begin{aligned} \mu_0 \frac{\partial\Phi}{\partial r}(c_+) &= \mu_1 \frac{\partial\Phi}{\partial r}(c_-) & \frac{\partial\Phi}{\partial\theta}(c_+) &= \frac{\partial\Phi}{\partial\theta}(c_-) \\ \mu_1 \frac{\partial\Phi}{\partial r}(b_+) &= \mu_2 \frac{\partial\Phi}{\partial r}(b_-) & \frac{\partial\Phi}{\partial\theta}(b_+) &= \frac{\partial\Phi}{\partial\theta}(b_-) \\ \mu_2 \frac{\partial\Phi}{\partial r}(a_+) &= \mu_3 \frac{\partial\Phi}{\partial r}(a_-) & \frac{\partial\Phi}{\partial\theta}(a_+) &= \frac{\partial\Phi}{\partial\theta}(a_-) \end{aligned} \tag{B2}$$

Here μ_1, μ_2, and μ_3 are relative magnetic permeability of the outer shell, intermediate shell, and inner core, respectively; μ_0 is relative magnetic permeability of the medium external to the sphere. Combining the systems of Eqs (B1) and (B2), all but the $i = 1$ coefficients vanish, yielding the six simultaneous equations

$$\begin{aligned} 2\mu_0\alpha + \mu_1 c^3\beta - 2\mu_1\gamma + \mu_0 c^3 H_0 &= 0 \\ -\mu_1 b^3\beta + 2\mu_1\gamma + b^3\mu_2\delta - 2\mu_2\epsilon &= 0 \\ -a^3\mu_2\delta + 2\mu_2\epsilon + a^3\mu_3\xi &= 0 \\ -\alpha + c^3\beta + \gamma + c^3 H_0 &= 0 \\ -b^3\beta - \gamma + b^3\delta + \epsilon &= 0 \\ a^3\delta + \epsilon - a^3\xi &= 0 \end{aligned} \tag{B3}$$

We are primarily interested in α, the induced dipole moment, which is obtained by solving the system (B3). The term G is defined as follows:

$$G \equiv \frac{\alpha}{H_0 c^3} = \frac{E}{F} \tag{B4}$$

where

$$E = 2a^3c^3(\mu_0-\mu_1)(\mu_1-\mu_2)(\mu_2-\mu_3) + a^3b^3(\mu_0+2\mu_1)(\mu_1+2\mu_2)(\mu_2-\mu_3)$$
$$+ b^6(\mu_0+2\mu_1)(\mu_1-\mu_2)(2\mu_2+\mu_3) + b^3c^3(\mu_0-\mu_1)(2\mu_1+\mu_2)(2\mu_2+\mu_3)$$
$$F = 2a^3c^3(2\mu_0+\mu_1)(\mu_1-\mu_2)(\mu_2-\mu_2) - 2a^3b^3(\mu_0-\mu_1)(\mu_1+2\mu_2)(\mu_2-\mu_3)$$
$$- 2b^6(\mu_0-\mu_1)(\mu_1-\mu_2)(2\mu_2+\mu_3) - b^3c^3(2\mu_0+\mu_1)(2\mu_1+\mu_2)(2\mu_2+\mu_3)$$

Outside the surface of the sphere ($r > c$), the magnetic field B, in spherical coordinates ($\hat{r}$, $\hat{\theta}$, $\hat{\phi}$), is

$$\mathbf{B} = \mu_0\mathbf{H} = -\mu_0\nabla\Phi = \mu_0\left[H_0\cos\theta\hat{r} - H_0\sin\theta\hat{\theta}) + \left(2\frac{\alpha}{r^3}\cos\theta\hat{r} + \frac{\alpha}{r^3}\sin\theta\hat{\theta}\right)\right] \tag{B5}$$

where the first term in parentheses is the external field H_0 and the second is the dipolar induced magnetization field. We rotate the coordinate system about the $\hat{r}$ (or ALSEP $\hat{x}$) axis so that $\hat{\theta}$ and $\hat{\phi}$ correspond to the ALSEP $\hat{y}$ and $\hat{z}$ axes; then the total field just outside the surface of the sphere ($r = c_+ \equiv c$) is

$$\mathbf{B} = \mu_0[(1+2G)H_x\hat{x} + (1-G)H_y\hat{y} + (1-G)H_z\hat{z}] \tag{B6}$$

Ionosphere and Atmosphere of the Moon in the Geomagnetic Tail

WILLIAM D. DAILY,[1] WILLIAM A. BARKER,[2] MARK CLARK,[3]
PALMER DYAL,[4] AND CURTIS W. PARKIN[2]

During the 4-day period when the moon is in the geomagnetic tail, the principal constituents of the lunar atmosphere are neon and argon. The surface concentrations of neon and argon are calculated from a theoretical model to be 3.9×10^3 and 1.7×10^3, respectively. The lunar atmosphere is ionized by solar ultraviolet radiation, resulting in electrons at a temperature of about 1.5×10^5 °K and ions at about 370°K. We investigated dynamic properties of the lunar ionosphere in the high-latitude tail lobes during quiescent times when plasma energy density from external sources is below the sensitivity threshold of the suprathermal ion detector at the lunar surface. We found that a hydrostatic model of the ionospheric plasma is inadequate because the gravitational potential energy of the plasma is considerably smaller than its thermal energy. A hydrodynamic model, comparable to that used to describe the solar wind, is developed to obtain plasma densities and flow velocities as functions of altitude. The hydrodynamic flow of the ionospheric particles is away from the sunlit hemisphere, in a direction parallel to the magnetic field, and forms a cylinder whose base is the lunar diameter. At 100-km altitude the calculated ionospheric density is 1.2×10^{-2} cm^{-3}, with a flow velocity of 4–7 km/s. The corresponding energy density is 2.5×10^{-13} erg/cm^3. Flow under these quiescent conditions exists approximately one third of the time in the geotail. During other times when cross-tail electric fields are present, the steady flow away from the moon is disrupted by drift velocity components perpendicular to the geomagnetic field lines, also, sporadic occurrences of plasma sheet or lobe plasma temporarily dominate the plasma environment during nonquiescent times. The electromagnetic properties of the quiescent ionosphere are investigated, and it is concluded that plasma effects on lunar induction studies can be neglected for quiescent conditions in the geomagnetic tail lobes.

1 INTRODUCTION

The purpose of this paper is to present a quantitative model of the lunar ionosphere and its associated atmosphere during the 4-day period when the moon is in the geomagnetic tail and thereby shielded from the solar wind plasma. Previous investigations of the lunar ionosphere and atmosphere have concentrated on the 26 days of each lunation when the moon is exposed to the solar wind [e.g., *Weil and Barasch*, 1963; *Hinton and Taeusch*, 1964, *Johnson*, 1971; *Hodges et al.*, 1974; *Benson and Freeman*, 1976]. Prior to the Apollo landings, occultation experiments, with light and radio sources, were used to place limits on the lunar atmosphere and ionosphere. The observations were made by *Elsmore* [1957], *Bailey et al* [1964], and *Pomalaza-Diaz* [1967]; theoretical calculations, based on various models, were made by *Weil and Barasch* [1963] and *Hinton and Taeusch* [1964]. A. S. Vyshlov et al. (unpublished report, 1976) have recently obtained electron densities near the lunar sunrise terminator from a dual-frequency dispersion interferometry experiment using Luna 19 and Luna 22 data.

In situ measurements of neutral and charged particles in the lunar atmosphere were first made by the cold cathode gage [*Johnson et al.*, 1970] and the suprathermal ion detector (Side) in the Apollo 12, 14, and 15 surface experiments (see, for example, *Freeman et al* [1970]) and later by the Apollo 17 lunar atmospheric composition experiment [*Hoffman et al.*, 1973]. These experiments, the results of which are reviewed and interpreted by *Manka* [1972], *Hodges et al.* [1974], and *Benson and Freeman* [1976], provide much of our present knowledge on the lunar atmosphere and ionosphere.

A quantitative description of the lunar atmosphere and ionosphere for times when the moon is shielded from the solar wind in the geomagnetic tail is important to our knowledge of the moon's interior. Surface and orbital magnetic data measured in the geotail are used to calculate the lunar electrical conductivity and magnetic permeability [*Dyal et al.*, 1975, 1976; *Parkin et al.*, 1973, 1974]. Accurate interpretation of these data requires knowledge of the plasma in the lunar environment. For example, Apollo subsatellite magnetometer data, measured during the 4-day period that the moon is in the geomagnetic tail, have been used by *Russell et al* [1974*a*, *b*] to measure the induced magnetic dipole moment of the volume included within the subsatellite orbit. This moment was found to oppose the direction of the external magnetizing field, and this result was initially interpreted to be due to the diamagnetic properties of the lunar ionosphere. Reexamination of these data led *Goldstein and Russell* [1975] to suggest that a more likely interpretation of the phenomenon is eddy current induction in a small highly conducting lunar core. At present, there is no unambiguous explanation for this interesting effect [*Goldstein et al.*, 1976, *Dyal et al.*, 1976].

In this paper we present calculations of the densities and energies of the various constituents of the lunar ionosphere during the time that the moon is in the earth's geomagnetic tail. In section 2, a quantitative description of the lunar atmosphere, the ionospheric source which we consider in this paper, is presented. In section 3, various hydrostatic models of the lunar ionosphere are considered, and their limitations are reviewed. We consider the hydrodynamic description, developed in section 4, to be the most realistic model of the lunar ionosphere. In section 5, we compare and contrast the solar wind flow with the hydrodynamic ionosphere model and discuss its features. In addition, the diamagnetic susceptibility of the lunar ionosphere is calculated and compared with other calculations, including the value required to account for the subsatellite measurement of a negative induced global magnetic moment [*Russell et al*, 1974*a*, *b*].

2 THE LUNAR ATMOSPHERE

We consider the ionosphere of the moon that has as its source the constituents of the lunar atmosphere, which in turn

[1] Eyring Research Institute, Provo, Utah 84601
[2] University of Santa Clara, Santa Clara, California 95053
[3] University of California, Los Angeles, California 90024
[4] NASA Ames Research Center, Moffett Field, California 94035

Copyright © 1977 by the American Geophysical Union

Paper number 7B0449

has as its sources the solar wind and radioactive decay products vented from the lunar interior. When the moon is outside the geomagnetic tail, the solar wind plasma impinges directly on the lunar surface. The plasma is then neutralized, thermalized, and reemitted from the surface to build up the major constituents of the atmosphere: hydrogen, helium, neon, and argon (^{36}Ar). In addition, ^{40}Ar, formed in the radioactive decay of ^{40}K, is vented from the lunar surface. Gases such as CH_4, NH_3, and CO_2 are likely to be present in small amounts at the sunrise terminator [*Hoffman and Hodges,* 1975]. They are essentially absent from the nightside atmosphere, owing to rapid adsorption on the lunar surface. Other minor constituents are also present [see *Hodges et al.,* 1974].

Two principal loss mechanisms affect the lunar atmosphere in the solar wind or in the geotail: thermal escape and photo-ionization. The thermal loss mechanism, which affects the most abundant constituents, hydrogen and helium, is most responsible for the tenuous nature of the lunar atmosphere. Lifetimes of the heavier noble gases in the atmosphere are determined primarily by photo-ionization rates. An excellent review of the properties of the lunar atmosphere in the solar wind is given by *Hodges et al.* [1974]. A summary of these and other lunar atmosphere parameters that we use in this paper is presented in Table 1 Also, in a very recent interpretation of data from the lunar suprathermal ion detector experiment, using a two-gas model of the lunar exosphere, *Benson and Freeman* [1976] calculated daytime surface concentrations of $\sim 10^5$ and $\sim 10^4$ cm^{-3} for neon and argon, respectively. These concentrations are an order of magnitude larger than those we use from *Hodges et al.* [1974]. Use of these larger densities would result in a corresponding increase in neutral and ion concentration from the calculations which follow, but the qualitative results would remain unchanged.

During the 4 days that it is in the geomagnetic tail, the moon is shielded from the solar wind plasma, and the source for hydrogen, helium, neon, and argon (^{36}Ar) in the atmosphere is cut off. However, the venting of ^{40}Ar from the surface is unaffected. Likewise, the atmospheric losses due to thermal escape and photo-ionization continue. Following *Hinton and Taeusch* [1964] we present a simplified model of the lunar atmosphere time history in the geotail under these conditions We assume that all of the particles of a particular species of mass m are uniformly distributed with a concentration n_0 from the surface to the scale height h, where $h = kT/mg$ (k is Boltzmann's constant, T is the temperature, and g is the acceleration due to gravity at the lunar surface). The total number of particles of a particular type is $N = n_0V$, where $V = \frac{4}{3}\pi[(r_0 + h)^3 - r_0^3]$ is the scale volume and r_0 is the lunar radius.

The total number of molecules in the atmosphere, as a function of time, depends on the sources and sinks appropriate to each species. While the moon is shielded from the solar wind, the only source of particles we consider is from surface venting of ^{40}Ar produced in the radioactive decay of ^{40}K. This contribution is taken to be 8.7×10^{20} atoms/s, as given by *Hodges et al.* [1974] (see Table 1).

We consider two atmospheric loss mechanisms for the moon in the geomagnetic tail, photo-ionization and thermal escape. In the daytime hemisphere, each species is ionized by solar ultraviolet (UV) radiation to an extent dependent on its density, its photo-ionization cross section, and the UV flux. The photo-ionization loss rate of neutrals per second for each species in the dayside scale volume V_1 is

$$\left(\frac{dN}{dt}\right)_{\text{photo}} = -n_1(t)V_1 \sum_{\lambda} \sigma(\lambda)\Phi(\lambda) \qquad (1)$$

where σ is the photo-ionization cross section for that species at the wavelength λ, Φ is the corresponding photon flux, and n_1 is the daytime particle concentration. The solar flux is virtually unattenuated by the tenuous lunar atmosphere. Therefore we have assumed in (1) that this flux is independent of altitude. We used the photoabsorption cross sections in our calculations; for atomic systems, they are essentially equal to the photo-ionization cross sections. Numerical values for the cross sections from *McDaniel* [1964] and fluxes from *Hinteregger* [1970] were used. We obtained the following results for the summation $\sum \sigma\Phi$ in (1): for neon, 1.29×10^{-7} s^{-1}; for argon, 3.25×10^{-7} s^{-1}; and for helium, 6.07×10^{-8} s^{-1}. The loss rate of hydrogen is dominated by thermal escape and not by photo-ionization.

In both the lunar daytime and nighttime hemispheres, thermal escape of an atmospheric molecule is determined by competition between the particle's kinetic energy and its gravitational potential energy. The thermal loss rate of molecules per second for each species of mass m and particle density $n_0(t)$ is

$$\left(\frac{dN}{dt}\right)_{\text{thermal}} = -2\pi r_0^2 n_1 \left(\frac{kT_1}{2\pi m}\right)^{1/2} \exp\left(-\frac{mgr_0}{kT_1}\right)\left(1 + \frac{mgr_0}{kT_1}\right) - 2\pi r_0^2 n_2 \left(\frac{kT_2}{2\pi m}\right)^{1/2} \exp\left(-\frac{mgr_0}{kT_2}\right)\left(1 + \frac{mgr_0}{kT_2}\right) \qquad (2)$$

Particle densities and temperatures differ on the dayside and the nightside hemispheres of the moon. The first term on the right-hand side of (2) is the daytime thermal loss rate (subscript 1), and the second term is the nighttime thermal loss rate (subscript 2). This well-known form of the thermal loss rate expression for a collision-free atmosphere, valid for the lunar exosphere, was first derived by *Jeans* [1916] (see also *Milne* [1923], *Hinton and Taeusch* [1964], and *Johnson* [1971]).

The day-night asymmetry described above is a result of the interaction between the molecules and the lunar surface. The

TABLE 1. Lunar Atmosphere Parameters—Moon in Solar Wind

	H	H_2	^{4}He	^{20}Ne	^{36}Ar	^{40}Ar
Solar wind influx, ions/s	2.8×10^{25}	···	1.3×10^{24}	2.2×10^{21}	8.0×10^{19}	···
Lunar venting, atoms/s	···	···	···	··	···	8.7×10^{20}
Photo-ionization loss time, days	116	116	116	90*	36*	36*
Thermal loss time	0.98 hours	1.2 hours	3.2 hours	10^2 years	10^5 years	10^9 years
Daytime surface concentration, cm^{-3}	2.7×10^3	3.5×10^3	1.9×10^3	4×10^3	1.3×10^2	1.6×10^4

Adapted from *Hodges et al* [1974].
*Calculation of these values, which differ from those of *Hodges et al* [1974], is discussed in the text.

particles execute ballistic trajectories between collisions with the surface In this,random walk process the mean step size is proportional to the temperature Therefore these average steps are longer on the hotter dayside hemisphere, resulting in a higher density on the cooler lunar nightside

The asymmetry effect was discussed quantitatively by *Hodges and Johnson* [1968] and by *Hodges* [1973]. We use their results to find the night-day density ratio

$$\rho \equiv \frac{n_2}{n_1} = \frac{f(T_1)}{f(T_2)} \left(\frac{T_1}{T_2}\right)^{5/2} \tag{3}$$

for each species. In our model we take $T_1 = 370°K$ and $T_2 = 100°K$. In (3), f is a complicated function of mgr_0/kT Numerical values of f, valid for an exosphere, may be obtained from *Hodges* [1973] (our $f \equiv P_2$ in this reference) We take $n_2 = \rho n_1$ because the lateral diffusion lifetime is small in comparison with the photo-ionization and thermal escape lifetimes. (For example, the lateral transport time for H_2 is 30 times smaller than the thermal loss time.) It should be noted that this density versus temperature relationship does not hold for argon, which is absorbed on the nightside lunar surface.

In contrast to the $\rho \propto T^{-5/2}$ relationship derived by *Hodges* [1973], which we have used to infer nightside densities, *Benson and Freeman* [1976] report a $\rho \propto T^{-1/2}$ relationship based on lunar suprathermal ion detector data. If the $T^{-1/2}$ relationship were used in our calculations, the resultant nightside densities would be reduced by 93% in comparison with our present results. It will become apparent later that our lunar ionosphere calculations are based only on the dayside atmosphere and therefore will not be affected by this discrepancy in the density versus temperature relationship

In our lunar atmosphere model the time rate of change of the number of particles for each species is described by

$$\frac{dN}{dt} = V_1 \frac{dn_1}{dt} + V_2 \frac{dn_2}{dt} \tag{4}$$

where $V_1 \equiv \frac{4}{3}\pi[(r_0 + h_1)^3 - r_0^3]$ and V_2 is defined by a similar expression with a scale height of $h_2 = kT_2/mg$ All source and sink contributions to dN/dt, which have been discussed, may now be combined and (4) solved for dn_1/dt:

$$\frac{dn_1}{dt} = n_1 A + C \tag{5}$$

where

$$A \equiv \frac{1}{v} V_1 \sum \sigma\Phi + 2\pi r_0^2 \left(\frac{kT_1}{2\pi m}\right)^{1/2} \exp\left(-\frac{mgr_0}{kT_1}\right)\left(1 + \frac{mgr_0}{kT_1}\right) + \rho \left(\frac{kT_2}{2\pi m}\right)^{1/2} \exp\left(-\frac{mgr_0}{kT_2}\right)\left(1 + \frac{mgr_0}{kT_2}\right) \tag{6}$$

$$C = J_s(4\pi r_0^2)/v \tag{7}$$

J_s is the venting rate per unit area, and $v = V_1 + \rho V_2$. Equation (7) gives a value only for ^{40}Ar, where the value for $J_s(4\pi r_0^2)$, lunar venting in atoms per second, is obtained from Table 1 For the other atmospheric constituents we assume that there is no surface venting, and therefore for them, $C = 0$ Equation (5) may be integrated to yield

$$n_1(t) = -(C/A)(e^{-At} - 1) + n_1(t = 0)e^{-At} \tag{8}$$

Of the two contributions to the exponential loss factor, photoionization is the primary loss mechanism for argon and neon, and thermal escape dominates for hydrogen and helium. In Figure 1 the dayside number density for each species is plotted as a function of time for the 4-day period that the moon is in .he geomagnetic tail.

Two days after the moon enters the geotail, the total particle density of the atmospheric constituents at the lunar surface is calculated to be $7\,5 \times 10^3$ cm^{-3}. In comparison, the total atmospheric density when the moon is in the solar wind is about 14×10^3 cm^{-3} [*Hodges et al*, 1974] The primary reason for the difference in densities is that the light elements, hydrogen and helium, which undergo rapid thermal escape from the lunar atmosphere, are continually replenished in the solar wind but not in the geotail. The contribution of the lunar atmosphere to the lunar ionosphere can now be considered for the moon in the geomagnetic tail. Figure 1 indicates that argon and neon are the two principal sources, helium and hydrogen make negligible contributions.

3. LUNAR IONOSPHERE: HYDROSTATIC MODEL

In this section we calculate the production rates of lunar ionosphere constituents that are formed, primarily, by photoionization of the lunar atmosphere in the geomagnetic tail Then we investigate the time variation of this ionosphere by first employing a hydrostatic model, that is, thermal energies tending to cause charged particles to escape from the moon are counteracted only by lunar gravitational attraction. Our purpose here is to determine whether the hydrostatic case is adequate to describe conditions expected to exist at the moon

There are several sources of charged particles in the lunar environment. A photoelectron layer is produced that has a density of $\sim 10^4$ cm^{-3} near the lunar surface; the density decreases rapidly with height and terminates several hundred meters above the surface. The energy of these photoelectrons ranges between 40 and 200 eV. This near-surface layer establishes a surface potential ranging from 10 to 200 V [*Reasoner and Burke*, 1972; *Walbridge*, 1973; *Freeman and Ibrahim*, 1974].

The ambient plasma density in the geomagnetic tail taken in the vicinity of the lunar orbit is less than the average plasma sheet density of ~ 0.1 cm^{-3}. The average temperature of the ambient lobe plasma is approximately 10^5 °K [*Rich et al.*, 1973]. Occasional density enhancements that occur in this background lobe plasma have been reported *Anderson* [1965] observed clouds of particles in the geomagnetic lobes with energies above 40 keV. Using suprathermal ion detector measurements, *Hardy et al.* [1975] and *Hardy* [1976] observed intermittent plasma regimes with densities ranging from 0.1 to 3 cm^{-3}, energies up to 80 eV, and bulk velocities of 60–200 km/s

A. S Vyshlov et al. (unpublished report, 1976) have used Luna 19 and Luna 22 spacecraft data in a dual-frequency dispersion experiment designed to determine the density of the lunar ionosphere. They report electron number densities up to 10^3 cm^{-3} at an altitude of ~ 10 km. This value seems to be an extremely high estimate; it is inconsistent with other measurements made in the lunar environment and also difficult to justify on theoretical grounds This result may be an artifact of the analytical technique, for example, the authors have assumed a spherically symmetric plasma distribution, an, obvious oversimplification in view of the fact that the authors reported that they themselves observed no plasma over the lunar nightside. Another possible explanation of their results involves the well-known locally enhanced ^{40}Ar concentration near the sunrise terminator [e g , *Hodges et al*, 1974], because measurements used in their analysis were all made near the

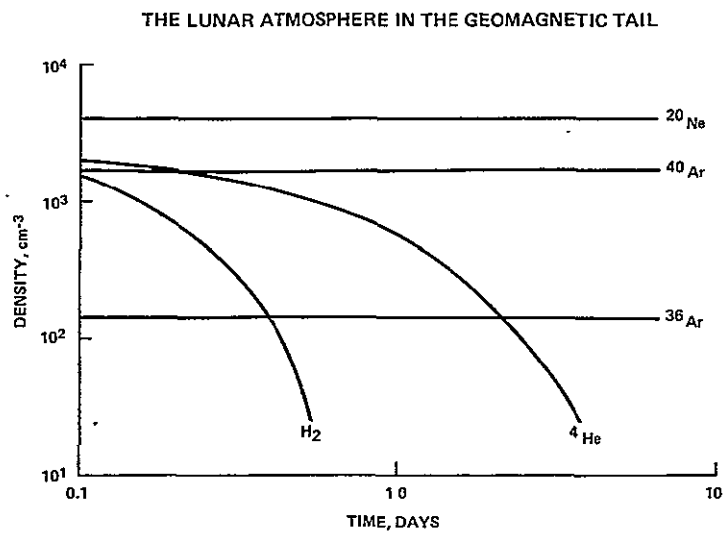

Fig 1. Density of the atmospheric components plotted as a function of time for the case when the moon is in the lobes of the geomagnetic field and shielded from the solar wind At time $t = 0$ the moon enters the geomagnetosphere (the solar plasma is shut off), and the initial densities are the equilibrium values for the moon in the solar wind plasma.

sunrise terminator, their results could have been biased by the argon enhancement phenomenon. Until further evidence is presented, we will consider the high-density estimate to be indicative of a local effect, not representative of the whole moon.

In the preceding discussion we have outlined results that have been reported in the literature concerning properties of the plasma in the lunar environment. In the remainder of this section we present a theoretical development to describe the plasma that results specifically from ionization of the lunar atmosphere when the moon is in the geomagnetic tail.

In the photo-ionization process a photon ionizes a neutral atom and the electron acquires the excess energy:

$$\epsilon_k \doteq h\nu - I_p \tag{9}$$

where ϵ_k is the photoelectron kinetic energy, $h\nu$ is the photon energy, and I_p is the neutral atom's ionization potential. The most intense solar UV radiation impinging on the lunar atmosphere is hydrogen Lyman alpha, for which $h\nu \sim 10$ eV; this energy is insufficient to ionize any of the neutral species in the atmosphere. The ionizing UV spectrum has its maximum flux near $h\nu \sim 37$ eV [*Hinteregger,* 1970]. The lowest ionization potentials of Ne and Ar are 21 and 16 eV, respectively. Using the photon spectrum as measured by *Hinteregger* [1970] and the corresponding ionization cross sections for Ne and Ar [*McDaniel,* 1964], we estimate the average photoelectron energy to be 19 eV, corresponding to a temperature of 1.5×10^5 °K. The electron acquires most of the excess energy when an atom is photo-ionized, while the positive ion is left essentially in thermal equilibrium with the lunar surface at about 370°K.

The expressions given by *McDaniel* [1964] for mean free paths yield values of $\sim 10^4$ lunar radii for electron-neutral collisions and $\sim 10^8$ lunar radii for electron-ion collisions. These values are based on a neutral density of 7.5×10^5 cm^{-3} (see Figure 1) and an ion density of 10^{-2} cm^{-3} (see Figure 2). Therefore the photoelectron and ion temperatures remain constant. Electrons that collide with the lunar surface are neutralized and replaced by photoelectrons from the surface. These photoelectrons preserve charge neutrality. We conclude therefore that an essential feature of the lunar ionosphere is that it consists of hot photoelectrons and relatively cool positive ions, all of which retain their thermal energies.

The properties of a gravitationally bound ionosphere are described by the equation for hydrostatic equilibrium, which is modified to account for an electric field necessary to maintain local charge neutrality Let us consider the hydrostatic properties of a static lunar ionosphere consisting of positive ions of mass m_+ and temperature T_+ and electrons of mass m_- and temperature T_-. We neglect magnetic field effects. For neutral particles the appropriate equation of hydrostatic equilibrium is

$$dP/dr = -\rho(r)g(r) \tag{10}$$

where P is the pressure, r is the radial distance from the center of the moon, $\rho(r)$ is the neutral particle mass density, and $g(r)$ is the acceleration due to gravity. The equation of state for an ideal gas is applicable to the lunar exosphere:

$$P(r) = n(r)kT(r) = \frac{\rho(r)}{m}\,kT(r) \tag{11}$$

where $n(r)$ is the particle number density.

To consider the lunar ionosphere, we modify (10) to insure charge neutrality: $n_+(r) = n_-(r)$. If gravitational and thermal effects tend to separate the ions from the electrons, then an electric field E (called the Rosseland field [*Alfvén,* 1965]) is generated which restores the system to local neutrality. (We note that the physics of the surface photoelectron layer is different; there charge neutrality is violated and hydrostatic pressure is balanced by electrostatic forces [*Reasoner and Burke,* 1972].) Separate equations of hydrostatic equilibrium for the ions and electrons, modified to include this electrostatic field, can be solved for the mass distribution of the plasma Gravitational binding requires of the solutions that $\lim_{v\to\infty} n_\pm(r) = 0$ It is found (see Appendix A for details) that essentially the same conditions must be met for ionospheric binding, independent of the form of polytrope law used:

$$T_{\text{crit}}/T^* > 1 \tag{12}$$

where

$$T_{\text{crit}} = m^* g(r_0) r_0 / k \tag{13}$$

and $m^* = m_+ + m_-$ and $T^* = T_+ + T_-$ are the sums of the ion and electron masses and temperatures, respectively.

For the parameters appropriate to the moon, $T_{\text{crit}} \simeq 6772$°K. However, $T^* = 1.5 \times 10^5$ °K, and thus (12), the

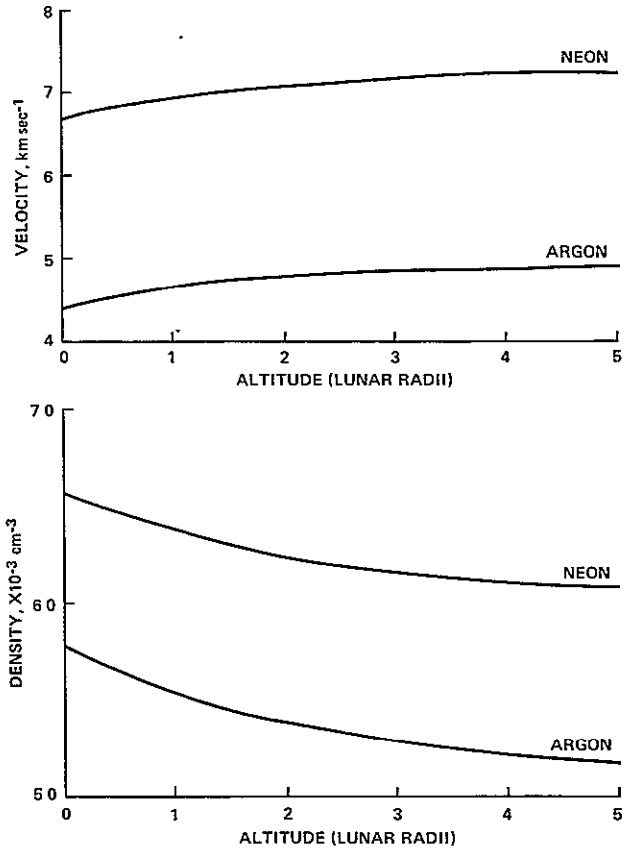

Fig. 2. The plasma bulk velocity and number density of the lunar ionosphere in the geomagnetic tail, plotted as functions of altitude above the reference level for the case $s = 0$ (uniform external magnetic field) and $\alpha = 1$ (isothermal plasma at $T_e + T_i = 1.5 \times 10^{5}$°K)

condition for gravitational binding of the lunar ionosphere, is not satisfied. Therefore we conclude that the lunar ionosphere is not in hydrostatic equilibrium with the moon We now turn to a hydrodynamic model, where we find that a number of concepts introduced here (the Rosseland field, the polytrope laws relating pressure and density, and the ratio of the gravitational energy to the thermal energy, $m^*g(r_0)r_0/kT^*$) play a significant role.

4. Lunar Ionosphere: Hydrodynamic Model

Description of the dynamic lunar ionosphere, which we have found not to be gravitationally bound to the moon, requires a hydrodynamic approach. In our analysis we have developed a two-fluid model that is applied first to neon ions and electrons and then independently to argon ions and electrons. Although a three-fluid approach applied to the Ne^+, Ar^+, and electron plasma would be more internally consistent, it would be far more complex and difficult to develop and would yield results close to those of the two-fluid approach. A three-fluid treatment should yield a flow velocity between the two predicted for neon and argon plasmas separately; changing the separate velocities calculated in the two-fluid approximation to a single intermediate velocity and using equation (17) to recalculate the plasma densities, we estimate that the total densities in the two-fluid and three-fluid approaches would differ by less than 15%. We feel therefore that the simpler two-fluid treatment yields results that are accurate enough for our purposes.

The dynamic behavior of the lunar plasma will be strongly influenced by the magnetic field in the lunar environment We therefore begin the development of the hydrodynamic model, which is analogous to that of *Parker* [1963] for the solar wind and to that of *Banks and Holzer* [1969] for the polar wind, by briefly reviewing properties of the geomagnetic tail field. The interaction of the solar wind with the earth's permanent dipole field results in the formation of a cylindrical magnetic region (the geomagnetic tail) on the earth's antisolar side At the distance where the moon's orbit intersects the tail, the magnetic field magnitude is about 10 γ. The solar wind plasma is essentially excluded from this region. The moon is in the geomagnetic tail for about 4 days of each 29 5-day lunation The structure of the tail consists of 2 lobes; the upper or northward lobe has its magnetic field pointing roughly toward the earth, whereas the magnetic field of the lower lobe points away from the earth. The region between the lobes, the neutral sheet, is characterized by a very low magnetic field magnitude and plasma energy density larger than the values found in the lobes. The path of the moon through the tail depends on the characteristics of the particular orbit, the geomagnetic dipole orientation, and perturbations of the geomagnetic tail caused by solar wind pressures. We model these conditions by assuming that the moon is in a uniform external magnetic field of 10 γ, and we take the external plasma density to be zero. The ionospheric plasma energy density is small in comparison with the magnetic field energy density (their ratio is $\beta = 6.2 \times 10^{-4}$; see the discussion in the next section). Therefore the hydrodynamic streamlines are parallel to the magnetic field lines

In this hydrodynamic model, charged particles of the lunar ionosphere flow along the magnetic field lines away from the lunar sunlit side toward the earth The gyromagnetic radius for an electron is 1 5 km and for an argon ion is 20 km; the Debye length is 0 6 km (as will be shown later) Because these values are small in comparison with the lunar radius, $r_0 = 1738$ km, the ionosphere can be characterized by a plasma that flows along the geomagnetic field defining a cylinder which has a diameter of $2r_0$ and extends from the lunar dayside hemisphere toward the earth. Our approach and results, presented in this section, are similar to those of *Parker* [1963] for the solar wind

The Bernoulli equation for a plasma consisting of ions and electrons of different temperatures (T_+ and T_-), which includes an electric potential ϕ to maintain charge neutrality, is

$$\tfrac{1}{2}m_\pm v_\pm^2(r) + \frac{\alpha}{\alpha - 1} kT_\pm(a) \left[\frac{n_\pm(r)}{n_\pm(a)}\right]^{\alpha-1} + m_\pm\Phi(r) \mp e\phi(r)$$

$$= \tfrac{1}{2}m_\pm v_\pm^2(a) + \frac{\alpha}{\alpha - 1} kT_\pm(a) + m_\pm\Phi(a) \mp e\phi(a) \qquad (14)$$

where $v_\pm(r)$ is the ion or electron flow velocity at a position r along a streamline. The gravitational potential $\Phi(r) = g(r)r$. The Rosseland potential ϕ is added to insure charge neutrality $n_+(r) = n_-(r) = n(r)$, where n is number density; α is the polytrope index, $m_\pm$ is the ion or electron mass, and e is the electron charge The sphere $r = a$ defines the altitude above the moon at which the surface lunar remanent field becomes negligible For $r > a$ the total magnetic field is the geomagnetic field, which is assumed to be uniform; whereas for $r < a$ the total field includes the surface remanent fields, which are highly nonuniform. We have chosen $a = r_0 + \delta$, where $\delta = 20$ km (from results reported by *Russell et al* [1975]). This choice will be further discussed later in this section.

Equation (14) can be solved requiring charge neutrality of the flow along streamlines, which for convenience, are viewed

as tubes of flow with cross-sectional area $A(r)$ described by $A(r)/A(a) = (r/a)^s \equiv (\zeta)^s$. The parameter s can be adjusted to correspond to the flow geometry. In our case the streamlines are parallel to the approximately uniform geomagnetic tail field; therefore the flow tube cross section $A(r)$ is a constant, and $s = 0$. The solution of interest (see Appendix B for details) for the limit as $s \to 0$ is, for $\alpha \neq 1$,

$$U_c = \left(\frac{\alpha}{2}\right)^{1/(\alpha+1)} [U(a)]^{(\alpha-1)/(\alpha+1)} \qquad \zeta_c = \infty$$

$$U^2(a) + \frac{\alpha}{\alpha - 1} - Q(a) = \frac{\alpha + 1}{\alpha - 1}\left[\left(\frac{\alpha}{2}\right)^{2/(\alpha+1)} U(a)^{2(\alpha-1)/(\alpha+1)}\right] \tag{15}$$

and for $\alpha = 1$,

$$U_c = \frac{1}{2^{1/2}} \qquad \zeta_c = \infty$$

$$U^2(a) - \ln U(a) - Q(a) = \tfrac{1}{2}(\ln 2 + 1) \tag{16}$$

where $U^2(r)$ is the ratio of flow kinetic energy to thermal energy, $Q(a)$ is the ratio of the plasma gravitational and thermal energy, and the critical solution $U(\zeta_c) = U_c$ is found which, with the asymptotic boundary conditions, gives the physically valid solution.

Equations (15) and (16) enable us to calculate the bulk velocity $v(r)$ as a function of altitude; we also wish to calculate density as a function of altitude. Ions produced in the atmosphere have a loss rate $A(r)v(r)n(r)$, where $A = 2\pi r_0^2$ is the cross-sectional area of our assumed cylindrical flow pattern and $n(r)$ is the ion number density. The ion production rate in the atmosphere is $2\pi\beta_0 n_0 r_0^2 h$, where β_0 is the photo-ionization rate, n_0 is the neutral particle density, and h is the neutral scale height. In equilibrium the ion production and loss rates are equal, and therefore

$$n(r) = \frac{\beta_0 n_0 h}{v(r)} \tag{17}$$

We have established the mathematical base necessary for the discussion of the hydrodynamic properties $v(r)$ and $n(r)$ of the lunar ionosphere. Two more important physical parameters must be considered, however, before we arrive at our final values for $v(r)$ and $n(r)$: (1) the fraction of the total number of electron-ion pairs produced by photo-ionization that are not absorbed by the lunar surface and are therefore available as constituents of the lunar ionosphere and (2) the radius of the reference level $r = a$, above which the dominant magnetic field is the geomagnetic tail field (the lunar remanent field is negligible).

In the preceding discussions we have assumed that all electron-ion pairs produced by solar UV radiation flow away from the moon. In the photo-ionization process the angular distribution of the photoelectrons is proportional to $\sin^2\theta$, where θ is the angle between the directions of motion of the photon and the electron [*Heitler*, 1944]. Ion pairs with $\theta \geq 90°$ will flow away from the moon. The ion pairs that move toward the moon will either be absorbed by the surface or reflected by the surface magnetic fields. We estimate that $\gtrsim 80\%$ of these will be reflected [see *Lin et al.*, 1976] and therefore that a total of $\sim 90\%$ of the ion pairs participate in the hydrodynamic flow. We have multiplied the calculated plasma densities by 0.9 in order to account for this 10% loss.

To determine the appropriate reference level ($r = a$) we estimate the altitude at which the total magnetic field is predominantly the uniform geomagnetic field, that is, where the surface remanent field is negligible. The Apollo 15 and 16 subsatellite and lunar surface magnetometers have made direct measurements of surface remanent fields. The total field as a function of altitude can be approximated by the empirical relationship

$$B = 10 + 0.1\left(\frac{93}{Z + 7}\right)^{2.6} \tag{18}$$

where B is the total field in gammas and Z is the altitude in kilometers [*Coleman et al.*, 1972]. This equation is a model of the mean field magnitude and does not precisely represent the field at any one location near the surface. The second term in (18) is the remanent field contribution. Below an altitude of about 20 km the remanent field contribution becomes significant, and the total magnetic field rises sharply above the geomagnetic tail value of 10 γ. Magnetic field measurements have also been made on the lunar surface at the Apollo 12, 14, 15, and 16 landing sites; reported field magnitudes range between 3 and 327 γ [*Dyal et al.*, 1973].

The orientations of the surface fields vary widely over distances of a few kilometers. Low-altitude (0–20 km) measurements from the Apollo 16 subsatellite confirm this variability of the vector surface magnetic field. The remanent surface fields have been measured along the lower-altitude trajectories, the field components vary with a scale size of roughly 30 km [*Russell et al.*, 1975].

These measurements provide an overall model for the magnetic field in the vicinity of the moon in the lobes of the geomagnetic tail. Above an altitude of approximately 20 km the field is relatively uniform, with a magnitude of $\sim 10\ \gamma$, and directed along the earth-sun line; below 20 km the field is highly convoluted, and its average magnitude increases rapidly to a maximum of a few hundred gammas at the surface.

We have now completed the description of our hydrodynamic model of the lunar ionosphere. Using equations (15), (16), and (17), we calculate bulk velocity $v(r)$ and number density $n(r)$ for the ionosphere, which, deep in the geomagnetic tail, is comprised primarily of ^{20}Ne and ^{40}Ar (see Figure 1). We have already discussed in section 2 the parameters relating $n(r)$ to $v(r)$ in (17); we list them here for reference: for neon, $\beta_0 = 1.29 \times 10^{-7}\ s^{-1}$, $n_0 = 4 \times 10^3\ cm^{-3}$, and $h = 95$ km; for argon, $\beta_0 = 3.53 \times 10^{-7}\ s^{-1}$, $n_0 = 1.7 \times 10^3\ cm^{-3}$, and $h = 47.5$ km.

The flow velocity $v(r)$ is calculated and plotted as a function of altitude in Figure 2 for neon and argon. The characteristic bulk velocity of the lunar ionosphere is in the range 4–7 km/s away from the moon and toward the earth. Corresponding particle densities are calculated using (17) (adjusted by the 0.9 factor to account for surface absorption), and they too are plotted in Figure 2. The average ionospheric density is $\sim 1.2 \times 10^{-2}\ cm^{-3}$ at 100-km altitude. If the neutral atmospheric densities reported by *Benson and Freeman* [1976] and discussed in section 2 were used in the calculation, the corresponding plasma densities would be larger by a factor of 25. In these calculations there is uncertainty in the physical parameter α. We have considered $\alpha = 1$, the isothermal case, as characteristic of limiting behavior. Actually, we expect α to increase slightly with r, corresponding to a decrease in temperature as the ionosphere expands. Adiabatic expansion, for which $\alpha = \frac{5}{3}$, is another limiting form of behavior. In order to show the effect of changing α and s, values of v and n at an altitude of 100 km for a few different combinations of s and α are listed in Table 2. The altitude dependences of v and n for these cases are similar to those shown in Figure 2. Note from Table 2 that the

TABLE 2 Bulk Velocity and Ion Density at an Altitude H = 100 km for Neon and Argon

		Neon		Argon	
s	α	$v(H)$, km/s	$n(H)$, 10^{-3} cm^{-3}	$v(H)$, km/s	$n(H)$, 10^{-3} cm^{-3}
0	1	6 75	6.54	4.45	5.76
0	⅔	7 73	5 71	5.15	4 98
0	½	8.94	4 92	6.13	4 19
0.2	1	12.2	3 60	7.84	3 27
0.2	⅔	17 4	2.54	11.0	2 34
0 2	½	26 7	1 65	16.5	1.55

bulk velocity at a given altitude increases with s and α. Equations (B2), (B8), and (B9) indicate this behavior. It is clear from equation (B9) that as s increases, the quantity s ln ζ, which remains positive, increases, thereby enhancing the value of $U^2(r)$, which is proportional to $v^2(r)$. As α increases without limit in equations (B2) and (B8), the term raised to the $\alpha - 1$ power goes to zero, and $U^2(r)$ attains its maximum value for a given altitude. Therefore the case presented in Figure 2 represents a physically reasonable upper limit for the ion density.

5. Results and Discussion

Lunar atmosphere and ionosphere for quiescent geotail conditions. The concentrations of the constituents of the lunar atmosphere when the moon is in the geomagnetic tail are found to differ substantially from properties in the solar wind, which is a primary source of the lunar atmosphere. This is especially true during 'quiescent' geotail conditions when effects due to external plasma are minimal (e.g., in lobe regions when little or no plasma is detected by Apollo solar wind spectrometers or suprathermal ion detectors). Argon 40 has a source both in the solar wind and the geotail; it is vented from the surface as a radioactive decay product of subsurface ^{40}K. Hydrogen and helium existing in the lunar atmosphere initially as the moon enters the geotail are lost rapidly, primarily through thermal escape, whereas the heavier constituents, neon and argon, are lost very much more slowly through photo-ionization. After 2 days in the tail, the constituent atmospheric densities are calculated to be as follows: H_2, <10 cm^{-3}; ^{4}He, ~ 500 cm^{-3}, ^{36}Ar, $\sim 1.3 \times 10^2$ cm^{-3}; ^{40}Ar, $\sim 1.6 \times 10^3$ cm^{-3}, and ^{20}Ne, $\sim 3.9 \times 10^3$ cm^{-3}.

Ultraviolet radiation from the sun continually ionizes the lunar atmosphere, above the sunlit hemisphere of the moon. When the moon is in the solar wind, these charged particles are quickly and efficiently removed from the lunar environment by the $\mathbf{V} \times \mathbf{B}$ electric field associated with the solar wind plasma flow past the moon [*Lindeman et al*, 1973; *Manka and Michel*, 1973]. When the moon is shielded from the solar wind by the geomagnetosphere, conditions are much different. The ionization produces electrons at $\sim 1.5 \times 10^5$ °K and ions at ~ 370°K from neon and argon, the two most abundant atmospheric species. A hydrostatic treatment of this problem leads to the concept of a Rosseland electric field, which is required to preserve charge neutrality in the presence of the differential competition between gravitational binding and thermal evaporation. A hydrostatically bound ionosphere is one in which the ion pair particle density vanishes at large altitudes. We find that binding requires that the gravitational potential energy exceed the thermal energy. For the conditions appropriate to the moon this does not occur; indeed, the thermal energy exceeds the gravitational energy by a factor of 20. Therefore a hydrostatic treatment is not applicable, and a bound ionosphere does not exist; a hydrodynamic approach is required to describe the lunar ionosphere in the geotail.

At the lunar orbit the earth's magnetic field is nearly uniform and ~ 10 γ. This field corresponds to a magnetic energy density of $\sim 4 \times 10^{-10}$ erg/cm^3, a value large in comparison with the energy density of the ionized atmosphere, which is $\sim 2 \times 10^{-13}$ erg/cm^3. Therefore the particles flow parallel to the magnetic field lines, forming a cylinder whose base has the lunar diameter. We have developed a hydrodynamic model which predicts ionospheric flow velocities in the range 4–7 km/s and corresponding ion pair densities of $\sim 1.2 \times 10^{-2}$ cm^{-3}.

Magnetic permeability of the quiescent ionosphere. From our calculations of ionospheric characteristics we can estimate electromagnetic properties of the ionosphere to determine the influence of the ionosphere on electromagnetic studies of the moon's interior. Our results from the previous section allow calculation of the lunar ionosphere's plasma energy density $nkT = 2.5 \times 10^{-13}$ erg/cm^3, from which we obtain diamagnetic properties of the ionosphere. The magnetization of the plasma is $\mathbf{M} = n\mathbf{m}$, where the magnetic moment $\mathbf{m} = mv^2\mathbf{B}/2B^2 = -kT\mathbf{B}/B^2$. Because $\mathbf{B} = \mathbf{H} + 4\pi\mathbf{M} = \mu\mathbf{H}$ and $\beta \equiv 8\pi nkT^*/B^2$, the relative magnetic permeability is

$$\mu = \frac{1}{(1 + \beta/2)} \tag{19}$$

The quantity β, the ratio of thermal to magnetic energy density, is $\sim 6 \times 10^{-4}$. The corresponding magnetic susceptibility of the ionosphere is $\chi = (\mu - 1)/4\pi \simeq -2.5 \times 10^{-5}$ emu/cm^3. This value is almost 3 orders of magnitude too low to account for the diamagnetic moment of the moon reported by *Russell et al.* [1974*a*]; furthermore, the tenuous lunar ionosphere is confined primarily on the lunar sunlit side and is not confined to regions of altitude below 100 km. We conclude that the lunar ionosphere contributes only negligibly to the plasma environment near the moon; therefore it is valid to neglect lunar ionospheric effects in studies of electromagnetic properties of the lunar interior [e.g., *Dyal et al.*, 1976; *Sonett et al.*, 1972; *Parkin et al.*, 1974; *Goldstein et al.*, 1976].

Effects of electric fields and external plasma on the lunar ionosphere. In the above discussion we have assumed that the only source of the lunar ionosphere is the lunar atmosphere, a condition that is often valid when the moon is in the high-latitude lobes of the geomagnetic tail. Several investigators have reported cross-tail electric fields and plasma flows occurring intermittently throughout the geomagnetosphere. In this section we describe these effects and include them in our model in a semiquantitative way.

Cross-tail electric fields occur sporadically in the lunar vicinity with a magnitude of ~ 0.1 mV/m [*McCoy et al.*, 1975]. During times when such electric fields exist at the moon, the ionospheric electrons and ions will, in addition, experience $\mathbf{E} \times \mathbf{B}/B^2$ drift velocities. A cross-tail electric field will add a cross-tail velocity component, resulting in ion pair number densities lower than the results presented here. For example, when the drift velocity equals the hydrodynamic flow velocity, the plasma density is reduced by $\sim 30\%$. In the absence of these fields the lunar ionosphere in the geomagnetic tail is confined to a cylindrical region extending from the lunar sunlit side along the geomagnetic field lines toward the earth. As the moon encounters sporadic electric fields $\gtrsim 0.1$ mV/m, this relatively smooth flow pattern will be temporarily disrupted. This condition will occur approximately 40% of the time in the geomagnetic tail.

Intermittent plasma flow in the geomagnetic tail will also affect the lunar ionosphere. *Hardy et al.* [1975] and *Hills et al.* [1976] have investigated properties of the plasma sheet and lobe plasma at the lunar orbit in the geotail. The plasma sheet has an ion pair number density ranging from 0.05 to 1.5 cm^{-3}, a thermal energy between 150 and 800 eV, and a bulk velocity of ~600 km/s. The lobe plasma has a number density ranging from 0.1 to 10 cm^{-3}, a thermal energy of $\leq$20 eV, and a bulk velocity between 50 and 200 km/s. These plasma regimes, like the cross-tail electric fields, are sporadic in nature, but they will tend to enhance rather than decrease the plasma energy density in the lunar vicinity. For example, on the assumption that a density of 0.5 cm^{-3} and an energy of 250 eV are representative of the plasma sheet and 0.1 cm^{-3} and 3 eV are typical of the lobe plasma, the corresponding energy densities are 125 and 0.3 eV cm^{-3}. These are both much larger than the values we have calculated for the ionosphere under quiescent conditions

Magnetic data analysis during quiescent conditions Suprathermal ion detector measurements [*Hardy*, 1976] indicate that the plasma energy density in the geomagnetic tail is below the sensitivity of the instrument about 30% of the time It is during these quiescent times in the geotail lobes that our hydrodynamic model for the ionosphere is applicable to the lunar plasma environment. The energy density calculated for the quiescent ionosphere is too low to be detectable by using presently available instrumentation. Lobe data measured during quiescent conditions have been used for our analyses of internal lunar electrical conductivity and magnetic permeability using magnetometer data [e.g., *Dyal et al.*, 1976]. We calculate magnetic susceptibility of the extralunar plasma to be -2.5×10^{-5} emu/cm^3, a value which would change the calculated lunar permeability [*Parkin et al.*, 1974; *Dyal et al.*, 1975] by an amount that is negligible in comparison with errors inherent in present data analyses We conclude that during times in the high-latitude tail lobes when lunar plasma energies are below the resolution of Apollo suprathermal ion detectors, plasma effects can be neglected for electromagnetic studies of the lunar interior.

APPENDIX A: HYDROSTATIC MODEL

The equation of hydrostatic equilibrium for ions and electrons, including the effect of the electrostatic field to maintain charge neutrality, can be written

$$\frac{dP_\pm}{dr} = -n_\pm(r)m_\pm g(r) \pm n_\pm eE \tag{A1}$$

Separate equations of state hold for the two ionospheric constituents:

$$P_\pm = n_\pm(r)kT_\pm(r) \tag{A2}$$

We consider two possible polytrope laws relating pressure to density:

$$\frac{P_\pm(r)}{P_\pm(r_0)} = \left[\frac{\rho_\pm(r)}{\rho_\pm(r_0)}\right]^\alpha \tag{A3}$$

and

$$\frac{P_\pm(r)}{P_\pm(r_0)} = \left[\frac{\rho_\pm(r)}{\rho_\pm(r_0)}\right]\left(\frac{r_0}{r}\right)^l \tag{A4}$$

These reduce to the isothermal case when $\alpha = 1$ or $l = 0$

Equation (A1) can be solved for the Rosseland field, E, on the assumption of charge neutrality:

$$n_+ = n_- \tag{A5a}$$

and

$$dn_+/dr = dn_-/dr \tag{A5b}$$

The required electrostatic force is

$$|e|\,\mathrm{E}(r) = \frac{g(r)[m_+T_-(r_0) - m_-T_+(r_0)]}{T_+(r_0) + T_-(r_0)}\hat{r} \tag{A6}$$

and is the same for both polytrope models. Substituting (A6) into (A1), we write

$$\frac{dP_\pm}{dr} = -n_\pm\mu_\pm g(r) \tag{A7}$$

which is the same form as (10) for the neutral case but is written now in terms of $\mu_\pm$, which are 'effective masses':

$$\mu_+ \equiv \frac{m_+ + m_-}{1 + (T_-/T_+)} \ll m_+ \tag{A8}$$

$$\mu_- \equiv \frac{m_+ + m_-}{1 + (T_+/T_-)} \gg m_- \tag{A9}$$

It is seen that the Rosseland field has effectively made each positive ion less massive and each electron more massive.

Using equations (A2), (A5), (A7), (A8), and (A9) and applying the first form of the polytrope law (equation (A3)), we establish that

$$n_+ = n_- = n(r_0)\left[1 - \frac{\alpha - 1}{\alpha}\frac{m^*g(r_0)r_0}{kT^*}\left(1 - \frac{r_0}{r}\right)\right]^{1/(\alpha-1)} \tag{A10}$$

where $m^* \equiv m_+ + m_-$ and $T^* \equiv T_+ + T_-$. If the second form of the polytrope law (equation (A4)) is used instead, it is found that

$$n_+ = n_- = n(r_0)\exp\left\{-\frac{m^*g(r_0)r_0}{(l-1)kT^*}\left[\left(\frac{r}{r_0}\right)^{l-1} - 1\right]\right\}^{1/(l+1)} \tag{A11}$$

Equations (A10) and (A11) may be used to determine the conditions that must be satisfied in order that the ionosphere be bound. Binding requires that $n_+(r) = n_-(r) \to 0$ as r becomes large. This condition is satisfied in (A10) if

$$\Lambda \equiv \frac{\alpha - 1}{\alpha}\frac{m^*g(r_0)r_0}{kT^*} > 1 \tag{A12}$$

In (A11), for $l > 1$, the exponential factor is negative, so that $\lim_{r\to\infty} n(r) = 0$. But for $l < 1$, the exponential factor remains finite as $r \to \infty$, so that binding does not occur. Finally, for $l = 1$,

$$n(r) = n(r_0)\left(\frac{r_0}{r}\right)^{[m^*g(r_0)r_0/kT^*]-1} \tag{A13}$$

Binding occurs in this case if

$$\frac{m^*g(r_0)r_0}{kT^*} > 1 \tag{A14}$$

Formally, it is possible to relate the polytrope indices l and α and thus to unify the conditions necessary for a bound ionosphere. Using (A3) and (A4), we note that

$$\frac{T(r)}{T(r_0)} = \left[\frac{n(r)}{n(r_0)}\right]^{\alpha-1} = \left(\frac{r_0}{r}\right)^l \tag{A15}$$

We now take $n(r)/n(r_0)$ as given by (A10) and solve for l, obtaining

$$l = \frac{\ln r - \ln (r - \Lambda r + \Lambda r_0)}{\ln r - \ln r_0} \tag{A16}$$

For l to be 1 or greater, $\Lambda \geq 1$. This leads to the conclusion that essentially the same conditions must be met for ionospheric binding, independent of the form of the polytrope law; that is,

$$\frac{m^* g(r_0) r_0}{kT^*} > 1 \tag{A17}$$

or

$$\frac{T_{\text{crit}}}{T^*} > 1$$

where

$$T_{\text{crit}} = \frac{m^* g(r_0) r_0}{k} \tag{A18}$$

APPENDIX B: HYDRODYNAMIC MODEL

Requiring charge neutrality, we can solve (14) simultaneously to yield

$$e\phi(r) = \frac{m_+ T_-(a) - m_- T_+(a)}{T_+(a) + T_-(a)} \Phi(r) + \frac{1}{2} \frac{m_+ v_+^2 T_-(a) - m_- v_-^2 T_+(a)}{T_+(a) + T_-(a)} \tag{B1}$$

We note that the Rosseland electrostatic force $eE = -e\nabla\phi$ is precisely the Rosseland force required to preserve charge neutrality in the hydrostatic case (equation (A6)). We insert this expression for $e\phi$ into (14) and combine the expressions to obtain one equation for a particle of mass $m^* \equiv m_+ + m_-$ at a temperature $T^*(a) \equiv T_+(a) + T_-(a)$. We also require that the ions and electrons move along the streamlines at the same velocity $v(r) = v_+(r) = v_-(r)$.

$$\tfrac{1}{2} m^* v^2(r) + m^* \Phi(r) + \frac{\alpha}{\alpha - 1} \left[\frac{n(r)}{n(a)}\right]^{\alpha - 1} kT^*(a) = \tfrac{1}{2} m^* v^2(a) + m^* \Phi(a) + \frac{\alpha}{\alpha - 1} kT^*(a) \tag{B2}$$

This equation holds for $\alpha \neq 1$. The isothermal case ($\alpha = 1$) leads to an equation of the form

$$\tfrac{1}{2} m^* v^2(r) + m^* \Phi(r) + kT^*(a) \ln [m^* n(r)] = \tfrac{1}{2} m^* v^2(a) + m^* \Phi(a) + kT^*(a) \ln [m^* n(a)] \tag{B3}$$

Conservation of matter requires that

$$n(r) v(r) A(r) = n(a) v(a) A(a) \tag{B4}$$

where $A(r)$ is the cross-sectional area of a tube of flow at r. It is convenient to assume that $A(r)/A(a) = (r/a)^s \equiv (\zeta)^s$, where s is a parameter that can be adjusted to correspond with the flow geometry. In our case the streamlines are parallel to the uniform geomagnetic tail field, the flow tube cross section $A(r)$ is a constant, and $s = 0$. In the following development we take s to be general and subsequently emphasize limiting solutions as $s \to 0$.

It is useful for further physical discussion to write (B2), (B3), and (B4) in terms of the dimensionless constant $Q(a)$, which is the ratio of the gravitational to the thermal energy, and the dimensionless parameter $U^2(r)$, which is the ratio of the kinetic energy to the thermal energy

$$Q(a) \equiv \frac{m^* g(a) a}{kT^*(a)}$$
$$U^2(r) \equiv \frac{1}{2} \frac{m^* v^2(r)}{kT^*(a)} \tag{B5}$$

For $\alpha \neq 1$,

$$U^2(r) + \frac{\alpha}{\alpha - 1} \left[\frac{U(a)}{U(r)\zeta^s}\right]^{\alpha - 1} - \frac{Q(a)}{\zeta} = U^2(a) + \frac{\alpha}{\alpha - 1} - Q(a) \tag{B6}$$

and for $\alpha = 1$,

$$U^2(r) - \ln U(r) - s \ln \zeta - \frac{Q(a)}{\zeta} = U^2(a) - \ln U(a) - Q(a) \tag{B7}$$

We seek solutions of U as a function of r from (B6) and (B7). It is noted that $U(a)$ is a constant to be determined. By means of (B5) and the equation of continuity (B4) we can find the corresponding values of $v(r)$ and $n(r)$. The solution to (B6) and (B7) is multivalued, therefore we need to use physical criteria to select the solution of interest. As $r \to \infty$, we require that $n(r) \to 0$, and as $r \to 0$, we require that $v \to 0$. These asymptotic boundary conditions are necessary but not sufficient. In addition to these conditions the branch of the solution that satisfies the zero density requirement at infinity must connect with the branch that satisfies the zero velocity condition at $r = 0$. This connection occurs at an intermediate point called the critical point. U_c and ζ_c are obtained by differentiating and evaluating at the critical point, (B6) and (B7). For $\alpha \neq 1$,

$$\frac{dU}{d\zeta} \left[2U - \frac{\alpha U(a)^{\alpha - 1}}{U^\alpha \zeta^{s(\alpha - 1)}}\right] = \frac{s\alpha U(a)^{\alpha - 1}}{U(r)^{\alpha - 1} \zeta^{s(\alpha - 1) + 1}} - \frac{Q(a)}{\zeta^2} \tag{B8}$$

and for $\alpha = 1$,

$$\frac{dU}{d\zeta} \left(2U - \frac{1}{U}\right) = \frac{s}{\zeta} - \frac{Q(a)}{\zeta^2} \tag{B9}$$

In order that U satisfy the asymptotic boundary conditions, U must be a monotonically increasing function of ζ. This means that the coefficient of $dU/d\zeta$ and the right-hand sides of (B8) and (B9) must vanish simultaneously. For a more complete discussion, see the book by *Parker* [1963].

The critical values of U and ζ from (B8) for $\alpha \neq 1$ satisfy the relations

$$U_c^2 \zeta_c = Q(a)/2s$$
$$\zeta_c = \left[\frac{Q(a)}{2s}\right]^{\alpha + 1)/[\alpha + 1 - 2s(\alpha - 1)]} \left[\frac{2}{\alpha U(a)^{\alpha - 1}}\right]^{2/[\alpha + 1 - 2s(\alpha - 1)]} \tag{B10}$$

The critical values of U and ζ from (B9) for $\alpha = 1$ satisfy the relations

$$U_c^2 = \tfrac{1}{2}$$
$$\zeta_c = Q(a)/s \tag{B11}$$

The physically correct solution for $U(\zeta)$ must go through the point (U_c, ζ_c). We insert these point coordinates into (B8) and

(B9), thereby determining a value of $U(a)$ consistent in each case with the boundary conditions. For $\alpha \neq 1$,

$$U^2(a) + \frac{\alpha}{\alpha - 1} - Q(a) = \left[\frac{\alpha + 1 - 2s(\alpha - 1)}{\alpha - 1}\right] \left\{\left[\frac{2s}{Q(a)}\right]^{2s\alpha - 1} \left(\frac{\alpha}{2}\right)^2 U_0^{2\cdot\alpha - 1)}\right\}^{1/[\alpha - 1 - 2s(\alpha - 1)]} \quad \text{(B12)}$$

and for $\alpha = 1$,

$$U^2(a) - \ln U(a) - Q(a) = \tfrac{1}{2}(\ln 2 + 1) - s\left[\ln \frac{Q(a)}{s} + 1\right] \quad \text{(B13)}$$

The values of $U(a)$, given by (B12) and (B13), now enable us to solve for $U(r)$ in (B8) and (B9). Although there is more than one solution for $U(a)$ that satisfies (B12) and (B13), each corresponding $U(r)$ does go through the critical point. We reject those numerical solutions that do not meet the asymptotic boundary conditions. In the limit as $s \to 0$, we find that for $\alpha \neq 1$,

$$U_c = \left(\frac{\alpha}{2}\right)^{1/(\alpha+1)} [U(a)]^{(\alpha-1)/(\alpha+1)} \qquad \zeta_c = \infty \quad \text{(B14)}$$

$$U^2(a) + \frac{\alpha}{\alpha - 1} - Q(a) = \frac{\alpha + 1}{\alpha - 1}\left[\left(\frac{\alpha}{2}\right)^{2/(\alpha+1)} U(a)^{2(\alpha-1)/(\alpha+1)}\right]$$

and for $\alpha = 1$,

$$U_c = \frac{1}{2^{1/2}} \qquad \zeta_c = \infty \quad \text{(B15)}$$

$$U^2(a) - \ln U(a) - Q(a) = \tfrac{1}{2}(\ln 2 + 1)$$

Acknowledgments The authors are grateful to Aaron Barnes of NASA Ames Research Center, Moffett Field, California, for helpful discussions and to James Arvin of Computer Sciences Corporation, Palo Alto, California, for his implementation of the computer program used in the numerical solution of the hydrodynamic equations We wish to thank Marion Legg and her co-workers Janice Hom, Anna Hood, and Donna Hafeman of Diversified Computer Applications, Mountain View, California, for their assistance during various phases of this work We are pleased to acknowledge support for William Daily under NASA grant NGR-45-001-040, for William Barker and Mark Clark under NASA grant NGR-05-017-027, and for Curtis Parkin under NASA grant NSG-2075. We also thank John Hoffman and George Siscoe for their constructive evaluation of this paper.

REFERENCES

Alfvén, H., Antimatter and the development of the metagalaxy, *Rev. Mod. Phys., 37* 652–665, 1965.

Anderson, K. A., Energetic electron fluxes in the tail of the geomagnetic field, *J. Geophys. Res., 70,* 4741–4763, 1965

Bailey, J. A., J. B. A. Branson, B. Elsmore, and P. A. G. Scheuer, Lunar occultation of the radio source 3C273, *Nature, 201,* 755–756, 1964

Banks, P. M. and T. E. Holzer, High-latitude plasma transport The polar wind, *J. Geophys. Res., 74,* 6317–6332, 1969

Benson, J., and J. W. Freeman, A two-gas model of solar wind accelerated lunar exospheric ions and its implications for models of the surface distribution of a non-condensible gas, paper presented at 7th Lunar Science Conference, Lunar Sci. Inst., Houston, Tex. 1976

Coleman, P. J., Jr., B. R. Lichtenstein, C. T. Russell, G. Schubert, and L. R. Sharp, Magnetic fields near the moon, *Proc. Lunar Sci. Conf. 3rd,* 2271–2286, 1972

Dyal, P., C. W. Parkin, and W. D. Daily, Surface magnetometer experiments Internal lunar properties, *Proc. Lunar Sci. Conf. 4th,* 2925–2945, 1973

Dyal, P., C. W. Parkin, and W. D. Daily, Lunar electrical conductivity and magnetic permeability, *Proc. Lunar Sci. Conf. 6th,* 2909–2926, 1975.

Dyal, P., C. W. Parkin, and W. D. Daily, Structure of the lunar interior from magnetic field measurements, *Proc. Lunar Sci. Conf. 7th,* 3077–3095, 1976.

Elsmore, B., Radio observation of the lunar atmosphere, *Phil. Mag., 2,* 1040–1046, 1957

Freeman, J. W., and M. E. Ibrahim, The lunar electric potential and its plasma sheath effects, paper presented at Conference on Lunar Interactions, Lunar Sci. Inst., Williams Bay, Wis., 1974

Freeman, J. W., Jr., H. Balsiger, and H. K. Hills, Suprathermal ion detector experiment (lunar ionosphere detector), Apollo 12 Preliminary Science Report, *NASA Spec. Publ. 235,* 83–92, 1970

Goldstein, B. E., and C. T. Russell, On the apparent diamagnetism of the lunar environment in the geomagnetic tail lobes, *Proc. Lunar Sci. Conf. 6th,* 2999–3012, 1975

Goldstein, B. E., R. J. Phillips, and C. T. Russell, Magnetic permeability measurements and a lunar core, *Geophys. Res. Lett., 3,* 289–292, 1976.

Hardy, D. A., Observation of plasma in the geomagnetic tail at lunar distances, Ph.D. thesis, Rice Univ., Houston, Tex., 1976

Hardy, D. A., H. K. Hills, and J. W. Freeman, A new plasma regime in the distant geomagnetic tail, *Geophys. Res. Lett., 2,* 169–172, 1975

Heitler, W., *The Quantum Theory of Radiation,* Oxford University Press, London, 1944.

Hills, H. K., D. A. Hardy, and J. W. Freeman, Low-energy regime in the geomagnetic tail at lunar distance, in *The Scientific Satellite Programme During the International Magnetospheric Study,* pp. 199–207, D. Reidel, Hingham, Mass., 1976

Hinteregger, H. E., The extreme ultraviolet solar spectrum and its variation during a solar cycle, *Amer. Geophys., 26,* 547–554, 1970

Hinton, F. L., and D. R. Taeusch, Variation of the lunar atmosphere with strength of the solar wind, *J. Geophys. Res., 69,* 1341–1347, 1964.

Hodges, R. R., Differential equation of exospheric lateral transport and its application to terrestrial hydrogen, *J. Geophys. Res., 78,* 7340–7346, 1973

Hodges, R. R., Jr., and F. S. Johnson, Lateral transport in planetary exospheres, *J. Geophys. Res., 73,* 7307–7317, 1968

Hodges, R. R., J. H. Hoffman, and F. S. Johnson, The lunar atmosphere, *Icarus, 21,* 415–426, 1974

Hoffman, J. H., and R. R. Hodges, Jr., Molecular gas species in the lunar atmosphere, *Moon, 14* 159–167, 1975.

Hoffman, J. H., R. R. Hodges, Jr., F. S. Johnson, and D. E. Evans, Lunar atmospheric composition experiment, Apollo 17 Preliminary Science Report, *NASA Spec. Publ. 330,* 17-1–17-9, 1973

Jeans, J. S., *The Dynamical Theory of Gases,* Cambridge University Press, New York, 1916.

Johnson, F. S., Lunar atmosphere, *Rev. Geophys. Space Phys., 9,* 813–823, 1971

Johnson, F. S., D. E. Evans, and J. M. Carroll, Cold cathode gage (lunar atmosphere detector), Apollo 12 Preliminary Science Report, *NASA Spec. Publ. 235,* 93–97, 1970.

Lin, R. P., K. A. Anderson, R. E. McGuire, and J. E. McCoy, Fine scale lunar surface magnetic fields detected by the electron reflection method, paper presented at 7th Lunar Science Conference, Lunar Sci. Inst., Houston, Tex., 1976.

Lindeman, R., J. W. Freeman, Jr., and R. R. Vondrak, Ions from the lunar atmosphere, *Proc. Lunar Sci. Conf. 4th,* 2889–2896, 1973

Manka, R. H., Lunar atmosphere and ionosphere, Ph.D. thesis, Rice Univ., Houston, Tex., 1972

Manka, R. H., and F. C. Michel, Lunar ion energy spectra and surface potential, *Proc. Lunar Sci. Conf. 4th,* 2897–2908, 1973.

McCoy, J. E., R. P. Lin, R. E. McGuire, L. M. Chase, and K. A. Anderson, Magnetotail electric fields observed from lunar orbit, *J. Geophys. Res., 80,* 3217–3224, 1975.

McDaniel, E. W., *Collision Phenomena in Ionized Gases,* p. 344, John Wiley, New York, 1964

Milne, E. A., The escape of molecules from an atmosphere, with special reference to the boundary of a gaseous star, *Trans. Cambridge Phil. Soc., 22,* 483–517, 1923

Parker, E. N. *Interplanetary Dynamical Processes,* Interscience, New York 1963

Parkin, C. W., P Dyal, and W. D. Daily, Iron abundance in the moon from magnetometer measurements, *Proc. Lunar Sci. Conf. 4th*, 2947–2961, 1973

Parkin, C W., W. D. Daily, and P. Dyal, Iron abundance and magnetic permeability of the moon, *Proc. Lunar Sci. Conf 5th*, 2761–2778, 1974

Pomalaza-Diaz, J C., Measurement of the lunar ionosphere by occultation of the Pioneer 7 spacecraft, *Rep SU-SEL-67-095*, Stanford Electron. Lab., Stanford, Calif., 1967

Reasoner, D L , and W J. Burke, Characteristics of the lunar photoelectron layer in the geomagnetic tail, *J. Geophys. Res.*, *77*, 6671–6687, 1972.

Rich, F. J., D. L. Reasoner, and W. J. Burke, Plasma sheet at lunar distance· Characteristics and interactions with the lunar surface, *J. Geophys Res.*, *78*, .80–97, 1973.

Russell, C. T , P. J Coleman, Jr , B R. Lichtenstein, and G. Schubert, The permanent and induced magnetic dipole moment of the moon, *Proc Lunar Sci. Conf 5th*, 2747–2760, 1974*a*.

Russell, C. T , P. J. Coleman, Jr., B. R. Lichenstein, and G. Schubert, Lunar magnetic field· Permanent and induced dipole moments, *Science*, *186*, 825–826, 1974*b*.

Russell, C. T., P J. Coleman, Jr., B. K. Fleming, L. Hilburn, G. Ionnidis, B. R Lichtenstein, and G. Schubert, The fine-scale lunar magnetic field, *Proc. Lunar Sci Conf 6th*, 2955–2969, 1975

Sonett, C. P., B. F. Smith, D. S Colburn, G. Schubert, and K. Schwartz, The induced magnetic field of the moon. Conductivity profiles and inferred temperature, *Proc Lunar Sci. Conf. 3rd*, 2309–2336, 1972

Walbridge, E., Lunar photoelectron layer, *J. Geophys. Res*, *78*, 3668–3687, 1973

Weil, H., and M. L. Barasch, A theoretical lunar ionosphere, *Icarus*, *1*, 346–356, 1963

(Received January 6, 1977;
revised May 1, 1977;
accepted May 22, 1977)

NASA SP-370
Part 1

THE SOVIET-AMERICAN CONFERENCE ON COSMOCHEMISTRY OF THE MOON AND PLANETS

Edited by
John H. Pomeroy
NASA Headquarters
and
Norman J. Hubbard
NASA Johnson Space Center

A conference held in Moscow, U.S.S.R.,
June 4-8, 1974

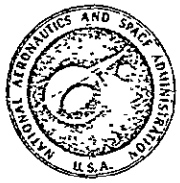

Scientific and Technical Information Office 1977
NATIONAL AERONAUTICS AND SPACE ADMINISTRATION
Washington, D.C.

Lunar Electrical Conductivity, Permeability, and Temperature from Apollo Magnetometer Experiments

P. Dyal
NASA/Ames Research Center
Moffett Field, California

C. W. Parkin
University of Santa Clara
Santa Clara, California

W. D. Daily
Brigham Young University
Provo, Utah

Magnetometers have been deployed at four Apollo sites on the Moon to measure remanent and induced lunar magnetic fields. Measurements from this network of instruments have been used to calculate the electrical conductivity, temperature, magnetic permeability, and iron abundance of the lunar interior. The measured lunar remanent fields range from 3 gammas (γ) minimum at the Apollo 15 site to 327 γ maximum at the Apollo 16 site. Simultaneous magnetic field and solar plasma pressure measurements show that the remanent fields at the Apollo 12 and 16 sites interact with, and are compressed by, the solar wind. Remanent fields at Apollo 12 and Apollo 16 are increased 16 γ and 32 γ, respectively, by a solar plasma bulk pressure increase of 1.5×10^{-7} dynes/cm^2. Global lunar fields due to eddy currents, induced in the lunar interior by magnetic transients, have been analyzed to calculate an electrical conductivity profile for the Moon. From nightside magnetometer data in the solar wind it has been found that deeper than 170 km into the Moon the conductivity rises from 3×10^{-4} mhos/m to 10^{-2} mhos/m at 1000-km depth. Recent analysis of data obtained in the geomagnetic tail, in regions free of complicating plasma effects, yields results consistent with nightside values. Conductivity profiles have been used to calculate the lunar temperature for an assumed lunar material of olivine. In the outer layer ($\sim$ 170 km thick) the temperature rises to 110° C, after which it gradually increases with depth to 1500° C at a depth of $\sim$ 1000 km. Simultaneous measurements by magnetometers on the lunar surface and in orbit around the moon are used to construct a whole-moon hysteresis curve, from which the global lunar magnetic permeability is determined to be $\mu = 1.012 \pm 0.006$. The corresponding global induced dipole moment is 2×10^{25} gauss-cm^3 for typical inducing fields of 10^{-1} gauss in the lunar environment. Lunar free iron abundance corresponding to the global permeability is determined to be 2.5 ± 2.0 wt. %. Total iron abundance (sum of iron in the ferromagnetic and paramagnetic states) is calculated for two assumed compositional models of the lunar interior. For a free iron/orthopyroxene lunar composition the total iron content is calculated to be 12.8 ± 1.0 wt. %; for a free iron/olivine composition, total iron content is 5.5 ± 1.2 wt. %. Other lunar models with an iron core and with a shallow iron-rich layer are also discussed in light of the measured global lunar permeability. Velocities and thicknesses of the Earth's magnetopause and bow shock have been estimated from simultaneous magnetometer measurements. Average speeds are determined to be about 50 km/s for the magnetopause and 70 km/s for the bow shock, although there are large variations in the measurement for any particular boundary crossing. Corresponding measured boundary thicknesses average about 2300 km for the magnetopause and 1400 km for the bow shock.

Magnetometers placed on the lunar surface and in orbit about the Moon have returned a wealth of information about the Moon which was not anticipated prior to the Apollo manned lunar missions. Earlier measurements, by U.S.S.R. and U.S magnetometers on unmanned spacecraft, indicated that the Moon might be electromagnetically inert; during that time investigators often concentrated on the interactions of the Moon with the solar wind plasma (refs. 1–4) rather than on magnetic studies of the lunar interior. Studies of the lunar interior prior to the Apollo landings (e.g., see refs. 2 and 5–9) were constrained by the lack of high resolution measurements of whole body induction fields near the Moon.

The measurement of magnetic fields in the vicinity of the Moon began in January 1959, when the U.S.S.R. spacecraft Luna 1 carried a magnetometer to within several hundred kilometers of the Moon. In September 1959, Luna 2, also equipped with a magnetometer, impacted the lunar surface. The instrument aboard Luna 2 set an upper limit of 100 gammas (1 gamma = 10^{-5} gauss) for a possible lunar field at an altitude of about 50 km above the Moon's surface (ref. 10). In April 1966, Luna 10 carrying a magnetometer 10 times more sensitive than that aboard Luna 2, was successfully placed in a lunar orbit that came to within 350 km of the Moon. The Luna 10 magnetometer recorded a time-varying magnetic field in the vicinity of the Moon, which was at that time interpreted as indicating the existence of a weak lunar magnetosphere (ref. 11), although later studies modified this interpretation.

A year later (July 1967) the United States placed the Explorer 35 satellite, with two magnetometers aboard, in orbit around the Moon. In its orbit the satellite passed to within 830 km of the Moon's surface. Explorer 35 successfully measured magnetic properties of the solar-wind cavity downstream from the Moon, but it did not detect the lunar magnetosphere indicated by Luna 10 measurements nor the lunar bow shock and induced-field configuration previously suggested by Gold (ref. 12). In an analysis of the Explorer 35 results, Sonett et. al. (ref. 13) concluded that if a permanent lunar field exists at all, its magnitude would be less than two gammas at an altitude of 830 km and therefore ≤ 4 gammas at the surface for a global permanent dipole field. The upper limit on the global permanent dipole moment was set at 10^{20} gauss-cm^3, i.e., less than 10^{-5} that of the Earth. In studies of the solar wind interaction with the lunar body (refs. 1 and 2), investigators found the solar wind field magnitude to be ~ 1.5 gammas greater in the diamagnetic cavity on the Moon's antisolar side than in the solar wind.

Surveyor spacecraft, used in the first U.S. unmanned lunar landings, carried no magnetometers. Permanent magnets were carried aboard the Surveyor 5 and 6 spacecraft, however, which demonstrated that soils at those two landing sites contain less than 1 percent (by volume) ferromagnetic iron (ref. 14).

During the early manned Apollo missions it was determined that the Moon is much more interesting magnetically then had been expected. Natural remanent magnetization in lunar samples was found to be surprisingly high at all U.S. Apollo sites and at the U.S.S.R. Luna 16 site (see, for example, refs. 15–21). Such high natural remanent magnetism implies that at some time in the past there existed an ambient surface magnetic field considerably higher than that which now exists on the Moon (refs. 16 and 22).

The first lunar surface magnetometer (LSM), deployed at the Apollo 12 site in November 1969, made the first direct measurement of an intrinsic lunar magnetic field (ref. 23). The 38-gamma field measurement showed that not only are individual rocks magnetized but also that magnetization in the lunar crust can be ordered over much larger regions of 2-km to 200-km scale sizes (refs. 23 and 24). The permanent and induced fields measured by the Apollo 12 magnetometer provided the impetus to develop portable surface magnetometers and satellite magnetometers for later Apollo missions. Permanent mag-

netic fields were subsequently measured at four other landing sites: Apollo 14 (103 γ maximum), Apollo 15 (3 γ), Apollo 16 (327 γ maximum), and more recently at several positions along the U.S.S.R. Lunokhod II traverse. The surface fields were attributed to local magnetized sources ("magcons"); their discovery prompted a reexamination of Explorer 35 magnetometer data by Mihalov et al. (ref. 25), who found indirect evidence that several magnetized regions exist in the lunar crust. Direct field measurements from Apollo 15 and 16 subsatellite magnetometers, activated in August 1971 and April 1972, respectively, yielded maps of some of the larger magnetized regions in the lunar crust (refs. 26 and 27) which confirmed the existence of magnetized regions over much of the lunar surface. Subsatellite magnetometer measurements have also placed an upper limit of 4.4×10^{13} gauss-cm^3 on the global permanent magnetic dipole moment (ref. 28).

Investigations of simultaneous surface magnetometer data and solar wind spectrometer data show that the surface remanent magnetic fields interact with the solar wind when on the dayside of the moon (refs. 29, 30, and 31). The interaction is interpreted as a compression of the surface remanent fields by the solar wind; the magnetic pressure at the surface increases in proportion to the dynamic bulk pressure of the solar wind plasma.

In addition to measuring permanent lunar fields, the network of lunar surface and orbiting magnetometers measured fields induced in the lunar interior by extralunar magnetic fields, allowing investigation of deep interior properties of the Moon. Behanon (ref. 8) placed an upper limit of 1.8 on the bulk relative magnetic permeability by studying Explorer 35 magnetometer measurements in the geomagnetic tail. Subsequently, simultaneous measurements of Explorer 35 and Apollo 12 magnetometers have been used to yield the more accurate value of 1.012 $\pm$ 0.006 (refs. 32 and 33). Recent Apollo 15 subsatellite magnetometer measurements have indicated the existence of a possible lunar ionosphere, which could affect the whole-Moon permeability calculations (ref. 34); effects of a lunar ionosphere on iron abundance determinations are considered by Parkin et al. (ref. 32).

The electrical conductivity of the lunar interior has been investigated by analyzing the induction of global lunar fields by time-varying extralunar (solar or terrestrial) magnetic fields. Since temperature and conductivity of geological materials are related, calculated conductivity profiles have been used to infer temperature of the lunar interior. Early estimates of bulk lunar electrical conductivity were made from lunar-orbiting Explorer 35 data by Colburn et al. (ref. 1) and Ness (ref. 7). For homogeneous-conductivity models of the Moon, Colburn et al. placed an upper limit of 10^{-6} mhos/m for whole-Moon conductivity, whereas Ness' upper limit was 10^{-5} mhos/m. These investigators also stated that their measurements were consistent with a higher conductivity lunar core surrounded by an insulating crust.

Theoretical studies of the electrodynamic response of the Moon to time-dependent external fields have been undertaken by many authors. Two types of whole-Moon magnetic induction fields have been treated: a poloidal field due to eddy currents driven by time-varying external magnetic fields, and a toroidal field due to unipolar currents driven through the Moon by the motional solar-wind $V \times B$ electric field.

The toroidal induction mode, first suggested to be an important process in the Moon by Sonett and Colburn (ref. 5), was later developed in detail theoretically for a lunar model totally confined by the highly conducting solar wind (refs. 35, 36, and 37). However, analysis of simultaneous Apollo 12 and Explorer 35 magnetometer data later indicated that for the Moon, toroidal induction is negligible in comparison to poloidal induction; upper limits on the toroidal field mode were used to calculate an upper limit of 10^{-9} mhos/m for electrical conductivity of the outer 5 km of the lunar crust (ref. 38). In subsequent analysis of lunar electromagnetic induction, toroidal induction has been assumed to be negligible relative to poloidal induction.

The eddy-current response of a homogeneous sphere in a vacuum to time-varying magnetic fields has been described by Smythe (ref. 39) and Wait (ref. 40). Early theoretical application of vacuum poloidal induction to studies of the lunar interior were presented by Gold (ref. 12) and Tozer and Wilson (ref. 41). Poloidal response theory for a lunar sphere totally confined by a highly conducting plasma was developed by Blank and Sill (ref. 42), Schubert and Schwartz (ref. 36), and Sill and Blank (ref. 37).

Since deployment of the Apollo 12 magnetometer in November 1969, electrical conductivity analysis has been developed with two basic approaches: a time-dependent, transient-response technique (refs. 43, 44, and 45) and a frequency-dependent, Fourier-harmonic technique (refs. 44 and 46–49). Past analyses have all used magnetometer data recorded at times when global eddy-current fields were asymmetrically confined by the solar wind plasma (refs. 45 and 50–53). The asymmetric confinement of lunar fields is particularly complex to model theoretically (ref. 54); indeed, the general time-dependent asymmetric induction problem has not been solved at the time of this writing. To avoid these complications, recent conductivity analysis has used field data recorded in the geomagnetic tail, which is relatively free of plasma and asymmetric confinement effects. Preliminary results of this analysis will be presented in this paper.

The purpose of this paper is to review the application of lunar magnetic field measurements to the study of properties of the lunar crust and deep interior. Following a brief descriptive section on lunar magnetometers and the lunar magnetic environment, measurements of lunar remanent fields and their interaction with the solar plasma will be discussed. The magnetization induction mode will be considered with reference to lunar magnetic permeability and iron abundance calculations. Electrical conductivity and temperature calculations from analyses of poloidal induction, for data taken in both the solar wind and in the geomagnetic tail, will be reviewed. Finally, properties of the Earth's magnetopause and bow shock measured by lunar magnetometers will be discussed.

The Apollo Surface Magnetometers

LUNAR SURFACE MAGNETOMETER (LSM)

Lunar surface magnetometers, designed to measure and transmit data continuously to Earth for at least one year, have been deployed at three sites on the moon: Apollo 12 (coordinates 3.0° south latitude, 23.4° west longitude), Apollo 15 (26.1° N, 3.7° E), and Apollo 16 (9.0° S, 15.5° E). A photograph of the LSM fully deployed and aligned at the Descartes landing site is shown in figure 1 and the Apollo 16 LSM characteristics are given in table 1. (A detailed description of this instrument is provided by Dyal et al., ref. 55).

Mechanical and Thermal Subsystems

In the exterior mechanical and thermal configuration of the Apollo LSM, the three fluxgate sensors are located at the ends of three 100-cm-long orthogonal booms that separate the sensors from each other by 150 cm, and position them 75 cm above the lunar surface (fig. 2). Orientation measurements with respect to lunar coordinates are made with two devices. A shadowgraph and bubble level are used by the astronaut to align the LSM and to measure azimuthal orientation with respect to the Moon-to-Sun line to an accuracy of 0.5°. Gravity-level sensors measure instrument tilt angles to an accuracy of 0.2° every 4.8 seconds.

In addition to the instrument normal mode of operation in which three vector field components are measured, the LSM has a gradiometer mode in which commands are sent to operate three motors, which rotate the sensors such that all simultaneously align in a parallel manner, first to one of the three boom axes, then to each of the other two boom axes in

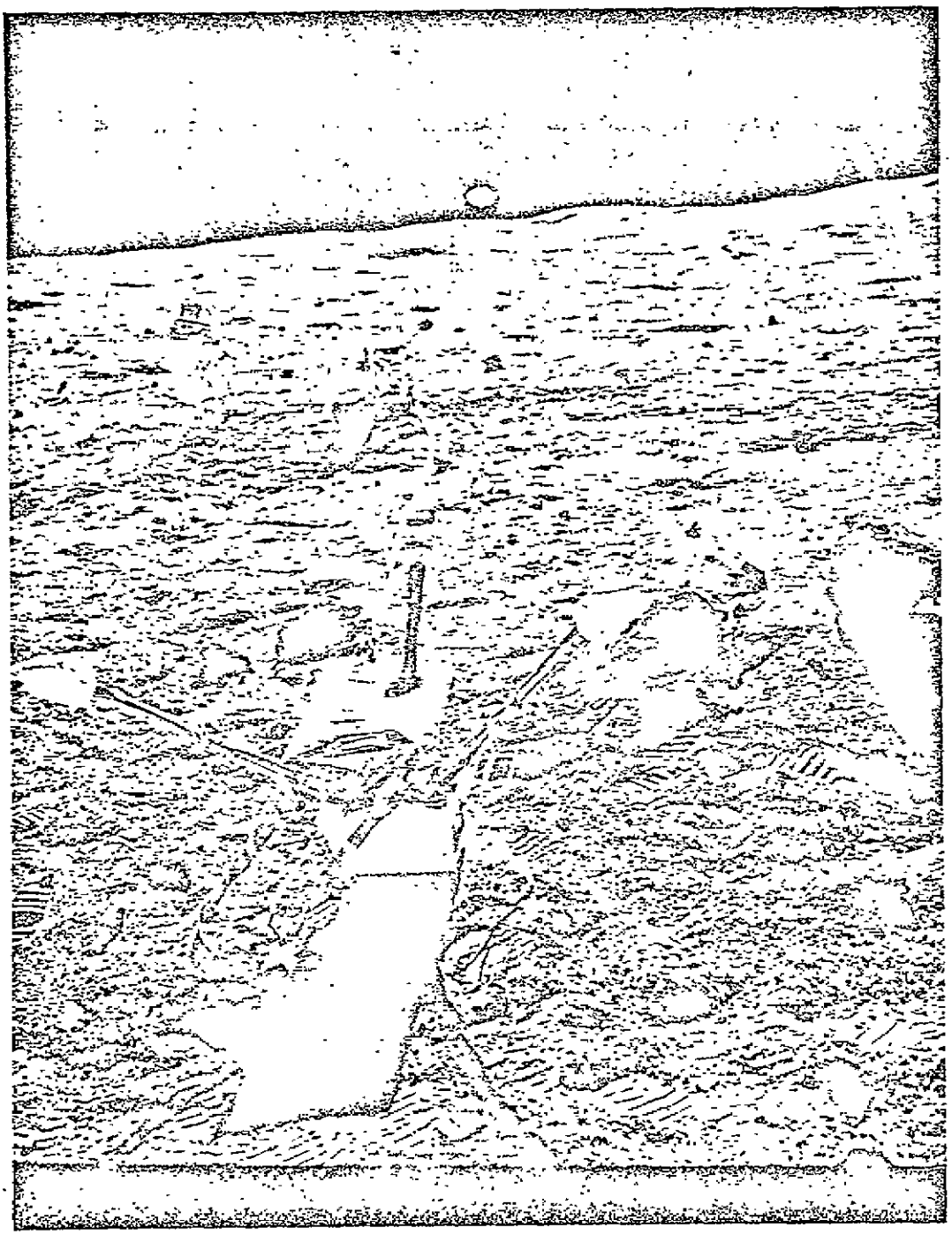

Figure 1.—*The Apollo lunar surface magnetometer (LSM) deployed on the Moon at the Apollo 16 Descartes site. Magnetic field sensors are at the top ends of the booms and approximately 75 cm above the lunar surface.*

ORIGINAL PAGE IS
OF POOR QUALITY

ORIGINAL PAGE IS
OF POOR QUALITY

Table 1.—*Apollo Surface Magnetometer Characteristics*

Parameter	Apollo 16 Stationary Magnetometer (LSM)	Apollo 16 Portable Magnetometer (LPM)
Ranges, Gammas (each sensor)	0 to ± 200 0 to ± 100 0 to ± 50	0 to ± 256
Resolution, Gammas	0.1	1.0
Frequency Response, Hz	dc to 3	dc to 0.05
Angular Response	Cosine of angle between field and sensor	Cosine of angle between field and sensor
Sensor Geometry	3 orthogonal sensors at ends of 100–cm booms	3 orthogonal sensors in 6–cm cube
Analog Zero Determination	180° flip of sensor	180° flip of sensor
Power, Watts	3.5	1.5 (battery)
Weight, kg	8.9	4.6
Size, cm	63 x 28 x 25	56 x 15 x 14
Operating Temperature, °C	−50 to +85	0 to +50
Commands	10 ground: 1 spacecraft	—

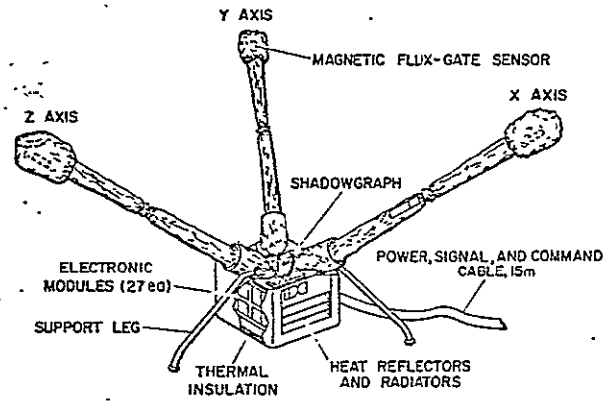

Figure 2.—*Schematic diagram of the lunar surface magnetometer (LSM) without the sunshade shown in figure 1. Sensors are at the top ends of the booms and approximately 75 cm above the ground. The electronics and motor drive assembly are located in the box, encased in a thermal blanket. Heat rejection during lunar day and retention during lunar night are controlled by a parabolic reflector array on two sides of the electronics box. The astronaut bubble level and azimuthal shadowgraph are shown on top of the box. Power, digital signals, and commands are provided through the ribbon cable which connects to the central station telemetry receiver and transmitter.*

turn. This rotating alignment permits the vector gradient to be calculated in the plane of the sensors, and also permits an independent measurement of the magnetic field vector at each sensor position.

The thermal subsystem is designed to allow the LSM to operate over the complete lunar day-night cycle. Thermal control is accomplished by a combination of insulation, control surfaces, and heaters that operate collectively to keep the electronics between 267 K and 319 K. A plot of the temperature of the X sensor and the electronics for the first post-deployment lunation is shown in figure 3 for the Apollo 16 LSM.

Electronics

The electronic components for the LSM are located in the thermally insulated box. The operation of the electronics is illustrated in figure 4. Long-term stability is attained by extensive use of digital circuitry, by internal calibration of the analog portion of the instrument every 18 hours, and by mechanical rotation of each sensor through 180° to determine the sensor zero offset. The analog output of the sensor electronics is internally processed by a low-pass digital filter and a telemetry encoder; the output is transmitted to Earth via the central-station S-band transmitter.

The LSM has two data samplers: the analog-to-digital converter (26.5 samples/second) and the central-station telemetry

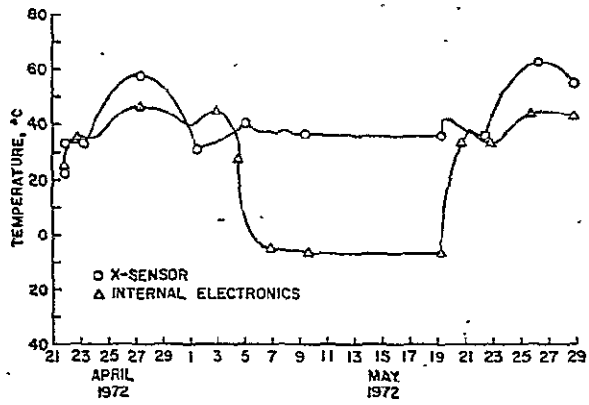

Figure 3.—*Temperature inside one of the Apollo 16 LSM flux-gate sensors and inside the electronics box during the first postdeployment lunation of the Apollo 16 instrument.*

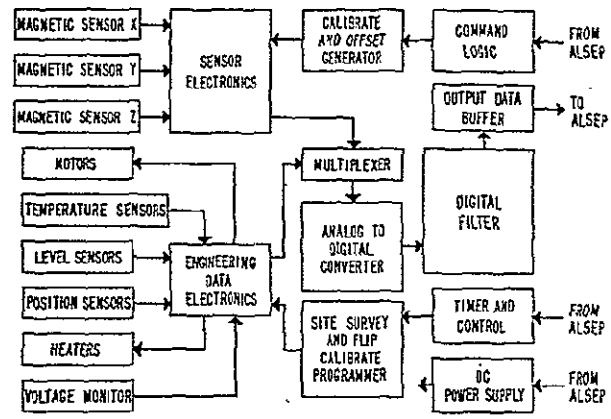

Figure 4.—*Functional block diagram for the Apollo LSM electronics.*

encoder (3.3 samples/second). The pre-alias filter following the sensor electronics has attenuations of 3 dB at 1.7 Hz, 64 dB at 26.5 Hz, and 58 dB at the Nyquist frequency (13.2 Hz), with an attenuation rate of 22 dB/octave. The four-pole Bessel digital filter limits the alias error to less than 0.5 percent and has less than 1 percent overshoot for a step function response. This filter has an attenuation of 3 dB at 0.3 Hz and 48 dB at the telemetry-sampling Nyquist frequency (1.6 Hz). The phase response is linear with frequency. The response of the entire LSM measurement system to a step function input is shown in figure 5. The digital filter can be bypassed by ground command in order to pass higher frequency information.

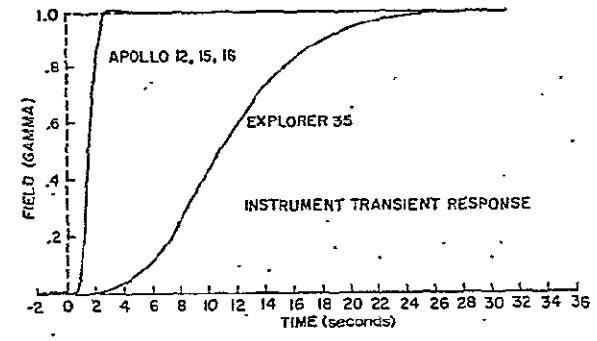

Figure 5.—*Laboratory measurements comparing instrument transient responses of the Apollo 12, 15, and 16 lunar surface magnetometers with the Explorer 35 lunar orbiting magnetometer for a 1.0-γ step change in the input magnetic field.*

Fluxgate Sensor

Three orthogonal vector components of the magnetic field are measured by three fluxgate sensors designed and fabricated by the U.S. Naval Ordnance Laboratory (ref. 56). The sensor shown schematically in figure 6 consists of a toroidal Permalloy core that is driven to saturation by a sinusoidal current having a frequency of 6000 Hz. The sense winding detects the superposition of the drive-winding magnetic field and the total lunar surface field; as a result, a second har-

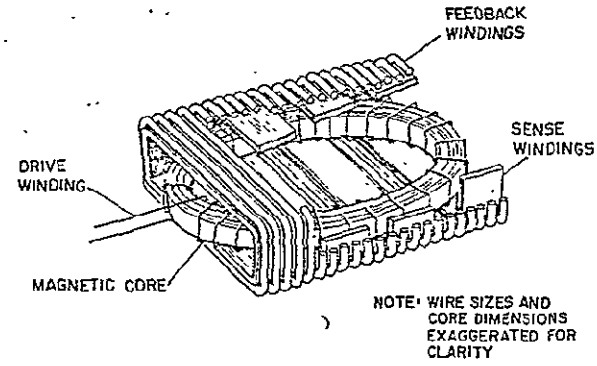

Figure 6.—*Simplified view of the ring core magnetometer sensor developed jointly by the U.S. Naval Ordnance Laboratory and NASA/Ames Research Center.*

ORIGINAL PAGE IS
OF POOR QUALITY

monic of the driving frequency is generated in the sense winding with a magnitude that is proportional to the strength of the surface field. The phase of the second harmonic signal with respect to the drive signal indicates the direction of the surface field with respect to the sensor axis. This output signal is amplified and synchronously demodulated to drive a voltage to the analog-to-digital converter and then through the central-station radio to Earth.

Data Flow and Mission Operation

The LSM experiment is controlled from the NASA/Johnson Space Center (JSC) by commands transmitted to the Apollo lunar surface experiments package (ALSEP) from remote tracking stations. The data are recorded on magnetic tape at the remote sites and are also sent directly to JSC for real-time analysis to establish the proper range, offset, frequency response, thermal control, and operating mode.

The Apollo 12 LSM returned useful scientific information from the time of its deployment on day 323 of 1969 to day 256 of 1971. The Apollo 15 LSM operated from its deployment on day 212 of 1971 to day 264 of 1972. The Apollo 16 LSM was deployed on day 112 of 1972 and continues to return useful information at the time of this writing.

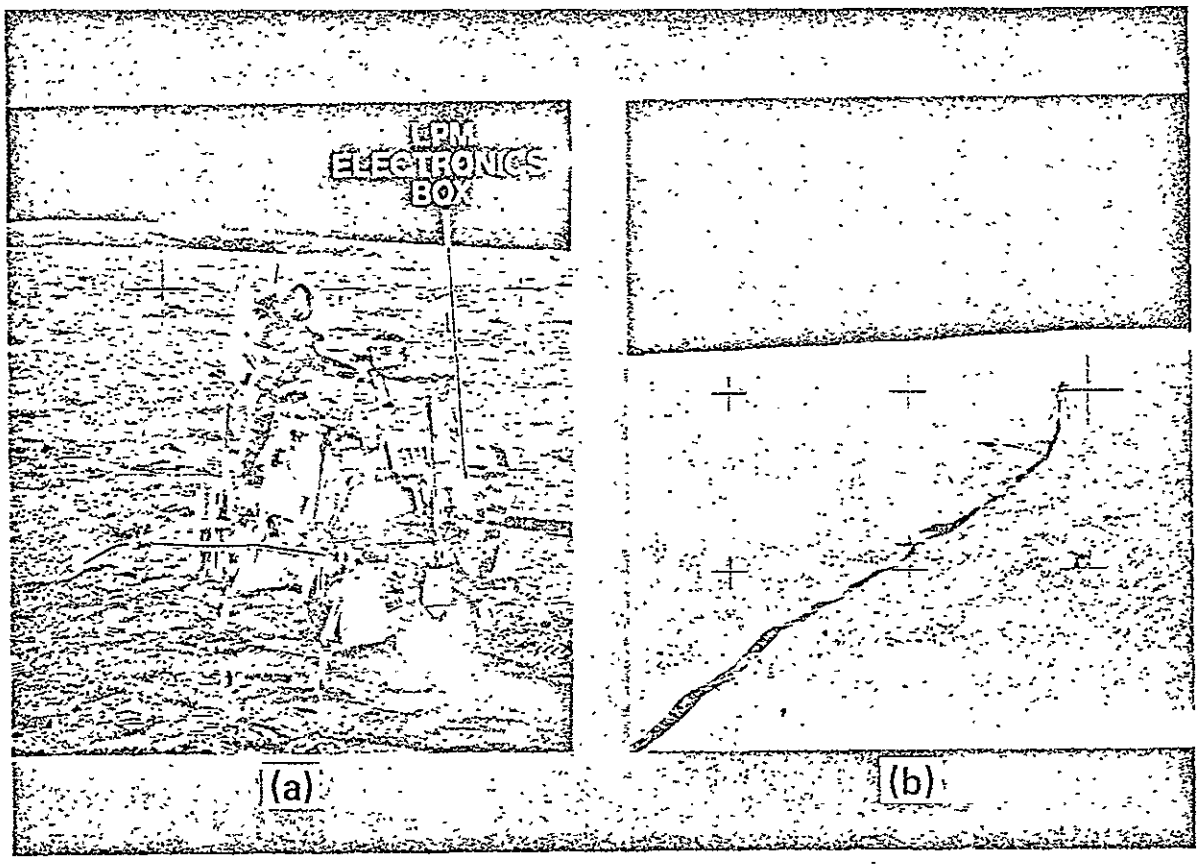

Figure 7.—*The Apollo 14 lunar portable magnetometer (LPM), shown (a) stowed aboard the mobile equipment transporter and (b) deployed during a magnetic field measurement. The sensor-tripod assembly is deployed 15 meters from the electronics box, which remains on the mobile equipment transporter so that magnetic fields of the astronaut's suit and other equipment will not be measured by the LPM.*

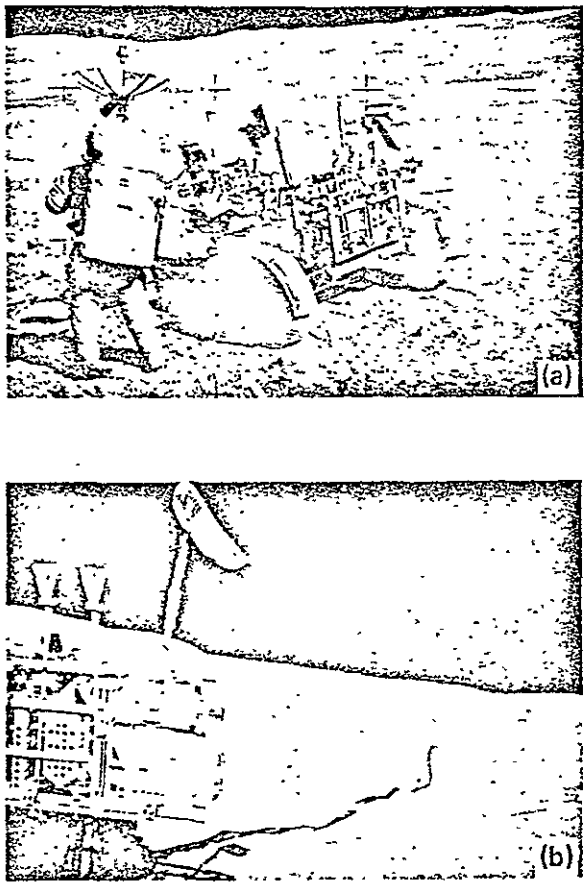

Figure 8.—*The Apollo 16 LPM (a) stowed on the lunar roving vehicle and (b) deployed during a magnetic field measurement.*

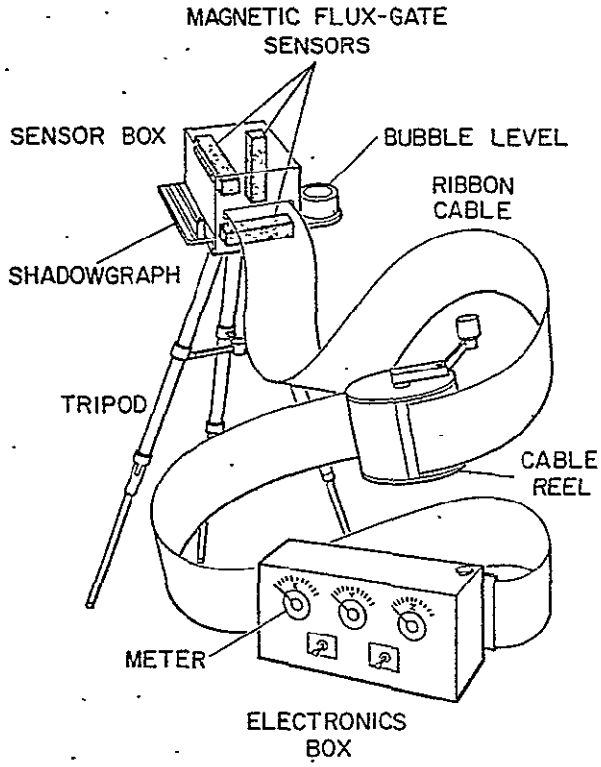

Figure 9.—*Schematic diagram of the Apollo 14 LPM. The sensor-tripod assembly is connected by means of a 15-meter ribbon cable to the electronics box, which contains a battery pack, electronics, and visual displays for three magnetic field vector components. Meter displays are used for the Apollo 14 LPM, and digital displays are used for the Apollo 16 LPM.*

LUNAR PORTABLE MAGNETOMETER (LPM)

The self-contained LPM is used to measure the steady magnetic field at different points along the lunar traverse of the astronauts. Two portable magnetometers have been deployed on the moon by the Apollo astronauts: one at the Apollo 14 site (3.7° S, 17.5° W) shown in figure 7, and one at the Apollo 16 landing site (9.0° S, 15.5° E) shown in figure 8.

The LPM field measurements are a vector sum of the steady remanent field from the lunar crust and of the time-varying ambient fields. The LSM simultaneously measures the time-varying components of the field; these components are later subtracted from the LPM measurements to give the desired resultant steady field values caused by the magnetized crustal material. The LPM consists of a set of three orthogonal fluxgate sensors mounted on top of a tripod (fig. 9); the sensor-tripod assembly is connected by means of a 15-m ribbon cable to the electronics box, which is mounted on the mobile equipment transporter (Apollo 14) or the lunar roving vehicle (Apollo 16).

The 15-m cable length was determined from magnetic properties tests of the mobile equipment transporter and lunar roving vehicle. The LPM was calibrated by using magnetic reference instruments directly traceable to the U.S. National Bureau of Standards. The pertinent LPM characteristics are listed in table 1.

ORIGINAL PAGE IS
OF POOR QUALITY

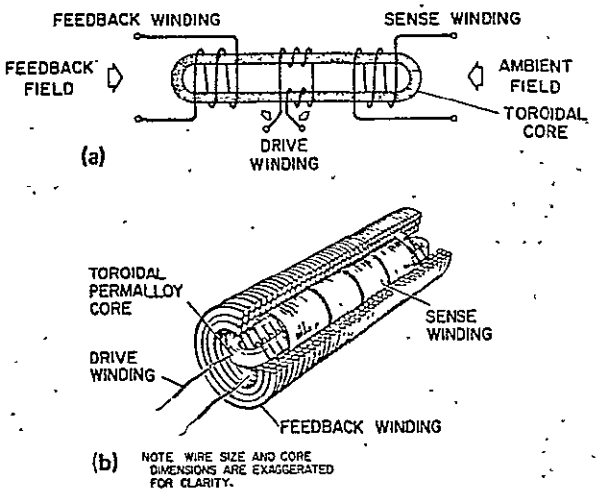

Figure 10.—*The fluxgate used in the LPM to measure each of three components of the magnetic field, (a) Functional schematic. (b) Cutaway view of the sensor windings and high-permeability core.*

Fluxgate Sensor

The fluxgate sensor, shown schematically in figure 10 is used to measure the vector components of the magnetic field in the magnetometer experiment. Three fluxgate sensors (refs. 56 and 57) are orthogonally mounted in the sensor block as shown in figure 9. Each sensor (see fig. 10) weighs 18 g and uses 15 mW of power during operation. The sensor consists of a flattened toroidal core of Permalloy that is driven to saturation by a square wave at a frequency f_o = 7250 Hz. This constant-voltage square wave drives the core to saturation during alternate half cycles and modulates the permeability at twice the drive frequency. The voltage induced in the sense windings is equal to the time rate of change of the net flux contained in the area enclosed by the sense winding. This net flux is the superposition of the flux from the drive winding and the ambient magnetic field. The signal generated in the sense winding at the second harmonic of the drive signal will be amplitude modulated at a magnitude proportional to the ambient magnetic field. The phase of this second harmonic signal with respect to the drive waveform indicates the polarity of the magnetic field. The sensor electronics amplifies and filters the 2 f_o sense-winding signal and synchronously demodulates it to derive a voltage proportional to the ambient magnetic field. After demodulation, the resulting signal is amplified and used to drive the feedback winding to null out the ambient field within the sensor. Operating at null increases thermal stability by making the circuit independent of core permeability variations with temperature.

The sensor block, mounted on the top of a tripod, is positioned 75 cm above the lunar surface. The tripod assembly consists of a latching device to hold the sensor block, a bubble level with 1° annular rings, and a shadowgraph with 3° markings used to align the device along the Moon-to-Sun line.

Electronics

The magnetometer electronics box is self-contained with a set of mercury cells for power and three digital displays for visual readout of the magnetic field components. A block diagram of the instrument is shown in figure 11. The sensors are driven into saturation by a 7.25-kHz square wave, and a 14.5-kHz pulse is used to demodulate the second harmonic signal from the sense windings. The amplifier output is synchronously demodulated, producing a direct-current output voltage proportional to the amplitude of the ambient magnetic field. This demodulated output is used to drive the feedback wind-

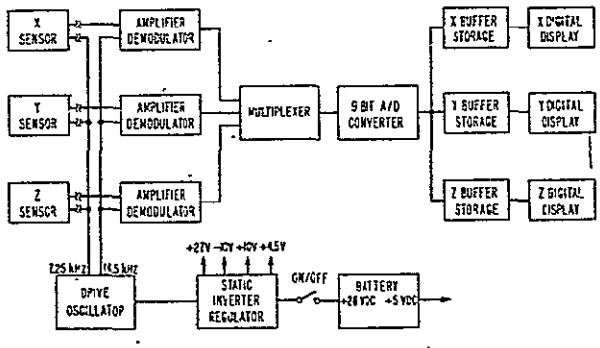

Figure 11.—*Functional block diagram of the LPM electronics.*

ing of the sensor so that the sensor can be operated at null conditions. The demodulated output from each channel is passed through a low pass filter with a time constant of 20 seconds.

Three meters were used to read the electronics output of the Apollo 14 LPM. The Apollo 16 LPM was actuated by a READ switch which caused the filtered analog signal to be converted to a digital 9-bit binary number. In system operation, the output of the analog-to-digital converter then goes to a storage register for display by the light-emitting diode numeric indicator. Three numeric indicators are used for each axis and read out in octal from 000 to 777 for magnetic field values from − 256 to + 256 γ.

Deployment and Operation

The astronaut operation was crucial to the execution of this experiment. The following measurement sequence was conducted: leaving the electronics box on the mobile equipment transporter (Apollo 14) or lunar roving vehicle (Apollo 16), the astronaut deployed the sensor-tripod assembly about 15 meters away, leveling and azimuthally aligning the instrument by bubble level and shadowgraph. The astronaut then returned to the electronics box, turned the power switch on, read the sensor meters (or digital displays) in sequence, and verbally relayed the data back to Earth. At the first deployment site only, two sets of additional readings were taken with the sensor block first rotated 180° about a horizontal axis and then rotated about a vertical axis. These additional readings allowed determination of a zero offset for each axis.

Explorer 35 Magnetometer

The ambient steady-state and time-dependent magnetic fields in the lunar environment are measured by the Explorer 35 satellite magnetometer. The satellite has an orbital period of 11.5 hrs., an aposelene of 9390 km, and a periselene of 2570 km (fig. 12). Two magnetometers are carried aboard Explorer 35, one provided by NASA/Ames Research Center and the other provided by NASA/Goddard Space Flight Center. Since most of the analysis of lunar internal properties has been carried out with the Ames magnetometer, its characteristics will be considered here. The Explorer 35 Ames magnetometer measures three magnetic field vector components very 6.14 seconds and has an "alias" filter with 18-dB attenuation at the Nyquist frequency (0.08 Hz) of the spacecraft data-sampling system. This instrument has a phase shift linear with frequency, and its step-function response is slower than that of the Apollo LSM instrument (fig. 5). Further information about the Explorer 35 magnetometer is given by Sonett et al. (ref. 58). Figure 12 also shows the orbit of the Apollo 16 particles and fields subsatellite which carried a magnetometer, and the three lunar surface magnetometers. Additional information on the subsatellite magnetometer is reported by Coleman et al. (refs. 59 and 60).

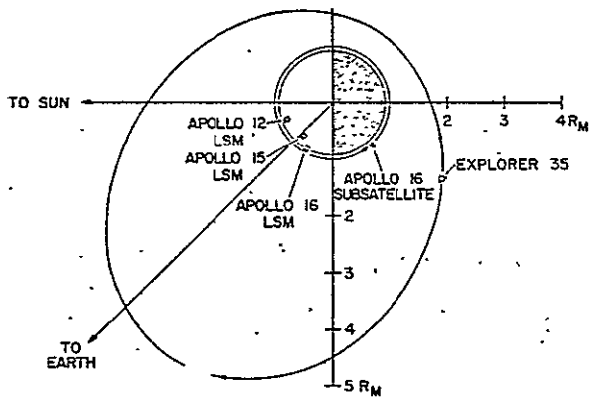

Figure 12.—*The Explorer 35 orbit around the Moon, projected onto the solar ecliptic plane. The period of revolution is 11.5 hrs. The Apollo 12, 15, and 16 surface instrument positions and Apollo 16 subsatellite trajectory are shown.*

The Lunar Magnetic Environment

In different regions of a lunar orbit, the magnetic environment of the Moon can have

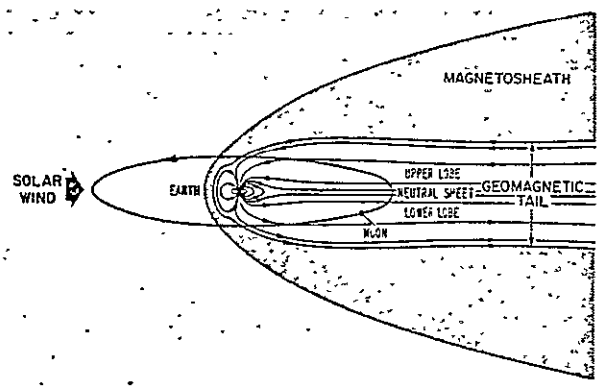

Figure 13.—*Magnetic environment of the Moon during a complete lunar orbit, with emphasis on the geomagnetic tail region. The plane of the lunar orbit very nearly coincides with the ecliptic plane of the Earth's orbit. The Earth's permanent dipole field is swept back into a cylindrical region known as the geomagnetic tail; at the lunar distance the field magnitude is ~ 10 gammas or 10^{-4} oersteds. Substructure of the tail consists of two "lobes"; the upper or northward lobe has its magnetic field pointing roughly toward the Earth, whereas the lower lobe field points away from the Earth. The Moon is immersed about four days of each orbit in the tail; the Moon can pass through either or both lobes (accented portion of orbit), depending upon the characteristics of the particular orbit.*

distinctly different characteristics (see figure 13). Average magnetic field conditions vary from relatively steady fields of magnitude ~ 10 γ in the geomagnetic tail to mildly turbulent fields averaging ~ 5 γ in the free-streaming solar plasma region, to turbulent fields averaging ~ 8 γ in the magnetosheath. Average solar wind velocity is ~ 400 km/s in a direction approximately along the Sun-Earth line.

Various induced lunar and plasma-interaction fields are assumed to exist at the lunar surface; for reference, we write the sum of these fields as

$$\underline{B}_A = \underline{B}_E + \underline{B}_R + \underline{B}_\mu + \underline{B}_P + \underline{B}_T + \underline{B}_D + \underline{B}_F \quad (1)$$

Here $\underline{B}_A$ is the total magnetic field measured on the surface by an Apollo lunar surface magnetometer; $\underline{B}_E$ is the total external (solar or terrestrial) driving magnetic field measured by the Explorer 35 and Apollo 15 subsatellite lunar orbiting magnetometers while outside the antisolar lunar cavity; $\underline{B}_R$ is the steady remanent field at the surface site; $\underline{B}_\mu$ is the magnetization field induced in permeable lunar material; $\underline{B}_P$ is the poloidal field caused by eddy currents induced in the lunar interior by changing external fields; $\underline{B}_T$ is the toroidal field corresponding to unipolar electrical currents driven through the Moon by the $\nabla \times \underline{B}_E$ electric fields; $\underline{B}_D$ is the field associated with the diamagnetic lunar cavity; and $\underline{B}_F$ is the field associated with the hydromagnetic solar wind flow past the Moon.

The interaction of the solar wind with the Earth's permanent dipole field results in formation of the characteristic shape of the Earth's magnetosphere; the solar wind in effect sweeps the Earth's field back into a cylindrical region (the geomagnetic tail) on the Earth's antisolar side. The Earth's field magnitude is about 30 000 γ at the equator; in the geomagnetic tail the field decreases with distance from the earth with a radial dependence expressible as $R^{-0.736}$ (ref. 61). At the distance where the Moon's orbit intersects the tail, the field magnitude is ~ 10 γ. The Moon is in the geomagnetic tail for about four days of each 29.5-day lunation (period between successive full Moons). Substructure of the tail consists of two "lobes": the upper or northward lobe has its magnetic field pointing roughly toward the Earth, whereas the lower lobe field points away from the Earth. The Moon can pass through either or both lobes, depending upon the characteristics of the particular orbit, the geomagnetic dipole axis orientation, and perturbations of the geomagnetic field by solar wind pressures. When the Moon is passing through a quiet region of the geomagnetic tail, solar wind interaction fields ($\underline{B}_T$, $\underline{B}_D$, and $\underline{B}_F$) and the induced poloidal lunar field $\underline{B}_P$ are negligible, and the total field at the lunar surface is

$$\underline{B}_A = \underline{B}_E + \underline{B}_\mu + \underline{B}_R \quad (2)$$

The induced magnetic field $\underline{B}_\mu$ is dependent on the relative magnetic permeability distribution of the lunar sphere and is proportional to the external magnetic field $\underline{B}_E$.

Therefore, when $B_E = 0$, $B_A = B_R$ and the Apollo magnetometer measures the steady remanent field alone. Once B_R is known, the relative magnetic permeability of the Moon μ/μ_0 can be calculated.

A different set of field terms in equation (1) is dominant when the Moon is immersed in free-streaming solar wind and the magnetometer is on the lunar sunlit side. $B_D \rightarrow 0$ outside the cavity, and the global fields B_μ and B_T can be neglected in comparison to B_P (ref. 38). The interaction field B_F has been found to be important during times of high solar wind particle density (ref. 29); therefore the interaction term B_F is not to be assumed negligible in general, and equation (1) becomes

$$B_A = B_P + B_E + B_R + B_F \qquad (3)$$

At low frequencies ($\leq 3 \times 10^{-4}$ Hz), $B_P \rightarrow 0$ and the interaction field B_F can be investigated.

When the magnetometer is located on the dark (antisolar) side of the Moon, it is generally isolated from solar plasma flow and $B_F \rightarrow 0$. Then for dark side data, equation (3) reduces to

$$B_A = B_P + B_E + B_R \qquad (4)$$

where cavity effects (B_D) are neglected to a

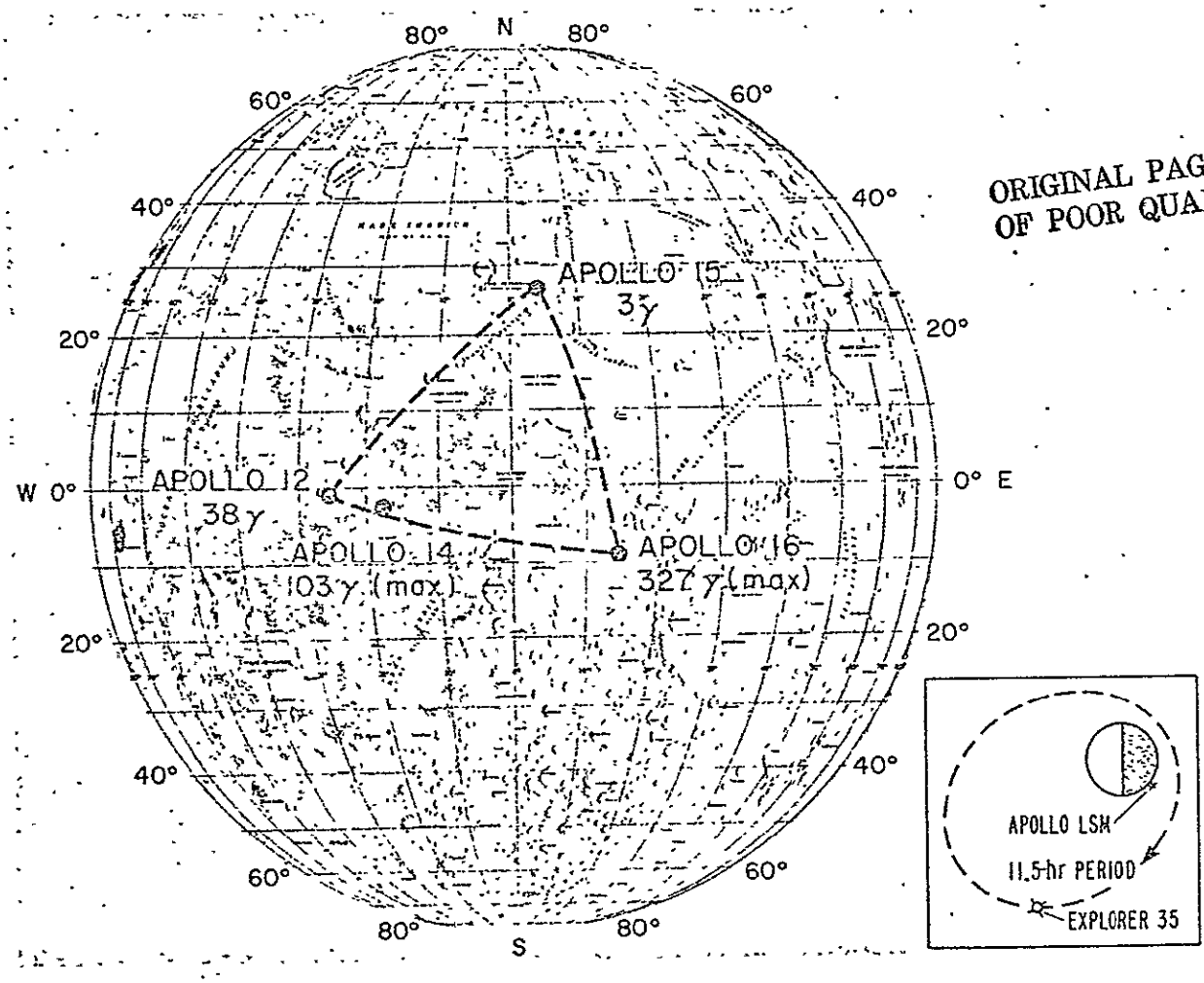

ORIGINAL PAGE I
OF POOR QUALIT

Figure 14.—*Apollo magnetometer network on the lunar surface. Maximum remanent magnetic fields measured at each landing site are shown.*

ORIGINAL PAGE IS
OF POOR QUALITY

first approximation for measurements made near lunar midnight (ref. 38). After B_R has been calculated from geomagnetic tail data, only the poloidal field B_P is unknown. Equation (4) can then be solved for certain assumed lunar models, and curve fits of data to the solution determine the model-dependent conductivity profile σ (R). Furthermore, electrical conductivity is related to temperature, and the lunar interior temperature can be calculated for assumed lunar material compositions.

Lunar Remanent Magnetic Fields

The permanent magnetic fields of the Moon have been investigated by use of surface magnetometer measurements at four Apollo sites (see fig. 14) and the U.S.S.R. Lunokhod II site; orbital measurements from Explorer 35 and two Apollo subsatellite magnetometers; and natural remanent magnetization measurements of returned lunar samples. Lunar remanent field measurements by Apollo surface magnetometers will be emphasized in this paper. Sample magnetization measurements have been reviewed elsewhere (refs. 62–65); orbital results have been reported by Mihalov et al. (ref. 25), Sonett and Mihalov (ref. 66), Coleman et al. (refs. 26, 59, and 60), Sharp et al. (ref. 27), and Russell et al. (refs. 28 and 34).

SURFACE SITE FIELD MEASUREMENTS

Analyses of Apollo 11 lunar samples first demonstrated the presence of a natural remanent magnetization (NRM) in the lunar surface material. This magnetization ranges from 10^{-3} to 10^{-7} gauss cm^3 g^{-1} and most likely arises from the thermoremanent magnetization of metallic iron grains (ref. 65). The discovery of NRM in the lunar samples, which was a surprise to most scientists, did not lead to the expectation that the magnetization would be ordered on sufficiently large scale to produce localized magnetic fields. Also, measurements from orbiting magnetometers had not been interpreted as indicating the presence of permanent lunar fields

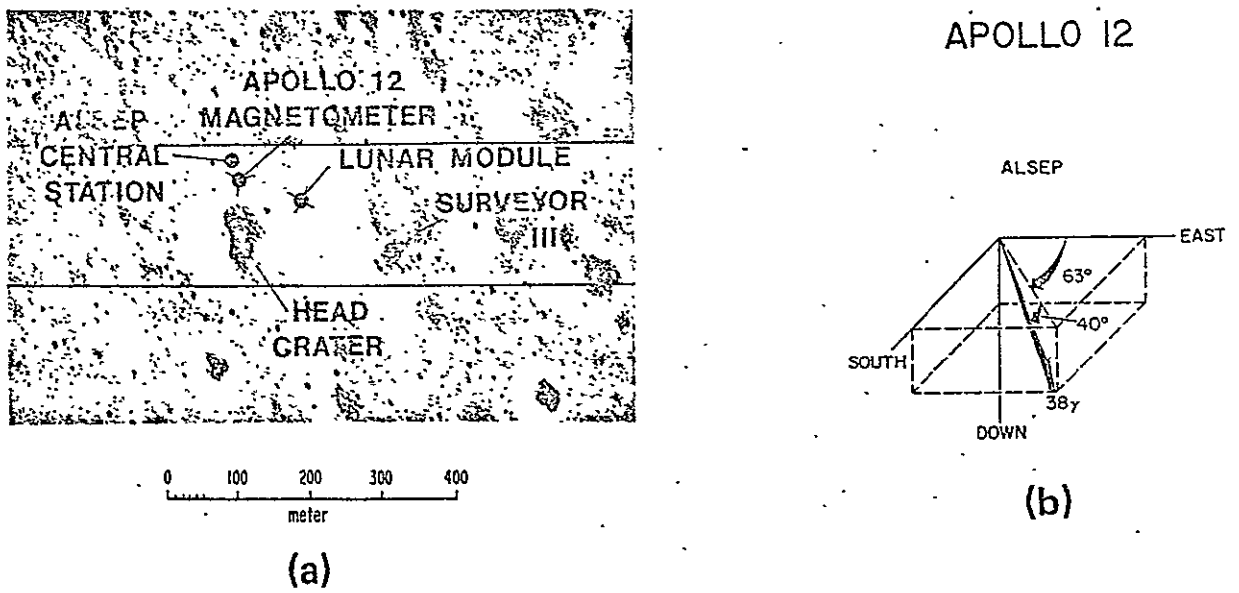

Figure 15.—*Lunar remanent magnetic field measured at the Apollo 12 site in Oceanus Procellarum. (a) Lunar Orbiter photograph showing the Apollo 12 landing site and location of the surface magnetometer where the remanent field measurements were made. (b) Magnitude and orientation of the measured vector magnetic field.*

prior to the Apollo 12 landing in November 1969.

However, a local remanent magnetic field was measured by the first (Apollo 12) lunar surface magnetometer, which was deployed on the eastern edge of Oceanus Procellarum. The permanent field magnitude was measured to be 38 ± 3 gammas and was attributed to local sources composed of magnetized subsurface material (refs. 23 and 24; see fig. 15). A remanent field this large was generally unexpected, and the origin of magnetized regions on the Moon yet remains a central problem in lunar magnetism. Subsequent to this measurement of an intrinsic lunar magnetic field, surface magnetometers have measured fields at the Apollo 14, 15, and 16 sites. Fields of 103 ± 5 and 43 ± 6 gammas, at two sites located about a kilometer apart, were measured by the Apollo 14 Lunar Portable Magnetometer (LPM) at Fra Mauro (see fig. 16). A steady field of 3.4 ± 2.9 gammas was measured near Hadley Rille by the Apollo 15 LSM (see fig. 17). At the Apollo 16 landing site both a portable and stationary magnetometer were deployed; magnetic fields ranging between 112 and 327 gammas were measured at five different locations over a total distance of 7.1 kilometers at the Descartes landing site. These are the largest lunar fields yet measured. A schematic representation of the measured field vectors is shown in figure 18. All the vectors have components pointing downward except the one at Site 5 near Stone Mountain, which points upward. This suggests, among other possibilities, that the material underlying Stone Mountain has undergone different geological processes than that underlying the Cayley Plains and North Ray Crater. In fact, Strangway et al. (ref. 67) proposed the possibility that the light-colored, relatively smooth Cayley formation is magnetized roughly vertically; the difference in the vertical component at site 5 was explained as an edge effect at the Cayley Plains-Stone Mountain boundary.

The similarities between the Apollo 12 and 14 field measurements (viz, all vectors are pointed down and toward the south, and have magnitudes that correspond to within a factor of 3) and the proximity of the two landing sites (see fig. 14) suggest that the two Apollo 14 sites and possibly the Apollo 12 site are located above a near-surface slab of material that was uniformly magnetized

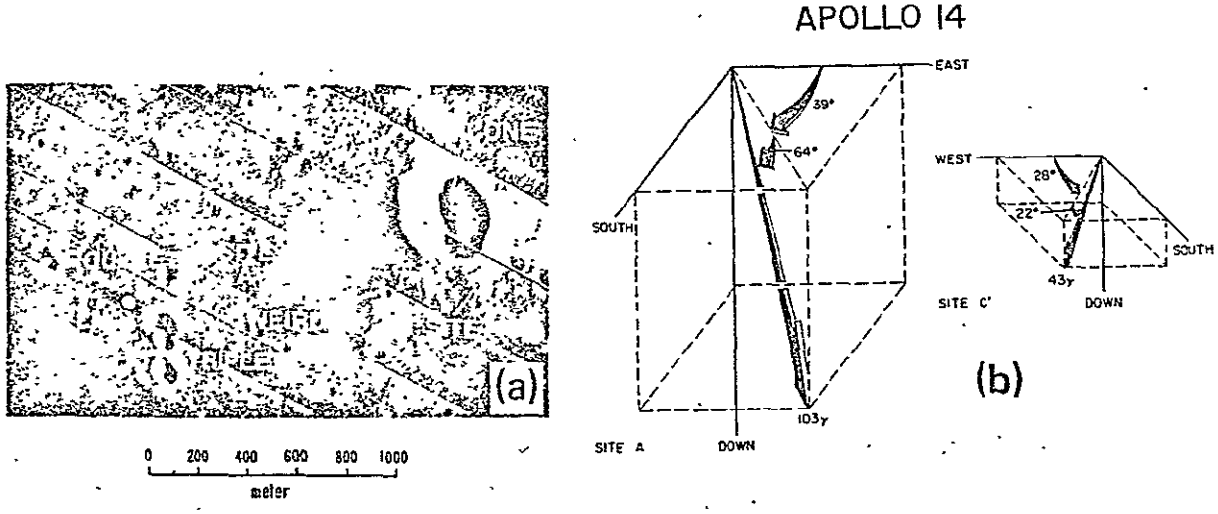

Figure 16.—*Lunar remanent magnetic fields measured at the Apollo 14 site at Fra Mauro. (a) Lunar Orbiter photograph showing the Apollo 14 landing site and the locations of sites A and C' where the lunar portable magnetometer measurements were made. (b) Magnitude and orientation of the measured remanent magnetic fields.*

ORIGINAL PAGE IS OF POOR QUALITY

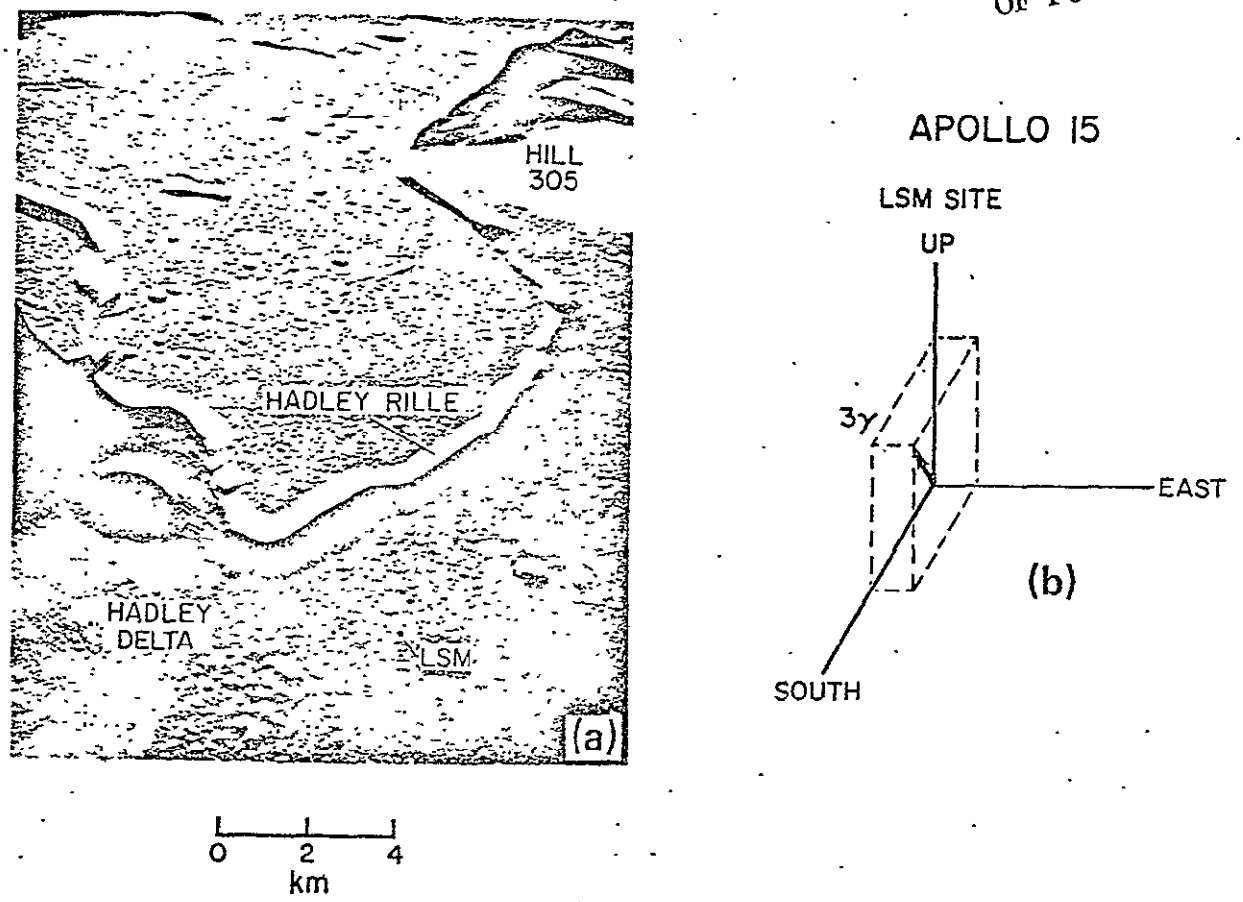

Figure 17.—*Lunar remanent magnetic field measured at the Apollo 15 site near Hadley Rille. (a) Photograph showing the Apollo 15 landing site and location of the surface magnetometer where the remanent field measurement was made. (b) Magnitude and orientation of the measured remanent magnetic field.*

at one time. Subsequently the magnetization in the slab was perhaps altered by local processes, such as tectonic activity or fracturing and shock demagnetization from meteorite impacts. This latter process is graphically illustrated in figure 19. The Apollo 12 and 14 steady magnetic fields could also originate in surface or subsurface dipolar sources, such as meteoroid fragments or ore bodies. Another possibility is that the region was subjected to a uniform magnetic field but that various materials with differing coercivities were magnetized to different strengths. Another model might involve a slow variation in the direction of the ambient field, causing regions that passed through the Curie temperature at different times to be magnetized in different directions. A summary of all remanent lunar fields measured by the magnetometers deployed on the surface is given in table 2, and the network of surface sites at which remanent fields have been measured is shown in figure 14.

Information on the scale sizes of the permanently magnetized regions near Apollo landing sites is given by gradient measurements of the lunar surface magnetometers, the spacing of vector measurements over the lunar surface, the known interaction properties of these remanent fields with the solar wind plasma, and limits imposed by satellite measurements. The field gradient in a plane parallel to the lunar surface is less than the instrument resolution of 0.13 gamma/meter

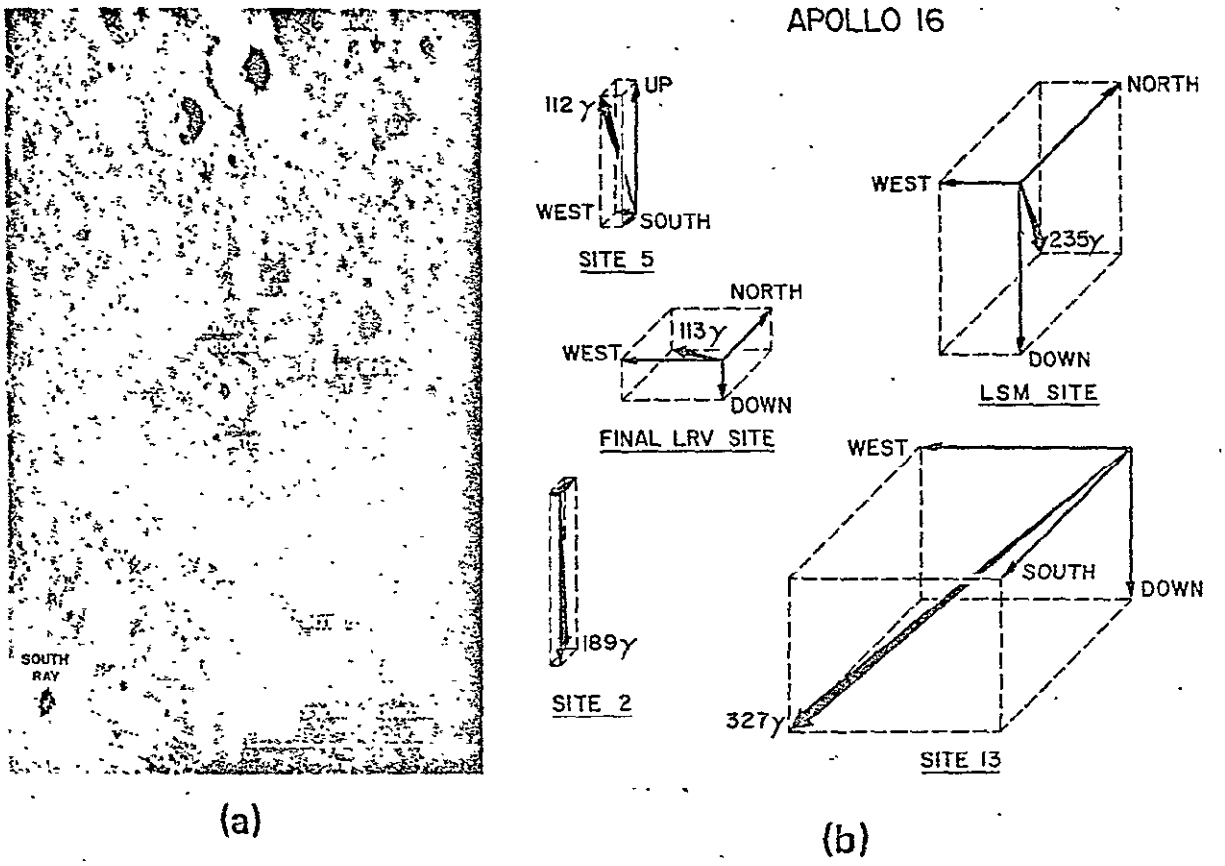

Figure 18.—*Lunar remanent magnetic fields measured at the surface Apollo 16 Descartes site. (a) Photograph showing the Apollo 16 landing site, the location of the surface magnetometer, and the traverse positions where the portable magnetometer was deployed. (b) Magnitude and orientation of the measured vector remanent magnetic fields.*

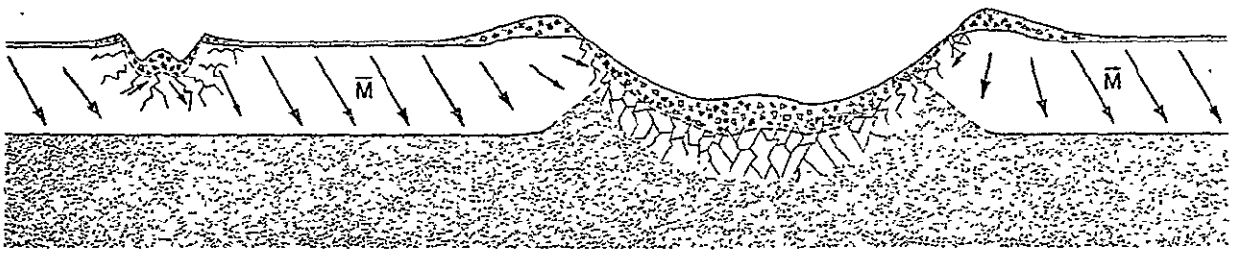

Figure 19.—*Conceptional diagram showing disruption of a previously uniformly magnetized subsurface layer by meteorite impact. The vectors* (M) *represent the direction and magnitude of remanent magnetization in the layer.*

Table 2.—*Summary of Lunar Surface Remanent Magnetic Field Measurements*

Site	Coordinates, Degrees	Field Magnitude, Gammas	Magnetic-Field Components, Gammas		
			Up	East	North
Apollo 16:					
ALSEP Site	8.9°S, 15.5°E	235 ± 4	−186 ± 4	−48 ± 3	+135 ± 3
Site 2		189 ± 5	−189 ± 5	+3 ± 6	+10 ± 3
Site 5		113 ± 4	+104 ± 5	−5 ± 4	−40 ± 3
Site 13		327 ± 7	−159 ± 6	−190 ± 8	−214 ± 6
LRV Final Site		112 ± 5	−66 ± 4	−76 ± 4	+52 ± 2
Apollo 15:					
ALSEP Site	26.1°N, 3.7°E	3.4 ± 2.9	+3.3 ± 1.5	+0.9 ± 2.0	−0.2 ± 1.5
Apollo 14:					
Site A	3.7°S, 17.5°W	103 ± 5	−93 ± 4	+38 ± 5	−24 ± 5
Site C′		43 ± 6	−15 ± 4	−36 ± 5	−19 ± 8
Apollo 12:					
ALSEP Site	3.2°S, 23.4°W	38 ± 2	−25.8 ± 1.0	+11.9 ± 0.9	−25.8 ± 0.4

at the Apollo 12 and 15 sites. At Apollo 14 a field difference of 60 γ was measured at two sites located 1.1 km apart. Gradient measurements and the absence of changes in the permanent field at the sites after lunar module ascent demonstrated that the field sources are not magnetized artifacts.

The scale size of the Apollo 12 remanent field has been calculated from local gradient and Explorer 35 measurements to be from 2 km to 200 km (ref. 29). For the Apollo 16 field, portable magnetometer measurements over the lunar roving vehicle traverse showed that the scale size for the field was greater than 5 km; the Apollo 16 subsatellite magnetometer showed no anomalous field attributable to the Descartes area at orbital altitude, implying a surface field scale size upper limit of 100 km. Therefore, the Apollo 16 remanent field scale size is between 5 and 100 km.

ORIGIN OF THE LUNAR REMANENT MAGNETIZATION

From the beginning of the Apollo missions the origin of the lunar remanent fields has been of great interest and there has been no shortage of mechanisms proposed to explain the origin of the lunar fields and remanence. Many authors have discussed various aspects of natural remanent magnetization (NRM) in the lunar surface material (e.g., refs. 22, 68, and 69). Possible source mechanisms for the remanent fields have been reviewed by Dyal et al. (refs. 70 and 72), Strangway et al. (ref. 71), and in detail by Fuller (ref. 65). Some of these possible mechanisms are discussed briefly here and displayed schematically in figures 20 and 21.

Large Solar or Terrestrial Field

The thermoremanent magnetization of the near-surface lunar material (such as might be responsible for the remanent fields measured by the surface and subsatellite magnetometers) was probably accomplished by the cooling of crustal material on a scale of tens of kilometers in a relatively steady external magnetic field of a few thousand gammas. It is possible that the Sun was the source of the external magnetic field (ref. 19). The early solar field may have been greatly en-

hanced during an early T-Tauri solar phase, as suggested by Sonett et al. (ref. 73), although at the lunar orbit such a field was probably even more variable than it is at the present time. A terrestrial field increase greater than 100 times its present value would probably be necessary to magnetize lunar material at the present-day lunar orbit. Such a large terrestrial field is not indicated by paleomagnetic studies. For an ancient terrestrial field of present-day magnitude, the Moon would have to have approached to within 2 to 3 Earth radii, close to the Roche limit (refs. 16 and 74) to be subjected to the necessary field strength. All of the alternatives for these hypotheses seem to have shortcomings.

Iron Core Dynamo

For this mechanism a whole-Moon field results from the self-generating dynamo action of a small iron core (refs. 75 and 76). The dynamo is assumed to have been active 3 to 4 billion years ago when surface rocks and breccias were formed. After the thermoremanent magnetization was established in the upper crust material, as it cooled through the Curie temperature, the dynamo turned off. Subsequently, meteorite impacts on the magnetized surface randomized the field's sources by a gardening process (see fig. 19) and destroyed the whole-body magnetization in the crust. The core dynamo hypothesis also has its shortcomings. In the first place it is not clear that even the most efficient dynamo mechanism in a lunar core of limited size would be self-sustaining at rotational speeds for which the Moon could hold together (ref. 77). In addition, it is doubtful that a dynamo, if ever operating, could produce the surface fields to explain the thermoremanent magnetization of some lunar samples (refs. 20 and 77).

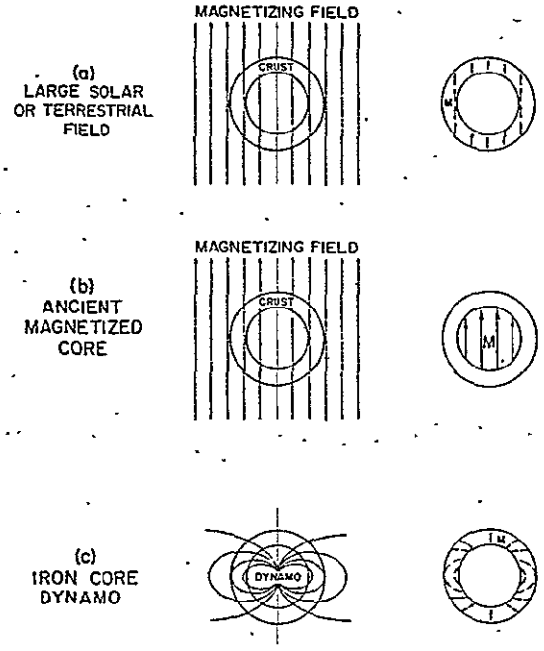

Figure 20.—*Schematic representation of some global mechanisms proposed to explain the origin of lunar remanent magnetic fields. (a) Large solar or terrestrial field. (b) Ancient magnetized core. (c) Iron core dynamo. Descriptions of the mechanisms are given in the text.*

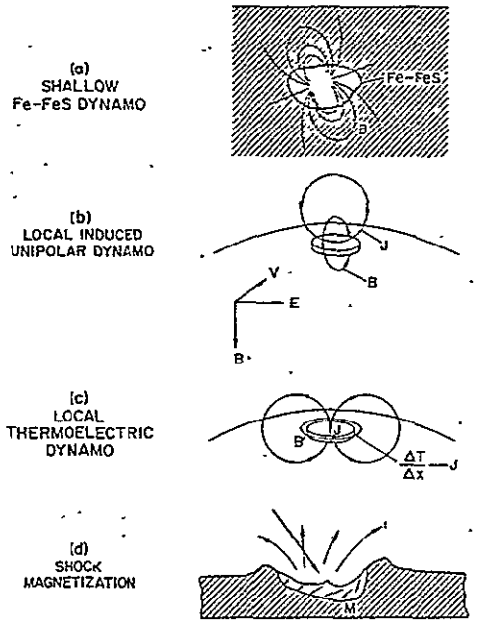

Figure 21.—*Schematic representation of some local mechanisms proposed to explain the origin of lunar remanent magnetic fields. (a) Shallow Fe-FeS dynamo. (b) Local induced unipolar dynamo. (c) Local thermoelectric dynamo. (d) Shock magnetization. Descriptions of the mechanisms are given in the text.*

ORIGINAL PAGE IS
OF POOR QUALITY

Ancient Magnetized Core

Urey and Runcorn (ref. 78) and Strangway et al. (refs. 64 and 71) have suggested that near-surface material may have been magnetized by the field of a lunar core which had been previously magnetized by one of several possible means: (1) magnetization achieved isothermally by a strong transient field, (2) viscous remanent magnetization by a weak field applied over a long period, (3) depositional remanent magnetization during early lunar formation in a weak field, or (4) thermoremanent magnetization of the core by cooling through the Curie point in a weak field. If the Moon formed in a cold state, neither accretion nor radioactivity would necessarily have raised the temperature of the deep interior above the Curie point of iron, with accompanying loss of magnetization, until 4.1 to 3.2 billion years ago. In the outer shell, perhaps 200 to 400 km thick, partial melting could easily have been realized during later stages of accretion. During the crystallization of the crustal rocks in the magnetic field of the core, they obtained a thermoremanence. Subsequently, radioactive heating in the interior raised the core temperature above the Curie point, resulting in loss of the magnetization in the core.

Shallow Fe-FeS Dynamo

A model related to the lunar core dynamo is one hypothesizing small pockets of iron and iron sulfide (Fe-FeS) melt a few hundred kilometers below the surface (ref. 79) which act as small localized dynamos. The proponents of this mechanism suggest that these "fescons" are about 100 km in diameter. A variation of this local dynamo idea is suggested by Smolychowski (ref. 80) wherein a thin layer of molten basalt generates the field. The existence of such local source regions for magnetic field should be evident once the surface fields have been mapped over more of the lunar surface. However, the recently discovered asymmetry in the electromagnetic field fluctuations at the Apollo 15 landing site (ref. 81) could be due to such a highly conducting subsurface body.

Local Induced Unipolar Dynamo

The solar wind transports magnetic fields past the Moon at velocities V of approximately 400 km/s; the corresponding $V \times B$ electric field causes currents to flow along paths of high electrical conductivity (refs. 19 and 35) such as molten mare regions, with the highly conducting solar wind plasma completing the circuit back to the lunar interior. The fields associated with these currents magnetize the materials as they cool below the Curie temperature. Because this induction mechanism has the strongest influence while the hot region is sunlit, an average preferred direction is associated with V. However, the $V \times B$ induction model requires solar wind magnetic fields or velocities much higher than the present-day Sun provides.

Local Thermoelectrically Driven Dynamo

Dyal et al. (ref. 45) have proposed a mechanism of thermoelectrically driven currents to account for remanent fields. Thermoelectric potential is a function of the thermal gradient and electrical properties of the geological material. For the mechanism, a mare basin is modeled by a disk which has an axial temperature gradient. Thermal gradients in the cooling mare lava could produce a Thomson thermoelectromotive force which would drive currents axially through the mare disk. The solar wind plasma, highly conducting along magnetic field lines, could provide a return path to complete the electrical circuit from the top surface of the lava to the lunar surface outside the mare and back into the mare through the lunar interior. The upper limit of the fields generated in terrestrial materials by this process is a few thousand gammas. Such fields near a mare disk would produce thermoremanent magnetization in the Moon of magnitudes measured in lunar samples. This mechanism

awaits experimental verification using materials characteristic of lunar mare composition.

Shock Magnetization

Anisotropic compression of rocks by meteorite impacts is suggested by Nagata et al. (ref. 82) as a means of inducing a remanence in certain samples which they studied magnetically. This piezo-remanent magnetization can be significantly large even when the external field is very weak (e.g., the solar wind field) if the uniaxial compression is very large. This mechanism is appealing since it relies on a well-established lunar process and may explain some correlation between craters and magnetic anomalies (ref. 27), but the details remain undeveloped.

Local Currents from Charged Particle Transport

Any process which results in plasma flow near the lunar surface may generate strong local currents and magnetic fields. Cap (ref. 83), for example, has shown that ionized volcanic ash flows may produce fields up to 10^3 gammas. As another example, Nagata et al. (ref. 82) proposed the idea that lightning may be generated as a result of exploding dust clouds from meteorite impacts. The large currents associated with an electrical discharge could produce transient magnetic fields up to 10 or 20 gauss, resulting in isothermal remanent magnetization of local material.

At this time it is difficult to determine which of the above mechanisms is responsible for the lunar sample NRM. Of course, several (or none) of these hypotheses may explain the phenomenon. It seems to the authors that the locally active mechanisms are preferable over the global mechanisms because of the very low upper limit on the permanent global magnetic dipole moment and the apparently random nature of the local fields on the scale of tens of kilometers. Certainly a large amount of work remains to be carried out using the available lunar data, simulations in the laboratory, and future orbital measurements before preferred hypotheses can be identified with any degree of certainty.

REMANENT FIELD INTERACTION WITH THE SOLAR WIND

Compression of the remanent lunar magnetic field by the solar wind has been measured at the Apollo 12 and 16 sites. Simultaneous surface magnetic field and plasma data show, to first order, a compression of the remanent field in direct proportion to the solar wind pressure as schematically illustrated in Figure 22.

In order to study the compression of the remanent field, it is advantageous to define a field $\underline{\Delta B}$ as

$$\underline{\Delta B} = \underline{B}_A - (\underline{B}_E + \underline{B}_R), \qquad (5)$$

where $\underline{B}_A$ is the total surface magnetic field, measured by an Apollo lunar surface magnetometer; $\underline{B}_E$ is the extralunar (solar) driving magnetic field, measured by the lunar orbiting Explorer 35 magnetometer; and $\underline{B}_R$ is the steady remanent field at the site due to magnetized material. For low frequencies, i.e., 1-hour averages of magnetic

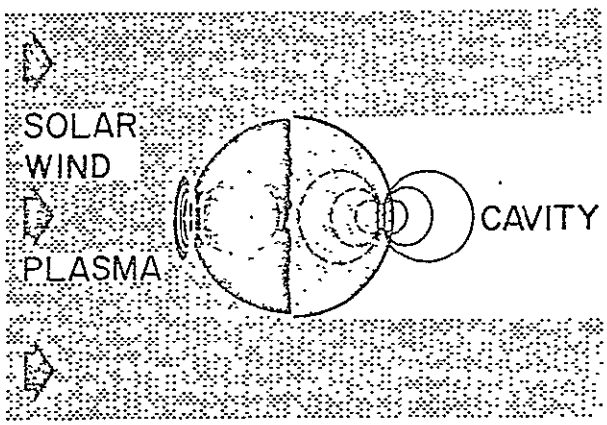

Figure 22.—*Schematic representation of remanent field compression by a high-density solar wind plasma. The remanent field is unperturbed during nighttime (antisolar side), while on the sunlit side it is compressed.*

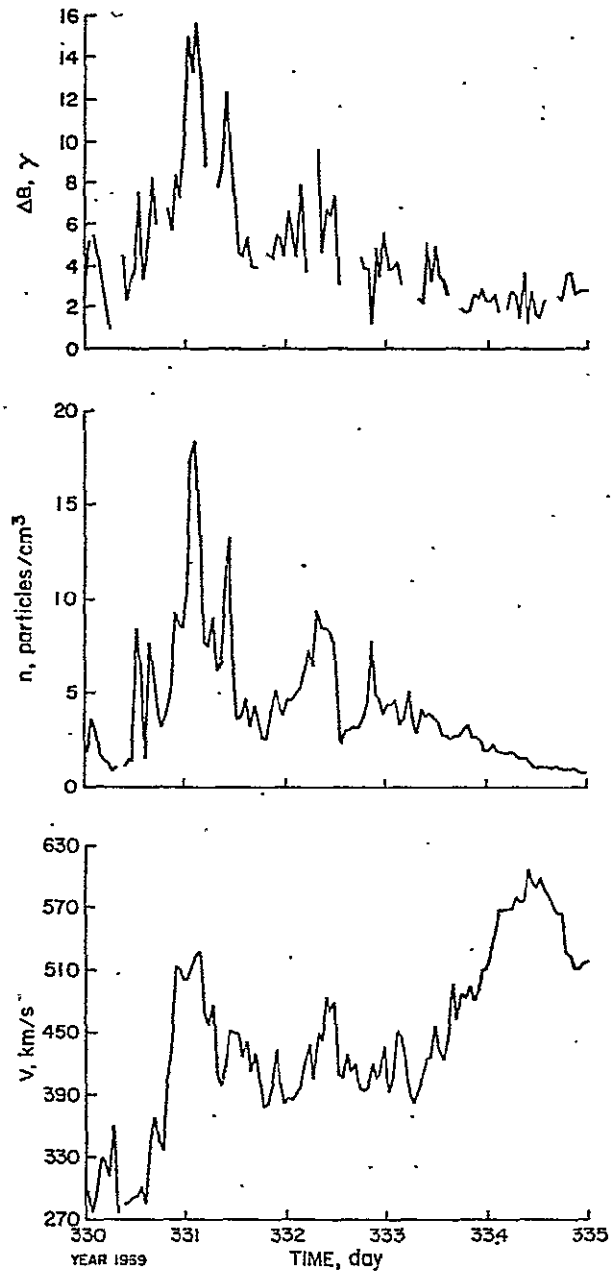

Figure 23.—*Simultaneous graphs of magnitude of the vector* $\Delta B = B_A - (B_E + B_R)$, *plasma density, and plasma velocity.* B_A *is the total surface field measured by the Apollo 12 lunar surface magnetometer,* B_E *is the extralunar field measured by lunar orbiting Explorer 35, and* B_R *is the remanent field at the Apollo 12 site.*

and solar wind data, the eddy-current poloidal field can be neglected and equation (5) contains all the vector fields, which are dominant at the lunar surface.

We shall show that to first order $\underline{\Delta B}$ is the vector change in the steady remanent field due to the solar wind pressure. Figure 23 shows simultaneous 1-hour average plots of the magnitude of the vector field difference $\underline{\Delta B}$, solar wind proton density n, and solar wind velocity magnitude V measured at the Apollo 12 site. All data are expressed in the surface coordinate system $(\hat{x}, \hat{y}, \hat{z})$ which has its origin at the Apollo 12 magnetometer site; $\hat{x}$ is directed radially outward from the surface while $\hat{y}$ and $\hat{z}$ are tangent to the surface, directed eastward and northward,

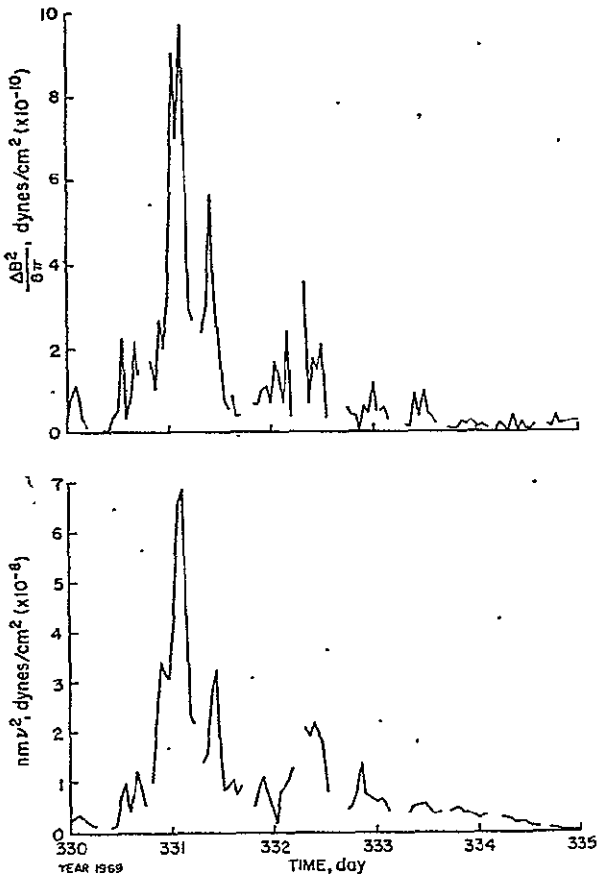

Figure 24.—*Simultaneous plots of the magnetic field pressure difference* $\Delta B^2/8\pi$ *and solar wind bulk pressure* nmv^2 *at the Apollo 12 surface site, showing the correlation between the pressures.*

ORIGINAL PAGE IS
OF POOR QUALITY

ORIGINAL PAGE IS
OF POOR QUALITY

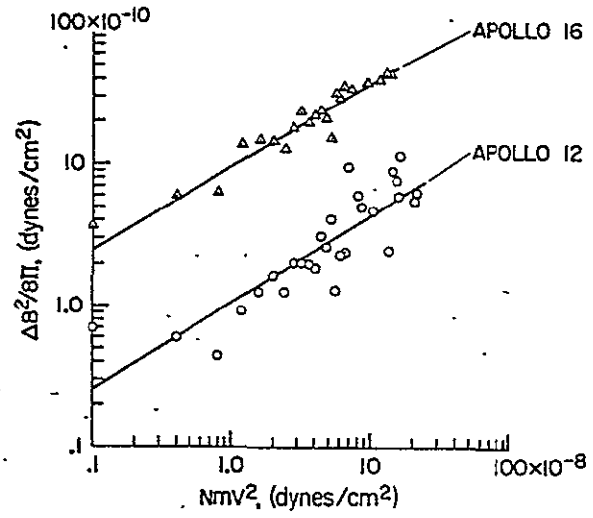

Figure 25.—*Magnetic energy density versus plasma energy density at two Apollo sites which have different remanent magnetic fields. Energies are defined in figure 24. Uncompressed remanent field magnitudes are 38 γ at Apollo 12 and 234 γ at Apollo 16. Apollo 12 magnetometer data are plotted versus Apollo 12 solar wind spectrometer (SWS) data, while Apollo 16 magnetometer data are plotted versus Apollo 15 SWS data. The SWS data are available by courtesy of C. W. Synder and D. R. Clay of the Jet Propulsion Laboratory.*

respectively. Components of the steady remanent field at the Apollo 12 site have been determined (ref. 38) to be $B_{Rx} = -25.8\ \gamma$, $B_{Ry} = +11.9\ \gamma$, and $B_{Rz} = -25.8\ \gamma$. By inspection we see a strong relationship between the magnitude ΔB and plasma proton density (n); no such strong correlation, however, is apparent between ΔB and velocity V alone.

The ratio of plasma pressure to total magnetic pressure is expressed

$$\beta = \frac{nmV^2}{B^2_{ST}/8\pi} \qquad (6)$$

where $\underline{B}_{ST} = \underline{B}_S + \Delta B$ is the total surface compressed field. During times of maximum plasma pressure shown in figure 24, we calculate $\beta = 5.9$; $\beta \leq 1$ would imply that the field had been compressed to the stagnation magnitude required to stand off the solar wind and possibly form a local shock. Compression of the remanent field alone therefore does not cause the stagnation condition to be reached during the time period of these data; however, at high frequencies the induced poloidal field $\underline{B}_P$ is also compressed ($\underline{\Delta B} = \underline{B}_P + \underline{B}_P$ in equation (3)), and thus it is possible that the stagnation pressure is reached for short time periods. Total surface fields of over 100 gammas have been observed (ref. 84) when large solar field transients pass the Moon; therefore a shock could be formed temporarily at the Apollo 12 site (as well as at the Apollo 14 and 16 sites).

The nature of the correlation between magnetic field and plasma pressures is further illustrated in figure 25, which shows data from several lunations at the Apollo 12 and 16 LSM sites. The pressures are related throughout the measurement range. The magnitudes of magnetic pressure changes at the Apollo 12 and Apollo 16 LSM sites are in proportion to their unperturbed steady field magnitudes of 38 γ and 234 γ, respectively.

Global Magnetization Induction: Magnetic Permeability and Iron Abundance

Magnetic permeability and iron abundance of the Moon are calculated by analysis of magnetization fields induced in the permeable material of the Moon. When the Moon is immersed in an external field it is magnetized; the induced magnetization is a function of the distribution of permeable material in the interior. Under the assumption that the permeable material in the Moon is predominately free iron and iron-bearing minerals, the lunar iron abundance can be calculated from the lunar permeability for assumed compositional models of the interior. Since the amount of iron present in the lunar interior should be consistent with the measured global magnetic permeability, the permeability in effect places a constraint on the physical and chemical composition of the Moon's interior.

GLOBAL MAGNETIC PERMEABILITY

Deployment of Apollo magnetometers on the lunar surface allowed simultaneous measurements of the external inducing field (by Explorer 25) and the total response field at the lunar surface (by an Apollo magnetometer). The total response field measured at the surface by an Apollo magnetometer is the sum of the external and induced fields:

$$\underline{B} = \mu \underline{H} = \underline{H} + 4\pi \underline{M} \qquad (7)$$

where $\underline{H}$ is the external magnetizing field and $\underline{M}$ is the magnetization field induced in the permeable lunar material (see fig. 26). The relative magnetic permeability is $\mu = 1 + 4\pi k$, where k is magnetic susceptibility in emu/cm³. Since the dipolar magnetization $\underline{M}$ is known to be below the Explorer 35 magnetometer resolution (ref. 8), it is assumed in the dual magnetometer analysis that Explorer 35 measures $\underline{H}$ alone.

For the two-layer lunar permeability model illustrated in figure 26 (which will be referred to later when iron abundance results are reviewed), the total field at the outer surface of the sphere is expressed

$$\underline{B} = H_x(1 + 2G)\hat{x} + H_y(1\text{-}G)\hat{y} + H_z(1\text{-}G)\hat{z} \qquad (8)$$

where

$$G = \frac{(2\eta + 1)(\mu_1 - 1) - \lambda^3(\eta - 1)(2\mu_1 + 1)}{(2\eta + 1)(\mu_1 + 2) - 2\lambda^3(\eta - 1)(\mu_1 - 1)} \qquad (9)$$

Here $\eta = \mu_1/\mu_2$; μ_1 and μ_2 are relative permeability of the shell and core, respectively. The permeability exterior to the sphere is $\mu_o = 1$, that of free space; $\lambda = R_c/R_m$; R_c and R_m are radius of the core and the Moon, respectively. Equation (8) expresses the total surface field in a coordinate system which has its origin on the lunar surface at an Apollo magnetometer site: $\hat{x}$ is directed radially outward from the lunar surface, and $\hat{y}$ and $\hat{z}$ are tangential to the surface, directed eastward and northward, respectively.

A plot of any component of equation (8) will result in a B–H hysteresis curve. Equation (9) relates the slope of the hysteresis curve to the lunar permeability. The average whole-Moon permeability μ is calculated from the hysteresis-curve slope by setting $\mu_1 = \mu_2 = \mu$ in equation (9):

$$G = \frac{\mu - 1}{\mu + 2} \qquad (10)$$

The hysteresis-curve method of permeability analysis was first employed by Dyal and Parkin (ref. 38) to calculate the whole-Moon permeability result 1.03 ± 0.13. Since then the error limits have been lowered by processing a larger number of simultaneous data sets and using more rigid data selection criteria (e.g., ref. 85).

In the most recent dual-magnetometer results (refs. 32 and 33), a hysteresis curve was constructed with 2703 data sets (see fig. 27). Since the external magnetizing field is so small (~ 10 gammas), the familiar "S" shape of the hysteresis curve degenerates to a straight line (ref. 86). The data were fit by a least-squares technique which yields the

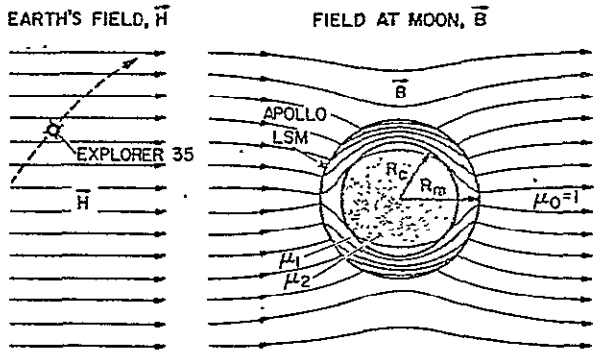

Figure 26.—*Magnetization induction in the Moon. When the Moon is immersed in a uniform external field* H *(in this case the steady geomagnetic tail field), a dipolar magnetization field* M *is induced in permeable material in the lunar interior, with the dipole axis of* M *aligned along the direction of* H. *The total magnetic field near the Moon is* B = H + 4 πM. *The magnetic permeabilities of the two layers are* μ_1 *and* μ_2, *and for regions outside the Moon,* $\mu = \mu_o = 1$ *(free space).* H *is measured by the lunar orbiting Explorer 35, whereas* B *is measured by an Apollo lunar surface magnetometer (LSM). Measurements of* B *and* H *allow construction of a* B-H *hysteresis curve for the sphere, from which permeability and iron abundance can be calculated.*

slope best-estimate of 1.008 ± 0.004. By use of this value with the radial (x) component of equation (8) and equation (10), the whole-Moon permeability was calculated to be $\mu = 1.012 \pm 0.006$ (2σ error limits). Both extremes are greater than 1.0, implying that the Moon, as a whole, acts as a paramagnetic or weakly ferromagnetic sphere. This result has been used to calculate the iron abundance of the Moon as discussed in the next section.

Russell et al. (ref. 34) have recently made permeability calculations using data from a single magnetometer, the Apollo 15 subsatellite magnetometer orbiting at an altitude about 100 km above the Moon. The results indicate that the relative permeability of the entire spherical volume enclosed by the satellite orbit is below 1.0, implying that the layer between the Moon and the satellite orbit is diamagnetic. The charged particles measured on the lunar surface by the Rice University suprathermal ion detector experiments (ref. 87) may be from a lunar ionosphere. If an ionosphere fills the entire region between the lunar surface and the subsatellite at 100 km altitude, the interior global lunar permeability would be higher than that calculated under the assumption of no ionosphere. The lunar permeability value of Parkin et al. (ref. 32) would be adjusted upward from 1.012 to 1.017, provided there exists a lunar ionosphere compatible with the measurements of Russell et al. (ref. 34). The corresponding free iron abundance value would be 3.9 instead of 2.5 wt.%. The existence of a lunar ionosphere is uncertain at present; further investigation is required, using both magnetic and plasma data.

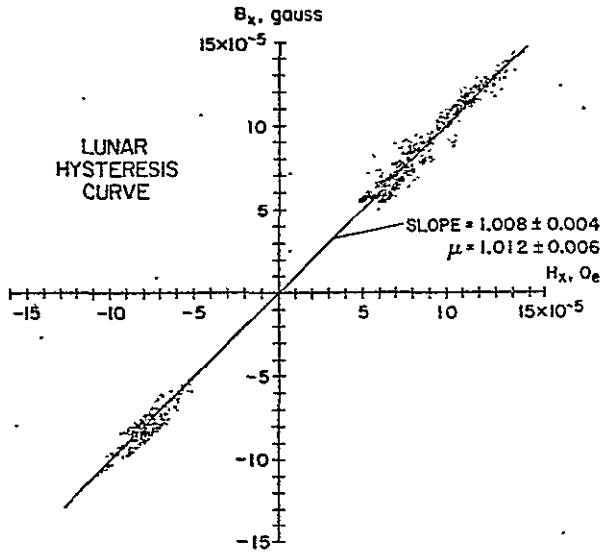

Figure 27.—*Hysteresis curve for the Moon. Data points are 2703 simultaneous 2-minute averages of radial components of the external geomagnetic field data* H *(measured by the lunar orbiting Explorer 35 Ames magnetometer) and total magnetic induction* B = μH *(*B *is measured by the Apollo 12 lunar surface magnetometer). Data points are selected from four lunations of measurements made when the Moon is immersed in the uniform geomagnetic tail field, far from the neutral sheet in the tail. In this low-external-field regime (~ 10 gammas or 10^{-1} Oe), the hysteresis curve is linear and is fitted by a least-squares line of slope 1.008 ±0.004. This slope corresponds to a whole-Moon magnetic permeability of 1.012 ± 0.006. The least-squares line intersects the origin exactly in this figure because the vertical-axis intercept (the radial or x-component of the remanent field at the Apollo 12 site) was subtracted out after the least-squares fit was made.*

LUNAR IRON ABUNDANCE

Iron abundance calculations have been presented by various authors, in theoretical treatments based on geochemical and geophysical properties calculated for bodies of planetary size (refs. 88, 89, and 90) or on measured compositions of meteorites (ref. 91). Recently Parkin et al. (refs. 32, 33, and 85) have used a global lunar permeability measurement, determined from magnetic field measurements, to calculate lunar iron abundance for the Moon. In their calculations the Moon is modeled by a homogeneous paramagnetic rock matrix (olivine and orthopyroxene models are used), in which free metallic iron is uniformly distributed. Pyroxenes and olivines have been reported to be major mineral components of the lunar surface fines and rock samples (refs. 18, 92, and 93), with combined iron present as the paramagnetic Fe^{2+} ion. The ferromagnetic

ORIGINAL PAGE IS
OF POOR QUALITY

ORIGINAL PAGE IS OF POOR QUALITY

component of lunar samples is primarily metallic iron which is sometimes alloyed with small amounts of nickel and cobalt (refs. 17 and 19). This free iron is thought to be native to the Moon (because of its low nickel content) rather than meteoritic in origin (ref. 71). Orthopyroxene and olivine models are consistent with geochemical studies (refs. 94–97) and geophysical studies (ref. 98).

Since the susceptibility of free iron changes several orders of magnitude at the iron Curie temperature (T_c), Parkin et al. have used a two-layer model with the core-shell boundary R_c at the Curie isotherm (see fig. 26). For $R > R_c$, $T < T_c$, and for $R \leq R_c$, $T > T_c$. Therefore, for $R > R_c$ any free iron is ferromagnetic while at greater depths where $T > T_c$, the free iron is paramagnetic. The Curie isotherm location is determined from the thermal profile used for a particular model. Three thermal models have been used in the calculations. For model profile T_1 the Curie isotherm is spherically symmetric and located at $R_c/R_m = 0.9$. Shell and core temperatures are 600° C and 1400° C, respectively. For the model profile T_2 the shell is 500° C and the core is 1300° C, while the Curie isotherm boundary is at $R_c/R_m = 0.85$. Temperatures are 300° C and 700° C for shell and core of model profile T_3, which has $R_c/R_m = 0.7$. In the outer shell there are both ferromagnetic and paramagnetic contributions to the total magnetic permeability $\mu_1 = 1 + 4\pi k_1$. The susceptibility of the shell is $k_1 = k_{1c} + k_{1a}$, where k_{1a} is "apparent" ferromagnetic susceptibility and k_{1c} is paramagnetic susceptibility. The ferromagnetic component is metallic free iron, assumed to be composed of multidomain, noninteracting grains; the paramagnetic component is Fe^{2+} combined in the orthopyroxene or olivine rock matrix. The measured ferromagnetic susceptibility of the shell material is an apparent value which differs from the intrinsic ferromagnetic susceptibility of the iron because of self-demagnetization of the iron grains and the volume fraction of iron in the shell. For $R < R_c$ the lunar material is paramagnetic only, with susceptibility $k_2 = k_{2c} + k_{2c}$; k_{2c} is the contribution of paramagnetic chemically combined iron, and k_{2a} is the apparent susceptibility of free paramagnetic iron above the Curie temperature.

Using the information described in the previous paragraphs, Parkin et al. (ref. 33) have generated the curves shown in figure 28, which relate free iron abundance (q) and total iron abundance (Q) to the hysteresis-curve slope. The results are summarized in table 3 and figure 29. The *minimum* total iron abundance consistent with the hysteresis curve can be calculated assuming the whole-Moon permeability corresponds

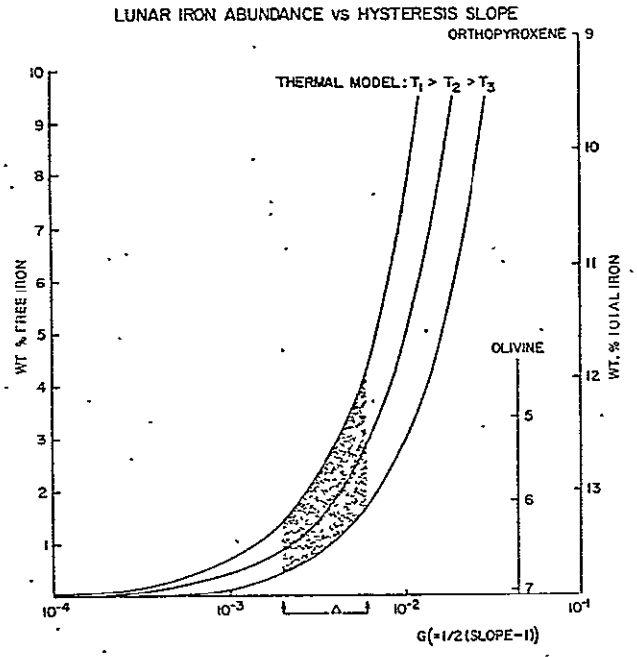

Figure 28.—*Iron abundance in the Moon as a function of global hysteresis curve slope. Free iron abundance (q) and total iron abundance (Q) versus the parameter G (hysteresis curve slope equals 2G + 1) for three temperature profiles described in the text. Total iron abundance is shown for two lunar composition models, orthopyroxene and olivine. Arrows below the horizontal axis show the range of the parameter G, experimentally determined from the hysteresis curve slope: G = 0.004 ± 0.002. The shaded region defines the allowed values of free and total iron abundances, bounded by hysteresis curve error limits and by thermal models T_1 and T_3.*

Table 3.—*Iron Abundance of the Moon as a Function of Thermal and Compositional Models*

Compositional Model \ Thermal Model	Free Iron Abundance, weight percent			Total Iron Abundance, weight percent		
	T_3	T_2	T_1	T_3	T_2	T_1
Orthopyroxene	1.0 ± 0.5	2.0 ± 1.0	3.0 ± 1.5	13.4 ± 0.3	13.0 ± 0.5	12.6 ± 0.6
Olivine	1.0 ± 0.5	2.0 ± 1.0	3.0 ± 1.5	6.5 ± 0.3	5.9 ± 0.7	5.3 ± 1.0

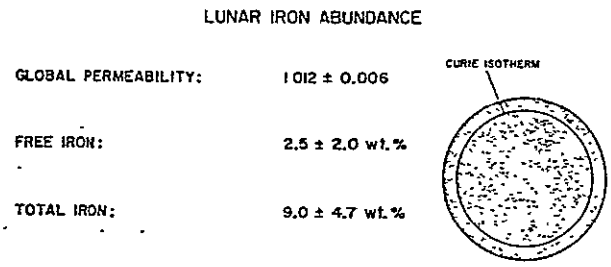

Figure 29.—*Summary of global lunar magnetic permeability, free iron abundance, and total iron abundance.*

entirely to ferromagnetic iron in the outer shell where the temperature is below the Curie point. For this case the bulk iron abundance is 0.9 + 0.5 wt.%. It is noted that the susceptibilities of both olivine and pyroxene are about an order of magnitude too small to account for the measured permeability without some ferromagnetic material present.

CONSIDERATIONS OF AN IRON CORE AND IRON-RICH LAYER

The whole-Moon permeability has also been used by Parkin et al. (ref. 32) to investigate the magnetic effects of a hypothetical iron core in the Moon. Density and moment of inertia measurements for the Moon limit the size of such a core to less than 500 km in radius (ref. 98). If this hypothetical iron core were entirely paramagnetic and the surrounding core were orthopyroxene of average temperature 1100° C the global permeability would be 1.0003. This value is small compared with the measured permeability of 1.012 ± 0.006, implying that if such a small paramagnetic iron core exists, its magnetization is masked by magnetic material lying nearer to the surface. Therefore, the hysteresis measurements can neither confirm nor rule out the existence of a small iron core in the Moon.

An iron-rich layer in the Moon has been considered by several investigators (refs. 94, 95, and 99). It is possible that early melting and subsequent differentiation of the outer several hundred kilometers of the Moon may have resulted in the formation of a high-density, iron-rich layer beneath a low-density, iron-depleted crust. Constraints have been placed on an iron-rich layer by Gast and Giuli (ref. 99) using geochemical and geophysical data (for example, measurements of lunar moments of inertia). One set of their models consists of high-density layers between depths of 100 km and 300 km. At a depth of 100 km the allowed layer thickness is 12 km; the thickness increases with increasing depth, to 50 km at 300-km depth. Also presented is a set of layers at 500-km depth. Using exactly the same considerations as were used in the iron abundance calculations, Parkin et al. have

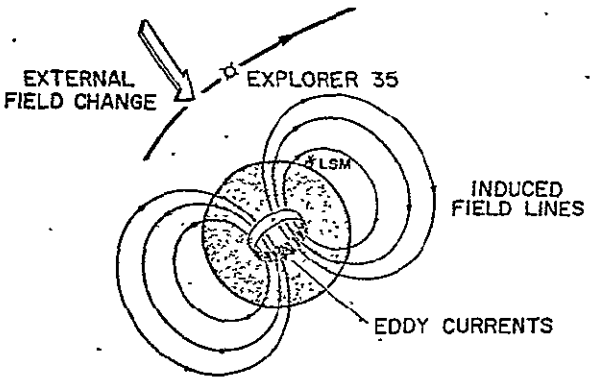

Figure 30.—*Global eddy-current induction: Moon in the geomagnetic tail. The induced poloidal field experiences greatly reduced plasma effects, especially in deep-lobe regions of the tail far from the neutral sheet. The poloidal field is considered to be an unconfined (vacuum) dipole field for analytical purposes.*

calculated whole-Moon permeabilities which would be expected from lunar models with these iron-rich layers. The calculations indicate that all iron-rich layers allowed by geophysical constraints as outlined by Gast and Giuli, if wholly above the iron Curie temperature, would yield global permeabilities of about 1.00006. As for the case of a small lunar iron core, the magnetization field of such paramagnetic layers would be masked by ferromagnetic materials elsewhere in the Moon, and the hysteresis curve measurements can neither confirm nor rule out these layers. This conclusion would particularly apply to the Gast-Giuli layers at 500-km depths, which are almost certainly paramagnetic. If the iron-rich layers are below the Curie temperature and therefore ferromagnetic, they yield global permeabilities of about 3.5. This is above the upper limit for the measured permeability of 1.012 ± 0.006 and the Gast-Giuli layers can be ruled out if they are cool enough to be ferromagnetic. It is important to realize that the high-density layers discussed by Gast and Giulu (ref. 99) can be thought of as limiting cases and that there are innumerable less dense and thinner layers which are allowed by geophysical, geochemical, and magnetic constraints.

Global Eddy-Current Induction: Electrical Conductivity and Temperature

Electrical conductivity and temperature of the Moon have been calculated from global eddy-current response to changes in the magnetic field external to the Moon. When the Moon is subjected to a change in the external field, an eddy-current field is induced in the Moon which opposes the change (see fig. 30). The induced field responds with a time dependence which is a function of the electrical conductivity distribution in the lunar interior. Simultaneous measurements of the transient driving field (by Explorer 35) and the lunar response field (by an Apollo surface magnetometer) allow calculation of the lunar conductivity. Since conductivity is related to temperature, a temperature profile can be calculated for an assumed compositional model of the lunar interior.

When the Moon is in the solar wind, lunar

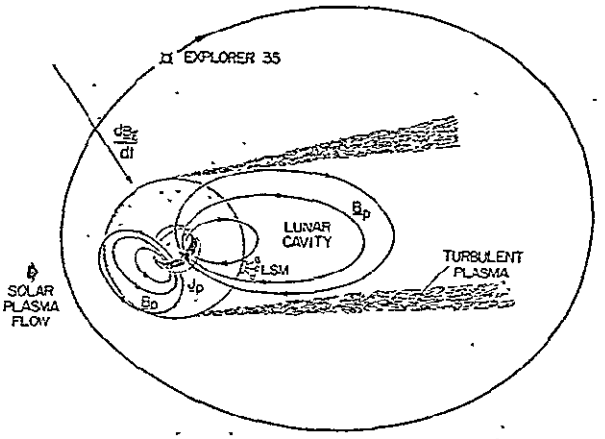

Figure 31.—*Global eddy-current induction: Moon in the solar wind. Eddy currents and corresponding poloidal magnetic fields are induced by response to time-dependent fluctuations in the external field* B_E. *The poloidal field has different characteristics, depending on the Moon's environment. When the Moon is in the solar wind, the global induced field is asymmetrically confined by the solar wind flowing past the Moon; the field is compressed on the day (sunlit) side and confined to the cavity region on the night (antisolar) side of the Moon.*

ORIGINAL PAGE IS
OF POOR QUALITY

eddy-current fields form an induced lunar magnetosphere which is distorted in a complex manner due to flow of solar wind plasma past the Moon. The eddy-current field is compressed on the dayside of the Moon and is swept downstream and confined to the "cavity" on the lunar nightside (see fig. 31). Because of the complexity, early analysis included a theory for transient response of a sphere in a vacuum in order to model lunar response as measured on the lunar nightside (refs. 43, 44, and 100). The transient technique has subsequently been further developed to include effects of cavity confinement on nightside tangential data and to introduce analysis of magnetic step transients measured on the lunar dayside (refs. 45 and 51). Recently time-dependent poloidal response of a sphere in a vacuum has been applied to data measured in the geomagnetic tail (refs. 72 and 101) where plasma confinement effects are minimized. The poloidal response analysis has been used to determine the electrical conductivity and temperature profiles of the lunar interior.

ELECTRICAL CONDUCTIVITY ANALYSIS: MOON IN SOLAR WIND PLASMA

Lunar Nightside Data Analysis

The lunar electrical conductivity has been investigated by analysis of the lunar response to transients in the solar wind magnetic field. The response, measured by an Apollo

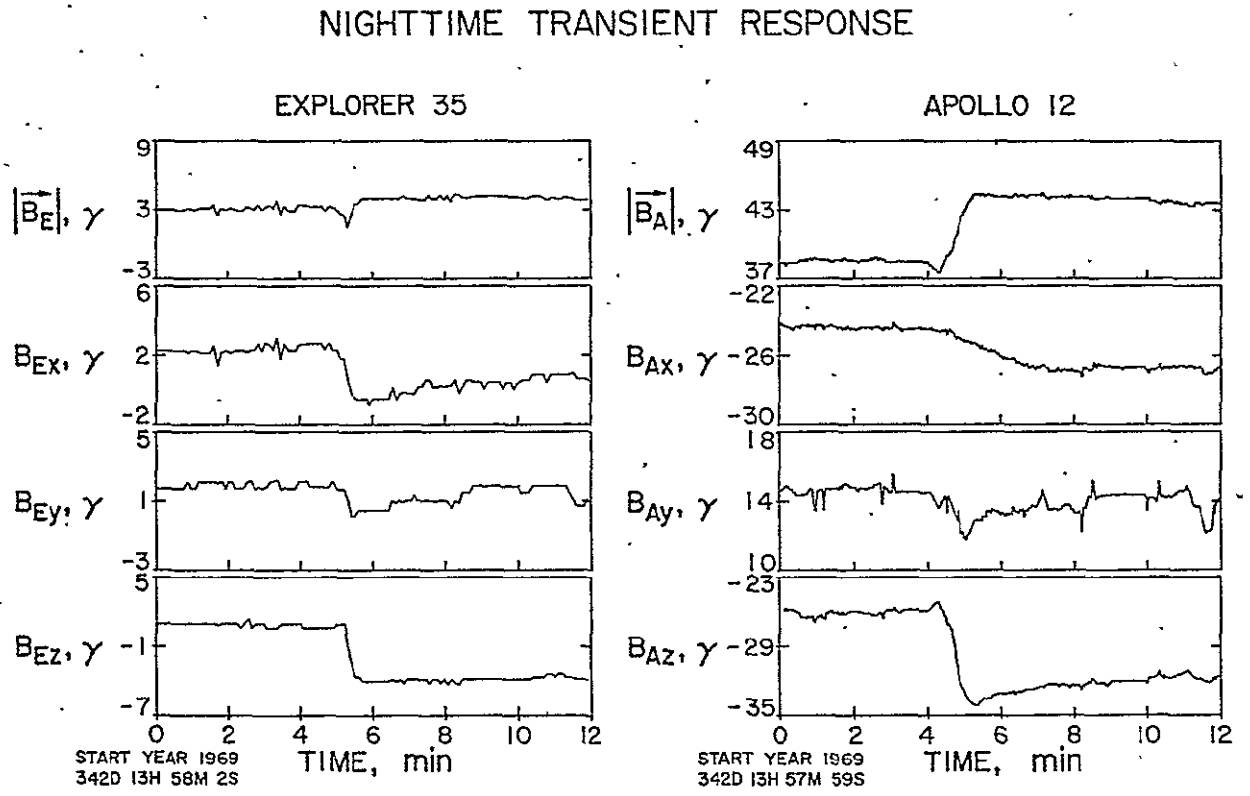

Figure 32.—*Nighttime transient response magnetic field data. A transient measured by an Apollo LSM while on the nighttime (antisolar) side of the Moon, showing simultaneous external solar wind field data measured by Explorer 35. Data are expressed in the surface coordinate system which has its origin at the Apollo 12 magnetometer site; $\hat{x}$ is directed radically outward from the surface, while $\hat{y}$ and $\hat{z}$ are tangent to the surface, directed eastward and northward, respectively.*

magnetometer on the nightside of the Moon, is theoretically approximated by the response of a conducting sphere in a vacuum. The theory has been developed by extending the work of Smythe (ref. 39) and Wait (ref. 40) for a radially varying lunar conductivity profile (ref. 102). Figure 32 shows an example of an event in which a transient in the external solar wind magnetic field is measured simultaneously by the Explorer 35 Ames magnetometer and an Apollo surface magnetometer. The transient is essentially a rotation in the external field, as indicated by the near-constancy of the field magnitude $|\underline{B}_E|$ measured by Explorer 35. Simultaneous field data ($\underline{B}_A$), measured on the nightside of the Moon by the Apollo 12 lunar surface magnetometer, are the vector sum of the external driving field $\underline{B}_E$, the induced eddy-current poloidal field $\underline{B}_P$, and the constant remanent field $\underline{B}_R$ (see equation (4)). Again, the field components are expressed in a coordinate system which has its origin located at the Apollo LSM site on the lunar surface; $\hat{x}$ is directed radially outward from the Moon, and $\hat{y}$ and $\hat{z}$ are tangential to the lunar surface, directed eastward and northward, respectively.

Figure 33 shows averages of radial components of the measured response field (B_{Ax}) for eleven normalized transient events of the type illustrated in figure 32. Error bars are standard deviations of the measured responses.

For models of the interior of the Moon a family of conductivity profiles (all of which monotonically increase with depth in the Moon), the theoretical response to a fast ramp is calculated and compared with the measured response. For this analysis the external field transient is represented by a ramp input function which falls from unity

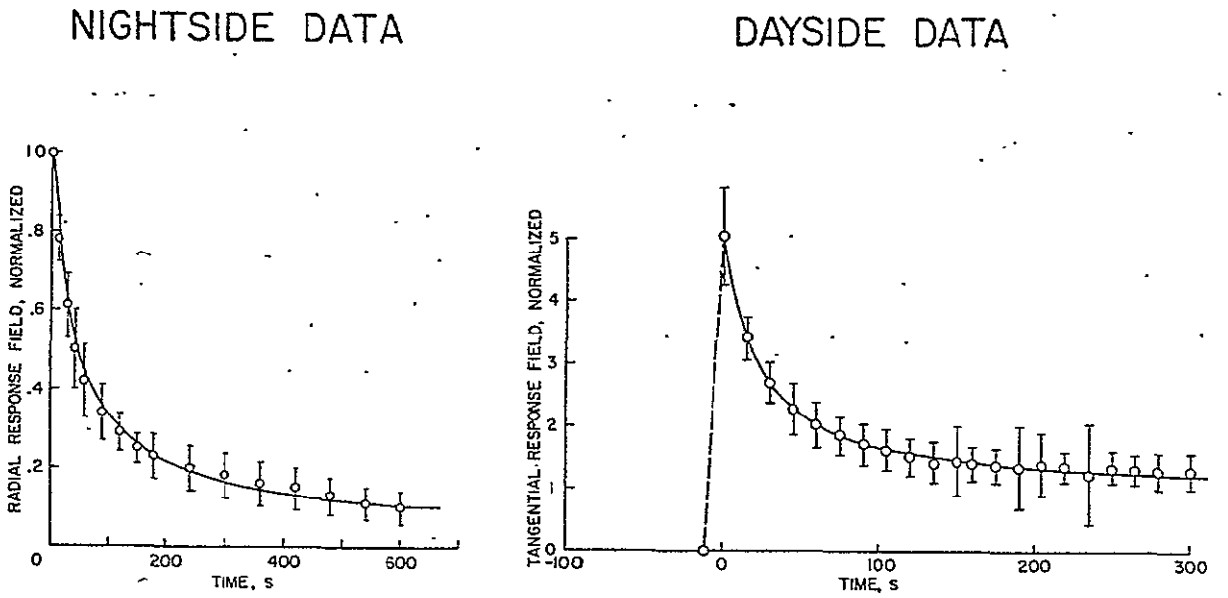

Figure 33.—*Normalized averages of transient response data, measured when Moon was in the solar wind. (a) Nightside transient response data, showing decay characteristics of the radial component of the total surface field* B_{Ax} *after arrival of a step transient which* reduces *the external magnetic field radial component by an amount* ΔB_{Ex}, *here normalized to one. The shape of the curve illustrates time characteristics of the decay of the induced poloidal eddy-current field. (b) Daytime transient response data, showing decay characteristics of tangential components* ($B_{Ay,z}$) *of the total surface field after arrival of a step transient which* increases *the external magnetic field tangential component by an amount* $\Delta B_{Ey,z}$, *here normalized to one. Shape of the curve again illustrates decay characteristics of the induced poloidal field. The overshoot maximum is amplified to ~ 5 by solar wind dayside compression; the theoretical overshoot maximum is 1.5 for an unconfined poloidal field.*

to zero in 15 seconds, a time characterizing convection of a solar wind dicontinuity past the Moon. (For a 400 km/s solar wind, this time is 10–20 seconds, depending on the thickness of the discontinuity and the inclination of its normal to the solar wind velocity.) The input field is constant before and after the field change. A particular set of conductivity profiles yield response functions which pass within all data error bars of figure 33. These profiles define the shaded region of figure 34 and are all consistent with the nightside response data.

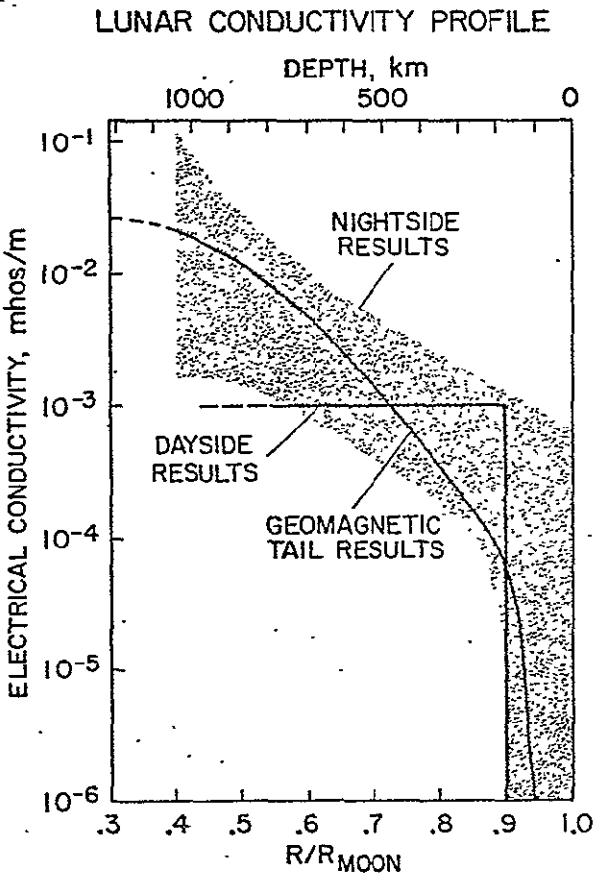

Figure 34.—*Electrical conductivity profiles for the lunar interior calculated from measurements in different regions of the lunar orbit around the Earth. The shaded region is from analysis of nightside transient data averages shown in figure 33 (a). The dayside conductivity profile is calculated by fitting totally confined two-layer Moon models to the dayside tangential component data illustrated in figure 33 (b). The curve labeled "geomagnetic tail results" is a profile consistent with analysis of transients in the geomagnetic tail lobes such as events illustrated in figures 37 and 39. Errors associated with this latter curve are approximately the same as the conductivity band shown for the nightside results.*

Lunar Dayside Data Analysis

Induced lunar eddy-current fields are confined, by the highly conducting solar wind, to the inside of the Moon and a small region above the lunar surface on the lunar dayside and to a "cavity" region on the nightside. Due to the complexity of the confinement, the conductivity analysis of transient magnetometer data measured on the lunar dayside has involved modeling the Moon by a sphere of homogeneous conductivity; the induced eddy-current field B_P is considered to be totally confined inside the lunar sphere (ref. 45). Figure 35 shows an example of a transient event in the solar wind magnetic field which is measured on the lunar dayside. Figure 33 shows averages of tangential components of response fields, measured on the lunar dayside, induced in response to rising fast-ramp transients in the free-streaming solar wind (error bars are standard deviations). The overshoot maximum is amplified by a factor of 5 over the external input field step change, by solar wind dayside confinement of the surface tangential field components. The data are fit by a lunar conductivity model with a homogeneous core of radius $R_c = 0.9\,R_m$ and conductivity $\sigma \sim 10^{-3}$mhos/m. This result is consistent with the nightside conductivity profile illustrated in figure 34 to depths allowed by the duration of the response data which is shown in figure 33.

The theoretical models outlined so far have all assumed spherical symmetry to describe lunar eddy-current response to changes in the external field. However, the nightside and dayside analyses have used data taken when the Moon was immersed in the solar wind plasma with asymmetric confinement of the inducing fields. The shortcomings of using spherically symmetric approximations to describe the induced lunar magnetosphere,

ORIGINAL PAGE IS OF POOR QUALITY

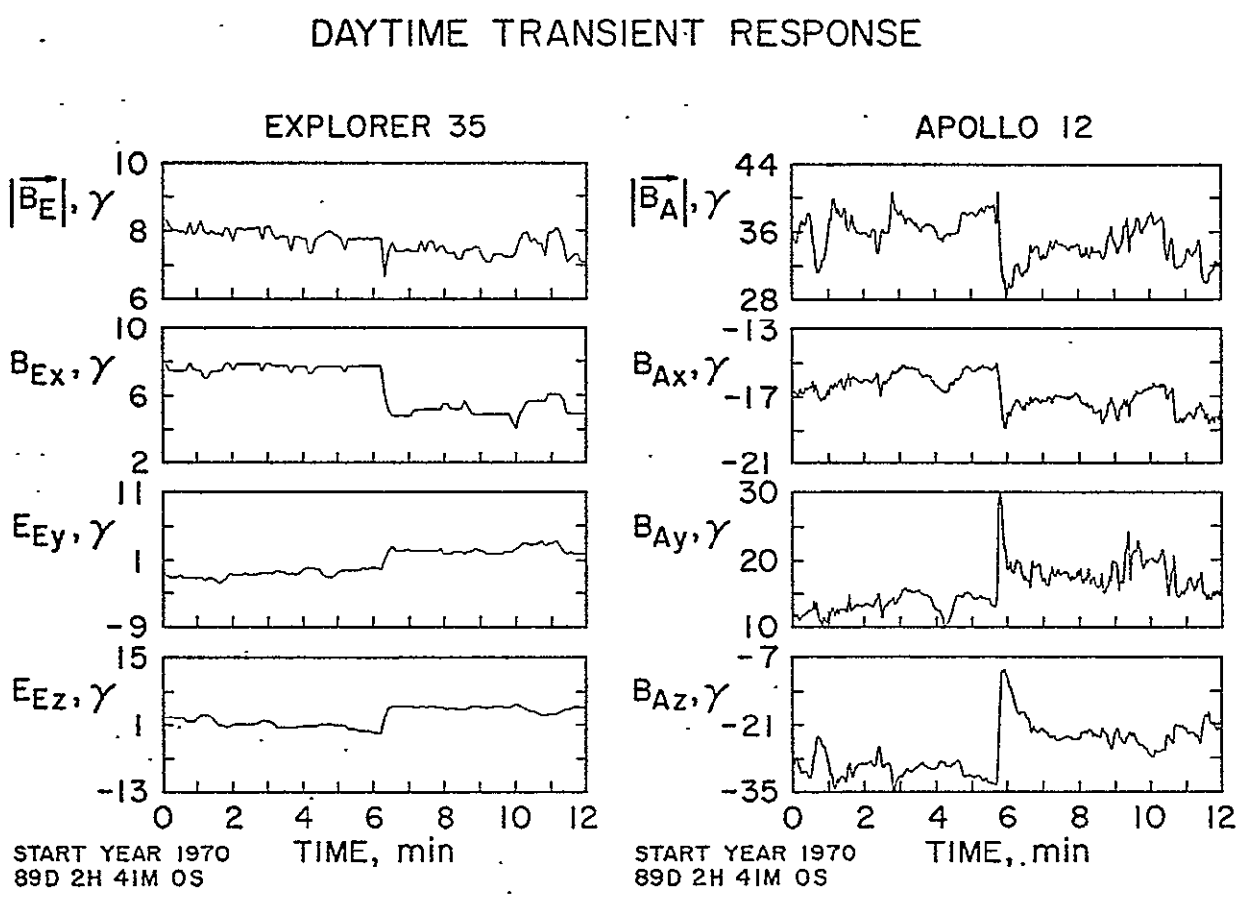

Figure 35.—*Daytime transient response magnetic field data, measured by an Apollo LSM while on the dayside (subsolar side) of the Moon, showing simultaneous external solar wind field data measured by lunar orbiting Explorer 35. The coordinate system is defined in the text. Note in particular the tangential components: dayside overshoot amplification is much higher relative to the Explorer-measured external step magnitudes than is nighttime amplification (shown in fig. 32).*

which is actually asymmetrically confined, have been pointed out in the literature for both the nightside vacuum approximation (see, e.g., ref. 52) and the dayside totally confined approximation (see e.g. ref. 51) Three-dimensional, dynamic asymmetric confinement presents a difficult theoretical problem which has not been solved at the time of this writing. Previous theoretical approximations of the asymmetric problem have included a two-dimensional approximation (ref. 50); three-dimensional static theory for a point-dipole source, with substantiating laboratory data (ref. 51); a three-dimensional dynamic theory for particular orientations of variations in the external field (ref. 103).

The confinement of the induced poloidal field by the highly conducting solar wind has been studied in the laboratory by considering a point-dipole field inside a superconducting cylinder (ref. 51). Two geometrical orientations of the point dipole have been considered: along the cylinder axis, and transverse to the cylinder axis. (See inserts in figure 36 for an illustration of these orientations.) The fields of the dipole-oriented transverse and axial with respect to the cylinder axis have been determined following Parker (ref. 104) and P. Cassen (private communication). The highly conducting solar wind plasma cavity is modeled by a thin lead superconducting capped cylinder and the instantaneous induced poloidal field is modeled by a small

C-2

dipolar samarium-cobalt magnet placed equidistant from the closed end and the side walls of the cylinder. The measured ratios of confined fields to unconfined fields are shown in figure 36. The theory and laboratory data presented in figure 36 represent to first order the effects of solar wind compression on a poloidal induced lunar field, as measured by a lunar surface magnetometer positioned at the antisolar point.

ELECTRICAL CONDUCTIVITY ANALYSIS: MOON IN THE GEOMAGNETIC TAIL

In order to circumvent the problem of asymmetry, recent analyses (refs. 72 and 101) have considered lunar eddy-current response during times when the Moon is in the geomagnetic tail where plasma interaction effects encountered in the solar wind (asymmetric confinement, remanent field compression, plasma diamagnetism, etc.) are minimal.

Poloidal Response of a Sphere in a Vacuum: Theory

In the conductivity profile analysis we assume that plasma effects are negligible in the lobe regions of the geomagnetic tail, and that the response of the Moon can be represented as that of a conducting sphere in a vacuum. To describe the response of a lunar sphere to an arbitrary input field in the geomagnetic tail, we define the magnetic vector potential $\underline{A}$ such that $\underline{\nabla} \times \underline{A} = \underline{B}$ and $\underline{\nabla} \cdot \underline{A} = 0$. We seek the response to an input $\underline{\Delta B_E} b(t)$, where $b(t) = 0$ for $t < 0$ and $b(t)$ approaches unity as $t \to \infty$. The direction of $\underline{\Delta B_E}$ is taken to be the axis of a spherical coordinate system (r,θ,ϕ). If the conductivity is spherically symmetric, the transient magnetic field response has no ϕ component,

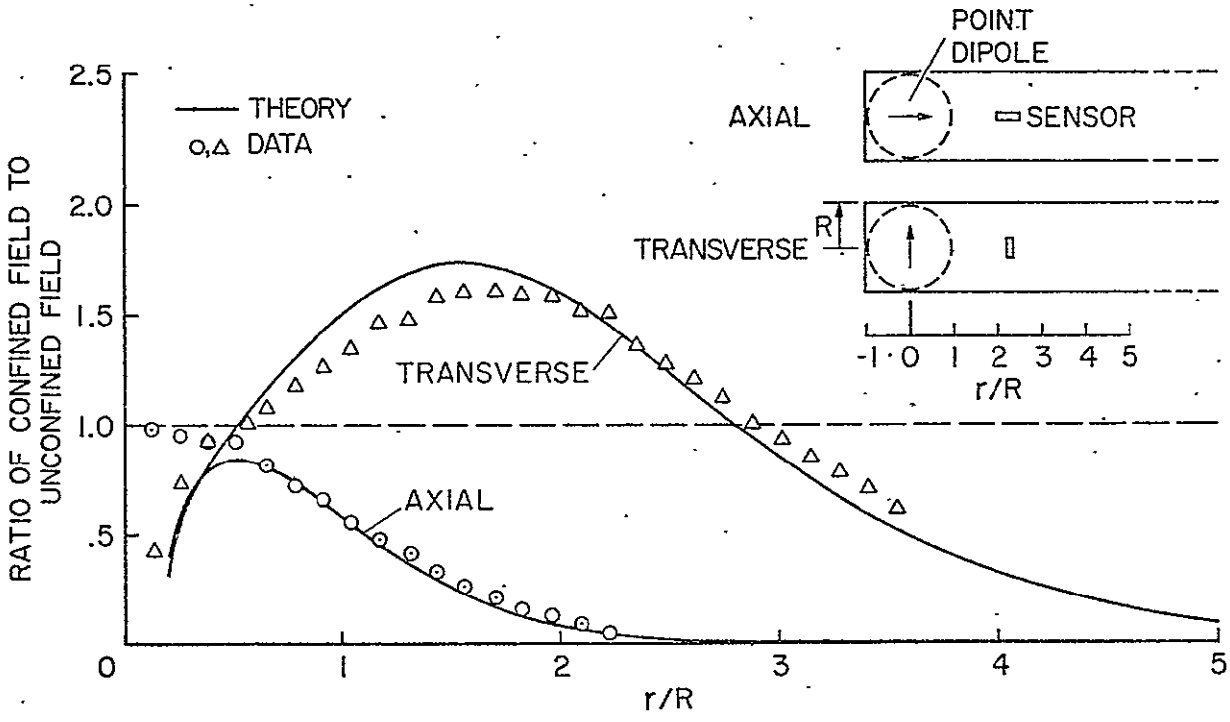

Figure 36.—*Confinement of a point dipole magnetic field, shown theoretically and experimentally. The inserts schematically show lunar confinement by the solar wind, approximated by a capped-cylinder superconductor enclosing a point dipole field. The theoretical curves show ratios of a confined to an unconfined dipolar field versus distance along the cylinder axis. Data are results of a laboratory experiment in which confinement of a small dipole magnet's field by a cylindrical superconductor is measured experimentally.*

and hence $\underline{A} = A\hat{e}_\phi$ and $\partial/\partial\ \phi = 0$. Under these conditions (and neglecting displacement currents) the laws of Faraday, Ampere, and Ohm combine to yield a diffusion equation (ref. 102) for the magnetic potential (in MKS units):

$$\Delta^2 \underline{A}\ (r, \theta; t) = \mu\, \sigma\ (r) \frac{\partial \underline{A}}{\partial t}(r, \theta; t) \quad (11)$$

From magnetization induction analysis it is shown that $\mu \cong \mu_o$, that of free space (ref. 32). Then, for $t > 0$, the magnetic field must be continuous at the surface, so that $\underline{A}$ and $\partial \underline{A}/\partial r$ must always be continuous at $r = R_m$, the radius of the sphere. We also have the boundary condition $\underline{A}\ (0,t) = 0$ and the initial condition $\underline{A}\ (r, \theta, \phi) = 0$ inside the Moon. Outside the Moon, where $\sigma = 0$,

$$A = \Delta B_E \left(\frac{r}{2}\right) b(t)\ \sin\theta + \frac{\Delta B_E}{r^2} f\ (t)\ \sin\theta. \quad (12)$$

The first term on the right is a uniform magnetic field modulated by $b(t)$; the second term is the (as yet unknown) external transient response, which must vanish as $r \to \infty$, and $t \to \infty$. Note that at $r = R_m$ where R_m is normalized to unity,

$$A = \Delta B_E \sin\theta \left(\frac{b(t)}{2} + f(t)\right) \quad (13)$$

and

$$\frac{\partial A}{\partial r} = \Delta B_E \sin\theta \left(\frac{b(t)}{2} - 2f(t)\right). \quad (14)$$

Therefore, at $r = R_m = 1$,

$$\frac{\partial A}{\partial r} = -2A + \frac{3}{2}\left(\Delta B_E \sin\theta\, b(t)\right). \quad (15)$$

Since the magnetic field is continuous at $r = r_m$, this is a boundary condition for the interior problem. Letting $G(r,t) = A/\ \Delta B_E \sin\theta$ and $\overline{G}(r,s)$ be the Laplace transform

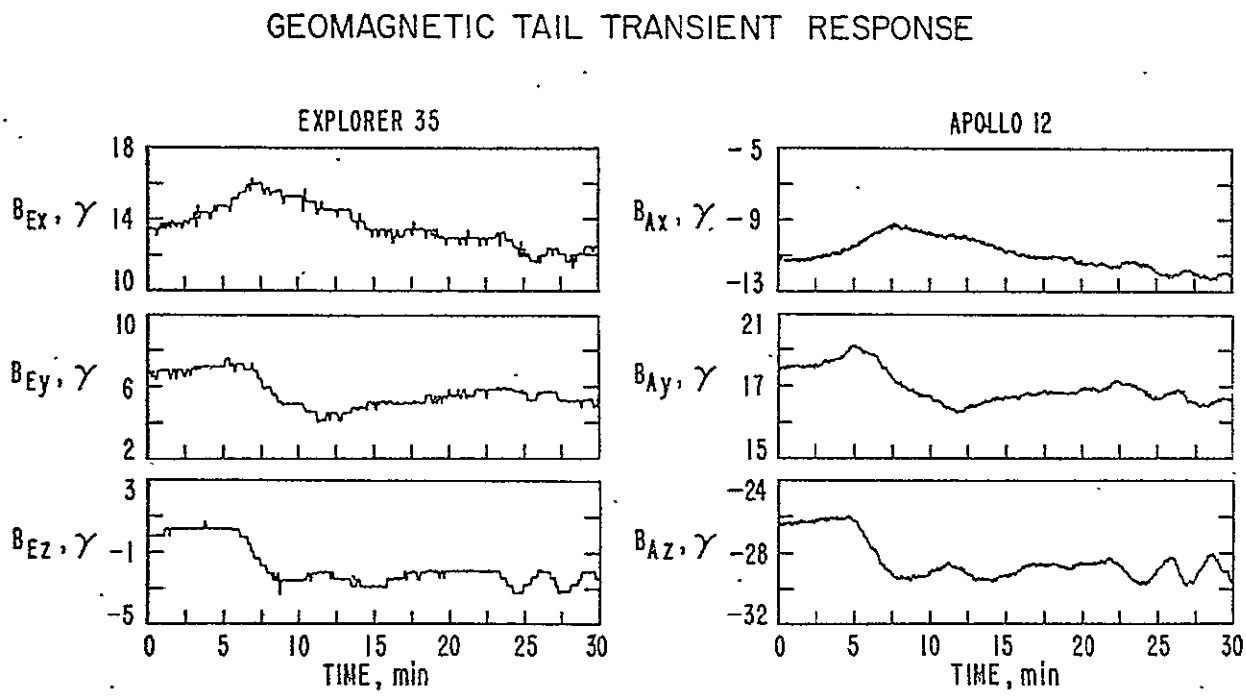

Figure 37.—*Magnetic transient event measured simultaneously by the Apollo 12 LSM and the Explorer 35 Ames magnetometer deep in the north lobe of the geomagnetic tail. Data are expressed in the surface coordinate system which has its origin at the Apollo 12 magnetometer site; x is directed radially outward from the surface, while y and z are tangent to the surface, directed eastward and northward, respectively. Due to poloidal field induction in the Moon, the Apollo 12 radial ($\hat{x}$) component is "damped" relative to the Explorer 35 radial component, whereas the Apollo 12 tangential ($\hat{y}$ and $\hat{z}$) field components are "amplified" relative to Explorer 35 data.*

of $\bar{G}$, equation (1) becomes

$$\frac{1}{r}\left(\frac{\partial^2}{\partial r^2}(r\bar{G}) - \frac{2}{r}\bar{G}\right) = s\mu_0\sigma(r)\bar{G} \quad (16)$$

for the interior. The boundary conditions are

$$\frac{\partial \bar{G}}{\partial r} = -2\bar{G} + \frac{3}{2}\bar{b}(s) \quad (17)$$

at $r = R_m$ and $\bar{G} = 0$ (18)

at $r = 0$.

Since the governing equations are linear, the response to a general time-dependent input function can be found by superposition of solutions as follows. The individual input function (that is, external field transient event measured by Explorer 35) is approximated by a succession of ramp functions $b_i(t)$. For each $b_i(t)$ and the given conductivity profile $\sigma(r)$, the above system of equations is numerically integrated to obtain $\bar{G}_i(r,s)$ in the range $02 \leq r \leq R_m$. The function $\bar{G}_i(r,s)$ is then numerically inverse Laplace transformed to find the characteristic transient response $f_i(t)$ for the system. Then the individual functions $f_i(t)$ are superposed to calculate the final time response function $F(t)$ corresponding to the arbitrary input function and $\sigma(r)$. This calculated time series response is compared with the measured time series response (Apollo magnetometer data) and iterated with a different function $\sigma(r)$ until the error between the calculated $F(t)$ and the measured $F(t)$ is minimized.

Conductivity Results: Geomagnetic Tail Data Analysis

Figure 37 shows an example of a magnetic transient measured in the northward lobe of the geomagnetic tail. The data components are expressed in a coordinate system which has its origin on the lunar surface at the Apollo 12 magnetometer site. Again the x-component is directed radially outward from the lunar surface, while the y- and z-components are tangent to the surface, directed eastward and northward, respectively. The

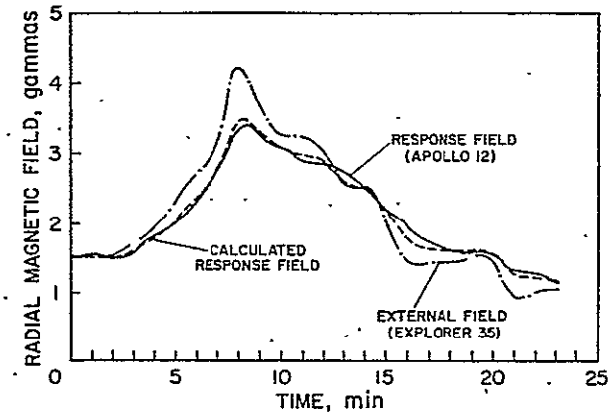

Figure 38.—*Electrical conductivity analysis for a transient event in the geomagnetic tail, deep in the north lobe. Shown are data from the radial component of the event of figure 37. Response to the Explorer 35 external field radial component is computed numerically for the conductivity profile shown in the insert of figure 40 and compared to the measured Apollo 12 response field. In the preliminary results of geomagnetic tail conductivity analysis, this selected conductivity profile, though not unique, yields a satisfactory fit of input and response data for this and thirteen other deep lobe tail events processed to date.*

external (terrestrial) driving magnetic field is measured by Explorer 35, whereas the total response field is measured on the lunar surface by the Apollo 12 magnetometer.

Figure 38 shows an example of calculated response for the Explorer 35 x-axis (radial) input function of figure 37, using the geomagnetic tail electrical conductivity profile illustrated in figure 34. Superimposed is the actual response which is the Apollo 12 x-component of figure 37. This conductivity profile yields the best fit of eighty profiles which have been run to date, although it is not unique. The profile also yields theoretical responses which fit well for the measured tangential components of figure 37 and the components of fourteen other deep-lobe geomagnetic tail transients which have been processed to date.

Figure 39 illustrates an example of a neutral sheet crossing. Figure 40 shows analysis of the radial components of the magnetometer measurements, using the conductivity profile determined from deep-lobe measurements. A

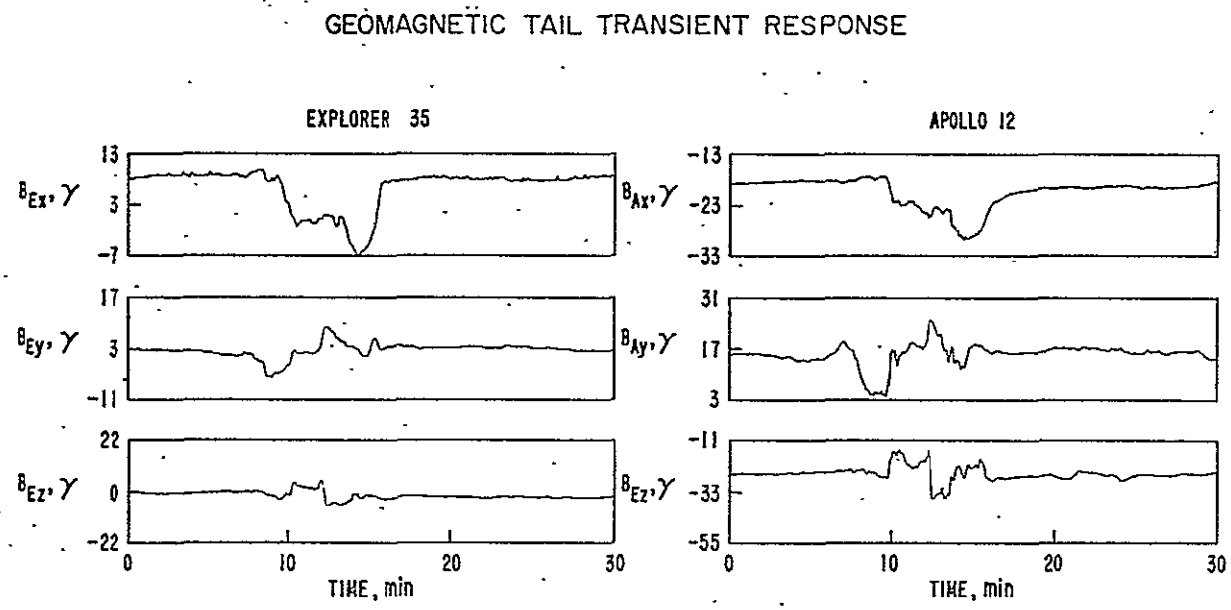

Figure 39.—*Another transient event, measured in the plasma sheet of the geomagnetic tail. Details concerning the data are given in the figure 37 caption.*

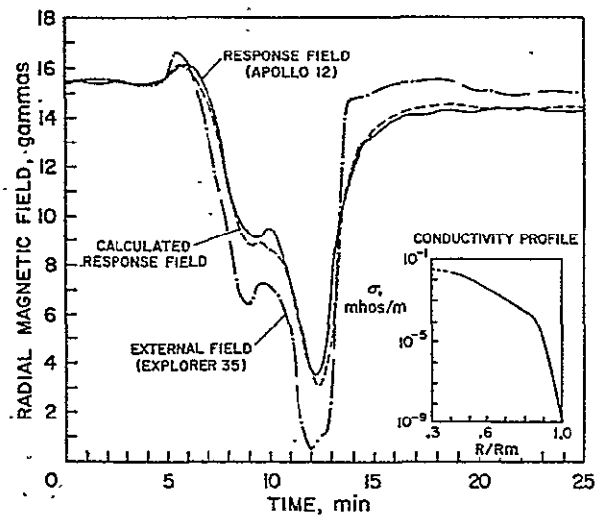

Figure 40.—*Electrical conductivity analysis for the transient event measured in the plasma sheet of the geomagnetic tail. Shown are data from the radial component of the event of figure 39. Response to the Explorer 35 external field radial component is computed numerically for the conductivity profile shown in the insert and compared with the measured Apollo 12 response field.*

qualitative fit of the data can be seen. It is surprising that these few selected neutral sheet data events are in such good agreement with the deep-lobe events. An explanation of this will require further analysis.

Figure 34 shows a plot of the conductivity profile derived from deep-lobe geomagnetic field transient events, superimposed on the conductivity profiles derived from nightside transient-response data in the solar wind (ref. 45). The results are in general agreement. The geomagnetic tail conductivity profile is not unique; rather, it is one of a family of profiles, which results from the geomagnetic tail transient response analysis. The range of profiles from the geomagnetic tail analysis is approximately that of the nightside analysis shown by the shaded region in figure 34. In the future many more geomagnetic transient events will be processed to determine a range of conductivity profiles consistent with a large data set.

LUNAR TEMPERATURE PROFILES FROM CONDUCTIVITY ANALYSES

From an electrical conductivity profile the internal temperature distribution of the Moon can be inferred for an assumed lunar material composition (ref. 105). Electrical conduc-

ORIGINAL PAGE IS OF POOR QUALITY

tivity measurements are particularly useful for determination of lunar temperature because of the strong dependence of conductivity on the temperature of geological materials. The conductivity σ and temperature T of geological materials can be described by an equation of the form

$$\sigma = \Sigma_i E_i \exp\left(-a_i/kT\right) \qquad (19)$$

where a_i represents the activation energies of impurity, intrinsic, and ionic conduction modes; E_i indicates material-dependent, temperature-independent constants; and k is Boltzmann's constant. Laboratory analyses relating conductivity to temperature for various minerals which are good geochemical candidates for the lunar interior, have been conducted by many investigators (e.g., refs. 106–110). These laboratory investigations have been designed to determine a_i and E_i of equation (19) and effects on these constants produced by the physical and chemical state of minerals. Duba (ref. 108) measured the conductivity of single olivine crystals as a function of temperature, pressure, and fayalite content. He concluded that conductivity was highly dependent on the oxidation state of the iron at temperatures below 1100° C. Later Duba and Nicholls (ref.111) reported that the conductivity of a single olivine crystal under an oxygen fugacity of 10^{-12} atm was almost three orders of magnitude lower than its conductivity measured in air. This decrease was attributed to the reduction of Fe^{3+} to Fe^{2+} in the sample. Duba et al. (ref. 110) measured the conductivity of olivine as a function of temperature up to 1440° C under controlled oxygen fugacity and found the measurements to be essentially pressure independent (up to 8 kbars). These recent measurements for olivine by Duba et al. were used to convert conductivity profiles in figure 34 labeled nightside results and geomagnetic tail results, respectively, to temperature profiles numbered 1 and 2 in figure 41. Also included in figure 41, for comparison, are profiles resulting from thermal history calculations of two other investigators. One must be aware that large uncertainties in the lunar temperature profile will remain until more definitive laboratory and space measurements are completed.

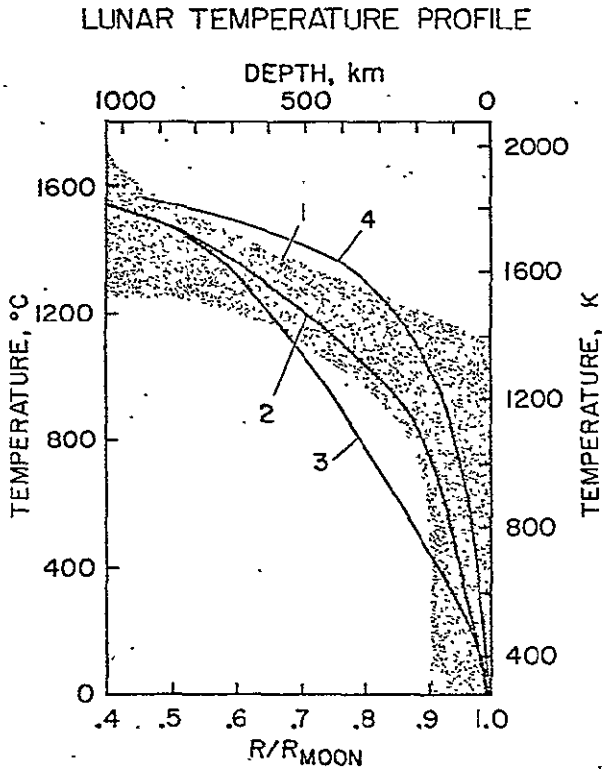

Figure 41.—*Comparison of lunar temperature profiles calculated by different investigators. 1: Temperature profile calculated from the "nightside" conductivity profile shown in figure 34, by use of laboratory data relating conductivity to temperature for olivine (ref. 110). 2: Profile calculated from the "geomagnetic tail" conductivity profile of figure 26 and the data from Duba et al. (ref. 110). 3,4: Temperature profiles from thermal history calculations of Toksöz (ref. 98) and Hanks and Anderson (ref. 119).*

Measurements of the Magnetopause and Bow Shock

With the use of simultaneous data from magnetometers on the lunar surface and in orbit around the Moon, the velocity and thickness of the Earth's magnetopause and bow shock (see fig. 42) have been measured at the lunar orbit. The boundary crossings are measured simultaneously by the Apollo 12

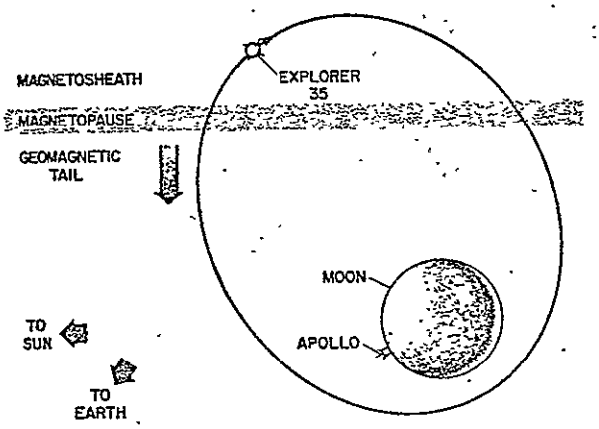

Figure 42.—*Schematic diagram depicting a crossing of the magnetosphere boundary layer (the magnetopause) past the Moon. Velocity of the layer is determined by using arrival-time difference measurements at the two instruments along with known distances between the instruments along the direction of travel of the magnetopause.*

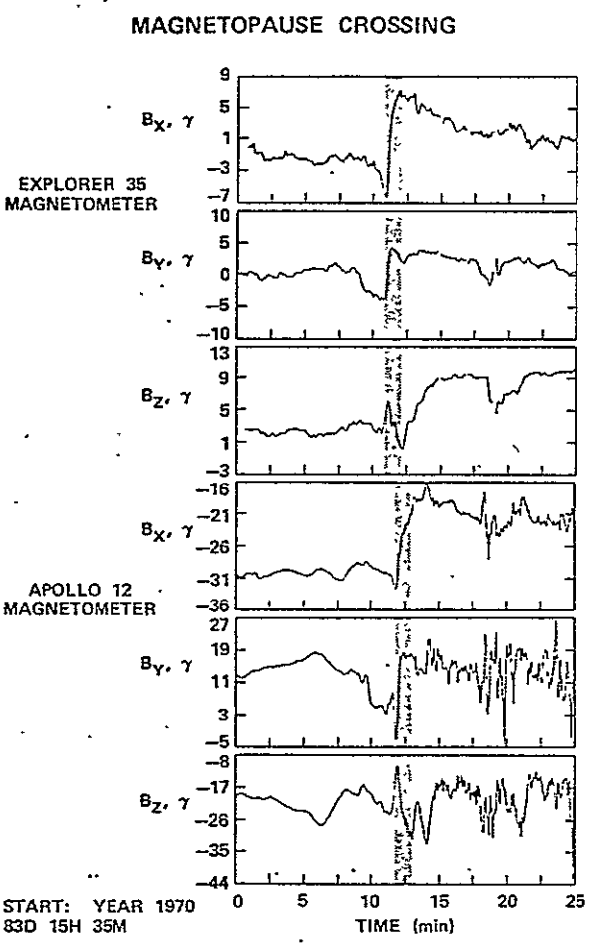

Figure 43.—*Magnetopause crossing, measured by the Apollo 12 lunar surface magnetometer and the lunar orbiting Ames Explorer 35 magnetometer. Data are expressed in the lunar surface coordinate system which has its origin at the Apollo 12 magnetometer site; x is directed radially outward from the surface, while y and z are tangent to the surface, directed eastward and northward, respectively. Shaded regions show arrival times at the two instruments.*

lunar surface magnetometer and the lunar orbiting Explorer 35 magnetometer (fig. 43 shows an example of a magnetopause crossing). Assuming that the plane of a passing boundary layer is perpendicular to the solar ecliptic plane and that the boundary layer moves along its normal at the lunar orbit, the velocity of the layer is measured from arrival-time difference measurements and the known separation of the two magnetometers. In addition, the thickness of the bow shock and magnetopause are estimated by use of the calculated boundary speeds and the signature of the boundary in the magnetometer data. Measurements of the magnetospheric boundaries at the lunar orbit are pertinent to a complete understanding of the magnetic and plasma environment during each part of the Moon's orbit. Of particular current interest, is the interaction of the solar plasma with the moon as a particle-absorbing body (refs. 112 and 113), with the lunar ionsphere (refs. 114, 115, and 116), with the lunar remanent magnetic fields (refs. 25, 29, and 117), and with the induced lunar magnetosphere (refs. 51, 53, and 54).

To date, analysis has been carried out on seven evening and fifteen morning magnetopause crossings, and one evening and ten morning bow shock crossings (ref. 118). There appear to be no significant differences in the measured properties of the morning and evening boundaries at the lunar orbit, although statistics are limited. Elapsed-time data for shock and magnetopause motions, as measured by the magnetometers separated from each other by as much as 10^4 km, indicate that these boundaries are nearly always in motion and can have highly variable velocities. The magnetopause has an average

ORIGINAL PAGE IS OF POOR QUALITY

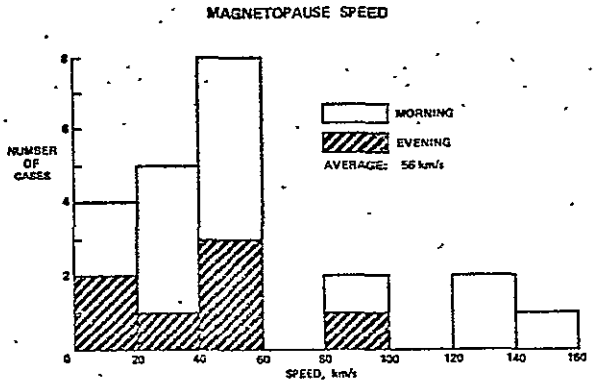

Figure 44.—*Magnetopause speed distribution for 15 morning and 7 evening magnetopause crossings.*

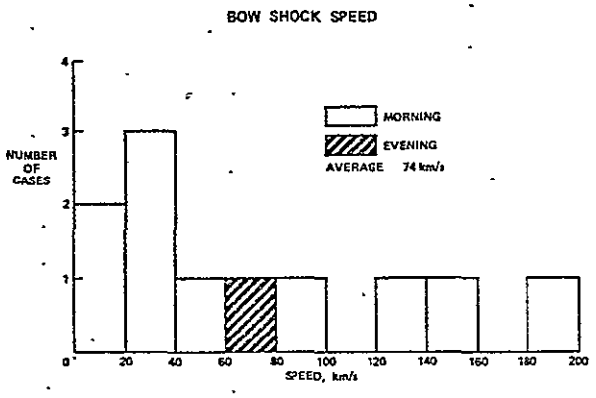

Figure 45.—*Bow shock speed distribution for 1 evening and 10 morning bow shock crossings.*

speed of about 50 kms/s but measurements vary from less than 10 km/s up to about 150 km/s (fig. 44). Similarly, the bow shock has an average speed of about 70 km/s but again there is a large spread in measured values from less than 10 km/s to about 200 km/s (fig. 45). The average measured magnetopause thickness is about 2300 km; however, individual magnetopause boundaries range from 500 km to 5000 km in thickness (fig. 46). The average bow shock thickness is determined to be about 1400 km, with a spread in individual values ranging from 220 km to 3000 km.

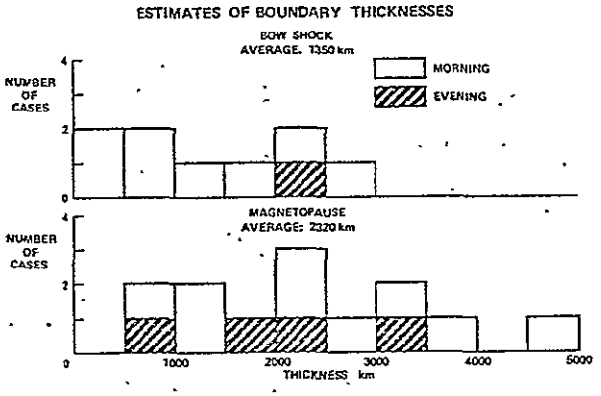

Figure 46.—*Boundary thickness distributions calculated for 9 bow shock and 13 magnetopause crossings.*

Summary

LUNAR REMANENT MAGNETIC FIELDS

Direct measurements of remanent fields have been made at nine sites on the lunar surface: 38 γ at Apollo 12 in Oceanus Procellarum; 103 γ and 43 γ at two Apollo 14 sites separated by 1.1 km in Fra Mauro; 3 γ at the Apollo 15 Hadley Rille site; and 189 γ, 112 γ, 327 γ, 113 γ, and 235 γ, respectively at five Apollo 16 sites in the Descartes region, over a distance of 7.1 km. Simultaneous data from Apollo surface magnetometers and solar wind spectrometers show that the remanent fields at the Apollo 12 and 16 sites are compressed by the solar wind. In response to a solar wind dynamic pressure increase of 1.5×10^{-7} dynes/cm^2, the 38-γ remanent field at the Apollo 12 LSM site is compressed to 54 γ, whereas the field at the Apollo 16 LSM site correspondingly increases from 235 γ to 265 γ. Scale sizes of fields at the Apollo 12 and 16 sites are determined from properties of the remanent field-plasma interaction and orbiting magnetometer measurements. The Apollo 12 field scale size L is in the range 2 km $\leq$ L $\leq$ 200 km, whereas for Apollo 16, 5 km $\leq$ L $\leq$ 100 km.

Measurements by Apollo lunar magnetometers, and remanance in the returned samples, have yielded strong evidence that the lunar crustal material is magnetized over

much of the lunar globe. The surface measurements indicate that fields tend to be stronger in highland regions than in mare regions. The origin of lunar remanent fields remains an enigma. Possibilities are generally grouped under three classifications: a strong external (solar or terrestrial) field, an ancient intrinsic field of global scale, and smaller localized field sources.

LUNAR MAGNETIC PERMEABILITY, INDUCED DIPOLE MOMENT, AND IRON ABUNDANCE

Simultaneous measurements by lunar magnetometers on the surface of the Moon and in orbit around the Moon are used to construct a whole-Moon hysteresis curve, from which the global lunar relative magnetic permeability is determined to be 1.012 $\pm$ 0.006. The global induced magnetization dipole moment corresponding to the permeability measurement is 2×10^{22}H cm^3 (where H is magnetizing field in gauss). For typical geomagnetic tail fields of H $\sim 10^{-4}$ gauss, the corresponding induced dipole moment is 2×10^{18} gauss-cm^3. Both error limits on magnetic permeability value are greater than 1.0, implying that the Moon as a whole is paramagnetic and/or weakly ferromagnetic. Assuming that the ferromagnetic component is free metallic iron of multidomain, noninteracting grains, the free iron abundance in the Moon is calculated to be 2.5 $\pm$ 2.0 wt.%. Total iron abundance in the moon is determined by combining free iron and paramagnetic iron components for two assumed lunar compositional models. For an orthopyroxene moon of overall density 3.34 g/cm^3 with free iron dispersed uniformly throughout the lunar interior, the total iron abundance is 12.8 $\pm$ 1.0 wt.%. For a free iron/olivine moon the total iron abundance is 5.5 $\pm$ 1.2 wt.%. Iron abundance results are summarized in table 3 and figure 29.

Lunar models with a small iron core and with an iron-rich layer have been investigated by using the measured global lunar permeability as a constraint. A small pure iron core of 500-km radius (the maximum size allowed by lunar density and moment of inertia measurements), which is hotter than the iron Curie point. ($T > T_c$), would not be resolvable from the data since its magnetization field would be small compared with the measured induced field. Similarly, an iron-rich layer in the Moon could not be resolved if the iron is paramagnetic, i.e., if the iron is above the iron Curie temperature. Gast and Giuli (ref. 99) have proposed a family of high-density-layer models for the Moon which are geochemically feasible. If these models are iron-rich layers lying near the lunar surface so that $T < T_c$, the ferromagnetic layers would yield a global permeability value well above the measured upper limit. Therefore, it is concluded that such shallow iron-rich-layer models are not consistent with magnetic permeability measurements.

LUNAR ELECTRICAL CONDUCTIVITY AND TEMPERATURE

The electrical conductivity of the lunar interior has been investigated by analyzing the induction of global lunar fields by time varying extralunar (solar or terrestrial) magnetic fields. An upper limit on the unipolar induction field has been determined which shows that at least the outer 5 km of the lunar crust is a relatively poor electrical conductor ($< 10^{-3}$ mhos/m) compared with the underlying material. Past conductivity analyses have used magnetometer data recorded at times when global eddy-current fields were asymmetrically confined by the solar wind plasma. A time-dependent, transient-response analytical technique has been used in the studies. Transient analysis using lunar nightside data yields a conductivity profile rising from a range of values lying between 1×10^{-4} and 2×10^{-3} mhos/m at 250-km depth in the Moon to values ranging between 2×10^{-3} and 8×10^{-2}/ mhos/m at 1000-km depth. Transient analysis of dayside data yields a conductivity profile generally compatible with nightside transient results.

Recent conductivity analysis has considered

lunar eddy-current response during times when the moon is in the geomagnetic tail, in order to minimize the analytical problems posed by asymmetric solar wind confinement of the induced lunar magnetosphere. Preliminary results show that the following conductivity profile, though not unique, is compatible with input and response data: the conductivity increases rapidly with depth, from 10^{-9} mhos/m at the surface to 10^{-4} mhos/m at 200-km, then less rapidly to 2×10^{-2} mhos/m at 1000-km depth. By use of the conductivity-to-temperature relationship for olivine reported by Duba et al. (ref. 110), a temperature profile is calculated from this conductivity profile: temperature rises rapidly with depth to 1100 K at 200-km depth, then less rapidly to 1800 K at 1000-km depth.

MAGNETOPAUSE AND BOW SHOCK PROPERTIES AT THE LUNAR ORBIT

Velocities and thicknesses of the Earth's magnetopause and bow shock at the lunar orbit have been estimated from simultaneous magnetometer measurements. Average speeds are about 50 km/s for the magnetopause and about 70 km/s for the bow shock, with large spreads in individual measured values. Average thicknesses are about 2300 km for the magnetopause and 1400 km for the bow shock, also with large spreads in individual measured values.

References

1. COLBURN, D. S., R. G. CURRIE, J. D. MIHALOV, AND C. P. SONETT, Diamagnetic Solar-Wind Cavity Discovered Behind the Moon. *Science*, Vol. 158, 1967, p. 1040.
2. NESS, N. F., K. W. BEHANNON, C. S. SCEARCE, AND S. C. CANTARANO, Early Results From the Magnetic Field Experiment on Explorer 35. *J. Geophys. Res.*, Vol. 72, 1967, p. 5769.
3. MICHEL, F. C., Magnetic Field Structure Behind the Moon. *J. Geophys. Res.*, Vol. 73, 1968, p. 1533.
4. SPREITER, J. R., M. C. MARSH, AND A. L. SUMMERS, Hydromagnetic Aspects of Solar Wind Flow Past the Moon. *Cosmic Electrodynamics*, Vol. 1, 1970, p. 5.
5. SONETT, C. P., AND D. S. COLBURN, Establishment of a Lunar Unipolar Generator and Associated Shock and Wake by the Solar Wind. *Nature*, Vol. 216, 1967, p. 340.
6. SONETT, C. P., AND D. S. COLBURN, The Principle of Solar Wind Induced Planetary Dynamo. *Phys. Earth Planet. Interiors*, Vol. 1, 1968, pp. 326–346.
7. NESS, N. F., Electrical Conductivity of the Moon (abs.). *Trans. Am. Geophys. Union*, Vol. 49, 1968, p. 242.
8. BEHANNON, K. W., Intrinsic Magnetic Properties of the Lunar Body. *J. Geophys. Res.*, Vol. 73, 1968, p. 7257.
9. NESS, N. F., *Electrical Conductivity and Internal Temperature of the Moon.* Goddard Space Flight Center Report X-616-69-191, 1969. (Also presented as paper k 11 at COSPAR, Prague, May 1969.)
10. DOLGINOV, SH. SH., E. G. EROSHENKO, L. N. ZHUZGOV, AND N. V. PUSHKOV, Investigation of the Magnetic Field of the Moon. *Geomagnetics and Aeronomy*, Vol. 1, 1961, p. 18.
11. DOLGINOV, SH. SH., E. G. EROSHENKO, L. N. ZHUZGOV, AND N. V. PUSHKOV, Measurements of the Magnetic Field in the Vicinity of the Moon by the Artificial Satellite Luna 10. *Akad. Nauk USSR, Doklady*, Vol. 170, 1966, p. 574.
12. GOLD, T., The Magnetosphere of the Moon. In *The Solar Wind*, R. J. Mackin, Jr., and M. Neugebauer, eds., Pergamon Press, New York, 1966.
13. SONETT, C. P., D. S. COLBURN, AND R. G. CURRIE, The Intrinsic Magnetic Field of the Moon. *J. Geophys. Res.*, Vol. 72, 1967, p. 5503.
14. DEWYS, J. N., Results and Implications of Magnetic Experiments on Surveyer 5, 6, and 7 Spacecrafts (abs.). *Trans. Am. Geophys. Union*, Vol. 49, 1968, p. 249.
15. STRANGWAY, D. W., E. E. LARSON, AND G. W. PEARCE, Magnetic Studies of Lunar Samples —Breccia and Fines. *Proc. Apollo 11 Lunar Science Conference, Geochimica et Cosmochimica Acta*, Supplement 1, Vol. 3, A. A. Levinson, ed., 1970, p. 2435.
16. RUNCORN, S. K., D. W. COLLINSON, W. O'REILLY, M. H. BATTEY, A. A. STEPHENSON, J. M. JONES, A. J. MANSON, AND P. W. READMAN, Magnetic Properties of Apollo 11 Lunar Samples. *Proc. Apollo 11 Lunar Science Conference, Geochimica et Cosmochimica Acta*, Supplement 1, Vol. 3, A. A. Levinson, ed., 1970, p. 2369.
17. PEARCE, G. W., D. W. STRANGWAY, AND E. E. LARSON, Magnetism of Two Apollo 12 Igneous Rocks. *Proc. Second Lunar Science Conference, Geochimica et Cosmochimica Acta*, Supplement 2, Vol. 3, 1971, p. 2451.

18. NAGATA, T., R. M. FISHER, F. C. SCHWERER, M. D. FULLER, AND J. R. DUNN, Magnetic Properties and Remanent Magnetization of Apollo 12 Lunar Materials and Apollo 11 Lunar Microbreccia. *Proc. Second Lunar Science Conference, Geochimica et Cosmochimica Acta*, Supplement 2, Vol. 3, 1971, p. 2461.
19. NAGATA, T., R. M. FISHER, F. C. SCHWERER, M. D. FULLER, AND J. R. DUNN, Rock Magnetism of Apollo 14 and 15 Materials. *Proc. Third Lunar Science Conference, Geochimica et Cosmochimica Acta*, Supplement 3, Vol. 3, 1972, p. 2423.
20. COLLINSON, D. W., A. STEPHENSON, AND S. K. RUNCORN, Magnetic Properties of Apollo 15 and 16 Rocks. *Proc. Fourth Lunar Science Conference, Geochimica et Cosmochimica Acta*, Supplement 4, Vol. 3, 1973, p. 2963.
21. PEARCE, G. W., W. A. GOSE, AND D. W. STRANGWAY, Magnetic Studies on Apollo 15 and 16 Lunar Samples. *Proc. Fourth Lunar Science Conference, Geochimica et Cosmochimica Acta*, Supplement 4, Vol. 3, 1973, pp. 3045–3076.
22. GOSE, W. A., D. W. STRANGWAY, AND G. W. PEARCE, A Determination of the Intensity of the Ancient Lunar Magnetic Field. *The Moon*, Vol. 7, 1973, pp. 196–201.
23. DYAL, P., C. W. PARKIN, AND C. P. SONETT, Apollo 12 Magnetometer: Measurement of a Steady Magnetic Field on the Surface of the Moon. *Science*, Vol. 169, 1970, p. 726.
24. BARNES, A., P. CASSEN, J. D. MIHALOV, AND A. EVIATAR, Permanent Lunar Surface Magnetism and its Deflection of the Solar Wind. *Science*, Vol. 171, 1971, pp. 716–718.
25. MIHALOV, J. D., C. P .SONETT, J. H. BINSACK, AND MOUTSOULAS, Possible Fossil Lunar Magnetism Inferred From Satellite Data. *Science*, Vol. 171, 1971, p. 892.
26. COLEMAN, P. J., JR., B. R. LICHTENSTEIN, C. T. RUSSELL, L. R. SHARP, AND G. SCHUBERT, Magnetic Fields Near the Moon. *Proc. Third Lunar Science Conference, Geochimica et Cosmochimica Acta*, Supplement 3, Vol. 3, D. R. Criswell, ed., 1972, pp. 2271–2286.
27. SHARP, L. R., P. J. COLEMAN, JR., B. R. LICHTENSTEIN, AND C. T. RUSSELL, Orbital Mapping of the Lunar Magnetic Field. *The Moon*, Vol. 7, 1973, p. 322.
28. RUSSELL, C. T., P. J. COLEMAN, JR., B. R. LICHTENSTEIN, G. SCHUBERT, AND L. R. SHARP, Subsatellite Measurements of the Lunar Magnetic Field. *Proc. Fourth Lunar Science Conference, Geochimica et Cosmochimica Acta*, Supplement 4, Vol. 3, W. A. Gose, ed., 1973, pp. 2833–2845.
29. DYAL, P., C. W. PARKIN, C. W. SNYDER, AND D. R. CLAY, Measurements of Lunar Magnetic Field Interaction With the Solar Wind. *Nature*, Vol. 236, 1972, pp. 381–385.
30. CLAY, D. R., B. E. GOLDSTEIN, M. NEUGEBAUER, AND C. W. SNYDER, Solar-Wind Spectrometer Experiment. *Apollo 15 Preliminary Science Report*, NASA SP–289, 1972, pp. 10–1 to 10–7.
31. DYAL, P., AND C. W. PARKIN, The Magnetism of the Moon. *Sci. Amer.*, Vol. 225, 1971, pp. 62–73.
32. PARKIN, C. W., W. D. DAILY, AND P. DYAL, Iron Abundance in the Moon. *Proc. Fifth Lunar Science Conference, Geochimica et Cosmochima Acta*, Vol. 3, 1974.
33. PARKIN, C. W., W. D. DAILY, AND P. DYAL, Lunar Iron Abundance From Magnetometer Measurements. *Lunar Science*, Vol. V, Part II, Lunar Science Institute, Houston, 1974, p. 589.
34. RUSSELL, C. T., P. J. COLEMAN, JR., B. R. LICHTENSTEIN, AND G. SCHUBERT, Permanent and Induced Magnetic Dipole Moment of the Moon. *Proc. Fifth Lunar Science Conference, Geochimica et Cosmochimica Acta*, Supplement 5, Vol. 3, W. A. Gose, ed., in press, 1974.
35. SCHWARTZ, K., AND G. SCHUBERT, Time-Dependent Lunar Electric and Magnetic Fields Induced by a Spatially Varying Interplanetary Magnetic Field. *J. Geophys. Res.*, Vol. 74, 1969, pp. 4777–4780.
36. SCHUBERT, G., AND K. SCHWARTZ, A Theory for the Interpretation of Lunar Surface Magnetometer Data. *The Moon*, Vol. 1, 1969, p. 106.
37. SILL, W. R., AND J. L. BLANK, Method for Estimating the Electrical Conductivity of the Lunar Interior. *J. Geophys. Res.*, Vol. 75, 1970, p. 201.
38. DYAL, P., AND C. W. PARKIN, The Apollo 12 Magnetometer Experiment: Internal Lunar Properties From Transient and Steady Magnetic Field Measurements. *Proc. Second Lunar Science Conference, Geochimica et Cosmochimica Acta*, Supplement 2, Vol. 3, 1971, p. 2391.
39. SMYTHE, W. R., *Static and Dynamic Electricity*. McGraw-Hill Book Co., New York, 1950.
40. WAIT, J. R., A Conducting Sphere in a Time Varying Magnetic Field. *Geophysics*, Vol. 16, 1951, p. 666.
41. TOZER, D. C., AND J. WILSON, The Electrical Conductivity of the Moon's Interior. *Proc. Roy. Soc. London*, Vol. A296, 1967, p. 320.
42. BLANK, J. L., AND W. R. SILL, Response of the Moon to the Time-Varying Interplanetary Magnetic Field. *J. Geophys. Res.*, Vol. 74, 1969, pp. 736–743.
43. DYAL, P., AND C. W. PARKIN, Electrical Conductivity and Temperature of the Lunar Interior From Magnetic Transient-Response

ORIGINAL PAGE IS OF POOR QUALITY

Measurements. *J. Geophys. Res.*, Vol. 76, 1971, pp. 5947–5969.

44. SILL, W. R., Lunar Conductivity Models From the Apollo 12 Magnetometer Experiment. *The Moon*, Vol. 4, 1972, pp. 3–17.
45. DYAL, P., C. W. PARKIN, AND W. D. DAILY, Surface Magnetometer Experiments: Internal Lunar Properties. *Proc. Fourth Lunar Science Conference, Geochimica et Cosmochimica Acta*, Supplement 4, Vol. 3, W. A. Gose, ed., 1973, pp. 2229–2945.
46. SONETT, C. P., G. SCHUBERT, B. F. SMITH, K. SCHWARTZ, AND D. S. COLBURN, Lunar Electrical Conductivity From Apollo 12 Magnetometer Measurements: Compositional and Thermal Inferences. *Proc. Second Lunar Science Conference, Geochimica et Cosmochimica Acta*, Supplement 2, Vol. 3, 1971, pp. 2415–2431.
47. SONETT, C. P., D. S. COLBURN, B. F. SMITH, G. SCHUBERT, AND K. SCHWARTZ, The Induced Magnetic Field of the Moon: Conductivity Profiles and Inferred Temperature. *Proc. Third Lunar Science Conference, Geochimica et Cosmochimica Acta*, Supplement 3, Vol. 3, 1972, p. 2309.
48. KUCKES, A. F., Lunar Electrical Conductivity Profile. *Nature*, Vol. 232, 1971, p. 249.
49. HOBBS, B. A., The Inverse Problem of the Moon's Electrical Conductivity. *Earth Planet. Sci. Letters*, Vol. 17, 1973, pp. 380–384.
50. REISZ, A. C., D. L. PAUL, AND T. R. MADDEN, The Effects of Boundary Condition Asymmetries on the Interplanetary Magnetic Field-Moon Interaction. *The Moon*, Vol. 4, 1972, pp. 134–140.
51. DYAL, P., AND C. W. PARKIN, Global Electromagnetic Induction in the Moon and Planets. *Phys. Earth Planet. Interiors*, Vol. 7, 1973, p. 251.
52. SCHUBERT, G., K. SCHWARTZ, C. P. SONETT, D. S. COLBURN, AND B. F. SMITH, Lunar Electromagnetic Scattering II. Magnetic Fields and Transfer Functions for Parallel Propagation. *Proc. Fourth Lunar Science Conference, Geochimica et Cosmochimica Acta*, Supplement 4, Vol. 3, W. A. Gose, ed., 1973, pp, 2909–2923.
53. SMITH, B. F., D. S. COLBURN, G. SCHUBERT, K. SCHWARTZ, AND C. P. SONETT, Induced Magnetosphere of the Moon 2. Experimental Results From Apollo 12 and Explorer 35. *J. Geophys. Res.*, Vol. 78, 1973, pp. 5437–5448.
54. SCHUBERT, G., C. P. SONETT, K. SCHWARTZ, AND H. J. LEE, Induced Magnetosphere of the Moon I. Theory. *J. Geophys. Res.*, Vol. 78, 1973, pp. 2094–2110.
55. DYAL, P., C. W. PARKIN, AND C. P. SONETT, Lunar Surface Magnetometer. *IEEE Trans. on Geoscience Electrons*, Vol. GE–8(4), 1970.
56. GORDON, D. I., R. H. LUNDSTEN, AND R. A. CHIRADO, Factors Affecting the Sensitivity of Gamma-Level Ring-Core Magnetometers. *IEEE Trans. on Magnetics*, Vol. MAG–1(4), 1965, p. 330.
57. GEYGER, W. A., *Nonlinear-Magnetic Control Devices*. McGraw-Hill Book Co., New York, 1964.
58. SONETT, C. P., D. S. COLBURN, R. G. CURRIE, AND J. D. MIHALOV, The Geomagnetic Tail: Topology, Reconnection and Interaction With the Moon. In *Physics of the Magnetosphere*, R. L. Carovillano, J. F. McClay, and H. R. Radoski, eds., D. Reidel Publishing Co., Dordrecht, Holland, 1967.
59. COLEMAN, P. J., JR., G. SCHUBERT, C. T. RUSSELL, AND L. R. SHARP, The Particles and Fields Subsatellite Magnetometer Experiment. *Apollo 15 Preliminary Science Report*, NASA SP–289, 1972, pp. 22–1 to 22–9.
60. COLEMAN, P. J., JR., B. R. LICHTENSTEIN, C. T. RUSSELL, G. SCHUBERT, AND L. R. SHARP, The Particles and Fields Subsatellite Magnetometer Experiment. *Apollo 16 Preliminary Science Report*, NASA SP–315, 1972, pp. 23–1 to 23–13.
61. MIHALOV, J. D., D. S. COLBURN, R. G. CURRIE, AND C. P. SONETT, Configuration and Reconnection of the Geomagnetic Tail. *J. Geophys. Res.*, Vol. 73, 1968, p. 943.
62. HINNERS, N. W., The New Moon: A View. *Rev. Geophys. and Space Phys.*, Vol. 9, 1971, p. 447.
63. NAGATA, T., R. M. FISHER, AND F. C. SCHWERER, Lunar Rock Magnetism. *The Moon*, Vol. 4, 1972.
64. STRANGWAY, D. W., H. N. SHARP, W. A. GOSE, AND G. W. PEARCE, Magnetism and the Early History of the Moon. *Geochimica et Cosmochimica Acta*, Supplement 4, Vol. 37, in press, 1973.
65. FULLER, M., Lunar Magnetism. *Rev. Geophys. and Space Sci.*, in press, 1974.
66. SONETT, C. P., AND J. D. MIHALOV, Lunar Fossil Magnetism and Perturbations of the Solar Wind. *J. Geophys. Res.*, Vol. 77, 1972, p. 588.
67. STRANGWAY, D. W., W. A. GOSE, G. W. PEARCE, AND R. K. MCCONNELL, Lunar Magnetic Anomalies and the Clayey Formation. *Nature*, Vol. 246, 1973, p. 112.
68. WOOD, J. A., Thermal History and Early Magnetism in the Moon. *Icarus*, Vol. 16, 1972, pp. 229–240.
69. STRANGWAY, D. W., AND H. A. SHARP, Lunar Magnetism and an Early Cold Moon. *Nature*, Vol. 249, 1974, p. 227.
70. DYAL, P., C. W. PARKIN, C. P. SONETT, R. L. DUBOIS, AND G. SIMMONS, Lunar Portable Magnetometer Experiment. *Apollo 14 Preliminary Science Report*, NASA SP–272, 1971, pp. 227-237.

ORIGINAL PAGE IS
OF POOR QUALITY

71. STRANGWAY, D. W., W. A. GOSE, G. W. PEARCE, AND J. G. CARNES, Magnetism and the History of the Moon. *Proc. 18th Annual Conference on Magnetism and Magnetic Material, J. Appl. Phys.*, in press, 1973.
72. DYAL, P., C. W. PARKIN, AND W. D. DAILY, Magnetism and the Interior of the Moon. Submitted to *Rev. Geophys. Space Phys.*, 1974.
73. SONETT, C. P., D. S. COLBURN, AND K. SCHWARTZ, Electrical Heating of Meteorite Parent Bodies and Planets by Dynamo Induction From Premain Sequence, T Tauri Solar Wind. *Nature*, Vol. 219, 1968, p. 924.
74. HELSLEY, C. E., Magnetic Properties of Lunar 10022, 10069, 10084, and 10085 Samples. *Proc. Apollo 11 Lunar Science Conference, Geochimica et Cosmochimica Acta*, Supplement 1, Vol. 3, 1970, p. 2213.
75. RUNCORN, S. K., D. W. COLLINSON, W. O'REILLY, A. STEPHENSON, M. H. BATTEY, A. J. MANSON, AND P. W. READMAN, Magnetic Properties of Apollo 12 Lunar Samples. *Proc. Roy. Soc. London, Ser. A*, Vol. 325, 1971, p. 157.
76. STRANGWAY, D. W., G. W. PEARCE, W. A. GOSE, AND R. W. TIMME, Remanent Magnetization of Lunar Samples. *Earth Planet. Sci. Letters*, Vol. 13, 1971, p. 43.
77. LEVY, E. H., Magnetic Dynamo in the Moon: A Comparison With Earth. *Science*, Vol. 178, 1972, p. 52.
78. UREY, H., AND S. K. RUNCORN, A New Theory of Lunar Magnetism. *Science*, Vol. 180, 1973, p. 636.
79. MURTHY, V. R., AND S. K. BANERJEE, Lunar Evolution: How Well Do We Know it Now. *The Moon*, Vol. 7, 1973, p. 149.
80. SMOLYCHOWSKI, R., Magnetism of the Moon. *The Moon*, Vol. 7, 1973, p. 127.
81. SCHUBERT, G., B. F. SMITH, C. P. SONETT, D. S. COLBURN, AND K. SCHWARTZ, Polarized Magnetic Field Fluctuations at the Site of Apollo 15: Possible Regional Influence on Lunar Induction. Submitted to *Science*, 1974.
82. NAGATA, T., Y. ISHIKAWA, H. KINOSHITA, M. KONO, Y. SYONO, AND R. M. FISHER, Magnetic Properties and Natural Remanent Magnetization of Lunar Materials. *Proc. Apollo 11 Lunar Science Conference, Geochimica et Cosmochimica Acta*, Supplement 1, Vol. 3, 1970, p. 2325.
83. CAP, F. F., Possible Production Mechanisms of Lunar Magnetic Fields. *J. Geophys. Res.*, Vol. 77, 1972, pp. 3328–3333.
84. DYAL, P., C. W. PARKIN, AND C. P. SONETT, Lunar Surface Magnetometer Experiment. *Apollo 12 Preliminary Science Report*, NASA SP-235, 1970, pp. 55–73.
85. PARKIN, C. W., P. DYAL, AND W. D. DAILY, Iron Abundance in the Moon From Magnetometer Measurements. *Proc. Fourth Lunar Science Conference, Geochimica et Cosmochimica Acta*, Supplement 4, Vol. 3, 1973, p. 2947.
86. ELLWOOD, W. B., A New Ballistic Galvanometer Operating in High Vacuum. *Rev. Sci. Inst.*, Vol. 5, 1934, pp. 300–305.
87. LINDEMAN, R., J. W. FREEMAN, JR., AND R. R. VONDRAK, Ions From the Lunar Atmosphere. *Proc. Fourth Lunar Science Conference, Geochimica et Cosmochimica Acta*, Supplement 4, Vol. 3, 1973, p. 2889.
88. UREY, H. C., *The Moon*. Z. Kopal and Z. K. Mikhailov, eds., Academic Press, 1962, p. 133.
89. REYNOLDS, R. T., AND A. L. SUMMERS, Calculations on the Composition of the Terrestrial Planets. *J. Geochim. Res.*, Vol. 74, 1969, p. 2494.
90. UREY, H. C., AND G. J. F. MACDONALD, Origin and History of the Moon. *Physics and Astronomy of the Moon*, Z. Kopal, ed., Academic Press, 1971, p. 213.
91. WÄNKE, H., H. BADDENHAUSEN, G. DREIBUS, M. QUIJANO-RICO, M. PALME, B. SPETTEL, AND F. TESCHKE, Multi-Element Analysis of Apollo 16 Samples and About the Composition of the Whole Moon. *Lunar Science*, Vol. IV, J. W. Chamberlain and C. Watkins, eds., Lunar Science Institute, Houston, 1973, pp. 761–763.
92. ZUSSMAN, J., The Minerology, Petrology and Geochemistry of Lunar Samples—A Review. *The Moon*, Vol. 5, 1972, p. 422.
93. WEEKS, R. A., Magnetic Phases in Lunar Material and Their Electron Magnetic Resonance Spectra: Apollo 14. *Proc. Third Lunar Science Conference, Geochimica et Cosmochimica Acta*, Supplement 3, Vol. 3, 1972, p. 2503.
94. UREY, H. C., K. MARTI, J. W. HANKINS, AND M. K. LIU, Model History of the Lunar Surface. *Proc. Second Lunar Science Conference, Geochimica et Cosmochimica Acta*, Supplement 2, Vol. 3, 1971, p. 987.
95. WOOD, J. A., J. S. DICKEY, U. B. MARVIN, AND B. J. POWELL, *Proc. Apollo 11 Lunar Science Conference, Geochimica et Cosmochimica Acta*, Supplement 1, Vol. 1, 1970, p. 965.
96. RINGWOOD, A. E., AND E. ESSENE, Petrogenesis of Lunar Basalts and the Internal Constitution and Origin of the Moon. *Science*, Vol. 167, 1970, pp. 607–610.
97. GREEN, D. H., A. E. RINGWOOD, N. G. WARE, W. O. HIBBERSON, A. MAJOR, AND E. KISS, Experimental Petrology and Petrogenesis of Apollo 12 Basalts. *Proc. Second Lunar Science Conference, Geochimica et Cosmochimica Acta*, Supplement 2, Vol. 1, A. A. Levinson, ed., 1971, pp. 601–615.

98. TOKSÖZ, M. N., Geophysical Data and the Interior of the Moon. *Ann. Rev. of Earth and Planet. Sci.*, Vol. 2, in press, 1973.
99. GAST, P. W., AND R. T. GIULI, Density of the Lunar Interior. *Earth Planet. Sci. Letters*, Vol. 16, 1972, p. 299.
100. DYAL, P., C. W. PARKIN, C. P. SONETT, AND D. S. COLBURN, *Electrical Conductivity and Temperature of the Lunar Interior From Magnetic Transient Response Measurements.* NASA TM X-62,012, 1970.
101. DYAL, P., C. W. PARKIN, AND W. D. DAILY, Temperature and Electrical Conductivity of the Lunar Interior From Magnetic Transient Measurements in the Geomagnetic Tail. *Proc. Fifth Lunar Science Conference, Geochimica et Cosmochimica Acta*, in press, 1974.
102. DYAL, P., C. W. PARKIN, AND P. CASSEN, Surface Magnetometer Experiments: Internal Lunar Properties and Lunar Surface Interactions With the Solar Plasma. *Proc. Third Lunar Science Conference, Geochimica et Cosmochimica Acta*, Supplement 3, Vol. 3, D. R. Criswell, ed., 1972, p. 2287.
103. SCHWARTZ, K., AND G. SCHUBERT, Lunar Electromagnetic Scattering, 1: Propagation Parallel to the Diamagnetic Cavity Axis. *J. Geophys. Res.*, Vol. 78, 1973, pp. 6496–6506.
104. PARKER, E. N., *Space Sci. Rev.*, Vol. 1, 1962, p. 62.
105. RIKITAKE, T., *Electromagnetism and the Earth's Interior.* Elsevier, Amsterdam, 1966.
106. ENGLAND, A. W., G. SIMMONS, AND D. STRANGWAY, Electrical Conductivity of the Moon. *J. Geophys. Res.*, Vol. 73, 1968, p. 3219.
107. DUBA, A., H. C. HEARD, AND R. N. SCHOCK, The Lunar Temperature Profile. *Earth Planet. Sci. Letters*, Vol. 15, 1972, p. 301.
108. DUBA, A., Electrical Conductivity of Olivine. *J. Geophys. Res.*, Vol. 77, 1972, p. 2483.
109. DUBA, A., AND A. E. RINGWOOD, Electrical Conductivity, Internal Temperatures and Thermal Evolution of the Moon. *The Moon*, Vol. 7, 1973, p. 356.
110. DUBA, A., H. C. HEARD, AND R. N. SCHOCK, Electrical Conductivity of Olivine at High Pressure and Under Controlled Oxygen Fugacity. *J. Geophys. Res.*, Vol. 79, 1974, p. 1667.
111. DUBA, A., AND I. A. NICHOLLS, The Influence of Oxidation State on the Electrical Conductivity of Olivine. *Earth Planet. Sci. Letters*, Vol. 18, 1973, pp. 59–64.
112. ANDERSON, K. A., L. M. CHASE, R. P. LIN, J. E. MCCOY, AND R. E. MCGUIRE, Solar-Wind and Interplanetary Electron Measurements on the Apollo 15 Subsatellite. *J. Geophys. Res.*, Vol. 77, 1972, pp. 4611–4626.
113. GEISS, J., F. BUHLER, H. CERUTTI, AND P. EBERHARDT, Solar Wind Composition Experiment. *Apollo 15 Preliminary Science Report*, NASA SP-289, 1972, pp. 15–1 to 15–7.
114. CRISWELL, D. R., Photoelectrons and Solar Wind/Lunar Limb Interaction. *The Moon*, Vol. 7, 1973, p. 202.
115. MANKA, R. H., AND F. C. MICHEL, Lunar Ion Energy Spectra and Surface Potential. *Proc. Fourth Lunar Science Conference, Geochimica et Cosmochimica Acta*, Supplement 4, Vol. 3, W. A. Gose, ed., 1973, pp. 2897–2908.
116. RICH, F. J., D. L. REASONER, AND W. J. BURKE, Plasma Sheet at Lunar Distance: Characteristics and Interactions With the Lunar Surface. *J. Geophys. Res.*, Vol. 78, 1973, pp. 8097–8112.
117. NEUGEBAUER, M., C. W. SNYDER, D. R. CLAY, AND B. E. GOLDSTEIN, Solar Wind Observations on the Lunar Surface With the Apollo 12 ALSEP. *Planetary and Space Sci.*, Vol. 20, 1972, pp. 1577–1591.
118. DAILY, W. D., P. DYAL, AND C. W. PARKIN, Magnetopause Velocity and Thickness From a Network of Apollo Magnetometers (abs.). *Trans. Amer. Geophys. Union (EOS)*, Vol. 55, 1974, p. 390.
119. HANKS, T. C., AND D. L. ANDERSON, Origin, Evolution, and Present Thermal State of the Moon. *Phys. Earth Planet. Interiors*, Vol. 5, 1972, pp. 409–425.

Proc. Lunar Sci. Conf. 8th (1977), p. 767–783.
Printed in the United States of America

ORIGINAL PAGE IS
OF POOR QUALITY

Global lunar crust: Electrical conductivity and thermoelectric origin of remanent magnetism

PALMER DYAL

NASA-Ames Research Center, Moffett Field, California 94035

CURTIS W. PARKIN

Department of Physics, University of Santa Clara, Santa Clara, California 95053

WILLIAM D. DAILY

Eyring Research Institute, Provo, Utah 86401

Abstract—An upper limit is placed on the average crustal conductivity from an investigation of toroidal ($V \times B$) induction in the moon, using ten minute data intervals of simultaneous lunar orbiting and surface magnetometer data. Crustal conductivity is determined as a function of crust thickness. For an average global crust thickness of ~80 km, the crust surface electrical conductivity is $\sim 10^{-8}$ mhos/m. The toroidal induction results lower the surface conductivity limit obtained from poloidal induction results by approximately four orders of magnitude. In addition, a thermoelectric (Seebeck effect) generator model is presented as a magnetic field source for thermoremanent magnetization of the lunar crust during its solidification and cooling. Magnetic fields from 10^3 to 10^4 gammas are calculated for various crater and crustal geometries. Solidified crustal material cooling through the iron Curie temperature in the presence of such ancient lunar fields could have received thermoremanent magnetization consistent with that measured in most returned lunar samples.

INTRODUCTION

IN THIS PAPER we examine the properties of the lunar crust by studying magnetic field data obtained in orbit and on the surface of the moon by several instruments (Dyal *et al.*, 1974). First we will study the electrical conductivity of the crust by analyzing the toroidal magnetic fields associated with unipolar currents driven through the moon by the motional solar wind electric field. This analysis has involved determining the relative accuracy of three instruments: the Explorer 35 Ames and Goddard magnetometers and the Apollo 12 lunar surface magnetometer. Results are given in the Appendix. Next we propose a mechanism for the origin of the remanent magnetization measured in returned samples, and the associated magnetic fields which have been measured by face and orbiting magnetometers. This mechanism involves thermoelectric eration of currents and associated magnetic fields during early crustal solification.

ELECTRICAL CONDUCTIVITY OF THE LUNAR CRUST

Electrical conductivity of the lunar interior can be studied by analysis of two es of global induction fields: the poloidal field due to eddy currents driven by

time-varying external magnetic fields, and the toroidal field due to unipolar currents driven through the moon by the motional solar wind $\mathbf{V} \times \mathbf{B}$ electric field. Poloidal field induction has been used by many researchers to investigate lunar electrical conductivity (e.g., Dyal and Parkin, 1971a; Sonett *et al.*, 1971, 1973; Kuckes, 1971, 1974; Dyal *et al.*, 1974, 1976). To date poloidal induction analysis has yielded the most accurate conductivity information at depths between 200 and 800 km. At shallower depths this technique is limited by instrumental frequency response, number of measurement sites, and lack of a rigorous analytical induction model.

Our objective in this section is to investigate the conductivity of the outer region, or crust, of the moon from the study of toroidal induction in the lunar sphere. In the toroidal mode (see Fig. 1) a unipolar current $\mathbf{J}_T$ is driven by an electric field $\mathbf{E} = \mathbf{V} \times \mathbf{B}_E$ which is produced as the solar magnetic field $\mathbf{B}_E$, frozen in the solar plasma, sweeps by the moon. $\mathbf{V}$ is the velocity of the moon relative to the solar plasma. Corresponding to the induced current $\mathbf{J}_T$ is the toroidal field $\mathbf{B}_T$, which has a magnitude inversely proportional to the total resistance to current flow through the moon; the magnitude of $\mathbf{J}_T$ (or likewise, $\mathbf{B}_T$) is limited by the region of lowest conductivity in the current path, which is probably the lunar crust. Previous electromagnetic studies have shown that the electrical conductivity of the outer region of the moon is very low. Strangway *et al.* (1972)

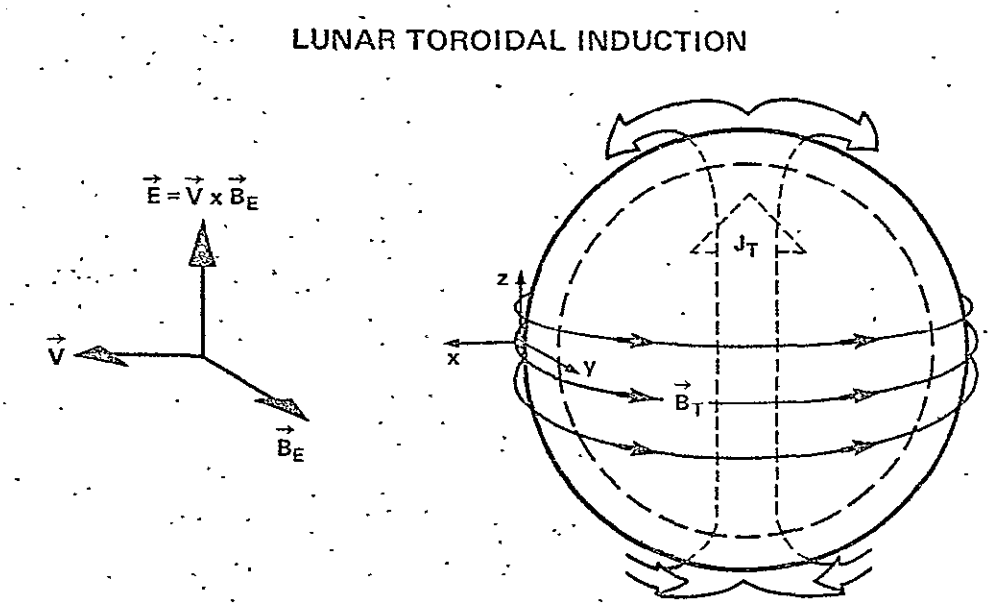

Fig. 1. Toroidal field $\mathbf{B}_T$, resulting from induced currents $\mathbf{J}_T$ within the moon. The $\mathbf{V} \times \mathbf{B}_E$ electric field which drives the currents through the lunar interior is due to the motion of the external solar magnetic field $\mathbf{B}_E$ past the moon. The Apollo 12 ALSEP coordinate system is shown; x, y, and z are directed radially outward, horizontally eastward, and horizontally northward, respectively.

found the d.c. conductivity of a lunar soil sample to be as low as 10^{-14}–10^{-15} mhos/m. Earth-based radar measurements have been interpreted by Strangway (1969) to yield a conductivity of $\sim 10^{-13}$ mhos/m for the outer 1 m of the moon. The Lunar Sounder Experiment (Phillips *et al.*, 1973) and the Surface Electrical Properties Experiment (Simmons *et al.*, 1973) have shown that displacement currents dominate the outer 1 km. Dyal and Parkin (1971b) calculated an upper limit of 10^{-9} mhos/m for conductivity of the outer 5 km of the lunar crust.

The toroidal induction mode has been described theoretically by several investigators (Sonett and Colburn, 1967; Schwartz and Schubert, 1969; Schubert and Schwartz, 1969; Sill and Blank, 1970). For the case when the moon is immersed in the solar wind plasma, the external field $\mathbf{B}_E$ is constant (eddy current induction vanishes), and the motional solar wind electric field induction drives currents in the moon resulting in a toroidal field $\mathbf{B}_T$, the total field $\mathbf{B}_A$ at the surface is

$$\mathbf{B}_A = \mathbf{B}_E + \mathbf{B}_T. \tag{1}$$

Following Schubert and Schwartz (1969), we solve for the toroidal field, $\mathbf{B}_T$, expressed in component form as follows:

$$B_{Tx} = B_{Ax} - B_{Ex}, \tag{2}$$

$$B_{Ty} = B_{Ay} - B_{Ey} = AE_z = A(V_x B_{Ey} - V_y B_{Ex}), \tag{3}$$

$$B_{Tz} = B_{Az} - B_{Ez} = -AE_y = A(V_x B_{Ez} - V_z B_{Ex}), \tag{4}$$

where, for a two-layer (core-crust) model of the moon

$$A = \sigma_1 \mu R_m \left(\frac{\frac{1}{2} + \beta + \alpha(1-\beta)}{1 - \beta + \alpha(2+\beta)}\right), \tag{5}$$

$$\alpha = \sigma_1/\sigma_2, \tag{6}$$

$$\beta = (R_2/R_m)^3. \tag{7}$$

The components x, y, z are up, east, north ALSEP coordinates at the Apollo 12 site; $\mathbf{V}$ is velocity of the moon relative to the solar wind; σ_1 and σ_2 are conductivity of crust and core, respectively; μ is the global permeability; R_2 and R_m are core and lunar radii. For the case where $\sigma_2 \gg \sigma_1$, Eq. (5) reduces to

$$A = \sigma_1 \mu R_m \left(\frac{\frac{1}{2} + \beta}{1 - \beta}\right). \tag{8}$$

Equation (8) is graphically displayed in Fig. 2.

These parametric solutions are valid at the low-frequency limit for the spherically symmetric case of the induction field totally confined to the interior or near-surface regions by a highly conducting plasma. The components of the toroidal field are calculated by subtracting the components of the external field $\mathbf{B}_E$, measured by an Explorer 35 magnetometer, from the total field $\mathbf{B}_A$ measured at the lunar surface by the Apollo 12 lunar surface magnetometer. We have

ORIGINAL PAGE IS
OF POOR QUALITY

ORIGINAL PAGE IS
OF POOR QUALITY

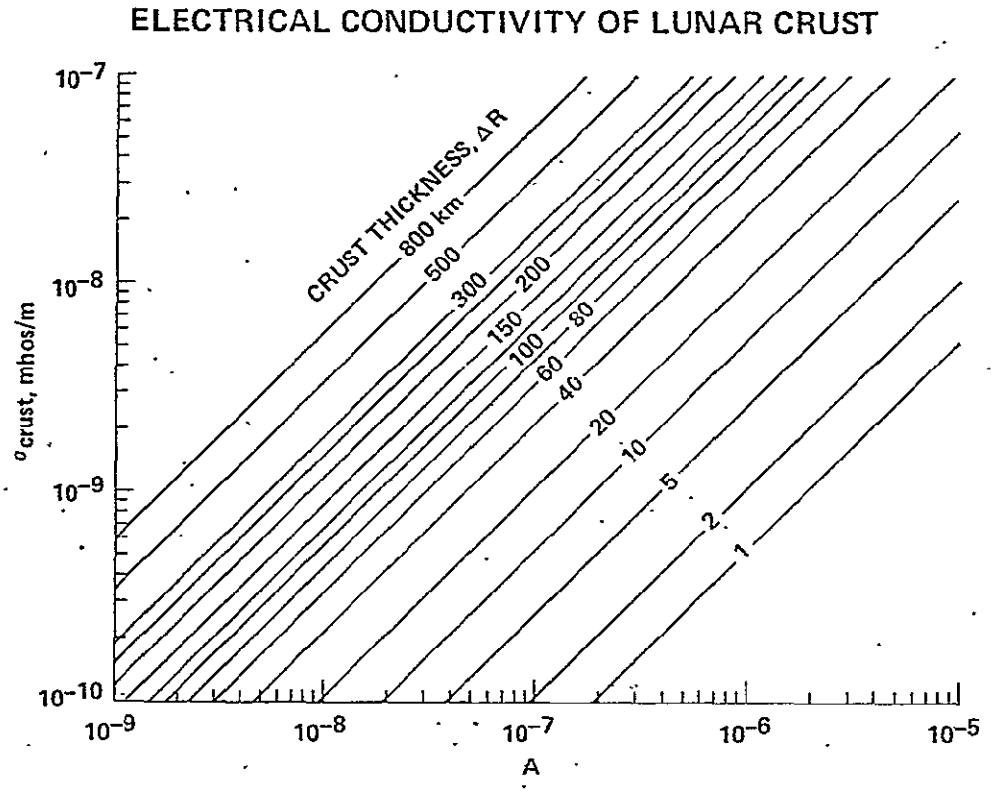

Fig. 2. Theoretical family of curves relating crustal conductivity σ_{crust} to the factor A (see text). Solutions are based on a lunar core-crust model where $\sigma_{crust} \ll \sigma_{core}$ [Eq. (8)].

determined the parameter A [Eq. (8)] by plotting components of toroidal field B_T versus the $V \times B_E$ electric field, using a data set of 100 ten minute averages from a total of 5 lunations, selected from time periods when the solar wind velocities and fields are approximately constant. All data have been selected from time periods when the Apollo 12 magnetometer was on the lunar nightside, to minimize solar wind compression effects on the surface remanent magnetic field (Dyal *et al.*, 1972).

According to Sill and Blank (1970), the toroidal induction transfer function is independent of frequency for frequencies $<2 \times 10^{-3}$ Hz at expected lunar conductivities. Use of 10 min averages therefore makes our analysis equivalent to the d.c. case for toroidal induction. Although our data are selected from times when the external field is nearly constant, there may be small but nonzero poloidal induction at 10 min periods; however, small poloidal induction effects are not expected to affect our results. The direction of the toroidal field is dependent on solar wind velocity V and external field B_E, whereas the poloidal field direction is dependent on the direction of the rate of change of the external field, dB_E/dt. For our data set of 100 ten minute averages we assume that dB_E/dt

has negligible correlation with either V or B_E, so if the poloidal field magnitude is nonzero when averaged over a 10 min period, the direction of the net poloidal field will be essentially random when considered for 100 cases. Therefore under this assumption poloidal "contamination" in the measurements would cause scatter in the graph relating toroidal field to electric field (Fig. 3) but would not affect the *slope* of a straight line through the data, from which we determine the toroidal field upper limit.

In Fig. 3 we plot $B_{Ty} = B_{Ay} - B_{Ey}$ versus the electric field component, E_z, which is the largest of the three components for average solar wind conditions. From these data we calculate a least squares slope $A = (-6.2 \pm 4.3) \times 10^{-2}$ sec/m, where the limits include only random statistical measurement errors. Systematic instrumental errors are discussed in the Appendix. Estimates of these errors are based upon comparisons between Apollo 12, LSM Explorer 35-Ames, and Explorer 35-Goddard magnetometers. From this comparison we estimate the systematic error inherent in the analysis. The systematic and random errors result in an upper limit slope of 2×10^{-7} sec/m.

Using this value of slope A, we can determine the upper limit on average crustal conductivity as a function of crust thickness (ΔR) by reference to Fig. 2. For an average crust thickness $\Delta R = 80$ km (Goins *et al.*, 1977) the conductivity upper limit is 9×10^{-9} mhos/m. We note that the average crust conductivity is not a strong function of crust thickness for thicknesses of the order of 80 km. (A 100 km crust would correspond to a 1.2×10^{-8} mhos/m upper limit, and a 60 km crust would correspond to about 7×10^{-9} mhos/m.)

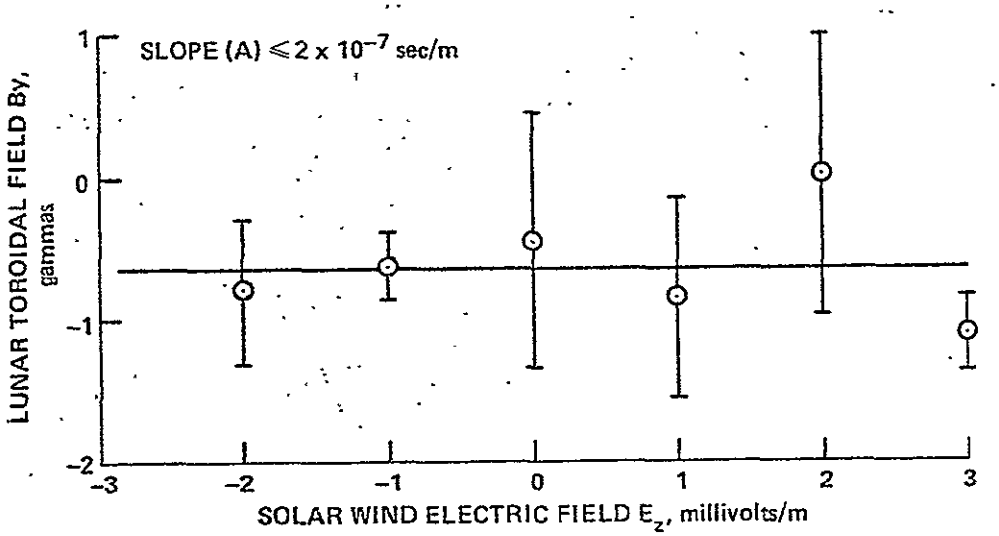

Fig. 3. Toroidal magnetic field data plotted as a function of solar wind electric field [see Eq. (3)], for a data set of 100 ten minute averages selected from times when solar wind field and velocity were approximately constant. Error bars represent one standard deviation in averaged data points. The slope upper limit includes systematic errors (gain differences of the magnetometers) as well as random statistical errors.

ORIGINAL PAGE IS
OF POOR QUALITY

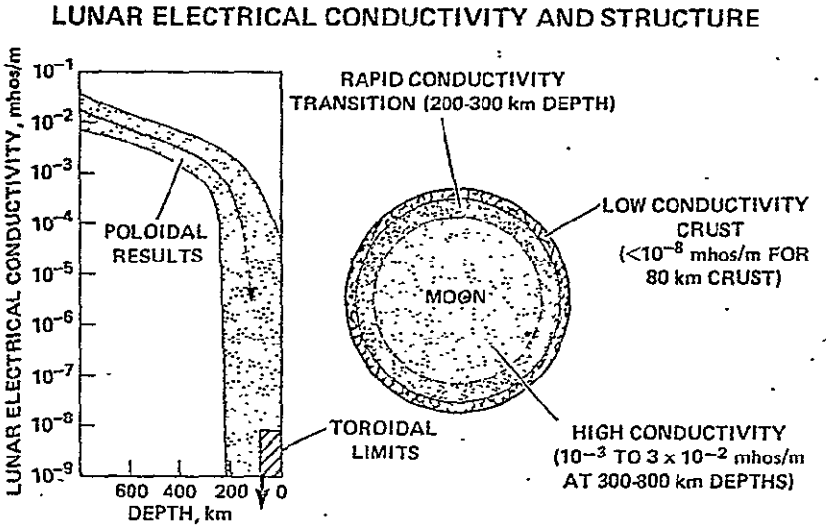

Fig. 4. Electrical conductivity and inferred structure of the lunar crust and interior. Results from toroidal calculations place an upper limit surface conductivity $\sim 10^{-8}$ mhos/m for an assumed 80 km lunar crust thickness. This lowers the upper limit determined in poloidal induction analysis (Dyal *et al.*, 1976) by nearly four orders of magnitude.

This crustal conductivity upper limit places an important new constraint on the lunar conductivity profile. The shaded region of Fig. 4 shows recent results from poloidal-induction analysis of conductivity (Dyal *et al.*, 1976), which are most accurate at intermediate depths of 200–800 km, and much less accurate for shallower depths. The toroidal induction results lower the crust conductivity upper limit by approximately four orders of magnitude.

Thermoelectric Origin for Crustal Remanent Magnetism

A principal unresolved problem in lunar magnetism is the lack of an adequate explanation for the natural remanent magnetization (NRM) of the lunar crust. Apollo lunar surface magnetometers and subsatellite magnetometers have measured remanent magnetic fields of scale lengths from 1 to 100 km (Dyal *et al.*, 1974, Russell *et al.*, 1975; Lin *et al.*, 1975). Analyses of returned lunar samples have indicated that the NRM ranges from 10^{-3} to 10^{-7} G-cm^3/g and was most likely acquired by the thermoremanent magnetization of metallic iron grains in the presence of 10^3–10^5 gamma magnetic fields (Strangway *et al.*, 1970; Collinson *et al.*, 1973; Dunlop *et al.*, 1975; Pearce *et al.*, 1976). Explaining the origin of fields this large is difficult since magnetic fields of the present day lunar environment are $\leq$20 gammas. In this section we propose that the magnetizing fields may have been produced by thermoelectrically driven currents in the early lunar crust.

According to most theories of lunar evolution (e.g., Wood *et al.*, 1970, Hubbard and Minear, 1975; Wood, 1975) the crust of the moon became highly differentiated as the outer 350 km of the lunar sphere solidified. After the accretion process was nearly complete 4.6 b.y. ago, crustal solidification proceeded as heat was lost to the lunar interior and radiated from the surface into space, forming a thin solid crust at the surface. The crust gradually thickened as the magma ocean cooled and solidified at greater and greater depths. During times when the crust was on the order of a few kilometers thick, meteorite impacts would have penetrated the crust, exposing the subsurface magma, and forming lava-filled basins.

We have considered the model in which two such basins in close proximity formed at approximately the same time and were connected below the solid crust by subsurface magma and above by the solar wind plasma (see Fig. 5). Heterogeneous cooling in the crust could have caused one basin to cool and solidify more rapidly than the other, producing a large temperature difference between the two basins. In this model we have the basic elements for generation of a thermoelectric current by the Seebeck effect. The Seebeck effect is produced in an electrical circuit which is composed of two dissimilar conductors, joined at two junctions which have different temperatures. The potential can be

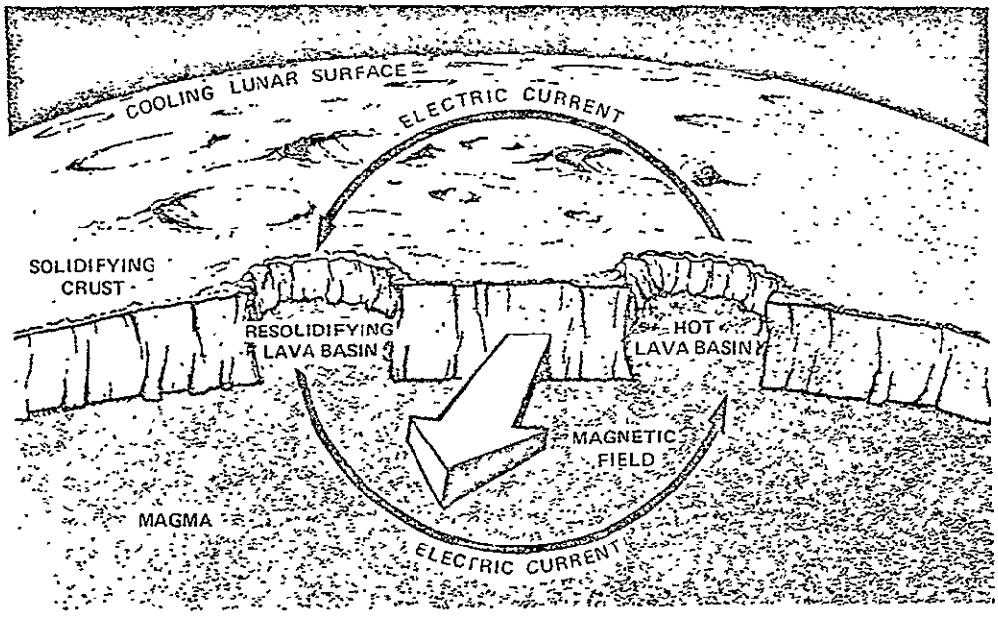

Fig. 5. Magnetic field generation by thermoelectrically driven currents. A thermoelectric voltage resulting from the thermal gradient at the surface of the cooling lava basin drives currents through the highly conducting lunar interior and solar wind. The resulting magnetic field is maximum in the crustal region lying between the two lava basins.

ORIGINAL PAGE IS
OF POOR QUALITY

expressed as $E_{AB} = \epsilon_{AB}(\Delta T)$, where E_{AB} is the Seebeck potential, ϵ_{AB} is the relative Seebeck coefficient for the combination of materials A and B, and ΔT is the temperature difference of the junctions. In our model the current flow is through the subsurface magma connecting the bottom of the solidifying basin out through the surface of the nearby unsolidified basin and through the highly conducting plasma above the lunar surface back to the top of the solidifying basin (Fig. 5). A magnetic field would be associated with this current flow and would magnetize the solid crustal material cooling through the iron Curie temperature near the basins. Material would have been most strongly magnetized between the basins in the presence of the maximum field strengths. However, this does not necessarily imply a correlation between magnetic anomalies and modern craters because the basins referred to in the description of this mechanism were formed during the initial crustal solidification of the moon. Most of the evidence of their existence was destroyed by subsequent cratering in the almost completely solidified crust. A quantitative estimate of the magnetic field produced by this mechanism requires a more detailed examination of the thermoelectric circuit.

We will first consider the thermoelectric properties of the lunar crustal material and solar wind plasma. The electrical conductivity and Seebeck coefficient of insulators, semiconductors, semimetals, and metals generally exhibit a systematic relationship which is illustrated in Fig. 6. Lunar crustal material exhibits semiconductor properties (Duba, 1972) and should have a large Seebeck coefficient. Many of the geologic minerals studied by Telkes (1950) and Noritomi (1955) also exhibited semiconductor-like Seebeck coefficients, although

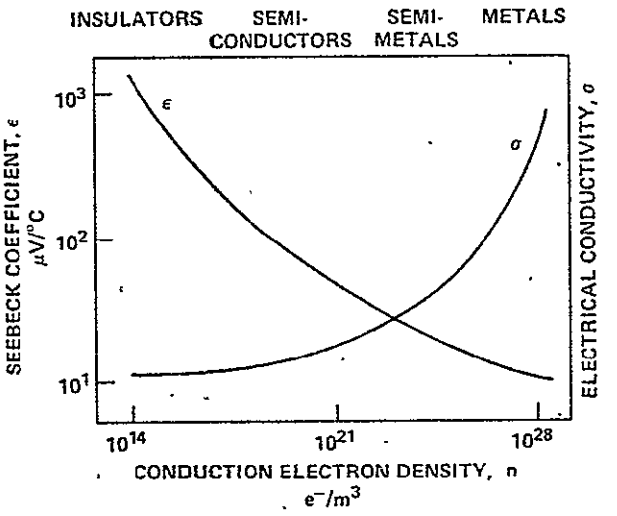

Fig. 6. Schematic representation of Seebeck coefficient and electrical conductivity for various materials as a function of conduction electron density. The electrical conductivity generally increases with the conduction electron density and is highest for metals. Conversely, the Seebeck coefficient is usually highest for insulators.

in general minerals have a wide range of coefficients, ranging from −3200 to +2100 μV/°K. A typical measured value for geologic minerals is $\sim 10^2$ μV/°K. We assume this value to be representative of the lunar magma as well as the lunar crust; for this case the magma-crust interface would produce no Seebeck potential.

A rigorous justification of this assumption would require a quantitative model of the electronic structure of liquid semiconductors. While a quantitative theory for liquid semiconductors is complex, certain simplified qualitative arguments can be made using solid state theory. There is evidence, from X-ray diffraction experiments in liquid semiconductors (Cadoff and Miller, 1960), that there is short-range order in liquids just above the solidus which gradually disappears at higher temperatures. The long-range disorder near the melting temperature should not greatly affect the applicability of the band approximation on which solid state thermoelectric theory depends (Cadoff and Miller, 1960). Therefore we might expect no significant discontinuity in the Seebeck potential of semiconductors at melting. This is substantiated by experimentation with Cu_2S reported by Cadoff and Miller (1960). The Seebeck coefficient of Cu_2S is 300 μV/°K from 673°K to the melting point, after which it rises to 450 μV/°K. With further temperature increase it returns to 300 μV/°K and remains constant between 1397°K and 1470°K. For this example the solid and liquid have approximately the same Seebeck potentials; therefore, the thermoelectric emf, which is proportional to the difference in Seebeck potentials, would also be small. We therefore conclude that the crust-magma interface on the early moon would have produced a negligibly small Seebeck potential compared to the surface-plasma potential, which we will discuss in the following paragraphs.

The thermoelectric properties of the solar wind plasma have not been measured; however, the Seebeck effect in laboratory plasmas has been observed to produce megagauss fields under laboratory conditions (Stamper *et al.*, 1971; Tidman, 1974; Stamper and Ripin, 1975). We theoretically estimate a Seebeck coefficient for the solar wind using an expression given by Ioffe (1957) for the Seebeck coefficient of solids whose conduction electrons, like those of a plasma, obey Maxwell–Boltzmann statistics:

$$e = \pm \frac{k}{e}\left[r + 2 + \ln \frac{2(2\pi mkT)^{3/2}}{h^3 n}\right], \tag{9}$$

where k is Boltzmann's constant, e is the electronic charge, m is the electron mass, T is the temperature, h is Planck's constant, n is the electron density, and r is a coefficient of order unity which depends on the electron scattering mechanism ($r = 0$ for atomic lattice; $r = \frac{1}{2}$ or 1 for ionic lattice; $r = 2$ for impurity ions). If in our case r is 0(1), this expression is not sensitive to r for expected electron densities. For an early solar phase, (e.g., T-Tauri), solar wind densities of $10^{14} e^-/m^3$ and temperatures of $T \sim 4 \times 10^5$°K are likely (Srnka, 1975). Using these parameters, Eq. (9) predicts a thermal emf of 3 mV/°K (present day solar wind conditions of $n = 10^6$ e^-/cm^3 and $T = 3 \times 10^5$°K yield $\epsilon = 5$ mV/°K). These plasma Seebeck coefficient values seem reasonable when compared to the

ORIGINAL PAGE IS
OF POOR QUALITY

insulator values illustrated in Fig. 6. Experiments must ultimately determine the appropriate Seebeck coefficient for a fully ionized hydrogen plasma of $0(10^{14}e^{-}/m^3)$ in contact with lunar crustal material. The purpose of our model is to demonstrate the feasibility of the thermoelectric mechanism and emphasize the importance of conducting these experiments.

A quantitative evaluation of the model requires an estimate of the relative thermoelectric potential, which is the difference in the Seebeck coefficients for the crust and plasma. We have assumed $\epsilon \sim 10^2\,\mu$V/°K for the crustal type material and $\epsilon \sim 10^3\,\mu$V/°K for the plasma, yielding a value of $\sim 10^3\,\mu$V/°K for the *relative* Seebeck coefficient. Therefore the plasma/moon thermoelectric potential dominates the magma/crust potential.

To estimate the magnetic fields resulting from these thermoelectrically produced currents, we approximate the circuit geometry by a torus as shown in Fig. 7. Many geometries other than that shown in Fig. 7 are possible. The only essential requirements are a net thermal gradient and a closed current path; we have chosen the case shown in Fig. 7 for convenience in modeling the current geometry and calculating a representative magnetic field. The basins are of length A on a side and are separated by a distance S, and the lunar crust thickness is D. The thermoelectric potential difference is $\epsilon\Delta T$, where ϵ is the thermoelectric coefficient in V/°K and ΔT is the temperature difference between the basins.

The total electrical resistance of the circuit has contributions from the solar wind plasma, the magma, and the resolidifying crust. Resistance of the crust and magma are expressed by $R = \int_0^l dl/A^2\sigma$, where A^2 is the area of the basin, l is the current path length, and σ is the conductivity. The conductivity is in turn related to temperature; we estimate this relationship using data from Fig. 2 of Presnall *et al.* (1972) for a synthetic basalt. The functional dependence of conductivity on temperature for the resolidifying crust at temperatures below the liquidus

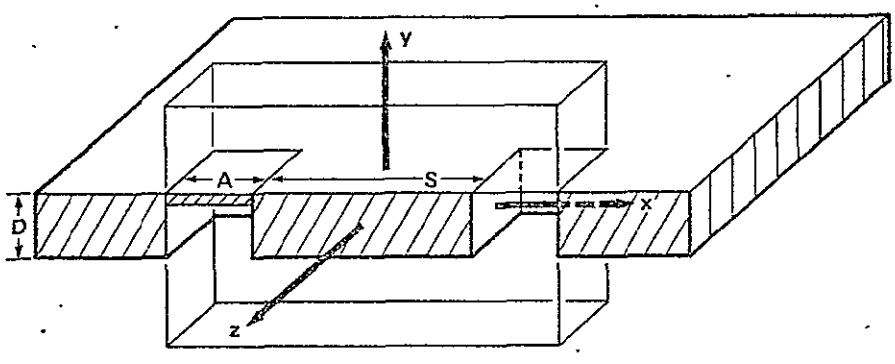

Fig. 7. Schematic model for magnetic field generation by thermoelectrically driven currents (corresponding to Fig. 5). The mechanism is modeled by square basins of length A on a side, separated by a distance S, with a crust thickness D. The current is confined to the square torus-like region containing the x–y plane, which connects the basins and extends into the plasma above the surface and into the magma below the surface.

($T < 1543$°K) falls into two distinct regimes. For $T \leq 1413$°K, the data are represented by $\sigma = \delta \exp(-\beta/kT)$ with $\delta = 1.1 \times 10^2$ mhos/m and $\beta = 1.7 \times 10^{-19}$ J. For 1413°K $< T <$ 1543°K, we use the above exponential relationship and require that $\sigma = 1.7 \times 10^{-2}$ mhos/m at 1413°K and 10 mhos/m at 1543°K to get $\delta = 9.4 \times 10^{27}$ mhos/m and $\beta = 1.3 \times 10^{-18}$ J. To represent the magma conductivity we assume the magma is at the liquidus temperature of 1543°K and has a conductivity of 10 mhos/m. We note that the crustal conductivity for depths on the order of 1 km calculated for the ancient lunar crust will differ from that of the present day conductivity due to different crustal temperatures and regolith formation by cratering processes.

The electrical conductivity of the early solar wind plasma, σ_p, can be calculated using the expression given by Spitzer (1962). For $n = 10^{14}$ e^-/m^3 and $T_e = 4 \times 10^5$°K representing a T-Tauri plasma at 1 a.u. (Parker, 1968; Srnka, 1975), $\sigma_p = 2.6 \times 10^5$ mhos/m parallel to the magnetic field and half that value perpendicular to the magnetic field. (Present day parameters of $n = 10^7$ e^-/m^3, $T_{e\perp} = 4 \times 10^4$°K, and $T_{e\parallel} = 10^5$°K yield $\sigma_p = 2 \times 10^4$ mhos/m parallel and 2.6×10^1 mhos/m perpendicular to the magnetic field). These calculations are valid for the plasma only if the current density does not trigger plasma instabilities. The condition for turbulence is $j_p \geq enC_e/2$ (where C_e is the electron thermal speed) when the current density j_p is along the field and $j_p \geq (m_e/m_i)^{1/2} enC_e$ (where m_e/m_i is the electron-ion mass ratio) when j_p is across the field. In an early T-Tauri solar plasma, current densities of about 6 amps/m^2 across the field and 125 A/m^2 parallel to the field are needed to trigger instabilities. The maximum j_p in the model calculations (to be described later) are $\sim 10^{-6}$ A/m^2; therefore, no instabilities are expected in the plasma and conductivities calculated from Spitzer (1962) are expected to be representative of the plasma. If the plasma current paths connect the lava basins close to the moon as modeled by the toroidal geometry, resistance in the plasma portion of the electrical circuit is negligible compared to that of the crust and magma. (Present day solar wind plasma conditions are stable for $j_p \sim 10^{-8}$ A/m^2 perpendicular and $\sim 10^{-7}$ A/m^2 parallel to the field. Therefore, instabilities leading to larger resistivity in the plasma would develop in some cases in the present solar wind.)

For the toroidal current geometry (Fig. 7) and the conditions described above, we calculate the maximum magnetic field between the basins using the Biot–Savart law. Results of our magnetic field calculations are shown in Fig. 8. The magnetic field is plotted as a function of basin size and separation for a crustal thickness of 1 km. The magnetic field in the crustal region between the basins ranges from a few hundred to over 10^4 gammas. In addition, compressive effects of the ancient solar wind could have increased these fields by a factor of 2 or 3 during lunar daytime (Dyal *et al.*, 1972).

The time dependence of the field is a strong function of the thickness of the resolidifying crust. When the crust is less than about 1 m thick, the current in the circuit is limited by the resistance of the subsurface magma. As the crust thickness exceeds ~ 1 m, its resistance becomes much larger than that of the subsurface magma. The exponential relationship between temperature and elec-

ORIGINAL PAGE IS
OF POOR QUALITY

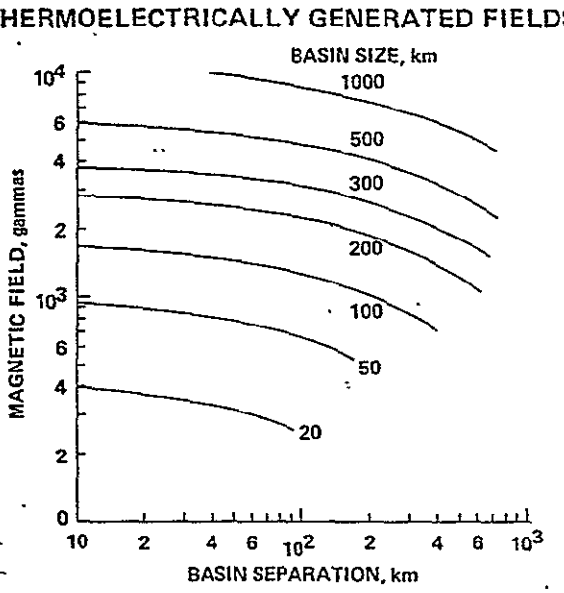

Fig. 8. Thermoelectrically generated magnetic field as a function of the basin separation for various basin sizes, evaluated at the coordinate system origin shown in Fig. 7. Calculations are based on a lunar crust thickness of 1 km and a thermoelectric potential of 10^3 μV/°K. The calculated field varies linearly with the thermoelectric potential but is a weak function of the crust thickness.

trical conductivity (Presnall *et al.*, 1972) results in a large increase in crustal resistance with a modest increase in crustal thickness. Using the measured temperature histories of terrestrial lava beds (Peck *et al.*, 1964) in our calculations, we obtain the result that the magnetic field rises approximately linearly with time as the basin lava cools. As the resolidifying crust thickens and its resistance continues increasing relative to that of the subsurface magma, the magnetic field value peaks and then declines rapidly. The magnetic fields calculated and shown in Fig. 8, which are the maxima for each given geometry, range from 10^3 to over 10^4 gammas. Fields of this magnitude, if present during lunar crustal cooling, could account for the measured remanence in returned lunar samples (Collinson *et al.*, 1973; Strangway *et al.*, 1970).

Summary and Conclusions

Crustal electrical conductivity

An upper limit on the electrical conductivity of the lunar crust has been determined from upper limits on toroidal induction in the moon by the solar wind $\mathbf{V} \times \mathbf{B}$ electric field. A theory is used for the spherically symmetric case of

the induction field totally confined to the lunar interior or near-surface regions by a highly conducting plasma. Components of toroidal field are calculated by subtracting components of the external field B_E measured by the Explorer 35-Ames magnetometer, from the total field B_A measured by the Apollo 12 lunar surface magnetometer. Comparing the appropriate components of toroidal magnetic field and electric field, we determine the upper limit of the proportionality factor relating these variables, $A = 2 \times 10^7$ sec/m. This factor is related to the average crustal conductivity upper limit of $\sigma_{crust} \sim 10^{-8}$ mhos/m for an assumed crustal thickness of 80 km. We note that the average crust conductivity is not a strong function of crust thickness for thicknesses ~80 km (e.g., a 100 km crust would correspond to a 1.2×10^{-8} upper limit, and a 60 km crust would correspond to about 7×10^{-7} mhos/m). A very thin outer shell of even lower conductivity (indicated by radar and sample measurements for depths up to ~1 km) are consistent with this upper limit. The surface conductivity upper limit, derived from toroidal induction analysis, places an important new constraint on the lunar conductivity profile (obtained from poloidal induction analysis); it lowers the crust conductivity limit nearly four orders of magnitude.

Thermoelectric origin for crustal remanent magnetism

Measurements of remanent magnetization in returned lunar samples indicate that magnetic fields of $\sim 10^3$ to $\sim 10^5$ gammas existed at the surface of the moon at the time of crustal solidification and cooling. We have derived a thermoelectric mechanism to model these magnetic fields as having resulted from currents flowing through cooling lava basins early in lunar history. When the crust was still only a few kilometers thick, infalling material could have penetrated it, exposing the magma beneath and forming many lava-filled basins. Our resulting model has two lava basins with different surface temperatures, connected beneath the surface by magma. The model has the basic elements of a thermoelectric circuit: two dissimilar conductors joined at two junctions which are at different temperatures. The thermal emf in the circuit depends on the electronic properties of the lunar crust and the plasma; in particular, on the difference in their Seebeck coefficients. Using a relative Seebeck coefficient of 10^3 μV/°K, we calculate thermoelectrically generated magnetic fields ranging from $\sim 10^3$ to $\sim 10^4$ gammas, as functions of basin sizes and separations. These fields are large enough to have produced the remanence in most of the returned lunar samples. Fields as high as $\sim 10^5$ gammas (indicated for some returned lunar samples) are attainable from our model if we use upper-limit values of the Seebeck coefficient and include effects of solar wind compression of lunar surface fields. The thermoelectric mechanism is compatible with the high degree of inhomogeneity found in measured remanent fields and with the absence of a measureable net global magnetic moment.

Acknowledgments—The authors thank Dr. William Barker of the University of Santa Clara for his help in developing theoretical concepts in the thermoelectric model; Dr. Thomas Mucha and Granger

ORIGINAL PAGE IS
OF POOR QUALITY

Lathrop of Computer Sciences Corporation for analysis and programming; and Marion Legg and Janice Hom of Diversified Computer Applications for their assistance in data reduction and analysis. We are pleased to acknowledge support for C.W.P. under NASA grant NSG-2075, and for W.D.D. under NASA grant NGR-45-001-040.

REFERENCES

Cadoff I. B. and Miller E. (1960) *Thermoelectric Materials and Devices*, p. 184–186. Van Nostrand Reinhold, New York.

Collinson D. W., Stephenson A., and Runcorn S. K. (1973) Magnetic properties of Apollo 15 and 16 rocks. *Proc. Lunar Sci. Conf. 4th*, p. 2963–2976.

Duba A. (1972) Electrical conductivity of olivine. *J. Geophys. Res.* 77, 2483–2495.

Dunlop D. J., Bailey M. E., and Westcott-Lewis M. F. (1975) Lunar paleointensity determination using anhysteretic remanence (ARM): A critique. *Proc. Lunar Sci. Conf. 6th*, p. 3063–3069.

Dyal P. and Parkin C. W. (1971a) Electrical conductivity and temperature of the lunar interior from magnetic transient-response measurements. *J. Geophys. Res.* 76, 5947–5969.

Dyal P. and Parkin C. W. (1971b) The Apollo 12 magnetometer experiment: Internal lunar properties from transient and steady magnetic field measurements. *Proc. Lunar Sci. Conf. 2nd*, p. 2391–2413.

Dyal P., Parkin C. W., and Daily W. D. (1974) Magnetism and the interior of the moon. *Rev. Geophys. Space Phys.* 12, 568–591.

Dyal P., Parkin C. W., and Daily W. D. (1976) Structure of the lunar interior from magnetic field measurements. *Proc. Lunar Sci. Conf. 7th*, p. 3077–3095.

Dyal P., Parkin C. W., Snyder C. W., and Clay D. R. (1972) Measurements of lunar magnetic field interaction with the solar wind. *Nature* 236, 381–385.

Goins N. R., Dainty A. M., and Toksöz M. N. (1977) The structure of the lunar interior as determined from seismic data (abstract). In *Lunar Science VIII*, p. 354–356. The Lunar Science Institute, Houston.

Hubbard N. J. and Minear J. W. (1975) A physical and chemical model of early lunar history. *Proc. Lunar Sci. Conf. 6th*, p. 1057–1085.

Ioffe A. F. (1957) *Semiconductor Thermoelements and Thermoelectric Cooling*. Infosearch, London. 184 pp.

King J. H. and Ness N. F. (1977) Data accuracy considerations for lunar permeability studies (abstract). In *Lunar Science VIII*, p. 546–548. The Lunar Science Institute, Houston.

Kuckes A. F. (1971) Lunar electrical conductivity. *Nature* 232, 249–251.

Kuckes A. F. (1974) Lunar magnetometry and mantle convection. *Nature* 252, 670–672.

Lin R. P., McGuire R. E., Howe H. C., and Anderson K. A. (1975) Mapping of lunar surface remanent magnetic fields by electron scattering. *Proc. Lunar Sci. Conf. 6th*, p. 2971–2973.

Noritomi K. (1975) Investigation of thermoelectricity for metallic and silicate minerals. *Geophysics* 7, 94–101.

Parker E. N. (1958) Dynamics of the interplanetary gas and magnetic fields. *Astrophys. J.* 128, 664–676.

Pearce G. W., Hoyle G. S., Strangway D. W., Walker B. M., and Taylor L. A. (1976) Some complexities in the determination of lunar paleointensities. *Proc. Lunar Sci. Conf. 7th*, p. 3271–3297.

Peck D. L., Moore L. G., and Kojima G. (1964) Temperatures in the crust and melt of Alae lava lake, Hawaii, after the August 1963 eruption of Kilauea volcano. A preliminary report. *U.S. Geol. Survey Prof. Paper 501D*, p. D1–D7.

Phillips R. J., Adams G. F., Brown W. E., Jr., Eggleton R. E., Jackson P., Jordan R., Peeples W. J., Porcello L. J., Ryu J., Schaber G., Sill W. R., Thompson T. W., Ward S. H., and Zelenka J. S. (1973) The Apollo 12 lunar sounder. *Proc. Lunar Sci. Conf. 4th*, p. 2821–2831.

Presnall D. C., Simmons C. L., and Porath H. (1972) Changes in electrical conductivity of a synthetic basalt during melting. *J. Geophys. Res.* 77, 5665.

Russell C. T., Coleman P. J., Jr., Fleming B. K., Hilburn L., Ioannidis G., Lichtenstein B. R., and Schubert G. (1975) The fine-scale lunar magnetic field. *Proc. Lunar Sci. Conf. 6th*, p. 2955–2969.

Schubert G. and Schwartz K. (1969) A theory for the interpretation of lunar surface magnetometer data. *The Moon* **1**, 106.

Schwartz K. and Schubert G. (1969) Time-dependent lunar electric and magnetic fields induced by a spatially varying interplanetary magnetic field. *J. Geophys. Res.* **74**, 4777.

Sill W. R. and Blank J. L. (1970) Method for estimating the electrical conductivity of the lunar interior. *J. Geophys. Res.* **75**, 201.

Simmons G., Strangway D., Annan P., Baker R., Bannister L., Brown R., Cooper W., Cubley D., de Bettencort J., England A. W., Groener J., Kong J., LaTorraca G., Meyer J., Nanda V., Redman D., Rossiter J., Tsang L., Urner J., and Watts R. (1973) Surface electrical properties experiment. In *Apollo 17 Prelim. Sci. Rep.*, NASA SP-330, p. 15-1 to 15-14.

Sonett C. P. and Colburn D. S. (1967) Establishment of a lunar unipolar generator and associated shock and wake by the solar wind. *Nature* **216**, 340.

Sonett C. P., Colburn D. S., Dyal P., Parkin C. W., Smith B. F., Schubert G., and Schwartz K. (1971) Lunar electrical conductivity. *Nature* **230**, 359.

Sonett C. P., Colburn D. S., Smith B. F., Schubert G., and Schwartz K. (1972) The induced magnetic field of the moon: Conductivity profiles and inferred temperature. *Proc. Lunar Sci. Conf. 3rd*, p. 2309.

Spitzer L., Jr. (1962) *Physics of Fully Ionized Gases.* Wiley, New York. 170 pp.

Srnka L. J. (1975) Sheath-limited unipolar induction in the solar wind. *Astrophys. Space Sci.* **36**, 177–204.

Stamper J. A. and Ripin B. H. (1975) Faraday-rotation measurements of megagauss magnetic fields in laser-produced plasmas. *Phys. Rev. Lett.* **34**, 138–141.

Stamper J. A., Papadopoulos K., Sudan R. N., Dean S. O., McLean E. A., and Dawson J. M. (1971) Spontaneous magnetic fields in laser-produced plasmas. *Phys. Rev. Lett.* **26**, 1012–1015.

Strangway D. W. (1969) Moon: Electrical properties of the uppermost layers. *Science* **165**, 1012–1013.

Strangway D. W., Larson E. E., and Pearce G. W. (1970) Magnetic studies of lunar samples-breccia and fines. *Proc. Apollo 11 Lunar Sci. Conf.*, p. 2435–2451.

Strangway D. W., Chapman W. B., Olhoeft G. R., and Carnes J. (1972) Electrical properties of lunar soil dependence on frequency, temperature, and moisture. *Earth Planet. Sci. Lett.* **16**, 275–281.

Telkes M. (1950) Thermoelectric power and electrical resistivity of minerals. *Amer. Mineral.* **35**, no. 7.

Tidman D. A. (1974) Strong magnetic fields produced by composition discontinuities in laser-produced plasmas. *Phys. Rev. Lett.* **32**, 1179–1181.

Wood J. A. (1975) Lunar petrogenesis in a well-stirred magma ocean. *Proc. Lunar Sci. Conf. 6th*, p. 1087–1102.

Wood J. A., Dickery J. S., Jr., Marvin U. B., and Powell B. N. (1970) Lunar anorthosites and a geophysical model of the moon. *Proc. Apollo 11 Lunar Sci. Conf.*, p. 965–988.

Appendix

Measurement accuracies of Explorer 35-Ames, Explorer 35-Goddard, and Apollo 12 magnetometers

Magnetic fields used in this study of the moon have been measured by magnetometers placed in lunar orbit and emplaced by astronauts on the lunar surface. The three instruments that were examined for errors were the two magnetometers onboard the Explorer 35 lunar orbiting spacecraft (one from Ames Research Center and one from Goddard Space Flight Center) and the Apollo 12 lunar surface magnetometer. The instrument characteristics are listed in Table 1.

Table 1. Lunar magnetometer characteristics.

Parameter	Apollo 12 LSM	Explorer 35 ARC	Explorer 35 GSFC
Ranges, gammas	0 to ±400	0 to ±200	0 to ±64
	0 to ±200	0 to ±60	0 to ±24
	0 to ±100	0 to ±20	
Resolution, gammas	0.2, 0.4, 0.8	0.2, 0.6, 2.0	0.094, 0.25
Frequency response, Hz	dc to 3	dc to 0.05	dc to 0.2
Sensors	3 orthogonal fluxgates	3 orthogonal fluxgates	3 orthogonal fluxgates
Analog zero determination	180° mechanical rotation of sensors	90° mechanical rotation of sensor	90°mechanical rotation of sensor
Power, watts	3.5	0.7	1.1
Weight, kg	8.9	2.4	2.7

The Apollo 12 surface instrument measured the three orthogonal vector components of the magnetic field with three sensors located at the end of three 100 cm long booms, and the orientation was determined by a shadowgraph and gravity level sensors. The two Explorer 35 instruments were located on ends of opposing booms several meters apart, and orientation was determined by sun sensors onboard the spacecraft. All three instruments were periodically calibrated by internal current sources, and the analog zero was determined by mechanical rotation of the sensors.

Direct comparisons of simultaneous time series magnetic field data have shown discrepancies in the two Explorer 35 magnetometer measurements. An example is shown in Fig. 9. The differences

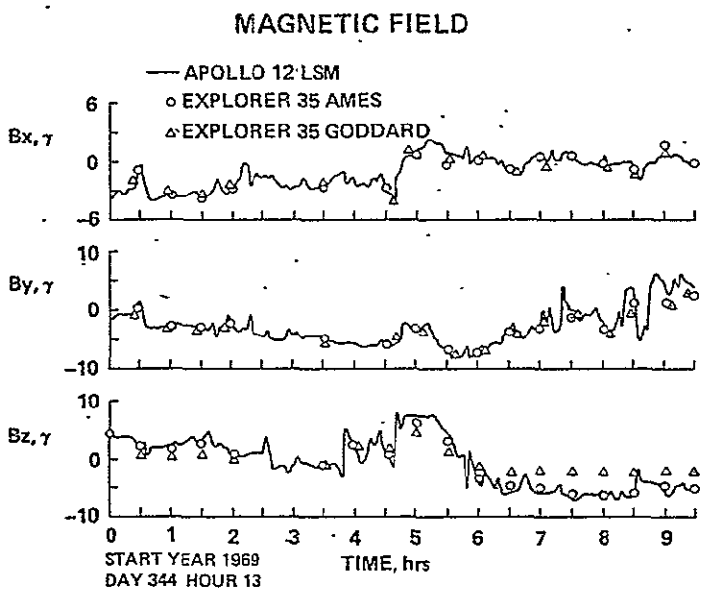

Fig. 9. Sample time-series data comparing all three vector components for the Apollo 12 lunar surface magnetometer (LSM), the Ames magnetometer aboard Explorer 35, and the Goddard magnetometer aboard Explorer 35. Although differences between the instruments are usually small (a few tenths of a gamma), occasionally differences imply errors of several gammas as indicated by the z-axis of the Goddard magnetometer in this figure.

ORIGINAL PAGE IS
OF POOR QUALITY

are usually on the order of 0.1 gamma; however, at hour 6 in the figure a difference of several gammas occurs in the z-axis measurement. The Apollo 12 surface instrument is more nearly in agreement with the Ames Explorer 35 magnetometer for this data set.

Further investigation of the instrument discrepancies has shown a relative gain difference (see also King and Ness, 1977) as well as the time-series amplitude difference shown in Fig. 9. The relative gain has been determined by statistically comparing the difference in two magnetometer measurements with the field measured by one of the magnetometers. The results for the x-axis in one lunation are shown in Fig. 10. The data show that the two Explorer 35 instruments have a 10% relative gain difference. A comparison with the Apollo 12 surface instrument indicates agreement with the Ames Explorer 35 magnetometer.

A history of the gain differences for the first five lunations after Apollo 12 deployment show that the relative error varies up to 10% in the x- and y-axes and up to 60% in the z-axis. Generally this relative gain difference between the Ames and Goddard Explorer magnetometers (typified by slopes shown in Fig. 10), when compared with Apollo 12 data, indicate the error to be due primarily to the Goddard magnetometer. The comparison of nine measured field components shows best consistency between the Explorer 35-Ames and Apollo 12 data. The Explorer 35-Ames instrument also has a spin demodulation problem which is indicated in the data beginning in March 1970. The spin demodulation error produces a monotonic drift of the field component in the instrument spin plane which can persist for 1–5 hr after exit from the lunar shadow. Errors due to this problem can be avoided by careful data selection. Therefore, we have used Ames Explorer 35 data for our analyses, after eliminating near-shadow data and after estimating the magnitude of systematic errors from the comparison of the Apollo 12 and Explorer 35-Ames data (approximately 3% maximum for the data sets that we have used).

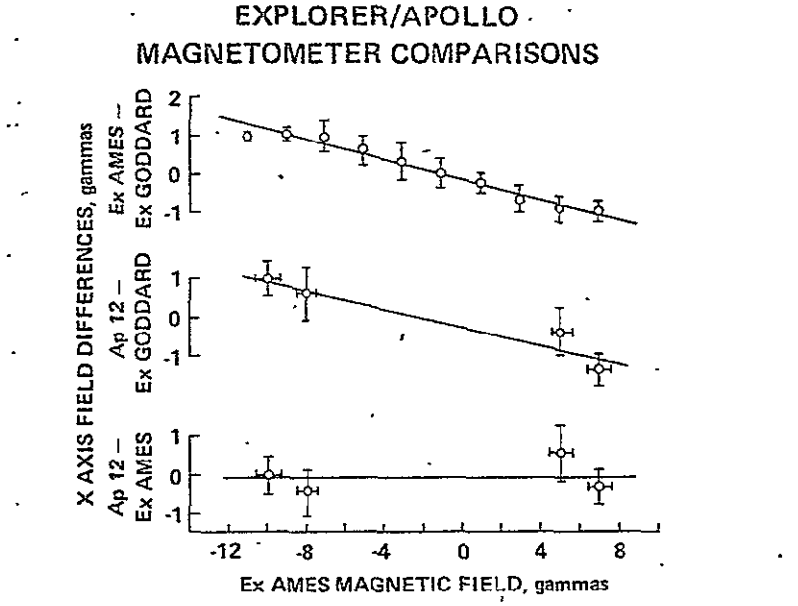

Fig. 10. Relative gain differences for the three lunar magnetometers (Apollo 12 LSM, Explorer 35-Ames, and Explorer 35-Goddard). Plotted are differences in each pair of magnetometer measurements versus the field measured by the Explorer 35-Ames magnetometer during one passage of the moon through the geomagnetic tail. With no gain differences between the three instruments the slopes of each plot would be zero. This example of radial x-axis data shows: (1) the two Explorer 35 magnetometers have a relative gain difference of about 10%, (2) the Apollo 12 and Explorer 35-Goddard magnetometers show a similar gain difference of about 10%, and (3) the Apollo 12 and Explorer 35-Ames magnetometers show the same gain to within statistical errors.

ELECTROMAGNETIC SOUNDING OF THE MOON USING APOLLO 16 AND LUNOKHOD 2 SURFACE MAGNETOMETER OBSERVATIONS (PRELIMINARY RESULTS)

L. L. VANYAN and T. A. VNUTCHOKOVA
Institute of Oceanology, U.S.S.R. Academy of Sciences, Moscow, U.S.S.R.

E. B. FAINBERG and E. A. EROSCHENKO
Institute of Terrestrial Magnetism, Ionosphere and Radiowave Propagation, U.S.S.R. Academy of Sciences, Moscow, U.S.S.R.

P. DYAL
NASA-Ames Research Center, Moffett Field, Calif., U.S.A.

C. W. PARKIN
Department of Physics, University of Santa Clara, Santa Clara, Calif., U.S.A.

and

W. D. DAILY
Eyring Research Institute, Provo, Utah, U.S.A.

(Received 5 September, 1977)

Abstract. A new technique of deep electromagnetic sounding of the Moon using simultaneous magnetic field measurements at two lunar surface sites is described. The method, used with the assumption that deep electrical conductivity is a function only of lunar radius, has the advantage of allowing calculation of the external driving field from two surface site measurements only, and therefore does not require data from a lunar orbiting satellite. A transient response calculation is presented for the example of a magnetic field discontinuity of February 13, 1973, measured simultaneously by Apollo 16 and Lunokhod 2 surface magnetometers.

Electromagnetic sounding of the Moon can be accomplished by simultaneously observing variations of the external and surface magnetic fields. The ratio of surface-response field to external field represents the electromagnetic response of the Moon. During times when the highly conducting solar wind plasma surrounds the day side of the Moon (all except for four days of each lunation when the Moon is in the geomagnetic tail), the external field can be calculated from surface measurements of the radial field component. This is possible since the induced field component radial to the Moon vanishes at the plasma-moon boundary if the included fields are confined to the lunar interior and cylindrical region downstream by the solar wind plasma. On the lunar day side, therefore, the measured total surface field radial component is equal to the radial component of the external inducing field. Furthermore, simultaneous measurements of radial components at any three locations on the day side not lying in the plane of the same great circle would allow calculation of all three components of the magnetic field external to the Moon.

We illustrate the new technique by modifying it for the case of two surface magnet-

The Moon 17 (1977) 259–262. *All Rights Reserved.*
Copyright © 1977 by D. Reidel Publishing Company, Dordrecht-Holland.

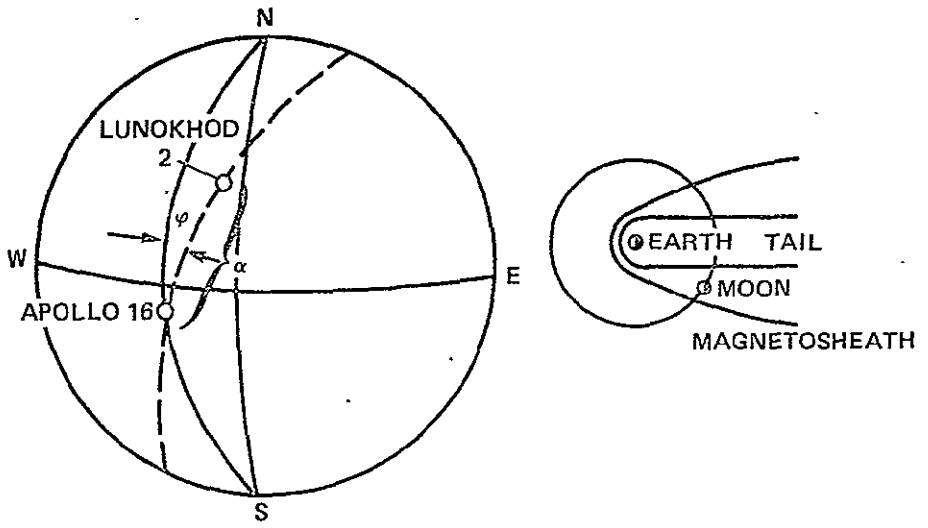

Fig. 1. (a) Apollo 16 and Lunokhod 2 site locations on the day side of the Moon for February 13, 1973. The great circle connecting the sites is shown as a dashed line. Here ϕ is the azimuthal angle between the meridian passing through the Apollo 16 site and the great circle passing through both landing sites; α is the angle between radius vectors to the two magnetometer sites. (b) Position of the Moon relative to the Earth on February 13, 1973.

ometers and applying it to synchronous Apollo 16 and Lunokhod 2 data. For convenience in this analysis we assume that the conductivity of the Moon is a function of radius only. We also employ the theory for induced fields totally confined to the lunar interior. This model is adequate if the field measurement sites are situated far enough from the terminator to neglect the field asymmetry caused by the plasma cavity behind the Moon. As has been shown by Schubert *et al.* (1973) for an infinitely extended cavity, and by Vanyan and Yegorov (1973) for a cavity of finite length, the assumption of a spherically symmetric model is valid over an angular range of 30 to 40° from the sub-solar point.

To develop this analysis with two surface measurements of the magnetic field, we consider a great circle on the lunar sphere through Apollo 16 and Lunokhod 2 surface sites (dashed line in Figure 1a). To estimate the lunar response we utilize the horizontal component tangent to the great circle at the Apollo 16 site

$$B_{\tau Ap} = B_{zAp} \cos \phi + B_{yAp} \sin \phi, \tag{1}$$

where ϕ is the angle between tangents to the great circle and the meridian intersecting at the Apollo 16 site; B_{zAp} and B_{yAp} are horizontal northward and eastward field components, respectively. A determination of the external field component $B^e_{\tau Ap}$ parallel to $B_{\tau Ap}$ will allow us to complete a transient response calculation. $B^e_{\tau Ap}$ can be determined from radial components B_{rAp} and B_{rL} recorded synchronously by Apollo 16 and Lunokhod 2. We note that both these components lie in the plane of the great-circle. From the equations which relate the Apollo 16 to Lunokhod 2 coordinate systems in the plane of their common great circle we obtain

ORIGINAL PAGE IS
OF POOR QUALITY

ORIGINAL PAGE IS
OF POOR QUALITY

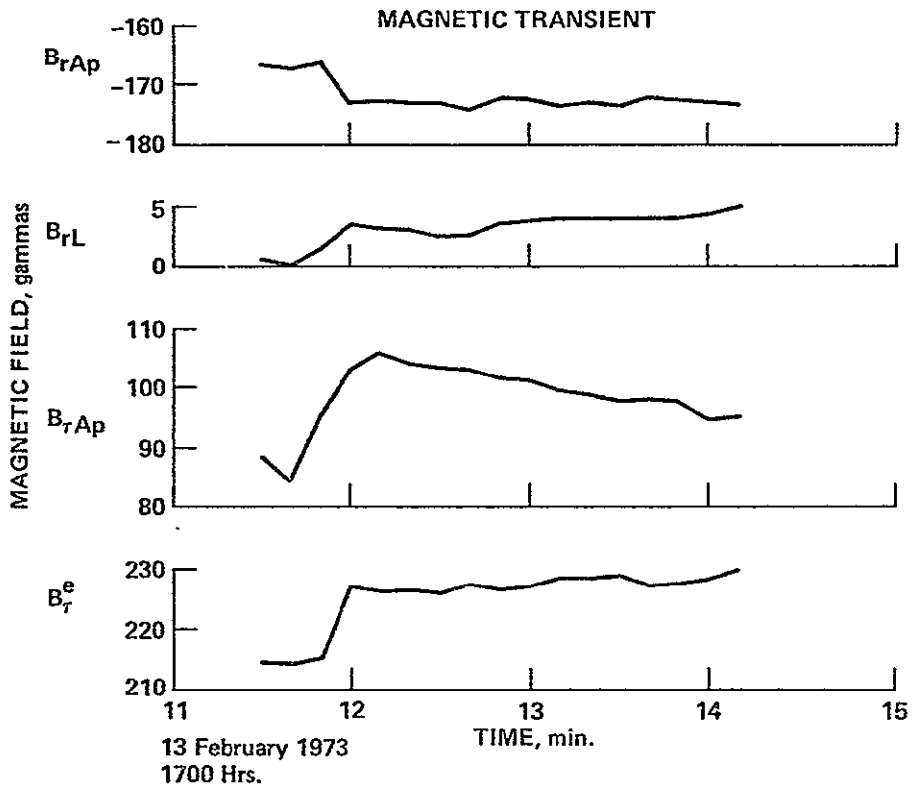

Fig. 2. Simultaneous Apollo 16 and Lunokhod 2 magnetograms from February 13, 1973. B_{rAp} and B_{rL} are the radial components of measured magnetic fields at the Apollo 16 and Lunokhod 2 sites respectively. $B_{\tau Ap}$ is the field component tangent to the lunar surface at the Apollo 16 site. B_τ^e is the field component external to the Moon (calculated using B_{rAp} and B_{rL} in Equation (2)) which corresponds to the measured total lunar response field $B_{\tau Ap}$.

$$B_\tau^e = B_{rL} \operatorname{cosec} \alpha - B_{rAp} \cot \alpha, \tag{2}$$

where $\alpha = 38^\circ$ is the angle between radius vectors to Apollo 16 and Lunokhod 2.

As an example to illustrate the new technique we consider the magnetic field discontinuity recorded at 17h 12m on February 13, 1973, when the Moon was in the magnetosheath (Figure 1b). Figure 1a shows the dayside of the Moon on that date, and we note that both the Apollo 16 and Lunokhod 2 sites were situated far enough from the terminator at that time to neglect field confinement asymmetry effects. Lunokhod 2 was located in the southern part of Le Monnier crater at the eastern boundary of Mare Serenitatis.

The Apollo 16 magnetometer is located at 8.9 °S latitude 15.5 °E longitude. Figure 2 shows plots of the radial components of the data, B_{rAp} and B_{rL}, at the two sites and the tangential component $B_{\tau Ap}$ at the Apollo site calculated from Equation (1). The magnetic transient external to the Moon, B_τ^e plotted in Figure 2 was calculated using Equation (2). The amplification of the tangential component

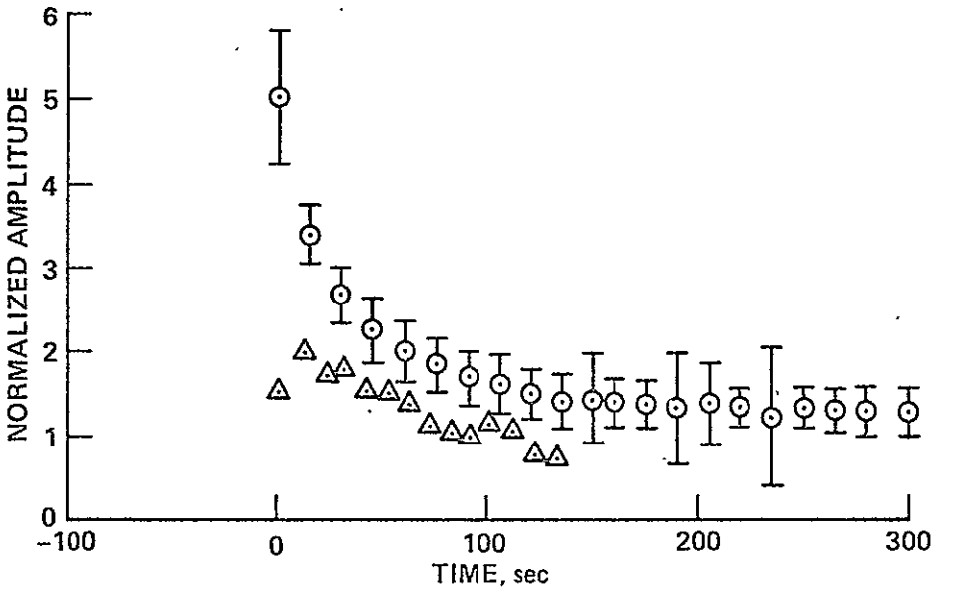

Fig. 3. Amplification of tangential components: $h = B_{\tau Ap}/B_\tau^e$ (triangles), determined from the bottom two curves in Figure 2, which were in turn calculated using simultaneous Apollo 16 and Lunokhod 2 magnetometer data. These data are compared with day side amplification results (open circles) determined from Apollo 12 and Explorer 35 data (Dyal *et al.*, 1973).

$$h_{Ap}(t) = B_{\tau Ap}/B_\tau^e \tag{3}$$

is calculated for the time interval $t = 5$ to 130 sec and plotted (triangles) in Figure 3. These results are compared with the statistical day side results of Dyal *et al.* (1973) obtained using synchronous Apollo 12 and Explorer 35 magnetometer data (open circles). We see that the transient response obtained by applying the present technique differs from the previous results especially during the initial part of the transient. This discrepancy most likely arises because we have compared an individual data set to statistically averaged data. We anticipate that superposition of many events will result in greatly enhanced accuracy, making this a valuable new technique for electromagnetic sounding of the lunar interior.

Acknowledgements

The Soviet authors are most grateful to Sh. Sh. Dolginov and L. I. Zhuzgov for their participation in the Lunokhod 2 experiment and for helpful discussions. Support is gratefully acknowledged by C.W.P. under NASA Grant NSG-2075 and W.D.D. under NASA Grant NSG-2082.

References

Dyal, P., Parkin, C. W., and Daily, W. D.: 1973, In *Proc. Fourth Lunar Sci. Conf.*, 3, (W. A. Gose ed.), pp. 2925–2945, Pergamon Press, New York.

Schubert, G., Sonett, C. P., Schwartz, K., and Lee, H. J.: 1973, *J. Geophys. Res.* 78, 2094–2110.

Vanyan, L. L and Yegorov, I. V.: 1973, *Cosmic Research 11*, 6, 823–834.